CATALYTIC OXIDATIVE CO_2 REFORMING OF METHANE OVER BIMETALLIC Pd-Ni CATALYST

USMAN OEMAR

NATIONAL UNIVERSITY OF SINGAPORE

2011

CATALYTIC OXIDATIVE CO_2 REFORMING OF METHANE OVER BIMETALLIC Pd-Ni CATALYST

USMAN OEMAR

(B.Sc, Parahyangan Catholic University, Indonesia)

A THESIS SUBMITTED

FOR THE DEGREE OF Ph.D. OF ENGINEERING

DEPARTMENT OF CHEMICAL AND BIOMOLECULAR ENGINEERING

NATIONAL UNIVERSITY OF SINGAPORE

2011

Acknowledgements

First of all, I would like to express my sincerest thanks to my supervisor, Prof. Kus Hidajat, for his help throughout my PhD candidature period. I also would like to express my thanks to Prof. Sibujing Kawi who always gave me many constructive suggestions, critics and ideas. I appreciate their constant encouragement and invaluable guidance, patience, and understanding. Their expertise in this area helped me a lot whenever I met problems during my research. This project had been a tough but enriching my experience in research.

I also want to take this chance to thank all our group members: Kesada Sutthiumporn, Warintorn Thitsartarn, Thawatchai Maneerung, Yasotha Kathiraser, Saw Eng Toon, Dr. Wu Xusheng, and Dr. Ni Jun. I also would like to thank all of my friends in Batam who has given me encouragement and support throughout my research time. They are all my best friends. They have given me a lot of help and suggestions. The time I spent with them will be priceless good memory.

Special mentions should go to Ang Wee Siong, Alyssa Tay, Novel Chew, Mdm Jamie Siew, and Mr. Ng Kim Poi for all the help they offered throughout my research. My thanks also should give to Mr. Liu Zhicheng, Mdm Samantha Fam, Dr. Yuan Ze Liang, and Mr. Chia Phai Ann.

Last but not least, I also wish to thank National University of Singapore for providing me scholarship, excellent environment, and abundant resources of research.

This PhD thesis is dedicated to my wife, Eva Suyenty, and my parents for their encouragement and support throughout my hard time.

Table of Contents

Summary

Catalytic CO_2 (dry) reforming of methane (DRM) is an attractive technology for syngas production as DRM utilizes CO_2 and CH_4, which are two major greenhouse effect gases are causing global warming. However, besides high energy requirement, serious problems in this reaction are high carbon deposition rate and metal sintering which can easily deactivate the catalyst. Due to these serious drawbacks, it is desirable to consider oxidative CO_2 reforming of methane (OCRM) which combines partial oxidation of methane (POM) – an endothermic reaction – with CO_2 reforming of methane (DRM) – an endothermic reaction. A combination of these two reactions not only can reduce the amount of carbon deposition since the oxygen can easily oxidize the deposited carbon on the catalyst, but also can reduce the total energy requirement since OCRM combines both exothermic POM and endothermic DRM reactions. This thesis reports the development of a stable and active bimetallic catalyst for OCRM reaction. A fundamental understanding causing high activity and stability of the catalyst was explored in depth in this thesis.

The catalyst activity and stability of Pd−Ni catalysts over various commercial catalyst supports were studied at various reaction temperatures. Among all tested Pd−Ni catalysts, Pd−Ni/Y_2O_3 and Pd−Ni/Al_2O_3 catalysts show very high CH_4 and CO_2 conversions due to the formation of metal−support compound (MSC) on these catalysts. The presence of MSC on these catalysts could prevent severe metal sintering on catalyst during reaction. However, the amount of deposited carbon on the spent Pd−Ni/Y_2O_3 catalyst is much lower than the one on the Pd−Ni/Al_2O_3 catalyst due to the presence of surface β−oxygen species and ability of Y_2O_3 to form oxycarbonate species, resulting in

stable catalytic performance without noticeable deactivation during reaction. The surface β−oxygen species are found to promote cracking of C−H bond in CH_4 while the oxycarbonate species can oxidize the deposited carbon, respectively, hence leading to the stability of the Pd−Ni/Y_2O_3 catalyst. A reaction mechanism over Pd−Ni/Y_2O_3 catalyst was then proposed.

Further investigation was performed to understand the role of Pd precursors on the Pd−Ni catalyst. A series of Pd−Ni/Y_2O_3 catalysts with various Pd/Ni ratios and Pd precursors ($PdCl_2$ and $Pd(NO_3)_2$) was synthesized. The catalytic activity of Pd−Ni/Y_2O_3 catalysts synthesized from either $PdCl_2$ or $Pd(NO_3)_2$ is much higher than the one on either Ni/Y_2O_3 or Pd/Y_2O_3 catalyst due to the presence of bimetallic particles on Pd-Ni catalysts. However, the Pd(C)−Ni/Y_2O_3 catalyst (Pd−Ni/Y_2O_3 catalyst prepared from $PdCl_2$) has higher catalytic activity than the Pd(N)−Ni/Y_2O_3 catalyst (Pd−Ni/Y_2O_3 catalyst prepared from $Pd(NO_3)_2$) due to smaller metal particle size. The results of effect of Pd/Ni ratio on Pd(C)−Ni/Y_2O_3 catalysts shows that the smallest metal particle size of Pd(C)−Ni/Y_2O_3 was observed on Pd(C)−Ni/Y_2O_3 catalyst with the highest reduction temperature of metal−support compound (Pd-Y_2O_3 compound), showing that the formation of Pd-Y_2O_3 compound on the Pd(C)−Ni/Y_2O_3 catalyst plays an important role on catalyst activity. The catalytic stability result shows that Pd(C)−Ni/Y_2O_3 catalyst has stable performance while Pd(N)−Ni/Y_2O_3 catalyst has decreasing performance, showing that the presence of Pd−Y_2O_3 compound on the Pd(C)−Ni/Y_2O_3 catalyst also play an important role in high catalyst stability of the Pd(C)−Ni/Y_2O_3 catalyst. Based on all characterization and catalytic results, a Ni−rich Pd−Ni alloy was proposed for Pd(C)−Ni/Y_2O_3 catalyst while a Pd−rich Pd−Ni alloy structure was proposed for Pd(N)−Ni/Y_2O_3 catalyst.

The monodispersed Y_2O_3 particles were then synthesized at various pH of the solution. The synthesized Y_2O_3 particles were used as the support of Pd−Ni catalyst. The Y_2O_3 particles synthesized at lower pH have smaller particle and crystal size, resulting in higher surface oxygen mobility. The catalytic activity results show that the performance of Pd−Ni catalyst over Y_2O_3 with smaller crystal size is higher than those with bigger crystal size. In addition, the carbon deposition rate on the spent Pd−Ni/Y_2O_3 catalyst with smaller crystal size at higher temperature is also lower than those with bigger crystal size. Furthermore, CH_4 decomposition reaction was also performed on the Pd−Ni/Y_2O_3 catalysts and the result shows the higher amount of CO produced from Pd−Ni/Y_2O_3 catalyst with smaller crystal size. These results show that surface oxygen mobility of Y_2O_3 support plays important roles in high catalytic activity and suppression of carbon deposition on Pd−Ni/Y_2O_3 catalyst.

Based on the proposed reaction mechanism and those of individual reactions probably occurred during OCRM reaction, two kinetic models for OCRM reaction over Pd−Ni/Y_2O_3 catalyst have been developed using Langmuir-Hinshelwood (LH) approach. A good agreement was obtained between experimental and model for the kinetic model based on dissociation of adsorbed methane by adsorbed oxygen for rate determining step (RDS) of DRM and reaction between adsorbed carbon and adsorbed oxygen for RDS of POM.

In summary, the important findings from this thesis are as follows: 1) The formation of bimetallic particle has synergetic effect on catalyst activity, 2) Small metal particle size resulted from the presence of metal-support compound is important for high catalyst activity, 3) The high amount of β-oxygen on Y_2O_3 support and its ability to form

oxycarbonate species is required for high catalyst stability, 4) surface oxygen mobility has important roles in high catalyst activity and reduction of carbon deposition, and 5) the developed kinetic model has a good agreement with experiment data and proposed mechanism.

Keywords: CO_2 utilization; Oxy-CO_2 reforming of methane; Syngas production; Pd-Ni catalyst; metal-support compound; surface oxygen mobility; kinetic model

Nomenclature

^{o}C	Centigrade degree
BET	Brunauer Emmett Teller method
DRM	CO_2 (dry) Reforming of Methane
FESEM	Field Emission Scanning Electron Microscope
FT-IR	Fourier Transform Infra-Red
GC	Gas Chromatography
GHSV	Gas Hourly Space Velocity
LH	Langmuir-Hinshelwood
OCRM	Oxidative CO_2 Reforming of Methane
POM	Partial Oxidation of Methane
rWGS	Reverse Water Gas Shift
SRM	Steam Reforming of Methane
TCD	Thermal Conductivity Detector
TEM	Transmission Electron Microscope
TGA	Thermal Gravimetric Analysis
TPR	Temperature Programmed Reduction
Vol-%	Volume percentage
XPS	X-ray Photoelectron Spectroscopy
XRD	X-Ray Diffraction
WGS	Water Gas Shift
Pd/Ni	Molar ratio of Pd and Ni

C_T	total surface concentration of active site, mol m^{-2}
ID	Inner diameter of reactor, mm
Dp	Catalyst particle size, mm
E_i	Activation energy for reaction I, kJ mol^{-1}
F	Molar flow rate of methane, mol s^{-1}
ΔH_i	Heat of adsorption for surface species i or heat of reaction for formation of surface species i, kJ mol^{-1}
K_i	Equlibrium constant of reaction i or adsorption coefficient for surface species $_i$
k_i	Rate constant for reaction i, m^2 s^{-1} mol^{-1}
A_i	Pre-exponential rate constant for reaction i, m^2 s^{-1} mol^{-1}
L	Catalyst bed height, mm
P	Operating pressure, atm or kPa
P_i	Partial pressure of component i, atm or kPa
r_i	Rate of reaction of component i, mol^2 s^{-1}
S_A	Surface area of catalyst, m^2 g_{cat}^{-1}
ΔS_i	Entropy of adsorption of species I, J mol^{-1} K^{-1}
W	Mass of catalyst, g

List of Figures

List of Tables

Chapter 1

Introduction

1.1 Background

In recent years, CO_2 amount has increased dramatically due to human activities, such as combustion of fuel for power generation, transportation, and industry. This has created accumulation of CO_2 gas in the earth. Since CO_2 absorbs solar radiation, the CO_2 accumulation causes increase in the earth's temperature, which is known as global warming. This global warming phenomenon is a major concern, and hence this has attracted many researchers to either capture and store or utilize CO_2 in order to reduce the amount of CO_2 gas present in the atmosphere.

Several technologies have been used to capture and store CO_2, for example adsorption by utilizing CaO as an adsorbent [1], membrane separation [2], as well as extraction and absorption [3, 4]. In the area of CO_2 utilization, several ways have been introduced, such as utilizing high amount of CO_2 to produce higher photosynthesis rate in microorganisms, such as algae or bacteria [5], CO_2 for organic synthesis to produce methanol, dimethyl ether (DME), dimethyl carbonate (DMC), urea, and polycarbonate [6-9], and CO_2 to produce hydrogen and/or syngas via CO_2 (dry) reforming of methane (DRM) reaction [10]. The DRM reaction has been getting increasing interest from academic and industrial point of views in the past few years since it involves utilization of not only CO_2, but also methane gas, which also contributes to global warming [11-12]..

Until now, Group VIII transition metals (Fe, Co, Ni, Ru, Rh, Pd, Ir, Pt) when distributed in reduced form on suitable supports have been found to be effective catalysts

for the DRM reaction. Among non-noble metals catalysts (Fe, Co, and Ni), Ni catalyst gives the highest conversion of methane and CO_2, but it is easily deactivated due to carbon formation. Over noble metals catalysts (Pd, Pt, Ir, Ru, and Rh), Rh catalyst is found intrinsically to be suitable catalyst for this reaction [13]. The activity of noble metal catalysts is comparable to the one of the nickel catalyst. However, the noble metal catalysts produce less carbon on catalyst surface. According to Hu and Ruckenstein [10], the carbon deposition rate decreases in this order: Ni >> Rh > Ir = Ru > Pt = Pd at 773 K and Ni > Pd = Rh > Ir > Pt >> Ru at 923 K.

Since noble metal catalysts are expensive, nickel catalyst appears to be the most suitable catalyst because it is very cheap. However, nickel catalyst has to be modified to improve its performance in terms of stability by reducing its carbon deposition rate. It is well established that catalyst support [14-16] and/or promoter [16, 17] have significant effect on the catalyst activity and stability of the nickel catalyst. For example, Zhang and Verykios [15] studied effect of catalyst supports and reported that the Ni/La_2O_3 catalyst showed higher activity and stability than the Ni/Al_2O_3 and Ni/CaO catalysts due to its ability to form oxycarbonate species ($La_2O_2CO_3$). Another example focusing on effect of promoters over Ni catalyst is shown by Horiuchi et al. [17]. They found that addition of basic metal oxides (Na_2O, K_2O, MgO, and CaO) enhanced CO_2 adsorption, resulting in more adsorbed oxygen atoms (O_{ad}). The higher amount of adsorbed oxygen atoms (O_{ad}) prevent adsorbed hydrogen-deficient hydrocarbon species ($CH_{x,ad}$) to decompose to surface carbon since the oxygen can easily react with the adsorbed hydrogen-deficient hydrocarbon species ($CH_{x,ad}$) to form CO.

Even though catalyst modification can reduce the carbon deposition rate, energy requirement for the DRM reaction is very huge because of its high endothermicity. The

high energy requirement is the drawback hindering the commercialization of the DRM reaction in industries. One way to overcome this drawback is by introducing an exothermic reaction, such as partial oxidation of methane (POM). The energy required for the DRM and released from the POM can be seen in the following reactions:

DRM: $CH_4 + CO_2 \rightarrow 2\ H_2 + 2\ CO \quad \Delta H°_{298} = 247.3$ kJ/mol

POM: $CH_4 + ½O_2 \rightarrow 2\ H_2 + \quad CO \quad \Delta H°_{298} = -35.6$ kJ/mol

This combined reaction system is named as Oxy-CO_2 Reforming of Methane (OCRM). The reaction system can reduce not only the total energy requirement, but also the amount of carbon deposition since the oxygen available in the reaction system can easily oxidize the deposited carbon on the catalyst. Another distinct advantage is that the OCRM reaction enables production of syngas with various ratios of H_2/CO via manipulation of the feed composition.

Ashcroft et al. [18] were the first ones to study the catalysts for OCRM reaction and they found that the order of catalyst activity for OCRM reaction was Ir/Al_2O_3 = Ni/Al_2O_3 > Rh/Al_2O_3 > Pd/Al_2O_3 > Ru/Al_2O_3. However, the carbon deposition in Ni/Al_2O_3 catalyst is the highest among the others with the order Ni/Al_2O_3 >> Pd/Al_2O_3 > Ir/Al_2O_3 = Rh/Al_2O_3 = Ru/Al_2O_3.

Even though Ir/Al_2O_3 catalyst was found to be the best catalyst for this reaction system, the price is very expensive due to its limited availability. Therefore, Ni catalyst appears to be suitable catalyst for this reaction since it is very cheap. However, the modification of Ni catalyst is required to reduce the carbon deposition rate.

Besides the carbon deposition problem, Ni catalyst was also reported to form hot-spot formation in the presence of oxygen in the feed, such as in POM reaction.

Dissanayake et al. [19] reported that even though the Ni/Al_2O_3 catalyst was fully reduced, oxygen in the feed easily oxidized metallic Ni particles to NiO particles. Therefore, the upstream section of catalyst bed consisted of mixture of $NiO+A1_2O_3$. This NiO species were active only for methane oxidation reaction, resulting in a sudden increase in temperature of the bed. Since oxygen had been consumed in the upstream section, the lower section of the catalyst bed consisted of a reduced Ni/Al_2O_3 phase, which catalyzed reaction to produce CO and H_2.

Tomishige et al. [20] reported that noble metals catalysts (Pd, Pt, Au, Ir, Rh, or Ru) were effective to suppress the hot-spot formation near the catalyst bed inlet in oxidative steam reforming of methane (OSRM) reaction. Among other noble metals, palladium (Pd) was found to be more superior since it could maintain the reduced state of metallic particles. Therefore, in order to develop a high performance Ni-based catalyst in terms of high activity and stability for the OCRM reaction, modification of Ni catalyst is carried out by adding a small amount of Pd.

1.2 Thesis objective

The main objective of this thesis is to develop high performance catalyst, in terms of activity and stability for OCRM reaction by focusing on modification of the Ni catalyst using a small amount of palladium (Pd). In order to achieve the main objective, the following steps of studies are carried out:

i) Investigation on effect of catalyst support over Pd-Ni catalyst

Catalyst support is well known to have strong effect on catalyst activity and stability. For example, Ruckenstein and Hu [21] showed that the Ni/MgO catalyst

had higher stability than Ni/SiO_2 and Ni/Al_2O_3 catalysts, due to less carbon deposition. Sufang et al. [22] also reported that the addition of Al_2O_3 to Ni/SiO_2 catalyst resulted in higher carbon deposition rate.

ii) Investigation on role of Pd and Ni in Pd-Ni catalyst.

Using the best result from study of catalyst supports, the roles of Pd and Ni in Pd-Ni catalyst on catalyst activity and stability are investigated.

iii) Investigation on effect of synthesized support

Since commercial metal oxide used in previous study as catalyst support has irregular morphology, it is necessary to synthesize metal oxide with regular morphology. The activity and stability of the Pd-Ni catalyst over synthesized support is then investigated to elucidate the effect of synthesized support.

iv) Development of a kinetic model based on Pd-Ni catalyst for OCRM reaction.

In order to understand OCRM reaction, a development of kinetic model is necessary to elucidate the reaction mechanism as well as to perform scale-up to commercial scale. The developed model incorporates all possible main and side reactions occurring during OCRM reaction.

1.3 Organization of thesis

This thesis consists of 6 chapters including Introduction as the Chapter 1. Chapter 2 presents literature review of the catalyst development and the mechanisms of all reaction pathways involved in OCRM reaction, such as DRM and POM reactions.

Chapter 3 discusses the main findings from effect of catalyst supports over Pd-Ni catalyst. In this chapter, results and discussion of the Pd-Ni catalysts synthesized over few

different commercial metal oxides as catalyst supports are presented. The catalyst activity is investigated at a wide range of temperature.

The best result from study of catalyst supports is further investigated to elucidate roles of Pd and Ni in Pd-Ni catalyst. The results and discussion is presented in Chapter 4. Two type of of Pd precursors, i.e. $PdCl_2$ or $Pd(NO_3)_2$ and various ratios of Pd/Ni are used to elucidate the role of Pd and Ni.

In Chapter 5, the catalyst supports were synthesized using homogeneous precipitation method at different pH to obtain monodisperse particles. They were then used as the support for Pd-Ni catalysts to study the effect of synthesized supports on catalyst activity of Pd-Ni catalysts.

Chapter 6 presents the kinetic modeling of the OCRM reaction over Pd-Ni/Y_2O_3 catalyst. The kinetic model is developed by incorporating all possible main and side reactions in which occur during OCRM reaction. The developed model is fitted to the experiment results to obtain the best model.

Chapter 7 is the final discussion of the catalyst developed in this thesis, the principal contributions of this thesis, and directions for future works.

Chapter 2

Literature Review

2.1. CO_2 reforming of methane

CO_2 (dry) reforming of methane (DRM) is an attractive method to utilize CO_2 and CH_4 in large amount. Both reactants are reported to be the two major greenhouse effect gases [23]. The DRM reaction is described as follows:

$$CO_2 + CH_4 \rightarrow 2CO + 2H_2 \qquad \Delta H°_{298} = 247.3 \text{ kJ/mol} \qquad (1)$$

$$\Delta G° = 61770 - 67.32T$$

This reaction is highly endothermic and favorable at low pressure. The reaction equilibrium of DRM is influenced by the simultaneous reverse water gas shift (rWGS) reaction (Eq. 2), which results in a H_2/CO ratio of less than unity and higher CO_2 conversion than CH_4 conversion. The rWGS reaction can be described as follows:

$$CO_2 + H_2 \rightarrow CO + H_2O \qquad \Delta H°_{298} = 41 \text{ kJ/mol} \qquad (2)$$

$$\Delta G° = -8545 + 7.84T$$

Due to high endothermicity, DRM reaction is usually performed at high temperature. The high reaction temperature favors carbon formation via methane (CH_4) decomposition (Eq. 3) and Boudouard (CO disproportionation) reactions (Eq. 4) which are thermodynamically feasible.

Methane decomposition: $CH_4 \leftrightarrow C + 2H_2$ $\Delta H°_{298} = 75 \text{ kJ/mol}$ (3)

$$\Delta G° = 21960 – 26.45T$$

Boudoudard reaction: $2CO \rightarrow C + CO_2$ $\Delta H°_{298} = -172 \text{ kJ/mol}$ (4)

$$\Delta G° = -39810 + 40.87.84T$$

Using standard free energies calculations, Wang et al. [24] showed the limiting temperatures of all reactions involved in DRM reaction and the results were tabulated in Table 2-1. From the calculation, they reported the following conclusions:

- The DRM reaction proceeds at temperature above 640°C, accompanied by methane decomposition.
- The rWGS and Boudouard reactions will not take place at temperatures above 820°C.
- Formation of carbon most likely takes place within the temperature range 557-700°C, from both the Boudouard reaction and methane decomposition.

Table 2-1 Limiting temperature for reactions in DRM reaction

Reaction	Temperature (°C)	
	Lower limit	Upper limit
DRM reaction	640	-
rWGS reaction	-	820
Methane decomposition	557	-
Boudouard reaction	-	700

The experiment results by Zhang et al. [25] also showed that CH_4 decomposition and Boudouard reactions were responsible for carbon deposition on the catalyst. In addition, they also showed the variation of equilibrium constants of the reactions involved as a function of temperature. Due to strong endothermicity, the equilibrium constant of the DRM reaction increases significantly with increasing reaction temperature. Therefore, high conversion of the DRM reaction can only be achieved at high temperature. However,

the equilibrium constants of methane decomposition and rWGS reactions also increase with temperature. In contrast, Boudouard reaction is unfavorable at high temperature because of exothermic reaction. Hence, equilibrium conversion of the DRM reaction increases much higher than those of the side reactions (Eq. 2-4) at high reaction temperatures (i.e. 750°C and above).

Numerous authors [23, 26-27] have presented calculations which predict thermodynamic potential of graphic carbon deposition as a function of operating conditions for gas mixtures containing CH_4, CO_2, H_2, and H_2O. From the calculations, they suggested operation for the DRM reaction at higher temperature, ~727°C, and with CO_2/CH_4 ratios far above unity to avoid regions where there is a potential for carbon formation. However, from an industrial point of view, lower temperature with CO_2/CH_4 ratios near unity is preferred due to cheaper operating cost. Therefore, a lot of studies have been performed to develop a catalyst which incorporates a kinetic inhibition of carbon formation with CO_2/CH_4 ratios near unity.

A lot of transition metals, especially Group VIII show catalytic activity for CO_2 reforming of methane. The metals in Group VIII (Fe, Co, Ni, Ru, Rh, Pd, Os, Ir, and Pt) in their reduced forms constitute effective catalytic components, except Fe, which appears to be inactive and there is no reported data for Os. Non-noble metals such as Ni and Co have advantage over noble metals in terms of price. Their prices are much cheaper than those noble metals, but they are easily deactivated due to carbon formation. Rostrup-Nielsen and Hansen [28] reported that the amount of carbon deposited on metal catalysts decreases in the order Ni >> Rh > Ir = Ru > Pt ≈ Pd at 773 K and Ni > Pd = Rh > Ir > Pt >> Ru at 923 K. Hence, the noble metal catalysts exhibit higher selectivity and much less carbon deposition than the nickel catalyst.

2.1.1. Non-noble metal catalysts

Ruckenstein and Hu [29] studied Ni catalyst over catalyst support such as Al_2O_3, SiO_2 or TiO_2. They found that the activity and selectivity of Ni-supported catalysts depended on the nature of support and decreased with order of Ni/Al_2O_3> Ni/SiO_2> Ni/TiO_2. The low activity in Ni/TiO_2 catalyst is due to strong metal support interaction (SMSI). During reduction, TiO_x molecules migrate over the surface of Ni particles, thus it blocks active sites and leads to a decrease in surface free energy of the system. Moreover, it was also reported that the carbon deposition depended strongly on the nickel loading [30]. A 13.6 wt% Ni/SiO_2 catalyst exhibited a greater carbon deposition than a 1 wt% Ni/SiO_2 catalyst. However, a physical mixture of SiO_2 and nickel minimized the amount of deposited carbon [31], while a physical mixture of Al_2O_3 and nickel produced a greater amount of carbon deposition [29]. The comparison showed that the Al_2O_3 surface promoted carbon deposition.

Chen and Ren [32] reported formation of spinel phase $NiAl_2O_4$ compound in Ni/Al_2O_3 catalyst during calcination as a result of strong $Ni\text{-}Al_2O_3$ interaction. The presence of this compound suppressed carbon deposition, due to strengthening of the Ni–O bond in $NiAl_2O_4$ compound when compared to that in the NiO crystal [33]. The stronger Ni–O bond decreases the reducibility of Ni^{2+} to Ni^0, resulting in smaller nickel crystallites on the catalyst surface. These smaller nickel crystallites are necessary for lower carbon deposition rate [34].

Similar results were also obtained by Wang and Lu [35]. Their results showed that Ni/Al_2O_3 catalyst had very high activity, stability and high coking compared to Ni/CeO_2 catalyst. They believed that the same reason of strong metal-support interaction (SMSI) for low activity of Ni/TiO_2 catalyst could be applied for Ni/CeO_2 catalyst. Nevertheless,

the addition of CeO_2 as promoter to Ni/Al_2O_3 catalyst had increased the catalytic activity, stability, and coking resistance [36]. A loading of 1–5 wt% CeO_2 was found to be the optimum range. These phenomena were attributed to the nature of different supports and the interaction between metal and support/promoter since CeO_2 as a promoter for the nickel catalysts decreases the strength of the interactions between the nickel oxide and support, resulting in an increase in the reducibility of the nickel oxide and higher nickel dispersion.

Bradford and Vannice [37] also studied nickel catalysts supported on MgO, TiO_2, SiO_2, or activated carbon. They found that different catalyst supports provided remarkable different influence on catalyst activity and carbon deposition resistance. Ni/SiO_2 catalyst had similar catalytic activity with Ni/C catalyst, but there was considerable formation of filamentous carbon over Ni/SiO_2 catalyst. Nevertheless, the initial loss of catalytic activity on Ni/SiO_2 catalyst was negligible. They argued that the lack of metal-support interaction in Ni/SiO_2 catalyst permitted substantial formation of filamentous whisker carbon. They also confirmed strong metal-support interaction (SMSI) on Ni/TiO_2 catalyst through TEM identification of TiO_x phases, supressed hydrogen chemisorption, and extremely low value of heat of adsoption from carbon monoxide adsorption isotherm. On the other hand, although the activity of Ni/MgO catalyst was the least active of all tested catalysts, Ni/MgO catalyst showed stable activity without detectable deactivation for up to 44 hours. It is well-known that MgO is a basic metal oxide and has the same crystal structure as NiO. As a result, the combination of MgO and NiO results in a solid solution catalyst with a basic surface [38-43].

Tomishige et al. [44] showed that $Ni_{0.03}Mg_{0.97}O$ solid solution catalyst had very high resistance to carbon deposition compared to 3 mol% Ni/MgO and 3 mol% NiO-

Al_2O_3 catalysts. They claimed that carbon deposition did not have a direct relation to the catalytic activity, indicating the selectivity of carbon formation was different on each catalyst. They also found that reactivity of carbon with CO_2 on all tested catalyst was almost same.

Horiuchi et al. [45] reported that basic additive such as Na_2O, K_2O, MgO, and CaO decreased carbon deposition in methane reforming with CO_2 as well as in thermal decomposition of methane. They explained that the added basic metal oxides enhanced CO_2 adsorption, resulting in more adsorbed oxygen atoms (O_{ad}). The higher amount of adsorbed oxygen atoms (O_{ad}) prevent adsorbed hydrogen-deficient hydrocarbon species ($CH_{x,ad}$) to decompose to surface carbon since the oxygen can easily react with the adsorbed hydrogen-deficient hydrocarbon species ($CH_{x,ad}$) to form CO.

Although it was reported that CeO_2 is not suitable for the catalyst support for Ni catalyst [35], the redox behavior and high mobility of lattice oxygen on CeO_2 lead Laosiripojana and Assabumrungrat [46] to synthesize it using surfactant-assisted method and used it as a catalyst without nickel metal. The high surface area of ceria showed almost twice of methane conversion compared to the low surface area of ceria. In addition, the carbon deposition on the high surface area of ceria was negligible. Even though 5wt% Ni/Al_2O_3 catalyst showed similar initial conversion of methane to the conversion from the high surface area of ceria, the activity decreased significantly due to the carbon deposition on catalyst surface. Therefore, they concluded that the high surface area of ceria significantly reduced the degree of thermal sintering causing deactivation.

Another unique catalyst support that was frequently reported for a number of catalyst systems in various catalytic reactions is ZrO_2. Hally et al. [47] studied the zirconia-supported nickel catalysts with emphasis on the stability of the catalysts and

reported that the Ni/ZrO_2 catalyst with lower metal loading (<2%) was more stable than those with higher metal loading for a stoichiometric CO_2/CH_4 ratio. Moreover, two type of deposited carbon were observed on the higher nickel content catalyst but only one type of carbon was observed on the lower nickel content one.

However, the result from Li et al. [48] showed that even with high nickel loading (13.2%), the Ni/ZrO_2 catalyst was stable without significant deactivation for 30h at 750°C and for 20h at 850°C. Using Temperature Programmed Surface Reaction (TPSR) analysis, they [49] reported that carbon deposits were formed at a very high rate on the reduced catalyst. However, the amount of deposited carbon remained constant during reaction at 700°C. These results showed that the carbon acts as a reaction intermediate and reacts with CO_2 to produce CO.

Lercher et al. [50] reported that the rate of carbon formation is proportional to the particle size of Ni on Ni/ZrO_2 catalysts. Below a critical Ni particle size (d<2nm), formation of carbon slowed down dramatically, hence, the Ni/ZrO_2 catalyst exhibited high stability.

The stability of Ni/ZrO_2 catalyst also depended largely on the preparation method of the support .Wei et al. [51] reported very high conversion of CH_4 as well as CO_2 and stable catalytic performance over 600 h using Ni catalyst over $Zr(OH)_4$ ultra-fine support. However, Ni-based catalyst over $Zr(OH)_4$ prepared using co-precipitation method only showed high performance up to 50 h, after which, deactivation took place. The similar results were reported by Rezaei et al. [52], who showed Ni catalyst over nanocrystalline ZrO_2 synthesized using surfactant-assisted method gave high CH_4 conversion.

The other catalyst support which has unique property in CO_2 reforming of methane is La_2O_3, which can form oxycarbonates species during introduction of CO_2 gas [53-54].

According to Zhang and Verykios [54], methane gas dissociates on the metal to form carbon and hydrogen, while carbon dioxide is adsorbed on and reacted with lanthana support to form $La_2O_2CO_3$ (lanthanum oxycarbonate) during DRM reaction. The oxygen species from $La_2O_2CO_3$ were proposed to interact with carbon species from methane decomposition to form carbon monoxide gas, resulting in the ease in removal of surface carbon species.

Ruckenstein and Hu [55] investigated the role of the anions (NO_3^- from $Ni(NO_3)_2$ or Cl^- from $NiCl_2$) on Ni/La_2O_3 catalyst in carbon deposition. The unreduced Ni/La_2O_3 catalyst prepared from nickel nitrate showed a high initial CO yield but a low stability. However, the unreduced Ni/La_2O_3 catalyst prepared from nickel chloride showed a high stability. This stabilization probably occurred due to formation of a stable lanthanum chloride which inhibited the formation of large ensembles of nickel atoms favorable for carbon deposition.

Many promoters have been used to improve the performance of Ni catalyst. Halliche et al. [56] investigated the effect of metal additive such as Co, Ce, Cu, or Fe on Ni/Al_2O_3 catalyst activity in CO_2 reforming of methane. They found that the order of activity was Ni, Ni-Co, Ni-Ce > Ni-Cu > Ni-Fe and reported that the activities of those catalysts depended on the nature of metal additives and their interaction with the nickel active phase.

Choi et al. [57] also examined the effect of Co, Cu, Zr, Mn, Mo, Ti, Ag, or Sn as promoter for Ni/Al_2O_3 catalyst. In comparison with the unmodified Ni/Al_2O_3 catalyst, they reported that those catalysts modified with Co, Cu, or Zr exhibited slightly improvement on catalyst activity, whereas other promoters reduced the catalyst activity. The Mn-promoted catalyst showed a remarkable reduction in coke deposition with only a

small reduction in catalytic activity compared to the unmodified catalyst. Furthermore, Seok et al. [58] explained that the addition of manganese to Ni/Al_2O_3 catalyst resulted in a partial coverage of nickel surface by patches of MnO_x. The presence of manganese also promoted the adsorption of CO_2. Both effects appear to be responsible for the decrease in carbon deposition on $Ni/MnO\text{-}Al_2O_3$ catalyst. These results were also observed in $Ni/Mo\text{-}Al_2O_3$ catalyst, which showed improvement in catalyst stability by reducing the carbon deposition [59].

Cheng et al. [60] investigated effect of promoters, such as alkaline earth (Mg and Ca) and lanthanide (La and Ce) over Ni/Al_2O_3 catalyst. All promoters, alkaline earth (Mg and Ca) and lanthanide (La and Ce), exerted promotion effect on the initial activity. However, the promotion effect for alkaline earth was observed to be sensitive to the method of catalyst preparation but not for lanthanide oxide. Hence, they argued that the promotion action of alkaline earth oxide was associated with the weakening of nickel-alumina interaction, whereas the promotion effect of lanthanide oxide was related to the nickel-lanthanide oxide interaction.

The similar results in effect of promoters on the Ni/ZrO_2 were reported by Li et al. [61]. The lanthanum doped Ni/ZrO_2 catalyst showed the highest activity compared to the cerium or manganese doped Ni/ZrO_2 catalyst. However, the $Ni/Ce–ZrO_2$ and $Ni/Mn–ZrO_2$ catalysts exhibited low carbon depositions during reaction. In addition, $Ni–Mg/ZrO_2$ catalyst exhibited the highest activity and stability due to increasing dispersion of nickel and enhancing the interaction between CO_2 and the catalyst.

Slagtern et al. [62] also investigated the stability of rare earth metal doped Ni/Al_2O_3 catalyst using Ln (mixture of rare earth consists of La, Nd, and Pr) in a fluidized bed reactor. The catalyst with 1.7% Ln was more active and stable than either the

unpromoted catalyst or the catalyst with 8.5% Ln. Moreover, it was also reported that nickel sintering was an initial major reason for catalyst deactivation, followed by coking at longer time on stream (>60h).

The combination of unique properties of CeO_2 and ZrO_2 over Ni catalysts was investigated by Montoya et al. [63]. They found that tetragonal ZrO_2 phase (t-ZrO_2) in the catalyst was stabilized by CeO_2 promoter, forming a solid solution, and thus avoiding transformation to the monoclinic phase (m-ZrO_2). It is generally known that ZrO_2 has a high thermal stability as catalyst support and its tetragonal phase (t-ZrO_2) is more active than its monoclinic phase (m-ZrO_2). Even though addition of higher content of ceria to ZrO_2 over Ni catalyst produced higher carbon deposition, its catalytic activity was higher than the others. Therefore, they concluded that catalyst deactivation was mainly a consequence of the phase transition and support sintering, instead of carbon formation.

Cobalt based catalyst was also investigated intensively for DRM reaction. It was reported that carbon deposition on Co/Al_2O_3 catalyst is much greater than that on Ni/Al_2O_3 catalyst [64]. Ruckenstein and Wang [65] studied carbon deposition on Co/γ-Al_2O_3 catalyst with varying metal content and found that the stability of Co/γ-Al_2O_3 catalysts was strongly dependent on the Co loading and calcination temperature. Different calcination temperature formed different type of Co particles, such as Co_3O_4, Co_2AlO_4, or $CoAl_2O_4$. According to them, the presence of reductive (CH_4, H_2, and CO) and oxidative (CO_2 and H_2O) species in the reactor would lead to severe catalytic deactivation. The reductive species stimulated the regeneration of metallic Co and the dissociation of CH_4, while the oxidative species favored the oxidation of metallic Co sites.

Ruckenstein and Wang [66-67] also investigated Co catalyst supported on an alkaline earth metal oxide (MgO, CaO, SrO, or BaO) as well as on SiO_2. The Co/MgO catalyst showed a high and stable activity without any deactivation for 50h of reaction time. However, the Co/γ-Al_2O_3, Co/SrO, and Co/BaO catalysts gave an initial high CO yield, which rapidly decayed, while the Co/CaO catalysts exhibited a low CO yield and stability. The high activity and stability in Co/MgO catalyst was characterized by formation of solid solution (Co, Mg)O which was similarly observed in Ni/MgO catalyst. Guerrero-Ruiz et al. [68] explained that the presence of MgO enhanced the formation of strongly adsorbed CO_2 species, which can easily react with the deposited carbon. Therefore, the carbon deposition on the surface of cobalt catalyst was markedly decreased and catalyst deactivation was prevented.

The bimetallic catalyst of nickel-cobalt over TiO_2 was studied by Takanabe et al. [69]. They combined cobalt which has strong affinity for oxygen species and nickel which has strong affinity for carbon species. Their finding showed that monometallic Co/TiO_2 catalyst deactivated very fast because of oxidation of cobalt metal during reaction. However, small addition of nickel to the catalyst significantly improved the catalytic activity and stability.

2.1.2. Noble metal catalysts

Noble metals were extensively used as catalyst for many reactions, including DRM reaction. Many studies showed that the activity and stability on noble metal catalysts for DRM reaction are much higher than the ones on non-noble metal catalysts. Up to date,

there are some of noble metals obtain interests from researchers, such as Rhodium (Rh), Ruthenium (Ru), Iridium (Ir), Platina (Pt), and Palladium (Pd).

Rezaei et al. [12] studied a series of noble metal catalysts (Rh, Ru, Ir, Pt, and Pd) supported on alumina-magnesia spinel compound and found that rhodium and ruthenium showed high activity and stability among the rest due to formation of more reactive carbon which was identified as C_α or superficial carbide. In contrast, the lower stability of Pd catalyst was mainly due to the formation whisker carbon which was less reactive compared to Rh and Ru catalysts.

Rhodium based catalyst has been investigated by many researchers, for example, Zhang et al. [70]. According to them, the specific activity of Rh catalysts was found to be strongly dependent on catalyst support and sensitive to the metal particle size. The activity was found to decrease with increasing metal particle size. The deactivation rates showed the decreasing order of Rh/TiO_2 >> Rh/Al_2O_3 > Rh/SiO_2. They explained that Rh/SiO_2 catalyst showed good stability due to the fact that SiO_2 was inert and capable of exhibiting weak or no metal-support interaction. In contrast, Rh/TiO_2 catalyst showed strong metal-support interaction (SMSI) causing poor stability.

According to Yokota et al. [71] who also studied the effect of catalyst support on Rh catalysts, the Rh dispersion was relatively low on the small specific surface area support and increased with increasing surface area. They also found that turn over frequency (TOF) decreased with increasing dispersion of Rh. Hence, TOF for CH_4 conversion decreased in the order of Rh/TiO_2 > Rh/La_2O_3 = Rh/CeO_2 > Rh/ZrO_2 = Rh/MgO = Rh/SiO_2 = Rh/MCM-41 > $Rh/\gamma\text{-}Al_2O_3$. Further studies using XANES revealed

that Rh existed as metal on TiO_2 while Rh on Al_2O_3 possessed a cationic character. Therefore, they concluded that Rh was structure sensitive in DRM reaction.

In contrast with Yokota's results [71], Mark and Maier [12] found that TOF over Rh, Ru, Ir, Pt, or Pd-supported catalysts did not depend significantly on metal dispersion, indicating that DRM reaction at high temperatures was structure insensitive. The support seemed only giving influence in stabilization of metal surface area, which was responsible for the catalyst activity. Therefore, they suggested that under reaction controlled temperatures, it was sufficient to consider one parameter only, the accessible metal surface area.

Platina (Pt) supported catalyst was also investigated extensively for DRM reaction. Nagaoka et al. [72] studied carbon deposition over Pt/Al_2O_3 and Pt/ZrO_2 catalysts and reported that both Pt particle and Al_2O_3 support formed coke. However, coke formed on Pt particles was easily oxidized by CO_2, but coke on Al_2O_3 support was not reactive at all. In addition, they also reported that coke was hardly formed on ZrO_2 support. Therefore, they concluded that the main reaction between CO_2 and CH_4 on all Pt particles occurred without significant participation of the support.

Further studies over Pt/Al_2O_3 and Pt/ZrO_2 catalysts were performed by Souza et al. [73-74]. Their results showed that the catalyst support played an important role in the activity and stability of catalyst. They also confirmed that Pt/Al_2O_3 catalyst showed fast deactivation during DRM reaction as a result of high carbon deposition rate. Meanwhile, addition of a small amount of ZrO_2 (> 5%) to Pt/Al_2O_3 catalyst improved its stability and activity. The low carbon deposition was attributed to the presence of $Pt\text{-}Zr^{n+}$ interfacial sites, which prevented coke formation and therefore enabled high stability and activity of zirconia-containing catalyst.

Bitter et al. [75] also reported that the stability of Pt catalysts increased in the order of Pt/ZrO_2> Pt/TiO_2>Pt/γ-Al_2O_3, while the carbon formation rate decreased in the order of Pt/ZrO_2 < Pt/TiO_2 << Pt/γ-Al_2O_3 [76]. These results indicated that carbon formation, which blocks the active metal site, was the main cause of deactivation of the platinum-supported catalysts.

Pd-based catalyst for CO_2 reforming of methane was studied in depth by Erdöhelyi et al. [77]. According to them, dissociation of carbon dioxide was greatly promoted by the presence of methane. Moreover, the decomposition of methane started at high rate yielding hydrogen and small amounts of ethane and ethlyene. Although carbon deposition was observed, the amount was very little at the stoichiometric ratio (1/1) of CH_4 and CO_2. Therefore, they concluded that supported palladium was an active catalyst at high temperature giving hydrogen and carbon monoxide with no or only very little carbon deposition.

2.1.3. Bimetallic and perovskite catalysts

Recently there are two trends of catalyst development for DRM reaction, i.e. bimetallic, from combination of noble and non-noble metal, and perovskite catalysts. Since noble metals show better performance but are more expensive than non-noble metals, the addition of small amount of noble metal to nickel or cobalt catalyst is extensively investigated.

Itkulova et al. [78] investigated the addition of noble metal such as Ir, Rh, Pt, or Pd to Co/Al_2O_3 catalyst with Co/M ratio of 1/1. All bimetallic catalysts showed strong resistance to coke formation as the weight loss of spent catalysts was not detected by

TGA. Similar results were reported by Nagaoka et al. [79], who investigated addition of trace amount of Pt or Ru to Co/TiO_2 catalyst. The addition of noble metals improved the catalytic stability of Co/TiO_2 catalyst drastically due to strong resistant to coke formation. Moreover, they found that cobalt was easier to be reduced in the presence of noble metal and suggested that the catalyst reducibility might play an important role in DRM reaction.

Chen et al. [80] also reported that although solid solution Ni/MgO catalyst had a stable activity in DRM reaction, the deactivation was still observed at low temperature 500°C due to oxidation of Ni active species. The addition of small amounts of Pt, Pd, or Rh to Ni/MgO catalyst increased the catalyst activity and stability significantly. They also addressed the improvement of catalyst performance to the easier reducibility of catalyst.

Perovskite-type catalysts represented by the general formula ABO_3 have been extensively investigated for applications involving high temperatures due to their high thermal stability [81-82]. In the structure of perovskite, the B-site cation is surrounded octahedrally and the A-site cation is located in the cavity made between these octahedral. These structures offer the possibility of varying the dimensions of the unit cell by the substitution of the A ion. Therefore, the covalence of the B-O bond in the ABO_3 structure is accordingly changed [83]. The replacement of A- and/or B-site cations by other metal cations often results in formation of lattice defects. The defects cause enhancement in adsorption of a large amount of O_2 and oxygen mobility within the crystal structure, hence, promotes catalytic activity.

The perovskite catalyst with rare earth metal La as the A site and Ni as the B site has been investigated thoroughly for DRM reaction. Batiot-Dupeyrat et al. [84] reported that the perovskite type oxide $LaNiO_3$ is reduced under hydrogen atmosphere in three steps. The first reduction step (200–500°C) corresponds to the formation of the $La_4Ni_3O_{10}$

phase, while the second step (600–650°C) leads to the formation of the spinel-type phase La_2NiO_4. In the last step (680-750°C), it decomposed to La_2O_3 and Ni metal. Therefore, they concluded that there were two consecutive reactions occurring simultaneously during the reaction as follow:

$$Ni^0 + La_2O_3 + CO_2 \leftrightarrow CO + La_2NiO_4$$

$$CH_4 + La_2NiO_4 \rightarrow CO + 2H_2 + La_2O_3 + Ni^0$$

Furthermore, they [85] reported that the catalytic activity of La_2NiO_4 perovskite catalyst was higher than those of Ni/La_2O_3 or $LaNiO_3$ catalyst due to formation of smaller nickel particle after reduction. The reduction treatment was so important in this La_2NiO_4 catalyst that carbon deposition was observed when the catalyst was used without treatment, while no carbon deposition was detected once the catalyst was reduced prior to the reaction. Since the role of La_2O_3 support was to allow the activation of carbon dioxide, the limited amount of La_2O_3 over unreduced La_2NiO_4 catalyst resulted in inhibition of carbon removal. Therefore, the carbon accumulation was observed.

2.1.4. Reaction mechanism

Although many papers published so far have aimed at the understanding of reaction mechanism for CO_2 reforming of methane, but it is still under debate. The reason is because it usually changes with type of active metals and catalyst supports. However, most of those published papers have similarity in the basic concept. The general reactions of CO_2 reforming are as follow:

$$CO_2 + CH_4 \rightarrow 2\,CO + 2\,H_2 \qquad \Delta H_r = 247\ kJ/mol$$

$$CO_2 + H_2 \rightarrow CO + H_2O \qquad \Delta H_r = 41.1\ kJ/mol$$

The latter reaction is generally known as reverse water-gas shift reaction (rWGS)

It is generally accepted that the CH_4 and CO_2 will undergo dissociation separately. The activation of methane usually takes place on the metal active site [86-87] to produce short-lived CH_x and carbon.

$$CH_{4(g)} \rightarrow CH_{3(a)} + H_{(a)}$$

$$CH_{3(a)} \rightarrow CH_{2(a)} + H_{(a)}$$

$$CH_{2(a)} \rightarrow CH_{(a)} + H_{(a)}$$

$$CH_{(a)} \rightarrow C_{(a)} + H_{(a)}$$

The above reaction is endothermic thermodynamically. Thus, the equilibrium constant will increase with increasing temperature.

Meanwhile, CO_2 dissociation will undergo according to the catalyst support. For the acid support, such as SiO_2, Ferreira-Aparicio et al. [88] reported that the SiO_2 had no role in the reaction mechanism. Therefore, activation of CH_4 and CO_2 takes place on the ruthenium surface. In details, the activation of CO_2 can be written as follow:

$$CO_{2(g)} \leftrightarrow CO_{2(a)}$$

$$CO_{2(a)} \leftrightarrow CO_{(a)} + O_{(a)}$$

The adsorbed O atom then reacts with either the CH_x radical or adsorbed H atom according to the following reaction steps:

$$CH_{x(a)} + O_{(a)} \rightarrow CO_{(a)} + x\ H_{(a)}$$

$$H_{(a)} + O_{(a)} \leftrightarrow OH_{(a)}$$

$$H_{(a)} + OH(a) \leftrightarrow H_2O_{(g)}$$

$$2\ H_{(a)} \rightarrow H_{2(g)}$$

$$CO_{(a)} \leftrightarrow CO_{(g)}$$

Due to limited adsorption of CO_2, the accumulation of coke deposit becomes severe, leading to a continuous loss of activity.

A different pathway was proposed for the catalyst with basic supports such as lanthania. The CO_2 activation was observed in lanthania support by formation of carbonate and formate intermediates on its surface that subsequently decompose releasing CO [89] as follows:

$$CO_{2(g)} \leftrightarrow CO_{2(support)}$$

$$CO_{2(support)} + O^{2-}{}_{(support)} \leftrightarrow CO_3{}^{2-}{}_{(support)}$$

$$CO_3{}^{2-}{}_{(support)} + 2H_{(support)} \leftrightarrow HCO_2{}^{-}{}_{(support)} + OH^{-}{}_{(support)}$$

$$HCO_2{}^{-}{}_{(support)} \leftrightarrow CO_{(support)} + OH^{-}{}_{(support)}$$

$$CO_{(support)} \leftrightarrow CO_{(g)}$$

In addition to both proposed mechanism for CO_2 activation, the Boudoudard reaction ($2CO \rightarrow C + CO_2$) also takes place simultaneously due to high temperature reaction.

The carbon deposits from both dissociation of methane and CO_2 consist of various forms which are different in terms of reactivity: adsorbed atomic carbon, amorphous carbon, vermicular carbon, bulk nickel carbide, and crystalline graphitic carbon [90]. Moreover, the reactivity of carbon deposit or its transformation is sensitive to the type of catalyst surface, the temperature of its formation, and the duration of thermal treatment. Dissociation of CH_4 alone is generally very fast on active metal side while the activation of CO_2 is very slow.

Although both CH_4 and CO_2 undergo dissociation separately, their decomposition products terminate the respective dissociation by covering the metal surface. While the dissociation of CH_4 is enhanced by adsorbed oxygen, the dissociation of CO_2 is also facilitated by adsorbed hydrogen and possibly by other CH_x residues [91].

The formation of undesired H_2O in the reverse water gas shift (rWGS) reaction will compete with CO_2 for subsequent reactions with carbon formed by dissociation of CH_4.

$$CO_2 + C \rightarrow 2CO$$

$$H_2O + C \rightarrow H_2 + CO$$

In Rostrup-Nielsen and Bak Hansen's [92] study over transition metals, the latter reaction which represents steam reforming appears to be faster than CO_2 reforming reaction. It indicates that the effectiveness of catalysts for CO_2 reforming depends on the catalyst ability to activate CO_2.

In addition, according to Basini and Safilippo [93], from thermodynamic point of view, the following reactions can also occur:

$$CO_2 + 4\ H_2 \rightarrow CH_4 + 2\ H_2O \qquad \Delta H_r = -164.9\ kJ/mol$$

$$CO + 3\ H_2 \rightarrow CH_4 + H_2O \qquad \Delta H_r = -205.9\ kJ/mol$$

However, their experimental data over Rh based catalyst showed that the first reaction has selectivity and rate an order of magnitude higher than the second reaction.

2.1.5. Kinetic modeling

Verykios [94] proposed a kinetic model for Ni/La_2O_3 catalyst using a range of techniques to elucidate the reaction mechanism. He observed that the stable $La_2O_2CO_3$ compound, formed from interaction of La_2O_3 with CO_2, partially covered Ni particles. Catalytic activity occurred at the interface of Ni and $La_2O_2CO_3$ species. This oxycarbonate species participated directly in the reaction by reacting with the deposited carbon. Therefore, the carbon deposition was less and the activity of Ni sites was restored. He also

reported that methane decomposition on Ni sites and surface reaction between deposited carbon and oxycarbonate species are the rate determining steps. Based on these observations, few steps of mechanism were proposed. Firstly, the adsorption of methane on the surface of Ni site was reversible reaction while the methane cracking was a slow step. Secondly, the strong interaction between CO_2 and La_2O_3 support to form $La_2O_2CO_3$ was considered a fast step and at equilibrium. Finally, the step where oxycarbonate species react with carbon deposited onto Ni particles was also considered to be a slow step. The detail mechanism and the kinetic model were proposed and presented in Table 2-2.

Table 2-2 Kinetic model of CO_2 reforming of methane on Ni/La_2O_3 catalyst

Mechanism		
Adsorption	$CH_4 + S \overset{K_1}{\rightleftharpoons} S-CH_4$	Equilibrium
Surface reaction	$S-CH_4 \xrightarrow{k_2} S-C+2H$	RDS
Adsorption	$CO_2 + La_2O_3 \overset{K_3}{\rightleftharpoons} La_2O_2CO_3$	Equilibrium
Surface reaction	$La_2O_2CO_3 + C-S \xrightarrow{k_4} La_2O_3 + 2CO + S$	RDS
Rate of reaction	$R_{CH_4} = \frac{K_1 k_2 K_3 k_4 P_{CH_4} P_{CO_2}}{K_1 k_2 K_3 P_{CH_4} P_{CO_2} + K_1 k_2 P_{CH_4} + K_3 k_4 P_{CO_2}}$	

Rate parameters

$$K_1 k_2 = 2.61 \times 10^{-3} \exp\left(\frac{-4300}{T}\right)(\text{mol/g s})(\text{kPa})^{-1}$$

$$K_3 = 5.17 \times 10^{-5} \exp\left(\frac{-8700}{T}\right)(\text{kPa})^{-1}$$

$$k_4 = 5.35 \times 10^{-1} \exp\left(\frac{-7500}{T}\right)(\text{mol/g s})$$

Since kinetic model also depends on the choice of metal and catalyst support, the proposed model by Verykios was only applicable to Ni/La_2O_3 catalyst. Therefore, a lot of kinetic models have been proposed. Table 2-3 tabulates some of the kinetic models found in the literature.

Table 2-3 Various kinetic models for CO_2 reforming of methane

Model	Catalyst	Reference
$r_{CH_4} = \frac{\hat{k}_1 P_{CH_4} P_{CO_2}}{(\hat{k}_{-1} K / \hat{k}_7) P_{CO} P_{H_2}^{(4-x)/2} + [1 + (\hat{k}_1 / \hat{k}_7) P_{CH_4}] P_{CO_2}}$	Ni/MgO Ni/TiO_2 Pt/TiO_2	29
$-r_{CH_4} = \frac{k(P_{CH_4})^n}{1 + K_1 \frac{P_{CO}}{P_{CO_2}} + K_2 (P_{H_2})^m}$	CeO_2	48
$r_{CH_4} = \frac{k_R [P_{CH_4} - (P_{H_2}^2 P_{CO}^2 / K_R P_{CO_2})]}{1 + (P_{CO}^2 / K_{R,C} P_{CO_2})}$	Ir/Al_2O_3	74

2.1.6. Potential applications

2.1.6.1 Production of chemicals and fuel

The lower H_2/CO ratio produced by the DRM reaction is suitable for Fischer-Tropsch reaction which was found by German scientists Franz Fischer and Hans Tropsch. It converts mixture of H_2 and CO to liquid fuels in various forms according to the following reaction:

$$(2n+1)\ H_2 + n\ CO \rightarrow C_nH_{(2n+2)} + n\ H_2O$$ (where n is positive integer)

Another large potential of new application using 1/1 ratio of H_2/CO is production of dimethyl ether (DME) using a new direct route which avoids the intermediate methanol production step [90]. DME is an intermediate product for the production of synthetic gasoline and isobutene via isobutanol. The isobutene then can react with methanol to produce octane enhancer methyl tertiary butyl ether (MTBE), according to the following reactions:

$$3\ CO + 3\ H_2 \rightarrow CH_3OCH_3 + CO_2$$

$$2\ CH_3OCH_3 \rightarrow C_4H_9OH + H_2O$$

$$C_4H_9OH \rightarrow C_4H_8 + H_2O$$

$$C_4H_8 + CH_3OH \rightarrow CH_3OC(CH_3)_3$$

2.1.6.2 Chemical energy storage and applications

The concept of chemical energy storage is reversible chemical reactions using renewable energy source. In this case, CO_2/CH_4 reforming and its reverse CO/H_2 methanation using solar energy are considered to be frontrunner for thermochemical heat pipe (TCHP) application in the storage and transmission of solar energy. This concept can be seen diagramatically in Figure 2-1 and 2-2 [90].

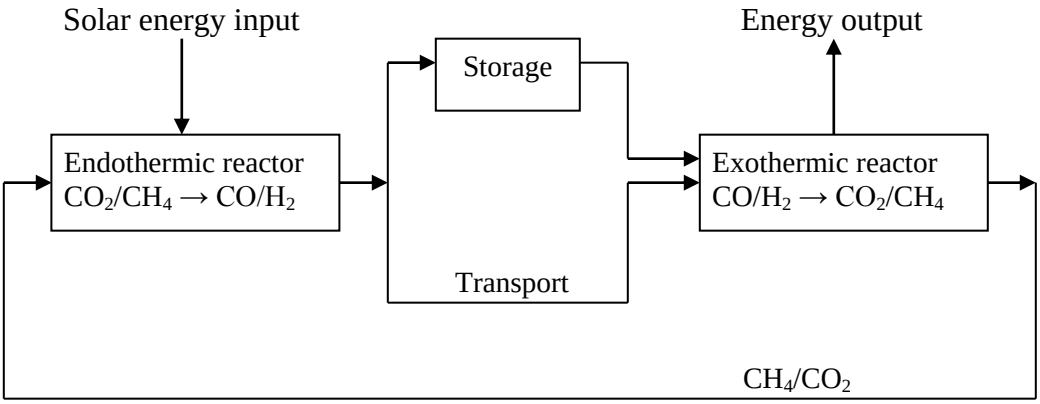

Figure 2-1 Concepts for closed-loop thermochemical heat-pipes

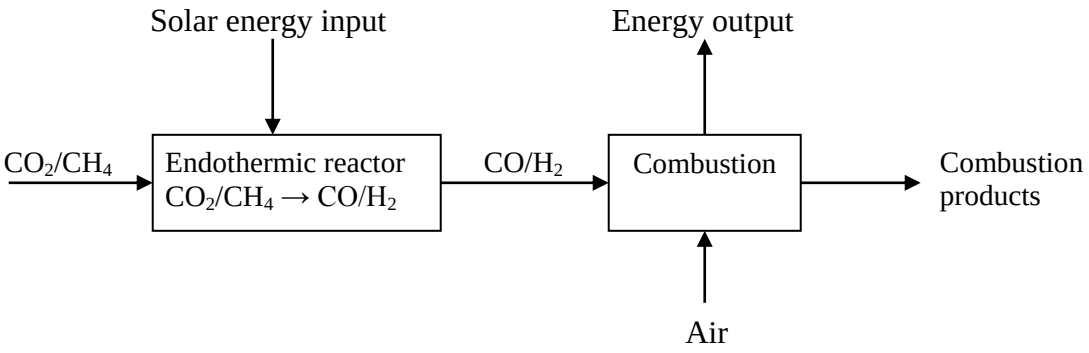

Figure 2-2 Concepts for open-loop thermochemical heat-pipes

In closed-loop TCHP, CO_2 reforming of methane using high temperature source of solar energy will produce CO and H_2. Both these products can be stored or transported to a separate site and subsequently used in CO/H_2 methanation to release the stored chemical energy. The products of reverse reaction are then sent back to the endothermic reactor to complete closed-loop cycle.

Unlike in the former case, the product gas (CO and H_2) from CO_2 reforming of methane is directly combusted to produce heat and power in open-loop TCHP. However,

in this case, it will produce more CO_2 and increase its concentration in the atmosphere. In addition, the open-loop cycle also requires a source of cheap CO_2.

2.2. Partial oxidation of methane

Besides CO_2 reforming of methane, partial oxidation of methane (POM) is also an attractive technology to produce syngas, but the H_2/CO ratio produced from POM reaction is 2.0 instead of 1.0 from DRM reaction. Figure 2-3 shows the schematic diagram of the POM reaction and the thermodynamic information. Based on the information, York et al. [95] showed some advantages of the POM reaction compared to steam reforming of methane (SRM).

1. Partial oxidation is a mildly exothermic reaction while steam reforming is highly endothermic. Therefore, in term of cost from the heat required, partial oxidation will be more economical. Moreover, combination with endothermic reactions, such as steam reforming or CO_2 reforming makes the whole processes more efficient.
2. The theoretical H_2/CO produced from partial oxidation is 2.0, while the H_2/CO ratio from steam reforming is 3.0. The H_2/CO ratio of 2.0 is ideal for downstream process such as Fischer-Tropsch, while it needs to remove some amount of valuable hydrogen from the product of steam reforming before sending to downstream process.
3. The CO_2 content produced from partial oxidation can be extremely low. However, it is usually removed before used in downstream process.
4. A large amount of expensive superheated steam is not required for partial oxidation technology. However, a gas separation plant is also costly but required to separate oxygen from nitrogen in air.

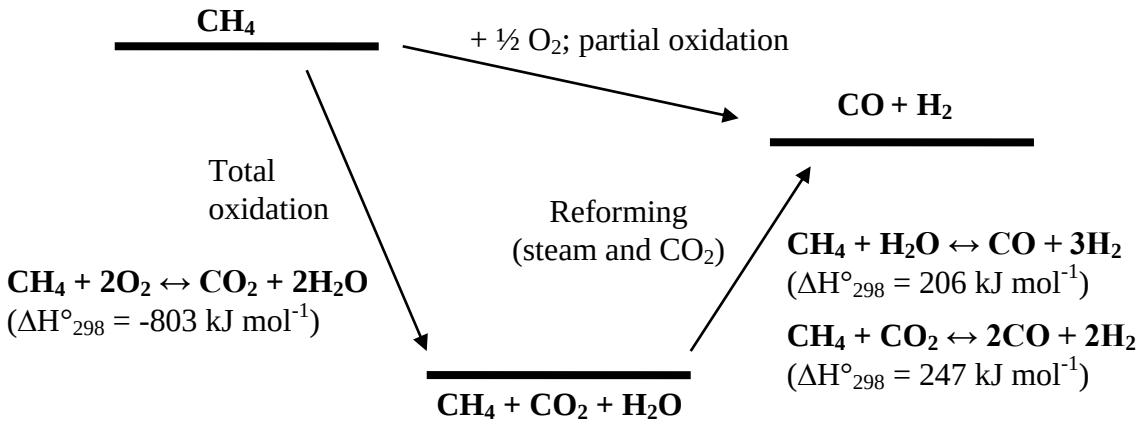

Figure 2-3 Thermodynamic diagram of partial oxidation of methane

Besides the main reaction, a lot of side reactions may occur during the reaction. Below are overall reactions possibly occurred in POM reaction [96]:

POM:	$CH_4 + ½\ O_2$	→	$CO + 2\ H_2$	$\Delta H°_{298}$ = -35.7 kJ/mol
Combustion:	$CH_4 + 2\ O_2$	→	$CO_2 + 2\ H_2O$	$\Delta H°_{298}$ = -803 kJ/mol
Methanation:	$CO + 3H_2$	→	$CH_4 + H_2O$	$\Delta H°_{298}$ = -206.2 kJ/mol
Water-Gas Shift:	$CO + H_2O$	↔	$CO_2 + H_2$	$\Delta H°_{298}$ = -41.2 kJ/mol
Cracking:	CH_4	↔	$C + 2H_2$	$\Delta H°_{298}$ = 74.9 kJ/mol
Boudouard:	2CO	↔	$C + CO_2$	$\Delta H°_{298}$ = -172.4 kJ/mol

The POM reaction generally operates at a very low contact time (about millisecond). However, since the reaction is very exothermic, a high methane conversion (>90%) coupled with very high space velocity (≥500,000 $cm^3g^{-1}h^{-1}$) leads to production of a large amount of heat in a small catalyst zone, even at very high selectivity (>95 %) for CO and H_2, causing a large adiabatic temperature rise. This sudden temperature rise is

difficult to control and ultimately results in the deactivation of a thermally unstable catalyst. Moreover, a small amount of coke is also reported to deposit on catalyst surface.

Prettre et al. [97] in 1946 are the first ones to report the use of 10wt% refractory supported on nickel catalyst to produce syngas via POM at temperature between 700-900°C. The observed exit gas composition had good agreement with the calculated equilibrium gas composition, indicating that thermodynamic equilibrium was achieved under all investigated conditions.

Since last few decades, extensive efforts have been made to investigate noble metal and non-noble metal catalysts for syngas production from the POM reaction.

2.2.1 Non-noble metal catalysts

Non-noble metal catalysts, especially nickel, have been investigated extensively since 1990. Dissanayake et al. [19] investigated a 25 wt% Ni/Al_2O_3 catalyst in the temperature range of 450-900°C and reported that selectivity of carbon was nearly 95% and complete conversion of methane could be achieved at temperatures >700°C. They observed that the catalyst bed consisted of three different regions: $NiAl_2O_4$ (upstream section), $NiO+Al_2O_3$ (middle section), and reduced Ni/Al_2O_3 (downstream section). In the upstream section, a moderate activity for complete oxidation of methane to CO_2 and H_2O was observed when the CH_4/O_2/He feed mixture contacted with $NiAl_2O_4$ compound. In the middle section, the mixture of NiO + $A1_2O_3$ catalyzed complete oxidation of methane to CO_2, resulting in a sudden increase in temperature of the bed. Since O_2 had been consumed in the second region, the third section of the catalyst bed consisted of a reduced Ni/Al_2O_3 phase. The Ni/Al_2O_3 phase catalyzed reaction between CO_2 or H_2O resulted from oxidation reaction in upstream and middle sections with CH_4 to produce CO and H_2.

Choudhary et al. reported a high conversion of methane and high selectivity to CO and H_2 over NiO/CaO [98], Ni/Al_2O_3 [99], Ni/rare earth oxide [100], and Co/rare earth oxide [101] catalysts. However, the main problem encountered with non-noble metals catalysts is the low stability [102], while the main causes of the catalyst deactivation are carbon deposition and metal sintering in the catalyst. Therefore, extensive efforts have been taken to develop high stability nickel catalyst and high resistance to metal sintering by incorporation in suitable supports, such as CeO_2 [103], $SrTiO_3$ [104], MgO [105], and La_2O_3 [106].

Choudhary et al. [107] also investigated the NiO-MgO catalyst over low surface area catalyst support and found that the methane conversion and product selectivity of the unsupported NiO-MgO catalyst were higher than those supported on low surface area support. However, when the catalyst was prepared by depositing NiO on the MgO-precoated-catalyst support, it showed comparable performance to that of the unsupported NiO-MgO catalyst. The difference was attributed to the role of MgO to avoid the chemical interaction of NiO and the support by providing a stable protective layer and to stabilize nickel on the support surface against sintering by forming a NiO-MgO solid solution.

Promoters are generally known to have significant influence in catalyst performance. For example, addition of La_2O_3 to Ni/Al_2O_3 catalyst was reported to lower down the ignition temperature of the reaction [108]. Furthermore, it was reported that the introduction of alkali and rare metal earth oxides, such as Li and La oxides to Ni/Al_2O_3 catalyst formed LiNiLaO/Al_2O_3 compound which showed high conversion of methane and high selectivity to CO as well as high coke resistance [109]. Fe was also reported to have positive effect on catalytic performance of Ni/La_2O_3 catalyst [110].

2.2.2 Noble metal catalysts

Noble metal catalysts have also been investigated extensively for POM reaction. Ashcroft et al. [111-112] investigated the catalytic performance of noble metal catalysts, such as Rh, Ru, Pd, Ir, and Pt compared to Ni catalyst supported on alumina. They found that all catalysts showed performance near to the equilibrium, probably due to the high temperature they used in the reaction, around 777°C. They also showed that the order of carbon formation rate for POM reaction was Ni> Pd> Rh> Ir [113].

Matsui et al. [114] investigated the reactivity of carbon species on noble metal catalysts, such as Ru over few commercial supports and reported that the reactivity of carbon species (CH_x) from methane decomposition on Ru catalyst depended on the supports. Ru/La_2O_3, Ru/Y_2O_3, and Ru/ZrO_2 catalysts gave higher reactivity than Ru/Al_2O_3 catalyst since they produced more uniform and reactive carbon species.

Boucouvalas et al. [115] reported that Ru/TiO_2 catalyst exhibited high selectivity to syngas in the methane conversion range below 25%, while Ru/SiO_2, $Ru/\gamma\text{-}Al_2O_3$, and Ru/YSZ catalysts showed zero selectivity under similar condition. Further observation using isotopic labeling experiments on Ru/TiO_2 catalyst showed that the direct partial oxidation route was largely responsible for the high CO and H_2 selectivity.

Elmasides et al. [116] further investigated the excellence of Ru/TiO_2 catalyst using XPS and FTIR. They reported that reduction temperature played an important role in direct route of syngas formation on Ru/TiO_2 catalyst. During hydrogen treatment at 300°C, the Ru/TiO_2 catalyst was incompletely reduced and oxidized Ru species were detected in the introduction of methane-oxygen mixture at 500°C and 700°C. In contrast, ruthenium was fully reduced during hydrogen treatment at 550°C and no re-oxidation of

Ru was observed during treatment with methane-oxygen mixuture, indicating the presence of interaction between Ru and TiO_2. This interaction was claimed to be the main reason to promote the direct route of syngas formation.

Ashcroft et al. [117] reported the use of pyrochlore type of rare-earth ruthenium catalysts, $Ln_2Ru_2O_7$ (where Ln is lanthanide) such as $Pr_2Ru_2O_7$, $Sm_2Ru_2O_7$, $Eu_2Ru_2O_7$, $Gd_2Ru_2O_7$, $Tb_2Ru_2O_7$, $Dy_2Ru_2O_7$, $Tm_2Ru_2O_7$, $Yb_2Ru_2O_7$, and $Lu_2Ru_2O_7$. Pure ruthenium oxide was found to be less effective compared to the rare-earth pyrochlore catalysts. Further examination of the catalysts after reaction showed reduction had occurred giving ruthenium metal particles on the surface of a defect fluorite $(Ln, Ru)O_{2-x}$.

Nakagawa et al. [118] investigated the effect of supports over iridium catalyst in POM reaction and reported that the catalyst activity decreased with the order of $Ir/TiO_2 \geq Ir/ZrO_2 \geq Ir/Y_2O_3 > Ir/La_2O_3 > Ir/MgO \geq Ir/Al_2O_3 > Ir/SiO_2$. The excellence of Ir/TiO_2 catalyst was reported due to its resistance to carbon deposition [119].

Jones et al. [120] examined europium iridate ($Eu_2Ir_2O_7$) catalysts and showed that the unreduced europium iridate was inactive. However, during catalyst reduction, it was active to produce syngas since it decomposed to iridium metal supported on europium oxide, Eu_2O_3.

Buyevskaya et al. [121] reported that the product distribution on $Rh/\gamma\text{-}Al_2O_3$ catalyst was strongly affected by degree of surface reduction. Moreover, methane oxidation proceeded via a redox mechanism with lattice oxygen to produce CO_2. This CO_2 underwent fast reaction with surface carbon species via reverse Boudouard reaction to form CO. Analogous results were also obtained for $Pd/\gamma\text{-}Al_2O_3$, $Ru/\gamma\text{-}Al_2O_3$, and $Pt/\gamma\text{-}Al_2O_3$ catalysts.

Wang et al. [122] reported that methane decomposition occurred on reduced metal sites and pre-adsorption of oxygen decreased the methane adsorption rate. They also reported that water adsorption on the support acted as an oxygen source through inverse spillover of water or OH onto the Rh particles. From their observation, it was claimed that CO_2 was formed by fast oxidation of CO with adsorbed oxygen or through the nucleophilic attack of OH, while H_2O was formed from rapid reduction by hydrogen of adsorbed OH and adsorbed oxygen. In addition, CO was produced from CH_x through oxidation by means of adsorbed oxygen or by the nucleophilic attack by adsorbed OH as well as from dissociation of CO_2.

Baranova et al. [123] investigated Rh/YSZ catalyst promoted with TiO_2 and reported that the remarkable increase in catalytic activity of Rh catalyst was affected by interfacing polycrystalline Rh films with a dispersed TiO_2 interlayer deposited on YSZ. The main reason of increase in catalytic activity was the lowered stability of surface Rh oxide against reduction to metallic Rh. The phenomenon was attributed to either electronic type strong metal–support interactions or self-driven wireless electrochemical promotion mechanism. In both cases, the ultimate cause of promotion was the different work function of catalyst and support. Equilibration of the Fermi level resulted in transfer of negative charge from Rh to TiO_2. The charge transfer weakened Rh–O bond and promoted the reduction of rhodium oxide.

Otsuka et al. [124] investigated performance of CeO_2 for POM reaction and obtained the H_2/CO (syngas) ratio of 2.0. However, the formation rate of H_2 and CO can be remarkably enhanced by adding Pt as a catalyst. The enhancement of methane conversion due to the presence of noble metals such as Rh or Pt was also reported by Fathi et al. [125]. They observed that the reducibility of cerium oxide was significantly

enhanced by adding Rh or Pt. Further observation showed that product ratio of $H_2/(H_2O+H_2)$ and $CO/(CO_2+CO)$ increased with increasing degree of reduction of the cerium oxide, indicating that carbon was formed on reduced Pt and Rh.

Yan et al. [126] studied the effect of modifying Pt/Al_2O_3 catalyst with CeO_2 and found that the addition of ceria could enhance the Pt dispersion, decrease the Pt crystalline size, and increase the product selectivity. The optimal amount of CeO_2 was 1-2wt%. They also reported that cerium oxide promoted water gas shift (WGS) reaction by a redox cycle mechanism, which increased the hydrogen selectivity. Mattos et al. [127] also investigated effect of addition of ceria to Pt/ZrO_2. Compared to Pt/ZrO_2 catalyst, $Pt/Ce\text{-}ZrO_2$ catalyst was more active, stable, and selective due to higher reducibility and oxygen storage/release capacity. These two properties allowed a continuous removal of coke deposition from the active sites and favoring the stability and activity of the catalyst.

Fangli et al. [128] investigated the influence of catalyst supports on palladium catalyst and reported that $Pd/CeO_2\text{-}ZrO_2$ catalyst exhibited higher catalytic activity and stability compared to $Pd/\alpha\text{-}Al_2O_3$. The main reason of high stability was lower carbon deposition rate due to lattice oxygen mobility of $CeO_2\text{-}ZrO_2$.

Furthermore, effect of promoter addition to Pd/Al_2O_3 catalyst was investigated by Feio et al. [129]. They reported that Pd/Al_2O_3 catalyst deactivated during POM reaction while CeO_2-promoted Pd/Al_2O_3 catalyst showed higher stability with higher CeO_2 loading. They found that the crystal size of ceria increased with increase in CeO_2 loading or calcination temperature. In contrast, the dispersion of Pd decreased with either use of supports calcined at lower temperature or increase of CeO_2 loading. The increase of

activity and stability with decreasing Pd dispersion was attributed to the partial coverage of Pd by $[CePd_xO]Pd^0$ species, which showed high activity to promote coke gasification.

Furthermore, Ryu et al. [130] pointed out that, compared to Pd/γ-Al_2O_3 catalyst, Pd/CeO_2/Al_2O_3, Pd/CeO_2/BaO/Al_2O_3, Pd/CeO_2/BaO/SrO/Al_2O_3 catalysts exhibited higher catalyst activity. Further observations concluded that addition of BaO gave a more stable support, while addition of ceria improved both the thermal stability of the support and the activity of the Pd catalyst. When ceria and BaO were added together to Pd/γ-Al_2O_3, the improvement in thermal stability of the support and activity of the Pd catalyst were observed. It was also reported that the addition of BaO, CeO_2, or BaO–CeO_2 to γ-Al_2O_3 prevented the transformation of alumina phase during the 3-day aging process at 1000°C. The addition of small amounts of SrO to the CeO_2/BaO/Al_2O_3 support increased the dispersion of the Pd particles, which led to higher catalyst activity. The other role of SrO was to enhance the thermal stability of the Pd particles, so that the deactivation due to the sintering of the Pd particles was minimized. The optimum composition of Pd catalyst which gave the highest activity and the best thermal stability was Pd(2)/CeO_2(23)/BaO(11)/SrO(0.8)/Al_2O_3.

2.2.3 Reaction mechanism

Up to date, there are three mechanisms proposed for the POM, i.e. combustion and reforming reaction mechanism (CRR), direct partial oxidation mechanism (DPO) [131], and catalytic partial oxidation (CPO).

2.2.3.1 Combustion and Reforming Reactions mechanism (CRR)

Prettre et al. [97] were the first ones proposing the CRR mechanism. They observed that the axial temperature profile of the catalyst bed was not uniform. At the front of catalyst bed, the temperature was much higher than the inner part and the furnace temperature. The temperature profile clearly showed the occurrence of initial exothermic methane combustion reaction to produce carbon dioxide and water followed by endothermic reactions (CO_2 reforming of methane and steam reforming of methane) as shown in Figure 2-2 and water-gas shift reaction to produce syngas. Indeed, the noble metal and nickel have been independently shown to catalyze CO_2 reforming of methane, steam reforming of methane, and water gas shift reactions very efficiently.

Vernon et al. [112] studied the effect of reaction condition on the product distribution and found that the selectivity to carbon dioxide and water increased with increasing either space velocities or methane/oxygen ratio. This indicated that syngas was a secondary product and confirmed the CRR mechanism.

2.2.3.2 Direct Partial Oxidation mechanism (DPO)

This mechanism was proposed by Hickman and Schmidt [132-135] who studied the rhodium and platinum coated monolith catalyst under adiabatic conditions at very short residence time ($<10^{-2}$s). They observed higher selectivity to H_2 over Rh catalyst compared to that for Pt catalyst (86 and 64%, respectively), while selectivity to CO were similar for both metals (95 and 89%, respectively). The higher selectivity to H_2 over Rh could be attributed to the much slower rate of OH formation on Rh surface. Interestingly, at double residence time, there was no significant improvement in conversion and

selectivity. Based on the observations, the syngas is produced as a primary product via following reactions:

$CH_4 \rightarrow CH_{x,s} + (4-x)\ H_s$

$2H_s \rightarrow H_{2,g}$

$O_{2,g} \rightarrow 2O_s$

$C_s + O_s \rightarrow CO_s \rightarrow CO_g$

However, any side reactions involving OH to produce H_2O and CO_2, such as

$CH_{x,s} + O_s \rightarrow CH_{x-1,s} + OH_s$

$H_s + O_s \rightarrow OH_s$

$OH_s + H_s \rightarrow H_2O_g$

$CO_s + O_s \rightarrow CO_{2,g}$

have to be considered because reverse reactions of these products are slow or thermodynamically unfavorable.

2.2.3.3 Catalytic Partial Oxidation mechanism (CPO)

This mechanism was recently proposed by Veser et al. [136] who found that partial oxidation of methane at very low contact time in millisecond proceeds in two stages: initial direct oxidation to CO and H_2O ($CH_4 + 1.5\ O_2 \rightarrow CO + 2\ H_2O$, $\Delta H = -519$ kJ/mol), followed by steam reforming of methane ($CH_4 + H_2O \rightarrow CO + 3\ H_2$, $\Delta H = 210$ kJ/mol). In addition, total oxidation of methane ($CH_4 + 2\ O_2 \rightarrow CO_2 + 2\ H_2O$, $\Delta H = -802.3$ kJ/mol) can also proceed as the side reaction. [137-138]. The mechanism was also in agreement with the results from kinetic study, isotopic data and density functional theory [139-140].

2.2.4 Kinetic modeling

Forzatti and co-workers [141-142] proposed kinetic models based on combustion-reforming reaction (CRR) mechanism, which consisted of methane combustion, steam reforming of methane, water gas shift reaction, reverse water gas shift reaction, H_2 oxidation, and CO oxidation. The proposed kinetic scheme and the parameter estimation are shown in Table 2-4.

Table 2-4 Kinetic model for partial oxidation of methane

Reaction	Rate equation $r_i\left[\frac{mol}{g_{cat}\,s}\right]$	$k_i^{873K}\left[\frac{mol}{atm\,g_{cat}\,s}\right]$	$E_{act}\left[\frac{kJ}{mol}\right]$
CH_4 total oxidation $CH_4 + 2O_2 \rightarrow CO_2 + H_2O$	$r_{tot_{ox}} = \frac{k_{tot_{ox}} P_{CH_4}}{1 + k_{ads_{H_2O}} P_{H_2O}} \sigma_{O_2}$	1.030×10^{-1}	92
CH_4 steam reforming $CH_4 + H_2O \rightarrow 3H_2 + CO$	$r_{SR} = \frac{k_{SR} P_{CH_4} (1-\eta_{SR})}{1 + k_{ads,CO} P_{CO} + k_{ads,O_2} P_{O_2}} \sigma_{H_2O}$	1.027×10^{-1}	92
Direct water gas shift $CO + H_2O \rightarrow CO_2 + H_2$	$r_{WGS} = \frac{k_{WGS} P_{H_2O} (1-\eta_{WGS})}{1 + k_{ads,H_2O} P_{H_2O}} \sigma_{CO}$ $\eta_{WGS} < 1$	6.239×10^{-2}	25
Reverse water gas shift $CO_2 + H_2 \rightarrow CO + H_2O$	$r_{RWGS} = k_{RWGS} P_{CO_2} (1-\eta_{RWGS}) \sigma_{H_2}$ $\eta_{RWGS} < 1$	1.276×10^{-2}	62
H_2 oxidation $H_2 + ½O_2 \rightarrow H_2O$	$r_{H_2,ox} = k_{H_2,ox} P_{H_2} \sigma_{O_2}$	2.638×10^{3}	62
CO oxidation $CO + ½O_2 \rightarrow CO_2$	$r_{CO,ox} = k_{CO,ox} P_{CO} \sigma_{O_2}$	1.938×10^{1}	76

Surface adsorption	$k_{ads,i}^{873K}\left[atm^{-1}\right]$	$\Delta H_{ads}\left[\frac{kJ}{mol}\right]$
O_2	5.461	-73
H_2O	3.901×10^2	-16
CO	2.114×10^2	-37

2.3. Combination of DRM and POM – Oxidative CO_2 Reforming of Methane

Even though the coke deposition rate in CO_2 reforming of methane can be minimized by modification of catalyst, the high energy requirement prevents it to be commercialized. On the other hand, although partial oxidation of methane is a highly energy efficient reaction due to exothermic reaction, it can also be potentially hazardous from the viewpoint of hotspot formation coupled with poor heat transfer. Moreover, the pure oxygen required for the POM is also costly. An interesting approach is to combine the advantages of both reactions to minimize the disadvantages. Combination of DRM and POM results in a reaction called oxy-CO_2 reforming of methane (OCRM).

There are few practical advantages of this combination reaction over either DRM reaction or POM reaction. The first major advantage is that the amount of carbon deposition can be reduced since the oxygen available in the reaction system can easily oxidize the deposited carbon on catalyst surface. Secondly, since the OCRM reaction combines both exothermic (POM) and endothermic (DRM) reactions, the total energy requirement for the OCRM reaction can be reduced as well. Third, the H_2/CO ratios can be tailored to suit the requirement of the downstream processes. The ratio range around 1-2 can be produced via adjustment of $CH_4/CO_2/O_2$ feed ratio.

According to Choudhary et al. [143-144], the following reactions can occur during OCRM reaction depending on the process conditions:

$CH_4 + ½\ O_2 \rightarrow CO + 2\ H_2$ $\Delta H_r = -5$ kcal/mol (5)

$CH_4 + CO_2 \rightarrow 2\ CO + 2\ H_2$ $\Delta H_r = 61$ kcal/mol (6)

$CH_4 + H_2O \rightarrow CO + 3\ H_2$ $\Delta H_r = 54$ kcal/mol (7)

$CH_4 + 2\ O_2 \rightarrow CO_2 + 2\ H_2O$ $\Delta H_r = -192$ kcal/mol (8)

$CH_4 + 1½\ O_2 \rightarrow CO + 2\ H_2O$ $\Delta H_r = -124$ kcal/mol (9)

$CO + H_2O \rightarrow CO_2 + H_2$ $\Delta H_r = -8$ kcal/mol (10)

$CO_2 + H_2 \rightarrow CO + H_2O$ $\Delta H_r = 8$ kcal/mol (11)

Reaction (5) represents the POM reaction, while reaction (6) and (7) represents the DRM reaction and the SRM reaction, respectively. Reactions (8) and (9) are expected to produce energy for the reaction. Reactions (10) and (11) are the water gas shift (WGS) and the reverse water gas shift (rWGS) reactions, respectively.

The exact mechanism for the OCRM reaction is not clear until now. However, the syngas production was postulated to occur via the simultaneous partial oxidation to CO and H_2 [144] or complete combustion of methane followed by steam and CO_2 reforming of methane to CO and H_2 [95].

Choudhary and Choudhary [146] emphasized two important issues for the catalyst development for OCRM reaction:

a. The catalyst should have a high activity for individual DRM and POM reactions.
b. The catalyst should have high thermal resistant and coke resistance towards carbon deposition as the coke deposition deactivates catalyst very fast.

Ashcroft et al. [18] found that the order of the catalyst activity for the OCRM was $Ir/Al_2O_3 = Ni/Al_2O_3 > Rh/Al_2O_3 > Pd/Al_2O_3 > Ru/Al_2O_3$. However, the carbon formation in Ni/Al_2O_3 is the highest among the others with the order $Ni/Al_2O_3 >> Pd/Al_2O_3 > Ir/Al_2O_3 = Rh/Al_2O_3 = Ru/Al_2O_3$. Even though Ir/Al_2O_3 was found to be the best catalyst for this reaction, the price was very expensive. Therefore, Ni appears to be the most promising catalyst due to the cheaper price.

Jing et al. [145] investigated Ni/SiO_2 and SrO-promoted-Ni/SiO_2 catalysts and found that the addition of SrO to Ni/SiO_2 catalyst increased the resistance to Ni aggregating, leading to a high and stable activity for the OCRM reaction. They claimed that the high and stable activity was due to enhanced interaction between Ni species and SrO-promoted support. The addition of La_2O_3 to Ni/SiO_2 catalyst was also found to enhance catalytic activity due to strong interaction between NiO and La_2O_3 to form a La-Ni complex oxide in the $Ni\text{-}La_2O_3/SiO_2$ catalysts [147].

Jing et al. also reported the effect of Ni precursors on Ni/SiO_2 catalyst [148]. The nickel citrate precursor enhanced interaction between NiO and support to form nickel silicate. Once reduced at high temperature, this nickel silicate could produce small crystallites of metallic nickel. The smaller nickel particles gave higher catalytic activity than the larger ones. The same results were obtained on Ni/SiO_2 and $Ni\text{-}Al_2O_3/SiO_2$ catalysts prepared from either nickel citrate or nickel nitrate precursors [22].

Ruckenstein and Hu [149] investigated the Ni/MgO, Ni/Al_2O_3, and Ni/SiO_2 catalysts and reported that the reduced Ni/MgO gave higher activity and stability than reduced Ni/Al_2O_3 and Ni/SiO_2 catalysts, due to formation of solid solution NiO/MgO which inhibited carbon deposition and Ni sintering. Furthermore, it was reported that the CH_4 conversion increased with increase of O_2/CO_2 ratio, while the apparent conversion of

CO_2 passed through a maximum. They also found that the formation of solid solution of CoO and MgO was identified as the main reason of higher activity and stability compared to Co/CaO and Co/SiO_2 catalysts [150].

Choudhary and Mamman [151] combined the excellence of Co/MgO catalyst and NiO/MgO catalyst and reported that the addition CoO to NiO-MgO catalyst improved the catalyst performance and coke resistance. They also reported that the presence of cerium oxide in the NiCoMgCeO_x/Zr-Hf catalyst not only provided an oxygen storage capacity, but also greatly enhanced the mobility of lattice oxygen in the catalyst and thereby kept the catalyst surface free from coke accumulation [152].

Goldwasser et al. [153] studied perovskite $LaFe_{1-x}Co_xO_3$ catalyst and reported that using citrate sol-gel method, it was possible to obtain highly crystalline, homogenous and pure solids with well-defined structures. Once reduced, this perovskite catalyst could produce highly dispersed Co metallic particles stabilized by iron, leading to inhibition of metal sintering and coke formation, hence, increased the catalyst stability.

The catalytic performance of noble metal catalyst, such as Pt was investigated by Wang et al [154]. The Pt/ZrO_2 catalyst showed a strong deactivation in OCRM reaction. However, the addition of CeO_2 to the Pt/ZrO_2 catalyst resulted in a more active, stable and selective due to increase of oxygen storage capacity and ability to facilitate fast removal of coke deposition from the metal particle.

Tomishige et al. [155-156] investigated the bimetallic Pt-Ni catalyst over Al_2O_3 support and reported that a large temperature gradient was observed near the catalyst bed inlet for Ni/Al_2O_3 catalyst. However, the addition of Pt to the Ni/Al_2O_3 catalyst showed a flat temperature profile, suggesting that the methane combustion and reforming could proceed simultaneously and heat of combustion was effectively supplied to the reforming

reaction. Further observation revealed that the surface Pt atoms on Ni catalyst contributed to the enhancement of the catalyst reducibility.

CHAPTER 3

Role of catalyst support over Pd−Ni catalysts on catalyst activity and stability

This chapter describes the role of catalyst support over Pd−Ni catalysts on catalyst performance. Pd−Ni catalysts over several commercial metal oxides were synthesized using incipient wet impregnation method. The activities of Pd−Ni catalysts for syngas production via oxy−CO_2 reforming of methane were investigated at temperatures ranging from 500°C to 800°C in a fixed−bed continuous−flow reactor. The Pd−Ni/Y_2O_3 and Pd−Ni/Al_2O_3 catalysts show very high CH_4 and CO_2 conversions due to the formation of metal−support compound on these catalysts. On the Pd−Ni/Y_2O_3 catalyst, Pd interacts with Y_2O_3 support to form $Pd_xO_yY_z$ compound while Ni interacts with Al_2O_3 support to form $NiAl_2O_4$ spinel compound on the Pd−Ni/Al_2O_3 catalyst. However, the amount of deposited carbon on the spent Pd−Ni/Y_2O_3 catalyst is much lower than the one on the Pd−Ni/Al_2O_3 catalyst due to the presence of surface β−oxygen species and ability of Y_2O_3 to form oxycarbonate species, resulting in stable catalytic performance without noticeable deactivation during reaction. The surface β−oxygen species are found to promote cracking of C−H bond in CH_4 while the oxycarbonate species can oxidize the deposited carbon, respectively, hence leading to the stability of the Pd−Ni/Y_2O_3 catalyst.

3.1 Introduction

Catalytic CO_2 (dry) reforming of methane (DRM) is an attractive technology for syngas production [157-160] as DRM utilizes CO_2 and CH_4, which two major green-house effect gases are causing global warming [161]. However, serious problems in this reaction are the high carbon deposition rate and metal sintering which can easily deactivate the catalyst. Although there is an extensive ongoing research to modify the Ni−based catalyst in order to improve its coke and metal sintering resistance, the requirement of extensive energy for this highly endothermic reaction currently prevents its commercialization in industry [162-166].

Due to these three serious drawbacks, it is desirable to consider oxy-CO_2 reforming of methane (OCRM) which combines partial oxidation of methane (POM) − an exothermic reaction − with CO_2 (dry) reforming of methane (DRM) − an endothermic reaction. The stoichiometric equations of POM and DRM reactions are written as follows:

DRM: $CH_4 + CO_2 \rightarrow 2\ H_2 + 2\ CO \quad \Delta H°_{298} = 247.3$ kJ/mol

POM: $CH_4 + ½O_2 \rightarrow 2\ H_2 + \ CO \quad \Delta H°_{298} = -35.6$ kJ/mol

A combination of these two reactions not only can reduce the amount of carbon deposition since the oxygen can easily oxidize the deposited carbon on the catalyst, but also can reduce the total energy requirement since OCRM combines both exothermic POM and endothermic DRM reactions.

For a supported metal catalyst, it has been well established that factors such as catalyst support affects the catalyst activity. Some researchers have performed OCRM reaction using few catalyst supports, for example, Ni/MgO [65], Ni/SiO_2 [22], and Ni/Al_2O_3 [166]. However, there is no literature reported on Pd−Ni catalyst for OCRM

reaction. Therefore, it is necessary to investigate the effect of catalyst support over Pd−Ni catalysts on catalyst performance using commercial metal oxides.

In this study, the effect of catalyst supports on the catalytic performance of the Pd−Ni catalysts was investigated using few commercial catalyst supports. The catalyst supports used in this study were alumina (Al_2O_3), yttria (Y_2O_3), ceria (CeO_2), lanthania (La_2O_3), and titania (TiO_2). All these supports were chosen due to their specific properties: alumina for its high surface area, yttria for its high surface oxygen mobility, ceria for its high oxygen storage capacity, lanthania for its ability to form oxycarbonate compound, and titania for its strong metal−support interaction (SMSI).

3.2 Experimental

3.2.1 Catalyst synthesis

The catalysts were synthesized using conventional wet−impregnation method over the selected catalyst supports (γ−Al_2O_3, CeO_2, Y_2O_3, La_2O_3 and TiO_2) with a mole ratio of Pd/Ni of 1/1. The precursor of Pd was $PdCl_2$ (99%) which was purchased from Nacalai Tesque, while the Ni precursor was obtained from Strem Chemicals in the form of $Ni(NO_3)_2.6H_2O$. γ−Al_2O_3 (Sigma Aldrich), La_2O_3 (Nacalai Tesque), CeO_2 (Strem) Y_2O_3 (Strem) and TiO_2 (Strem) were used as the catalyst supports. The catalysts were prepared by the wet impregnation of the Pd and Ni precursors at room temperature and the impregnated catalysts were dried in oven at 100^{o}C for 12 h before they were calcined under air at 800^{o}C for 4 h. The Pd/Y_2O_3 and Ni/Y_2O_3 catalysts, which were prepared similarly using the impregnation method, were used for reference in this study.

3.2.2 Characterization methods

3.2.2.1 Specific surface area measurement

The specific surface area of each catalyst was measured by adsorption and desorption of N_2 at −196°C on Autosorb−1. Prior to the surface area measurement, the catalyst was outgassed at 250°C for a minimum of 12 h. The specific surface area of the catalyst was determined from the linear portion of BET plot.

3.2.2.2 ICP−MS

The metal content of each catalyst was measured on Agilent ICP−MS 7700 series. The catalyst was dissolved in a mixture of HNO_3 0.5 M and HCl 0.5M followed by filtering using a microfilter. The exact amount of Pd and Ni on Pd−Ni catalyst was determined from the calibration curve using reference Pd and Ni solutions.

3.2.2.3 X−ray diffraction

The X−ray diffraction pattern of each catalyst was measured on a Shimadzu XRD−6000 diffractometer using Cu Kα radiation. The catalyst was placed on an aluminum slide and scanned from 2θ of 10^o to 80^o with a ramp rate of 2^o/min. The beam voltage and current used were 40 kV and 30 mA, respectively.

3.2.2.4 FESEM

The morphology of each catalyst after catalytic test was visually observed using a field emission scanning electron microscope (FESEM: JEOL JSM−6700F). Prior to the analysis, the sample was coated with Pt under Pt−sputtering for 60 sec at 20 mA.

3.2.2.5 TPR and TPD measurements

Temperature−programmed reduction (TPR) measurement for the each fresh catalyst was performed on Quantachrome Chembet−3000. Prior to the TPR measurement, 0.1 g of catalyst was outgassed in N_2 for 3 h at 350^{o}C to remove any impurities and then cooled down to room temperature. 5%H_2/He gas was then introduced to the catalyst while the temperature of the furnace was increased to 900^{o}C at a heating rate of 10K/min.

The reduction degree of metal is calculated with the assumption of hydrogen/metal ratio of 1. The similar assumption is used for calculation of hydrogen absorption degree for Pd-Ni catalysts with negative peak.

The best three catalysts from catalytic study were further characterized by temperature−programmed desorption of oxygen (TPD-O_2) using Quantachrome Chembet−3000. Prior to the TPD−O_2 measurement, 0.2 g of sample was outgassed in He for 1 h at 300^{o}C to remove any impurities. Purified O_2 gas was then introduced at 300°C for 1 h and cooled down to room temperature. Purified He gas was then introduced to the system to purge out all the remaining oxygen. The TPD−O_2 measurement was started from room temperature to a maximum furnace temperature of 1000°C under a heating rate of 10K/min.

3.2.2.6 X-ray photoelectron spectroscopy

The X-ray photoelectron spectroscopy (XPS) was performed on Kratos AXIS Ultra DLD using a concentric hemispherical analyzer. The Al Kα gun with photon energy of 1486.6 eV was used as the X−ray source. The wide scans were performed using 80 eV pass energy while the narrow scans were performed with 40 eV pass energy. Prior to the

analysis, the sample was reduced under pure H_2 at 600°C for 1 h, which was same as the reduction condition during reaction. The sample was then mounted on the standard sample stubs using double-sided adhesive tapes and put inside the vacuum chamber to prevent oxidation of the sample. The core level signals were obtained at a photoelectron takeoff angle (R, measured with respect to the sample surface) of 90°. The X-ray source was run at a reduced power of 150 W (15 kV and 10 mA). The pressure in the analysis chamber was maintained at 10^{-8} Torr or lower during each measurement. All binding energies were referenced to C 1s hydrocarbon peak at 284.5 eV.

3.2.2.7 TEM

The metal particle size of each catalyst was measured visually using HRTEM system JEOL JEM-2100F. The average size was then calculated over 50 particles. Prior to the TEM analysis, the catalyst was reduced at 600˚C in pure H_2 for 60 min. The catalyst was then ultrasonically dispersed in ethanol and spread over perforated copper grids.

3.2.3 Catalytic reaction

The catalytic reaction was carried out in a fixed bed quartz reactor with inner diameter of 4 mm and length of 400 mm. 0.1 g of catalyst was used in each reaction and held by the quartz wool placed in the middle of the reactor. The temperature of the catalyst bed was controlled and monitored by a thermocouple that was in contact with the top layer of the catalyst bed. The catalytic reaction was performed at atmospheric pressure and temperatures ranging from 500 to 800˚C. Prior to the catalytic test, the catalyst was reduced in 20 mL/min of H_2 at 600^{o}C for 1 h, followed by purging in 20 mL/min of He

while the temperature was increased to the reaction temperature. The feed mixture consisting of $CH_4/CO_2/O_2$ with a molar ratio of 2/1/1 was then introduced to the reactor at a flowrate of 20 mL/min. All the gases used here were research grade gases (99.95% CH_4, 99.99% CO_2, 99.8% O_2, and 99.9995% He). A cold trap filled with 50% glycerol and 50% water at temperature of −10°C was installed between the reactor exit and the GC sampling valve to condense any moisture formed. The gas product was analyzed using a gas chromatograph (HP 6890) equipped with a Hayesep D column and a TCD detector. The peak area in the chromatogram was then converted to volume−% using a calibration curve. The total flow rate of the product gases was measured using bubble flow meter. Figure 1 shows the schematic diagram of the experimental setup. The conversions of CH_4 and CO_2 were calculated using the following formula:

$$X_{CH_4}(\%) = \frac{n_{CH_4,in} - n_{CH_4,out}}{n_{CH_4,in}} x\,100$$

$$X_{CO_2}(\%) = \frac{n_{CO_2,in} - n_{CO_2,out}}{n_{CO_2,in}} x\,100$$

where *n* is molar flow rate of each gas.

The total amount of deposited carbon on the spent catalysts collected after the catalytic reaction was measured using thermogravimetric analysis (TGA) on a Shimadzu DTG−60 thermogravimetric analyzer. Around 10 mg of used catalyst was used in each TGA experiment and the used catalyst was heated in air from room temperature to 800ºC with a heating rate of 10K/min.

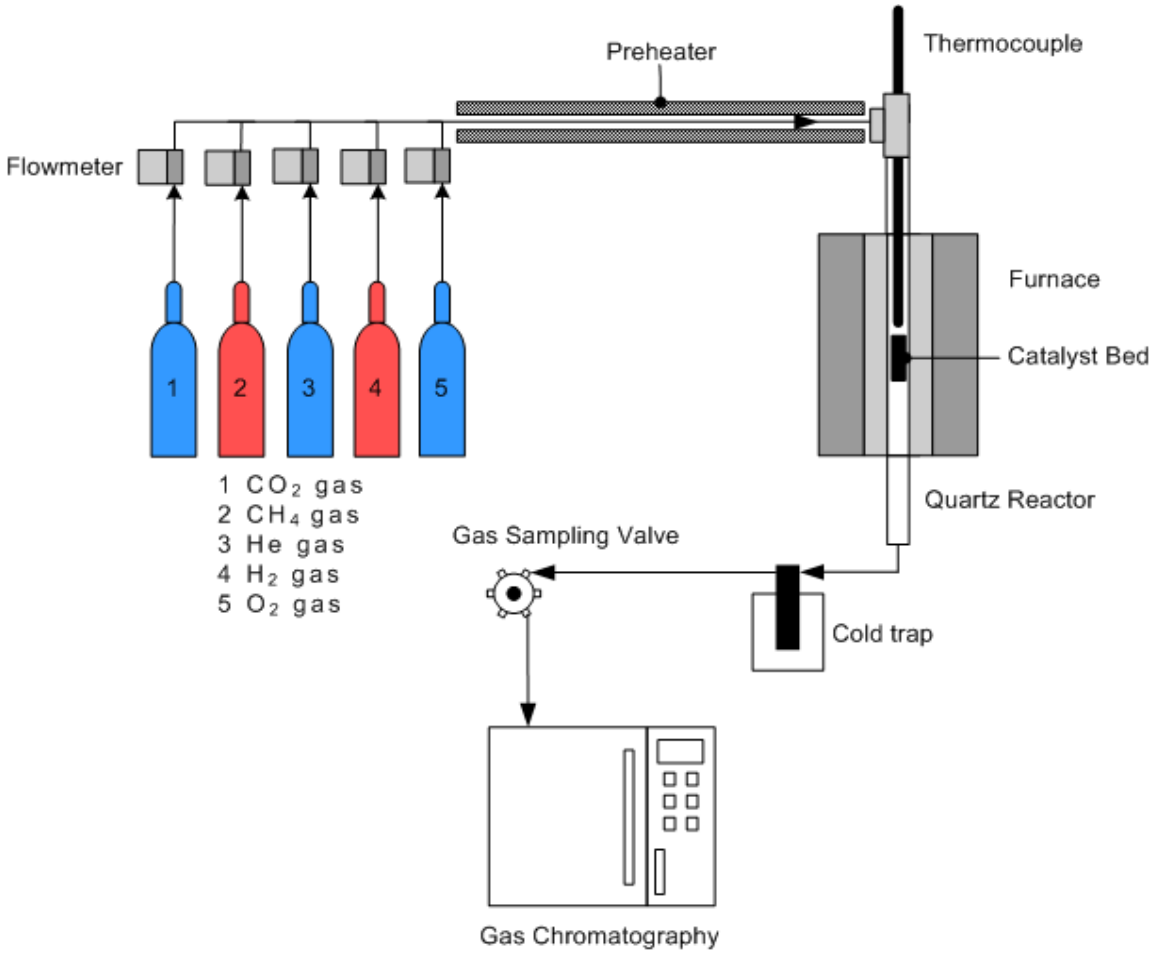

Figure 3−1 Schematic diagram of experimental setup

3.3 Results and discussion

3.3.1 Physical properties of Pd−Ni catalysts

Table 3-1 tabulates the physical properties of the prepared catalysts and their corresponding catalyst supports. The surface area of the catalyst supports decreases in the following order: Al_2O_3 > TiO_2 > Y_2O_3 > La_2O_3 > CeO_2. After impregnation of the catalyst supports with the Pd and Ni precursors, the surface area of the prepared Pd−Ni catalysts decreases significantly with the following order: Pd−Ni/Al_2O_3 > Pd−Ni/TiO_2 > Pd−Ni/Y_2O_3 > Pd−Ni/La_2O_3 > Pd−Ni/CeO_2. The order of the decreasing area for both the

catalyst supports and the catalysts is similar with each other, indicating that the impregnation of the Pd and Ni precursors did not change the nature of the catalyst supports.

Table 3-1 Physical properties of prepared catalysts

Catalysts	S_{BET} (m^2/g)	Metal content (wt-%)	
		Pd	Ni
Pd−Ni/Al_2O_3	133.7 ± 4.4	4.5 ± 0.2	2.6 ± 0.1
Pd−Ni/TiO_2	11.9 ± 1.5	4.3 ± 0.2	2.1 ± 0.1
Pd−Ni/La_2O_3	8.0 ± 0.3	4.5 ± 0.2	2.5 ± 0.1
Pd−Ni/Y_2O_3	8.6 ± 0.5	4.4 ± 0.2	2.8 ± 0.1
Pd−Ni/CeO_2	4.3 ± 0.5	4.5 ± 0.2	2.0 ± 0.1
Al_2O_3	174.9	−	−
TiO_2	12.8	−	−
La_2O_3	9.6	−	−
Y_2O_3	10.1	−	−
CeO_2	4.1	−	−

Metal content measured using ICP−MS

Table 3-1 also tabulates the metal contents of Pd and Ni in all the catalysts as analyzed by the ICP−MS. It can be seen that the metal contents of Pd and Ni in all the Pd−Ni catalysts were around 4.4 wt-% and 2.4 wt-%, respectively, showing that the synthesized catalysts have the Pd/Ni mole ratio of 1/1 as expected.

3.3.2 H_2-TPR profiles of Pd−Ni catalysts

Figure 3-2 shows the H_2−TPR profiles of fresh Pd−Ni catalysts and its reduction degree. The profiles of the Pd/Y_2O_3 and the Ni/Y_2O_3 catalysts are provided for references. It is observed that there are negative and positive peaks on the Pd/Y_2O_3 catalyst. The negative peak observed at temperatures of 100-130°C characterizes the decomposition of β-PdH_x phase (the x in β-PdH_x represents the H_2 absorption degree), which was formed during the H_2 flushing prior to the TPR analysis. The presence of β-PdH_x phase indicates the formation of large Pd particles [167]. Bakker et al. [168] reported that the H_2 absorption degree is determined by the Pd crystallite size: bigger Pd crystallites absorb more hydrogen in the β-PdH_x phase.

In addition, two positive peaks are observed at 75-230°C and 700°C. The former peak can be assigned to the reduction of the PdO species [13], while the latter peak is attributed to the formation of Pd−Y_2O_3 compound. The TPR peak at 700°C indicates the formation of metal−support compound (named here as MSC) between Pd and Y_2O_3, thus causing the shifting of the reduction of palladium to higher temperature. Costa et al. [169] observed a reduction peak of Pd/Y_2O_3 catalyst at high temperature of around 650°C and assigned this peak to the reduction of Pd_2O_4Y compound. However, Pd is known to form many complexes with Y_2O_3, such as Pd_2O_4Y [169], $Pd_2O_5Y_2$ [170], and $Pd_2O_7Y_2$ [171]. Therefore, the high temperature TPR peak for the Pd/Y_2O_3 catalyst observed in our study may be temporary associated to the reduction of $Pd_xO_yY_z$ compound. Beside Y_2O_3, the formation of a Pd−support compound has also been observed on the Pd/Al_2O_3 catalyst with the general formula of $Pd_xCl_yO_z$ [172]; in this particular case, Pd has been suggested

to form a metal−support compound with the Al_2O_3 surface as the reduction of Pd compound occurred only at a high temperature [173].

For the Ni catalyst, the peak observed at temperature from 370^oC to 530^oC characterizes the reduction of NiO species. The total amount of H_2 consumption agrees with the stoichiometric reaction ($NiO + H_2 \rightarrow Ni + H_2O$), suggesting that all the Ni species present in the oxidized state were reduced to the Ni metallic state [60].

Due to the addition of Pd to Ni catalyst, some changes in the TPR reduction patterns are observed on the Pd−Ni catalysts. Total amounts of hydrogen consumption and reduction degree are tabulated in Table 3-2. The TPR profile of the Pd−Ni/Al_2O_3 catalyst shows a negative peak at low temperature around 110^oC characterizing the decomposition of the β-PdH_x phase with H_2 absorption degree around 36%. In addition, a positive peak is observed at high temperature at around 675-880^oC characterizing the reduction of the $NiAl_2O_4$ spinel phase; the presence of this $NiAl_2O_4$ spinel phase shows the formation of metal−support compound (MSC) between the nickel and the alumina support, resulting in the formation of fine Ni particle size due to the stronger resistance to sintering [168]. It is also important to point out that there is no reduction of NiO, which is usually found at around 370-530^oC, indicating that all Ni particles have strong interaction with the alumina support as the reduction degree of Ni at around 675-880^oC is almost 100%.

Table 3-2 Amount of H_2 consumption and reduction degree of Pd−Ni catalysts

Catalyst	H_2 consumption (μmol/g)		Reduction degree (%)	
	Pd	Ni	Pd	Ni
Pd−Ni/γ−Al_2O_3	152	426	36*	96
Pd−Ni/TiO_2	127	364	32*	100
Pd−Ni/La_2O_3	359	408	85	96
Pd−Ni/Y_2O_3	393	457	95	96
Pd−Ni/CeO_2	152	352	36*	100

*H_2 absorption degree due to negative peak

The negative and positive peaks characterizing the decomposition of β-PdH_x phase and the reduction of NiO, respectively, are observed on the Pd−Ni/TiO_2 catalyst. The absorption degree of β-PdH_x phase on the Pd−Ni/TiO_2 catalyst is comparable with the one on the Pd−Ni/Al_2O_3 catalyst, indicating that the size of Pd particle on the Pd−Ni/Al_2O_3 catalyst is similar to the one on the Pd−Ni/TiO_2 catalyst. No other peaks are found on the TPR profile of the Pd−Ni/TiO_2 catalyst. The same negative and positive peaks observed on the Pd−Ni/TiO_2 catalyst are also found on the Pd−Ni/La_2O_3 catalyst. In addition to those peaks, there is another peak at 120-250^oC, which corresponds to the reduction of PdO species. The combination of β-PdH_x and PdO peaks on the Pd−Ni/La_2O_3 catalyst suggests that the Pd particles are present from small to big particles. The low absorption degree of PdH_x around 8% also confirms the presence of smaller Pd particles in the β-PdH_x phase.

In addition, the reduction of NiO of the Pd−Ni/TiO_2 and the Pd−Ni/La_2O_3 catalysts shifts to lower temperature due to the hydrogen spill-over from Pd which is reduced at lower temperature than Ni. Once Pd is reduced, the reduced Pd acts as hydrogen dissociation sites and the dissociated hydrogen migrates through the catalyst surface to reduce the Ni easier than the normal gaseous molecular hydrogen [175].

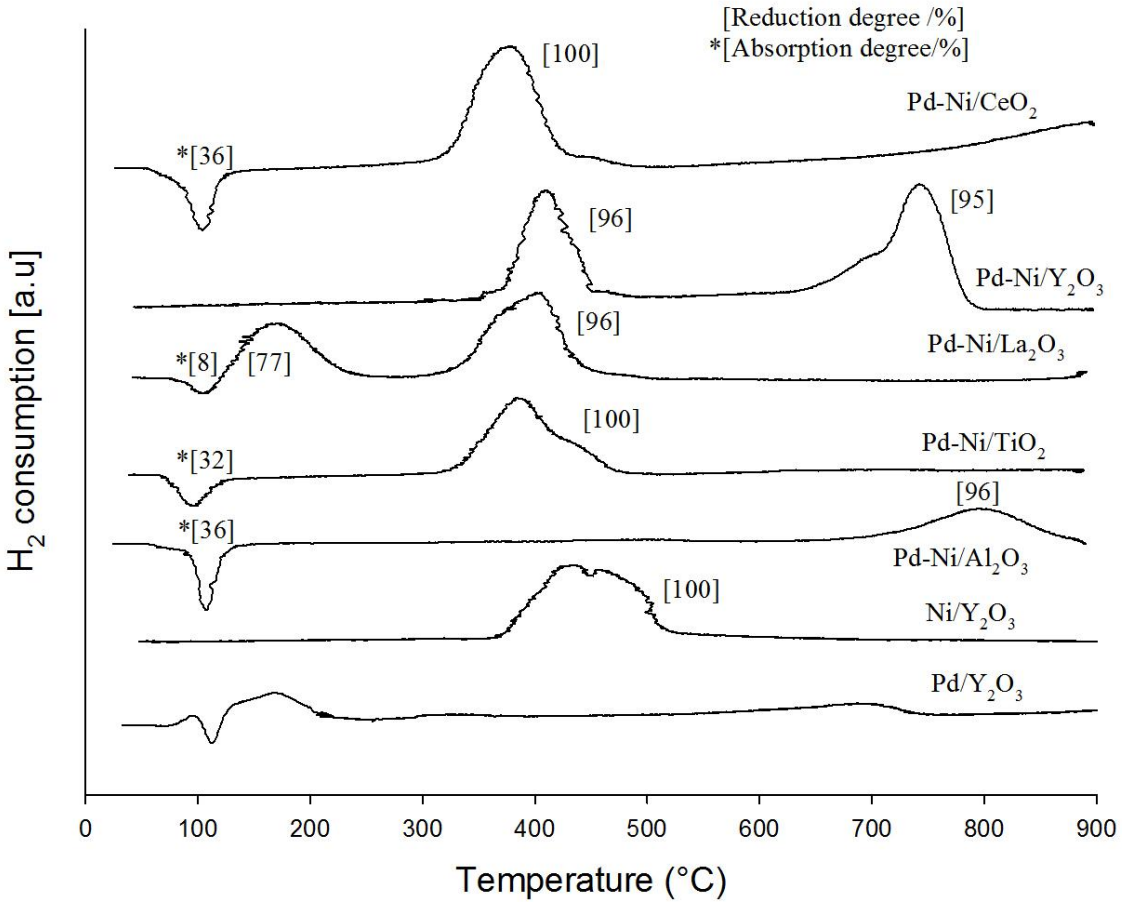

Figure 3-2 TPR profiles of Pd−Ni catalysts over several catalyst supports

In contrast with other catalysts, there is no negative peak around 100^{o}C characterizing the decomposition of the β-PdH_x phase on the Pd−Ni/Y_2O_3 catalyst,

indicating that the Pd particles on the Pd−Ni/Y_2O_3 catalyst are much smaller than those on other Pd−Ni catalysts. Moreover, one high reduction temperature is also observed around 630-800^oC. This peak is attributed to the reduction of $Pd_xO_yY_z$ compound, which reveals formation of MSC between Pd and Y_2O_3 support as in agreement with the high reduction degree of Pd almost 100%. However, the reduction temperature of this peak on the Pd−Ni/Y_2O_3 catalyst is much higher than those on the Pd/Y_2O_3 catalyst, indicating that the metal−support interaction on the Pd−Ni/Y_2O_3 catalyst is stronger than those on the Pd/Y_2O_3 catalyst.

Similar to the Pd−Ni/TiO_2 catalyst, the TPR profile of the Pd−Ni/CeO_2 catalyst also shows a negative peak at low temperature characterizing the decomposition of β−PdH_x phase and a positive peak at 330^oC to 430^oC characterizing the reduction of NiO species. The reduction temperature of NiO also shifts to lower temperature due to the hydrogen spill−over from Pd. These results show that there is no formation of MSC on the Pd−Ni/TiO_2, Pd−Ni/La_2O_3 and Pd−Ni/CeO_2 catalysts.

3.3.3 XRD patterns of fresh and reduced Pd−Ni catalysts

Figure 3-3 shows the XRD crystal structure of fresh Pd−Ni catalysts. The XRD patterns for NiO and PdO are also provided for reference. The diffraction peaks of NiO are observed at 37.4^o, 43.4^o, and 63.2^o whereas the diffraction peaks of PdO are observed at 33.9^o, 41.9° and 54.8°. The diffraction peaks of PdO at 33.9^o are observed in all catalysts. The presence of PdO peak at 33.9^o in those catalysts indicates the formation of big PdO particles. However, this peak should be interpreted carefully for the Pd−Ni/Y_2O_3 catalyst as the characteristic peak of Y_2O_3 is at 33.8^o. In addition, a small diffraction peak

is observed on the Pd−Ni/Y_2O_3 catalyst at 45.9^o, which corresponds to the formation of $Pd_xO_yY_z$ compound, as observed from the TPR results. The presence of this compound shows that Pd interacts with Y_2O_3 support to form MSC. In contrast, the NiO peak is hardly observed in all catalysts, indicating that the crystal size of NiO particle is too small which is beyond the detection limit of XRD.

The XRD crystal structure of reduced Pd−Ni catalysts is shown in Figure 3−3b. The diffraction peaks of metallic Pd at 40.1°, 46.6°, and 68° (PDF card 00-005-0681) are observed in the Pd−Ni/Al_2O_3, Pd−Ni/La_2O_3, Pd−Ni/TiO_2, and Pd−Ni/CeO_2 catalysts. However, these metallic Pd peaks are not observed in the Pd−Ni/Y_2O_3 catalyst since the catalyst was only reduced at 600°C while the reduction peak of $Pd_xO_yY_z$ compound is around 630−800^{o}C. In addition, no diffraction peaks of metallic Ni at 44.4°, 51.6°, and 76.1° (PDF card 00-001-1258) are observed in all catalysts, indicating that the crystal size of Ni particle is beyond the detection limit of XRD.

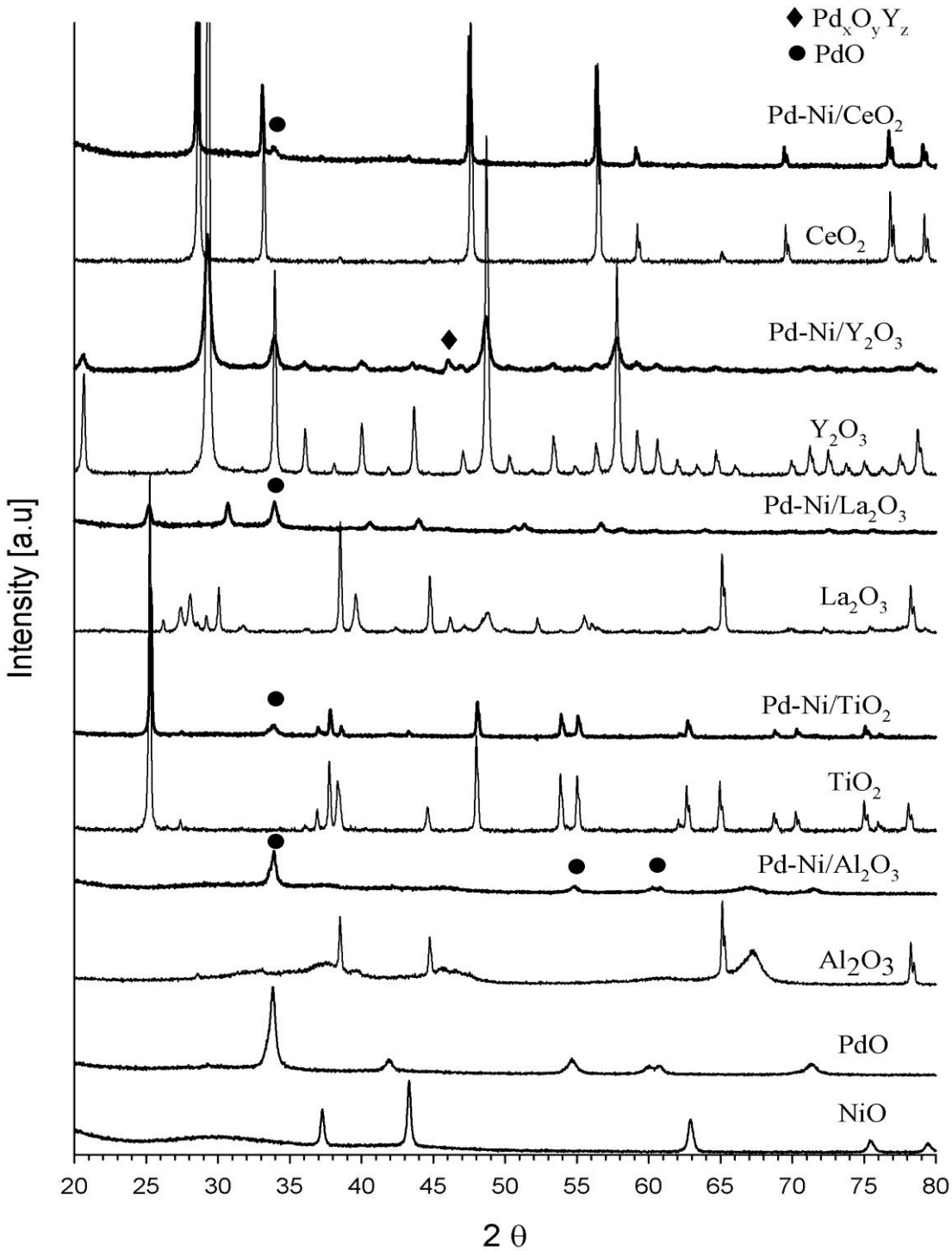

Figure 3-3a XRD profiles of fresh Pd−Ni catalysts over several catalyst supports

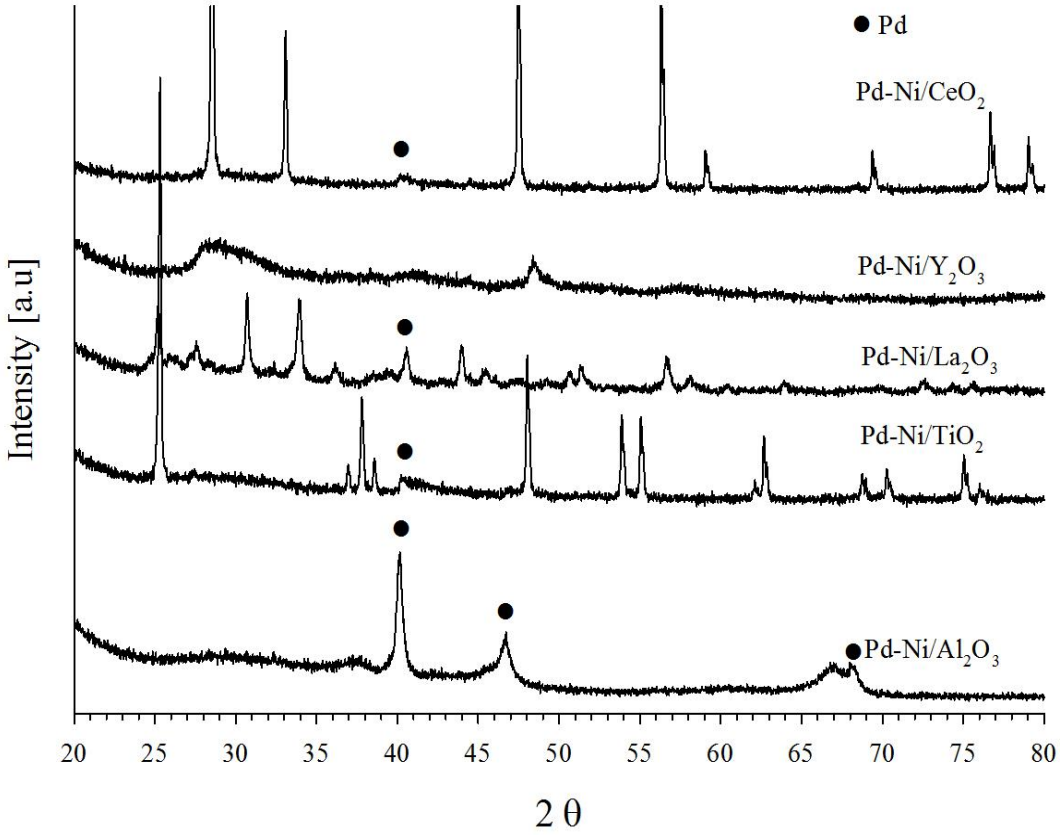

Figure 3-3b XRD profiles of reduced Pd−Ni catalysts

3.3.4 XPS analysis of fresh and reduced Pd−Ni catalysts

Figure 3-4a shows the XPS spectra of Pd 3d core level of Pd−Ni catalysts. It can be seen that the Pd−Ni/Al_2O_3, Pd−Ni/La_2O_3, Pd−Ni/TiO_2, and Pd−Ni/CeO_2 catalysts show the $3d_{5/2}$ peak at a binding energy of 336.8 ± 0.2 eV, showing that the Pd particles on those catalysts are essentially in Pd^{2+} oxidation state [176]. This result shows that no association between Pd and those supports took place during the catalyst preparation. In contrast, the Pd $3d_{5/2}$ peak of the Pd−Ni/Y_2O_3 catalyst has a binding energy at 337.5 eV, which is higher than the Pd^{2+} oxidation state, showing that electrons have been transferred

from Pd to Y_2O_3 support to form $Pd_xO_yY_z$ compound, as similarly observed from the TPR results.

Figure 3-4b shows the Ni 2p spectra of Pd−Ni catalysts. It can be seen that the Pd−Ni/TiO_2, Pd−Ni/Y_2O_3, and Pd−Ni/CeO_2 catalysts show a peak at the binding energy of 854.6eV. This peak corresponds to the Ni^{2+} oxidation state [176], indicating that there is no interaction between Ni particles and the catalyst support to form the complex oxide/spinel on those catalysts [177]. However, the Pd−Ni/La_2O_3 catalyst shows 2 peaks at 851.2 eV and 854.6 eV, respectively, which can be attributed to either La $3d_{3/2}$ peaks or Ni 2p peaks since the La 3d peaks overlap with the Ni 2p peaks due to very close binding energy between La and Ni [178-179]. In contrast, the Ni 2p peak of the Pd−Ni/Al_2O_3 catalyst shifts to higher binding energy (855.4eV), suggesting that there is an interaction between Ni particles and Al_2O_3 support. This XPS result is in agreement with the TPR results showing the formation of $NiAl_2O_4$ spinel phase on the Pd−Ni/Al_2O_3 catalyst.

Figure 3-4c the XPS O 1s spectra of Pd−Ni catalysts. It can be seen that only the Pd−Ni/Y_2O_3 catalyst shows two obvious peaks at 529.0 eV and 531.5 eV. The former peak can be attributed to the O^{2-} oxidation state, while the latter peak can be attributed to the adsorbed oxygen. The XPS O 1s peak on Y_2O_3 was reported at 529.6eV [180]. However, the peak observed on the Pd−Ni/Y_2O_3 catalyst has shifted to lower binding energy (529.0 eV). These results, which show the transfer of electrons from Pd to O, confirm the TPR result for formation of MSC, possibly in the form of $Pd_xO_yY_z$ compound.

While Pd has been observed to transfer electrons to O on the Pd−Ni/Y_2O_3 catalyst, this phenomenon has not been observed for other catalysts. The XPS O 1s peak of the Pd−Ni/Al_2O_3 catalyst appears at 530.75eV which is lower than the XPS O 1s peak of pure

Al_2O_3 (531.3eV) [181] showing that electron has been transferred from Ni instead of Pd to O to form $NiAl_2O_4$ spinel compound.

Contrary to the Pd−Ni/Y_2O_3 and Pd−Ni/Al_2O_3 catalysts, Pd or Ni is found not to transfer any electrons to O on the rest of the catalysts as there is no shift of the XPS O 1s peak on Pd−Ni/La_2O_3 (530.2eV), Pd−Ni/TiO_2 (529.3eV), and Pd−Ni/CeO_2 (529.5eV) catalysts. These XPS O 1s peaks correspond exactly to the binding energy of O−La^{3+} [182], O−Ti^{4+} [183], and O−Ce^{4+} [184], respectively.

Figure 3-4d shows the XPS Pd 3d of reduced Pd−Ni catalysts. It can be seen that all reduced catalysts, except Pd−Ni/Y_2O_3 catalyst, shows the peak at around 334.8eV, corresponding to the presence of Pd^0 [176]. However, the reduced Pd−Ni/Y_2O_3 catalyst shows the peak at higher binding energy around 338eV, showing that the Pd has transferred electron to Y_2O_3 to form $PdxO_yY_z$ compound.

The XPS Ni 2p (Figure 4e) of reduced Pd−Ni catalysts shows that Pd−Ni/La_2O_3, Pd−Ni/CeO_2, and Pd−Ni/TiO_2 catalysts show the peak at 854.9eV, corresponding to the presence of Ni^{2+} [176]. Even though the catalyst was reduced prior to the XPS analysis, it may oxidize during the sample preparation and transfer to the XPS chamber. It was reported by Kugai et al. [185] that all Ni metal particles from reduced Ni catalyst were oxidized when they were exposed to air at room temperature for 3 min. In contrast, the Pd−Ni/Y_2O_3 also shows the shifting of peak to higher binding energy, indicating that the electron has been transferred from Ni, probably to Pd to form bimetallic Pd−Ni particles. The shifting to higher binding energy is observed more intense in the Pd−Ni/Al_2O_3 catalyst due to the presence of $NiAl_2O_4$ compound.

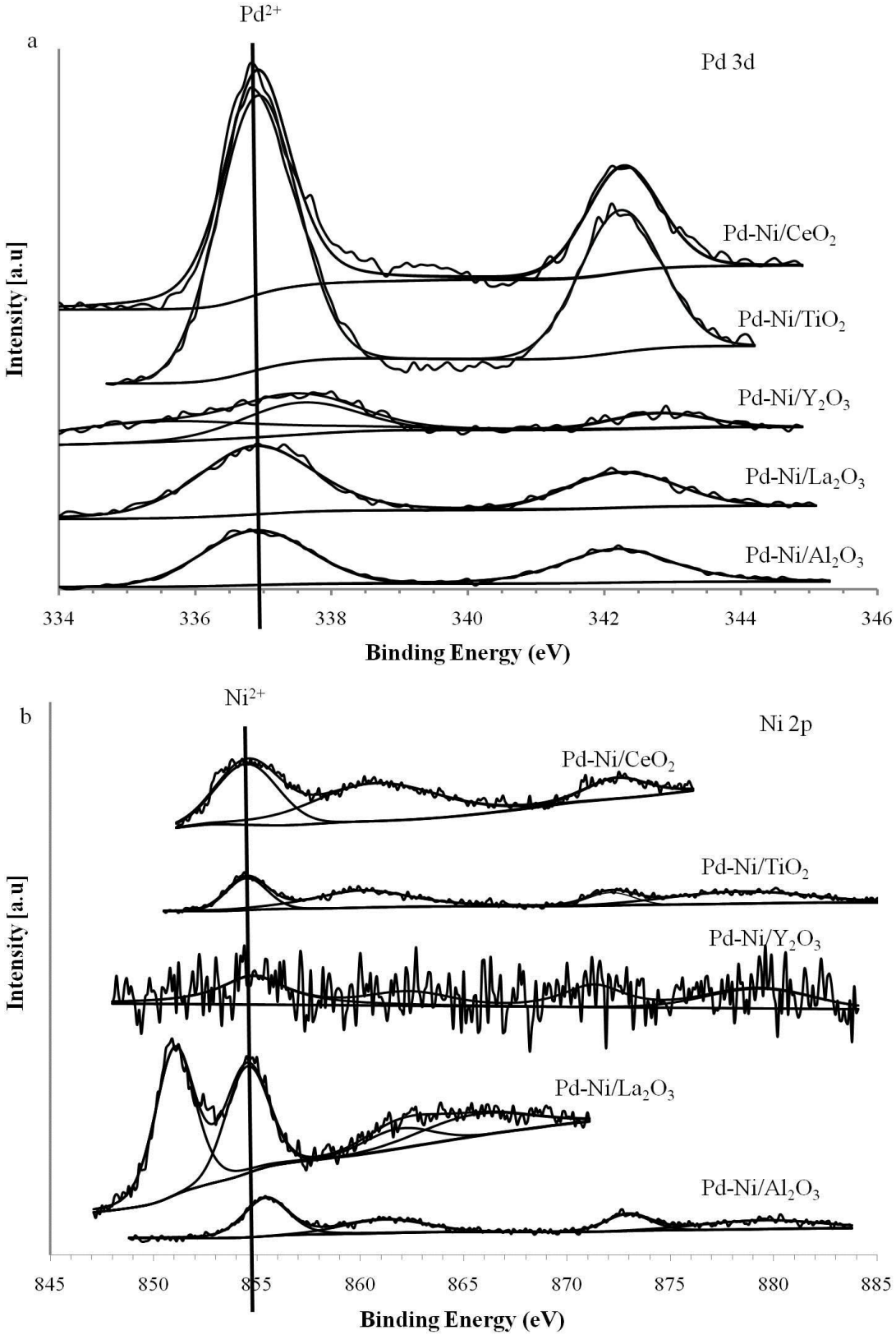
a
Pd2+
Pd 3d
Pd-Ni/CeO2
Pd-Ni/TiO2
Pd-Ni/Y2O3
Pd-Ni/La2O3
Pd-Ni/Al2O3
Intensity [a.u]
334
336
338
340
342
344
346
Binding Energy (eV)
b
Ni2+
Ni 2p
Pd-Ni/CeO2
Pd-Ni/TiO2
Pd-Ni/Y2O3
Pd-Ni/La2O3
Pd-Ni/Al2O3
Intensity [a.u]
845
850
855
860
865
870
875
880
885
Binding Energy (eV)

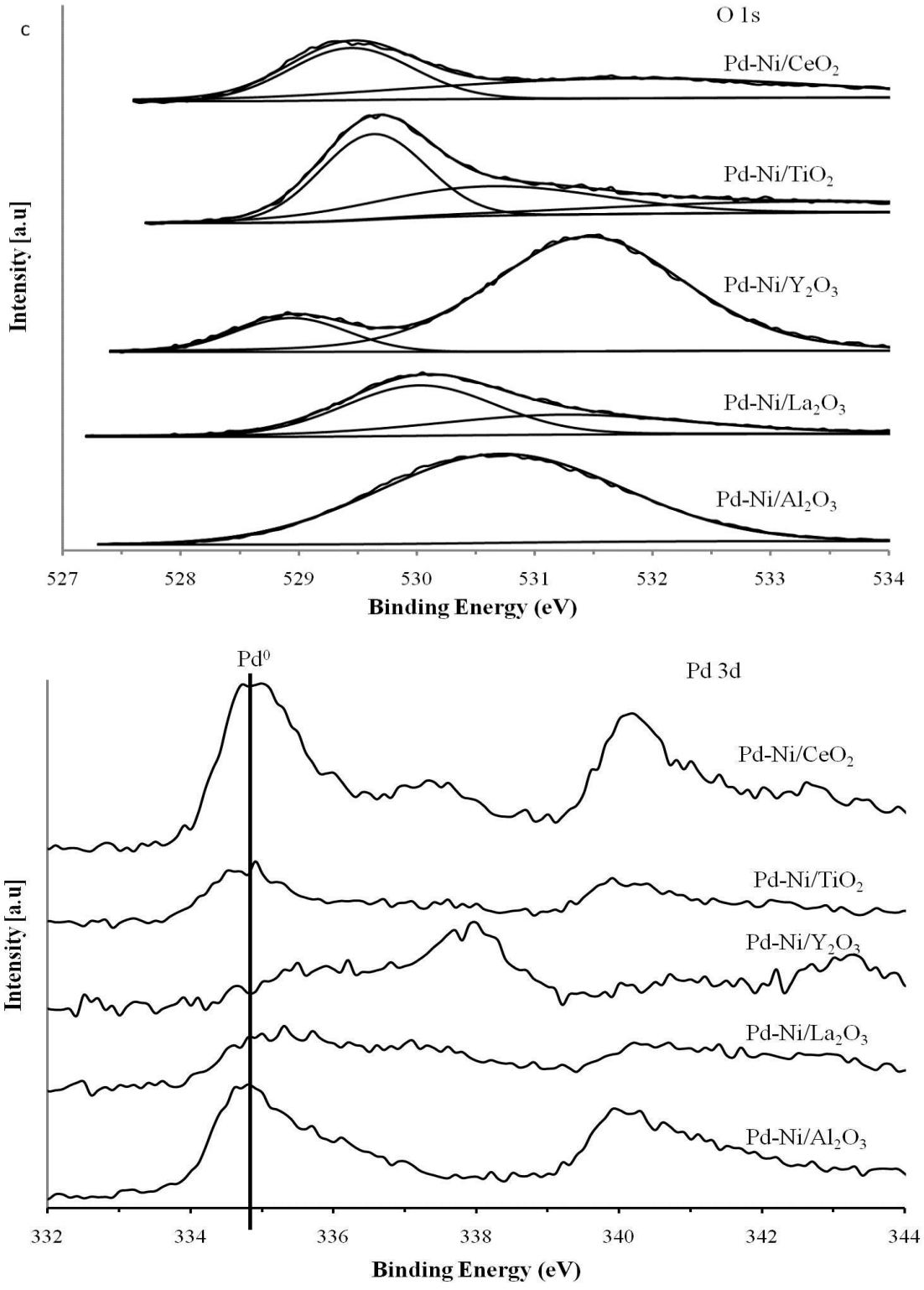
c
O 1s
Pd-Ni/CeO2
Pd-Ni/TiO2
Pd-Ni/Y2O3
Pd-Ni/La2O3
Pd-Ni/Al2O3
Intensity [a.u]
527
528
529
530
531
532
533
534
Binding Energy (eV)
Pd0
Pd 3d
Pd-Ni/CeO2
Pd-Ni/TiO2
Pd-Ni/Y2O3
Pd-Ni/La2O3
Pd-Ni/Al2O3
Intensity [a.u]
332
334
336
338
340
342
344
Binding Energy (eV)

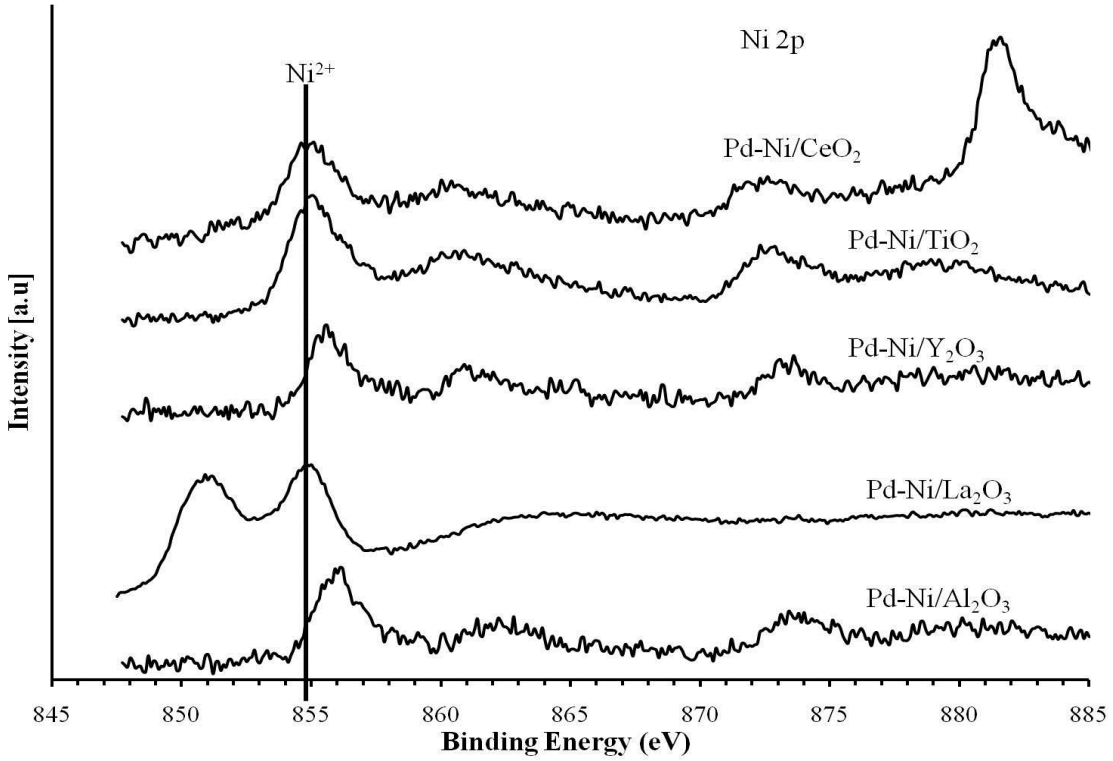

Figure 3-4 XPS spectra of Pd−Ni catalysts: a) Pd 3d; b) Ni 2p; c) O 1s of fresh catalysts; d) Pd 3d; e) Ni 2p of reduced catalysts

3.3.5 Particle size measurement of Pd−Ni catalysts

Figure 3-5 and Table 3-3 respectively show the TEM images and the metal particle size of the reduced Pd−Ni catalyst. It can be seen that the order of metal particle size of the Pd−Ni catalysts is Pd−Ni/Al_2O_3 = Pd−Ni/Y_2O_3 < Pd−Ni/La_2O_3 < Pd−Ni/CeO_2 < Pd−Ni/TiO_2. The Pd−Ni/Al_2O_3 and Pd−Ni/Y_2O_3 catalysts have the smallest metal particles due to formation of MSC as has been observed from the TPR and XPS results. On the Pd−Ni/Al_2O_3 catalyst, Ni interacts strongly with Al_2O_3 to form $NiAl_2O_4$ spinel compound, while Pd interacts strongly with Y_2O_3 support on the Pd−Ni/Y_2O_3 catalyst to form $Pd_xO_yY_z$ compound. The presence of these compounds prevents the aggregation of the

metallic particles formed during the reduction process, resulting in smaller metal particles. This phenomenon was also observed by Cheng et al. [60], who reported smaller Ni particle size on the Ni/Al_2O_3 catalyst due to the presence of $NiAl_2O_4$ compound. It is important to take note that only Pd on $Pd\text{-}Ni/Al_2O_3$ catalyst and Ni on $Pd\text{-}Ni/Y_2O_3$ catalyst are fully reduced at reduction temperature of 600°C. Therefore, the metal particle size observed on $Pd\text{-}Ni/Al_2O_3$ and $Pd\text{-}Ni/Y_2O_3$ catalyst could be attributed to the metal size of Pd and Ni, respectively. In addition, the TEM figure of $Pd\text{-}Ni/Y_2O_3$ catalyst clearly shows the presence of metal particles while the XRD of reduced $Pd\text{-}Ni/Y_2O_3$ catalyst shows no clear diffraction peak either due to metallic Ni or metallic Pd since the metal particle size on reduced $Pd\text{-}Ni/Y_2O_3$ catalyst is beyond the detection limit of XRD.

In contrast, the metal particle size of the $Pd{-}Ni/La_2O_3$, $Pd{-}Ni/CeO_2$, and the $Pd{-}Ni/TiO_2$ catalysts are quite big, due to the lack of MSC formation between metal (Pd or Ni) and the catalyst support. Moreover, the presence of $\beta{-}PdH_x$ phase on those catalysts as shown in the TPR results also suggests the formation of big Pd particles. Based on TPR results, at reduction temperature of 600°C, both Pd and Ni are fully reduced on $Pd\text{-}Ni/La_2O_3$, $Pd\text{-}Ni/TiO_2$, and $Pd\text{-}Ni/CeO_2$ catalysts, hence, the metal size observed on those catalysts could be combination of Pd and Ni.

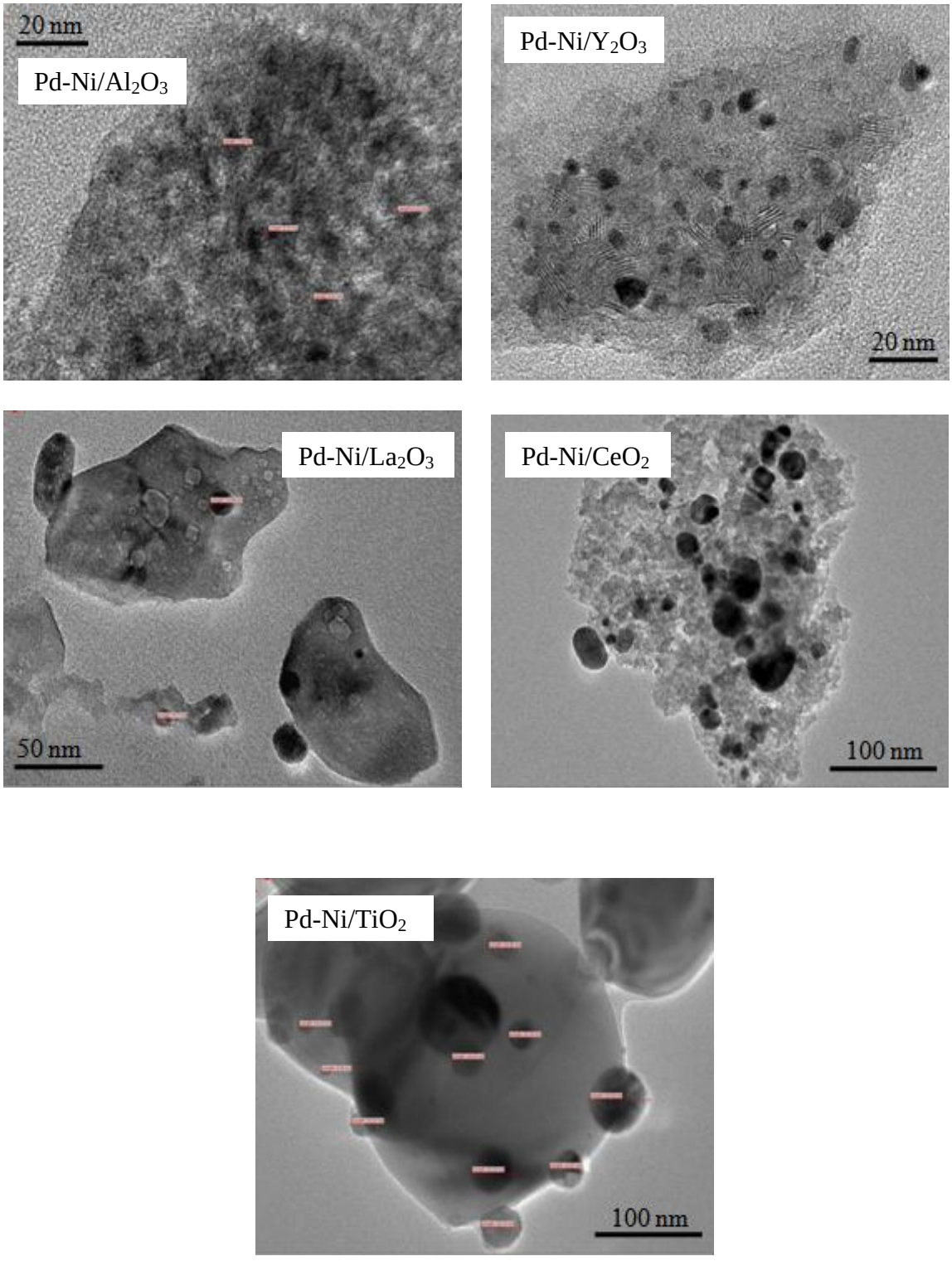

Figure 3-5 TEM images of Pd−Ni catalysts after H_2 reduction.

Table 3-3 Metal particle size of fresh and spent Pd−Ni catalysts

Catalysts	Metal particle size (nm)		
	Fresh catalysts	Spent catalysts (8 h)	Spent catalysts (24 h)
Pd−Ni/Y_2O_3	5.4 ± 1.0	11.8 ± 3.6	11.7 ± 4.9
Pd−Ni/Al_2O_3	5.3 ± 1.5	11.9 ± 2.1	11.0 ± 2.8
Pd−Ni/La_2O_3	9.9 ± 4.1	36.8 ± 16.2	57.0 ± 18.5
Pd−Ni/CeO_2	22.6 ± 11.9	98.1 ± 63[a]	−
Pd−Ni/TiO_2	27.2 ± 7.6	136.3 ± 41.6[a]	−

[a] spent Pd−Ni/TiO_2 and Pd−Ni/CeO_2 after 1 h reaction

3.3.6 Catalytic reaction

Figure 3-6 shows the performance of the Pd−Ni catalysts. It can be seen that the H_2 and CO productions decrease in this order: Pd−Ni/Y_2O_3 > Pd−Ni/Al_2O_3 > Pd−Ni/La_2O_3 > Pd−Ni/CeO_2 > Pd−Ni/TiO_2. The Pd−Ni/Y_2O_3 catalyst shows very stable performance without noticeable deactivation over 24-hour reaction time, while a decreasing trend in both H_2 and CO production is observed on the Pd−Ni/La_2O_3 and Pd−Ni/Al_2O_3 catalysts. In contrast, the Pd−Ni/CeO_2 and Pd−Ni/TiO_2 catalysts show a rapid decrease in both H_2 and CO production. Within an hour of reaction time, the system pressure was observed to be the same as the feed pressure, indicating that no reactants were flowing through the reactor. This blockage is due to the high production of graphitic carbon as shown later by TGA and DTA results.

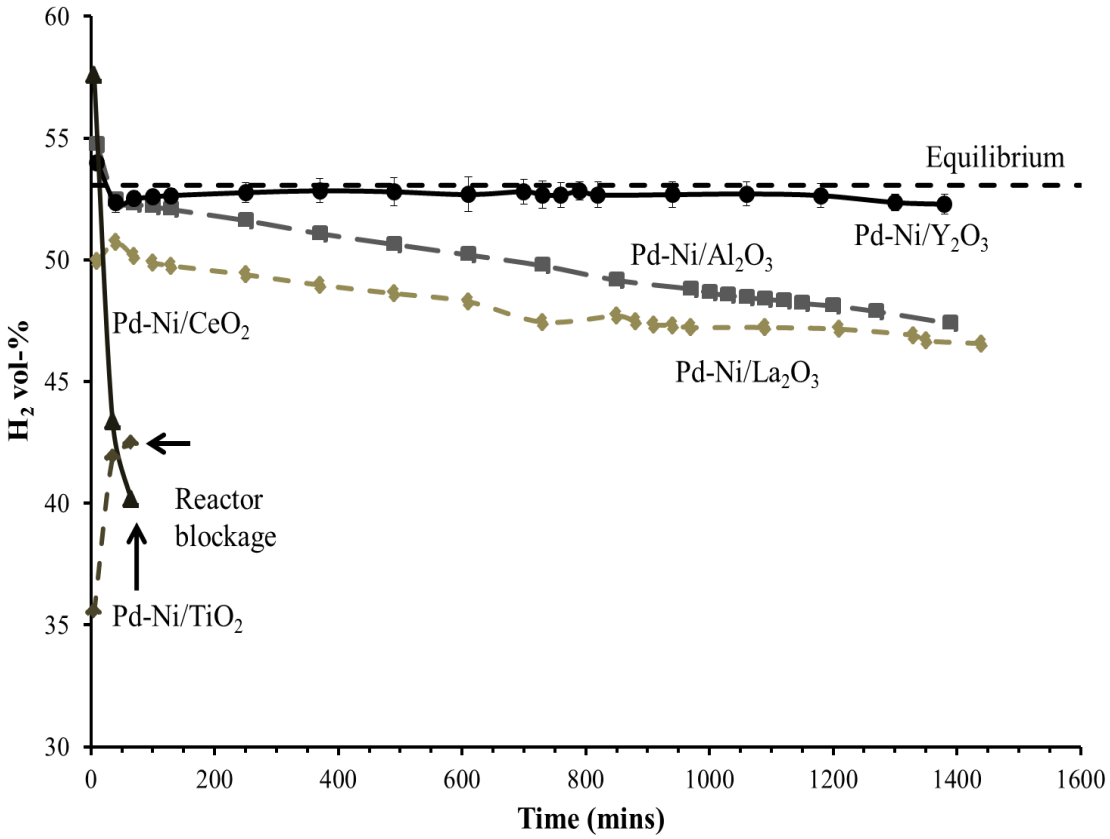
60
55
50
45
40
35
30
0
200
400
600
800
1000
1200
1400
1600
H2 vol-%
Time (mins)
Equilibrium
Pd-Ni/Y2O3
Pd-Ni/Al2O3
Pd-Ni/CeO2
Pd-Ni/La2O3
Reactor
blockage
Pd-Ni/TiO2

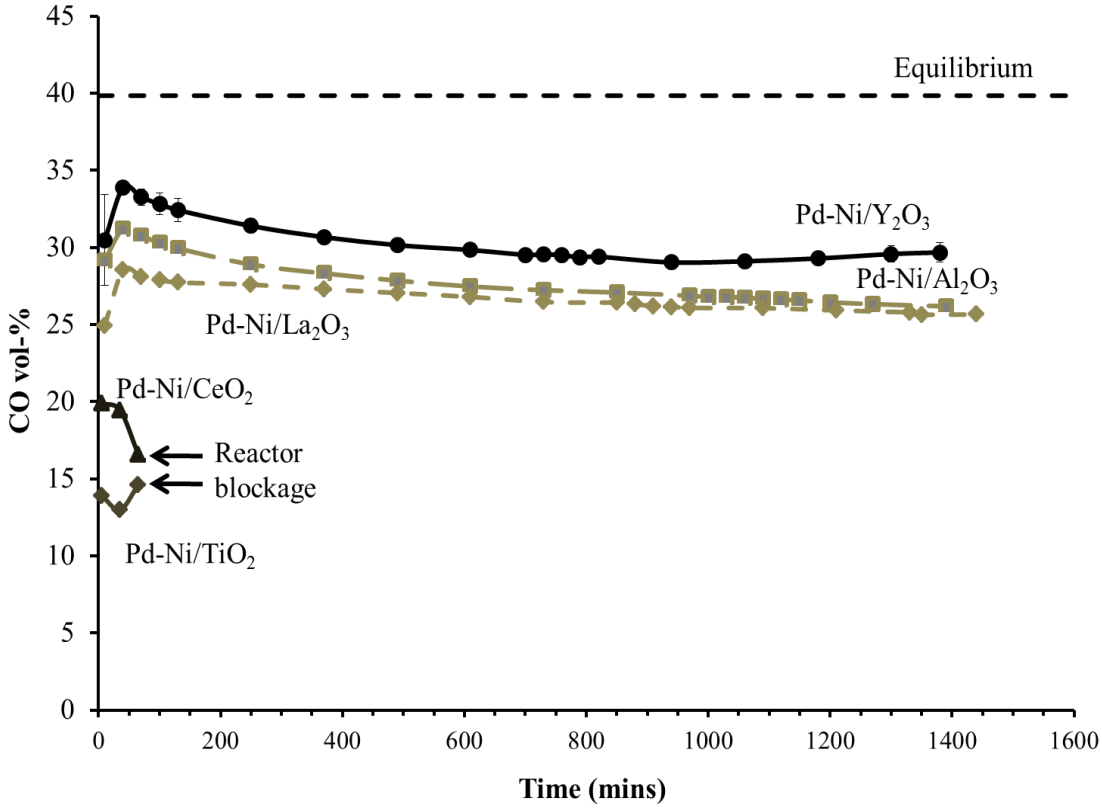

Figure 3-6 H_2 and CO volume−% produced from Pd−Ni catalyts

Reaction condition: P_{total} 1 atm, T = 700°C, $CH_4/CO_2/O_2$ = 2/1/1, GHSV = 12000 $cm^3/g/h$

Equilibrium composition for OCRM reaction is also shown in Figure 3-6. The equilibrium composition is calculated using Peng−Robinson equation of state (EOS) and all possible reactions occurring in OCRM as follows:

CO_2 (dry) Reforming of Methane (DRM): $CH_4 + CO_2 \rightarrow 2\ CO + 2\ H_2$

Partial Oxidation of Methane (POM): $CH_4 + ½\ O_2 \rightarrow CO + 2\ H_2$

Steam Reforming of Methane (SRM): $CH_4 + H_2O \rightarrow CO + 3\ H_2$

Methane Combustion: $CH_4 + 2\ O_2 \rightarrow CO_2 + 2\ H_2O$

Reverse Water Gas Shift (rWGS): $CO_2 + H_2 \rightarrow CO + H_2O$

The Pd−Ni/Y_2O_3 catalyst shows not only stable performance, but also high H_2 production almost near equilibrium. However, the CO production is much lower than the equilibrium. The high H_2 production in OCRM reaction can be understood since POM and SRM produce more H_2 than CO, while only rWGS reaction consumes H_2.

Table 3-4 tabulates the CH_4 and CO_2 conversions along with the product compositions produced from the Pd−Ni catalysts. It can be seen that the Pd−Ni/Y_2O_3 catalyst shows the best catalyst performance in terms of good stability and high conversions of CH_4 and CO_2. The high conversion of Pd−Ni/Y_2O_3 catalyst can be attributed to the small metal particle size due to formation of $Pd_xO_yY_z$ compound, which is difficult to agglomerate, hence leading to the formation of fine Pd particles size on the Pd−Ni/Y_2O_3 catalyst as shown from TEM results (Table 3-3). Similar finding was also reported by Damyanova et al. [186] who concluded that the highest CH_4 and CO_2 conversions in the DRM reaction was due to the formation of small metal particles on the Pd−Ni/MCM−41 catalyst.

Table 3-4 Product distribution produced from Pd−Ni catalysts on various supports

Catalysts	Dry gas composition (after 24 h)				Conversion (%)	
	H_2	CO	CH_4	CO_2	CH_4	CO_2
Pd−Ni/γ−Al_2O_3	47.38	26.19	11.95	14.48	76.10	42.08
Pd−Ni/TiO_2	42.42	14.61	20.39	22.58	59.22	9.69
Pd−Ni/La_2O_3	46.56	25.66	12.47	15.31	75.07	38.75
Pd−Ni/Y_2O_3	52.28	29.68	4.54	13.49	90.92	46.02
Pd−Ni/CeO_2	40.15	16.59	18.96	24.30	62.08	2.78
Equilibrium	53.06	39.85	0.24	6.85	99.23	56.25

Note: Reactor plugged after 1 hour for Pd−Ni/TiO_2 and Pd−Ni/CeO_2 catalysts

The initial performance of the Pd−Ni/Y_2O_3 catalyst is comparable to those of the Pd−Ni/Al_2O_3 catalyst, which can also be attributed to the formation of small metallic particles from the $NiAl_2O_4$ spinel compound as shown from TEM results (Table 3-3). However, the H_2 and CO productions decrease with time on stream, probably due to the deposited carbon. Bhattacharyya and Chang [32] reported that the $NiAl_2O_4$ spinel catalyst was not a good catalyst for the DRM reaction even though it showed excellent initial reforming activity; they explained that during reduction, $NiAl_2O_4$ spinel phase was reduced to the metallic Ni particle and α-alumina and this mixture, possibly consisting of large metallic Ni particle on low surface area α-alumina, was not effective for the DRM reaction.

Although the metal particle of the Pd−Ni/La_2O_3 catalyst is bigger than those of either the Pd−Ni/Y_2O_3 or Pd−Ni/Al_2O_3 catalyst, the Pd−Ni/La_2O_3 catalyst still shows stable and comparable performance with those of Pd−Ni/Al_2O_3 catalyst. The high stability of the Pd−Ni/La_2O_3 catalyst in the DRM reaction was also observed by Steinhaeur et al. [187]. According to Verykios [54] and Múnera et al. [188], the high activity and stability of the NiO/La_2O_3 catalyst in the DRM reaction was due to the formation of $La_2O_2CO_3$ (lanthanum oxycarbonate) species. During the DRM reaction, methane gas dissociates on the metal to form carbon and hydrogen while carbon dioxide is adsorbed on lanthana support to form $La_2O_2CO_3$ species. The oxygen species from $La_2O_2CO_3$ were proposed to interact with surface carbon species from decomposition of methane to form carbon monoxide gas [55].

The Pd−Ni/CeO_2 and Pd−Ni/TiO_2 catalysts are the worst catalysts in the OCRM reaction as the reactor blockage happens within an hour of reaction time. Despite having a redox behavior and high mobility of lattice oxygen [46], CeO_2 was reported to be an unsuitable catalyst support for the DRM reaction due to the high carbon deposition rate [189−191] and strong metal−support interaction (SMSI), similar to Ni/TiO_2 catalyst [192]. During reduction, TiO_x molecules migrated over the metal particles to reduce the surface free energy of system, thus the TiO_x molecules blocked the active metal [192]. Therefore, the amount of the active Ni or Pd species available for reaction was very little.

In the oxidative reforming of methane, the temperature gradient in the catalyst bed was usually very large [193-195]. Therefore, the inlet and outlet temperatures near the catalyst bed are measured and the results are tabulated in Table 3-5. It can be seen that the inlet temperature is higher than the outlet temperature for all catalysts, suggesting that

oxidation reaction always occurs near the inlet of catalyst bed, followed by reforming reaction [196-198]. However, no significant difference of inlet and outlet temperatures among Pd−Ni/Al_2O_3, Pd−Ni/Y_2O_3, and Pd−Ni/La_2O_3 catalysts is observed, probably due to thin layer of catalyst bed.

Table 3-5 Inlet and outlet temperature of Pd−Ni catalyst bed

Catalyst	Inlet (°C)	Outlet (°C)
Pd−Ni/γ−Al_2O_3	722 ± 2	711 ± 2
Pd−Ni/Y_2O_3	720 ± 2	710 ± 2
Pd−Ni/La_2O_3	720 ± 2	710 ± 2

Further study on the effect of reaction temperature is performed on the Pd−Ni/Y_2O_3 catalyst since the Pd−Ni/Y_2O_3 catalyst shows the highest stability and conversions of CH_4 and CO_2 among other catalysts. The results in Figure 3-7 show that the H_2 and CO yields as well as the CH_4 and CO_2 conversions increase with increasing temperature. However, the increase is more dramatic for CO_2 conversion. It is also observed that the increase in both CH_4 and CO_2 conversions from 500°C to 700°C are much higher than those from 700°C to 800°C. This suggests that the optimum temperature for the OCRM reaction is around 700°C.

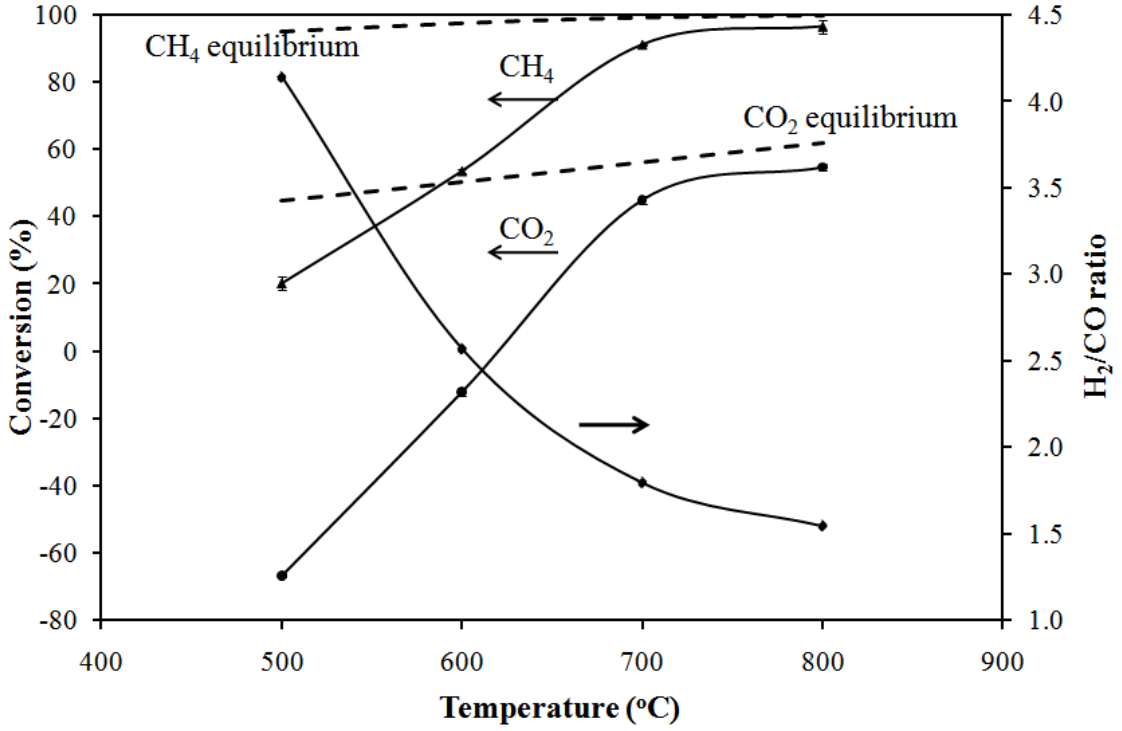

Figure 3-7 Effect of reaction temperature on catalytic performance of Pd−Ni/Y_2O_3 catalyst. Reaction condition: P_{total} 1 atm, T = 700°C, $CH_4/CO_2/O_2$ = 2/1/1, GHSV = 12000 $cm^3/g/h$

In order to understand the effect of reaction temperature, it is necessary to know the following possible reactions occurring in the OCRM reaction depending on reaction temperature and feed compositions [65]:

$CH_4 + CO_2 \rightarrow 2CO + 2H_2$ $\Delta H°_{298} = +61$ kcal/mol (1)

$CH_4 + ½ O_2 \rightarrow CO + 2H_2$ $\Delta H°_{298} = -5$ kcal/mol (2)

$CH_4 + 2O_2 \rightarrow CO_2 + 2H_2O$ $\Delta H°_{298} = -192$ kcal/mol (3)

$CO + H_2O \rightarrow CO_2 + H_2$ $\Delta H°_{298} = -8$ kcal/mol (4)

Reaction (1) represents the DRM reaction while reaction (2) represents the POM reaction. These two reactions are the main reactions in the OCRM reaction system. In

addition, reactions (3) and (4) are also possible occurring concurrently. Reaction (3) represents methane combustion reaction which is possible under excess oxygen, while reaction (4) represents reverse water gas shift (rWGS) reaction.

The CO_2 conversion is shown to be negative at temperature 600°C and below, showing that CO_2 is produced instead of consumed at these temperatures. From the above possible reactions, it can be seen that only methane combustion can produce CO_2. This can be explained from thermodynamics point of view since methane combustion is an exothermic reaction which favors at lower temperature conditions. The positive CO_2 conversion and lower H_2/CO (1.99) is observed at 700°C, suggesting that the dominancy of the POM reaction since the theoretical H_2/CO ratio for the POM reaction is 2.0. However, the H_2/CO ratio (1.91) at 800°C is even lower than those at 700°C, indicating participation of the DRM and/or rWGS reactions.

3.3.7 Role of oxygen on catalyst performance

The Pd−Ni/Y_2O_3, Pd−Ni/Al_2O_3, and Pd−Ni/La_2O_3 catalysts have been shown earlier to have comparable performance. However, TPD−O_2 results on fresh catalysts (Figure 3−8) show different oxygen desorption profiles. It can be seen that only one small peak is observed on the Pd−Ni/Al_2O_3 catalyst at around 700°C, which corresponds to the lattice oxygen − commonly named as β−oxygen − from catalyst support [199]. This β−oxygen peak is also observed on the Pd−Ni/La_2O_3 catalyst but at a lower temperature than 700°C, around 630-680°C. In addition, there is another peak observed on the Pd−Ni/La_2O_3 catalyst at around 400°C, corresponding to the surface chemisorbed oxygen (α−oxygen) on the catalyst support [200]. Similar TPD−O_2 profile is also observed on the

Pd−Ni/Y_2O_3 catalyst. However, the intensity of α−oxygen species is much higher than those of β−oxygen species, showing that the α−oxygen species is more easily adsorbed and desorbed on this catalyst. It has been reported that the α−oxygen species is more active than β−oxygen species at 300°C [201]. However, since OCRM reaction was performed at 700°C, the β−oxygen species may play an important role in OCRM reaction.

The amount of O_2 desorption from each catalyst was calculated and the result shows that Pd-Ni/Y_2O_3 and Pd-Ni/Al_2O_3 catalysts have the highest and lowest amount of O_2 desorption, respectively. However, it is more important to elucidate whether α- or β-oxygen plays an important role in the OCRM reaction.

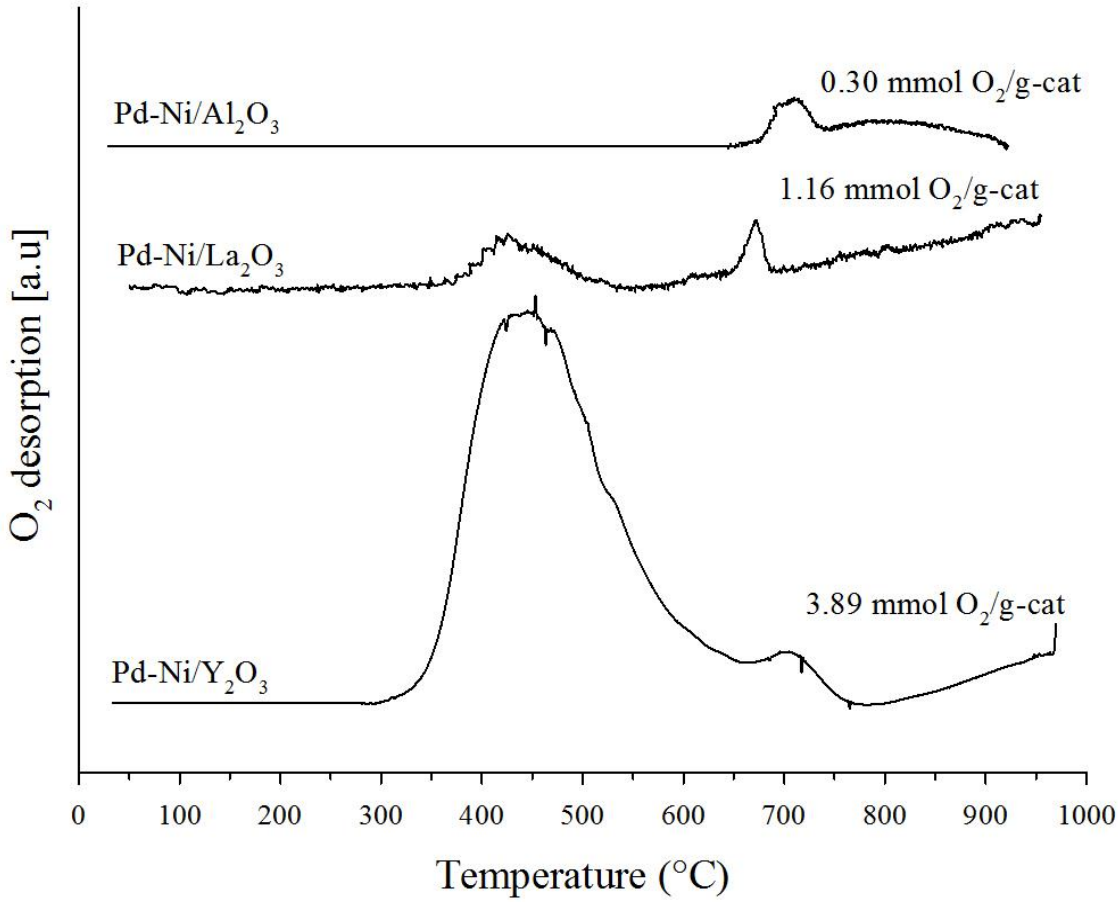

Figure 3-8 TPD−O_2 profiles of Pd−Ni catalysts

Further experiments were performed using methane decomposition reaction to understand the role of α− and β−oxygen species on Pd−Ni/Y_2O_3 catalyst. Methane decomposition reaction over the Pd−Ni/Y_2O_3 catalyst was performed at 450°C where the desorption of majority of α−oxygen species was observed. The result shows that there was no conversion of CH_4 at 450°C, suggesting that the α−oxygen species is not active for CH_4 decomposition.

With increasing temperature to 700°C, the CO production is observed on Pd−Ni/Y_2O_3 catalyst (Figure 3-9a) and Pd−Ni/Al_2O_3 catalyst (Figure 3-9b). Since Pd−Ni/Al_2O_3 catalyst only has β−oxygen species, these results show that the β−oxygen on the Pd−Ni/Al_2O_3 and Pd−Ni/Y_2O_3 catalyst may promote cracking of C−H bond in CH_4 to H_2 and CO. After 2 h reaction time, the CH_4 gas was stopped and CO_2 was introduced to the reactor. It can be seen that the amount of CO gas decreases with time on stream for Pd−Ni/Al_2O_3 catalyst, while it increases for Pd−Ni/Y_2O_3 catalyst. The increase of CO amount during the introduction of CO_2 gas over Pd−Ni/Y_2O_3 catalyst could be due to the fact that Y_2O_3 can form $Y_2O_2CO_3$ (yttrium oxycarbonate) species [202], similar to the $La_2O_2CO_3$ (lanthanum oxycarbonate) species. The oxycarbonate species can interact with surface carbon species from CH_4 decomposition to form CO gas [55]. However, the formation of oxycarbonate species on Al_2O_3 is not possible since Al_2O_3 is an acidic metal oxide, while formation of oxycarbonate requires basic rare earth metals such as Y, La, Nd, and Gd [202].

The similar CH_4 decomposition reaction followed by CO_2 dissociation reaction was also performed on pure Y_2O_3. The results (Figure 3-9c) show that a small amount of H_2 and CO is observed during methane decomposition reaction, confirming that the

β−oxygen species can promote the cracking of C−H bond in CH_4 to H_2 and CO. The H_2 and CO productions also decrease since the amount of β−oxygen species is depleted with time on stream. When CH_4 was replaced by CO_2, CO was not detected since there was no deposited carbon on the spent Y_2O_3.

In order to see the effect of oxygen in the feed in OCRM reaction, methane decomposition was performed on pure Y_2O_3, followed by introduction of oxygen for 15 minutes and the cycle is repeated twice. The results in Figure 3-9d show that the H_2 and CO productions increase after introduction of oxygen, showing that gas phase oxygen can replace the depleted β−oxygen. However, the increase in H_2 and CO productions is not high enough. The similar result is also obtained from the second cycle.

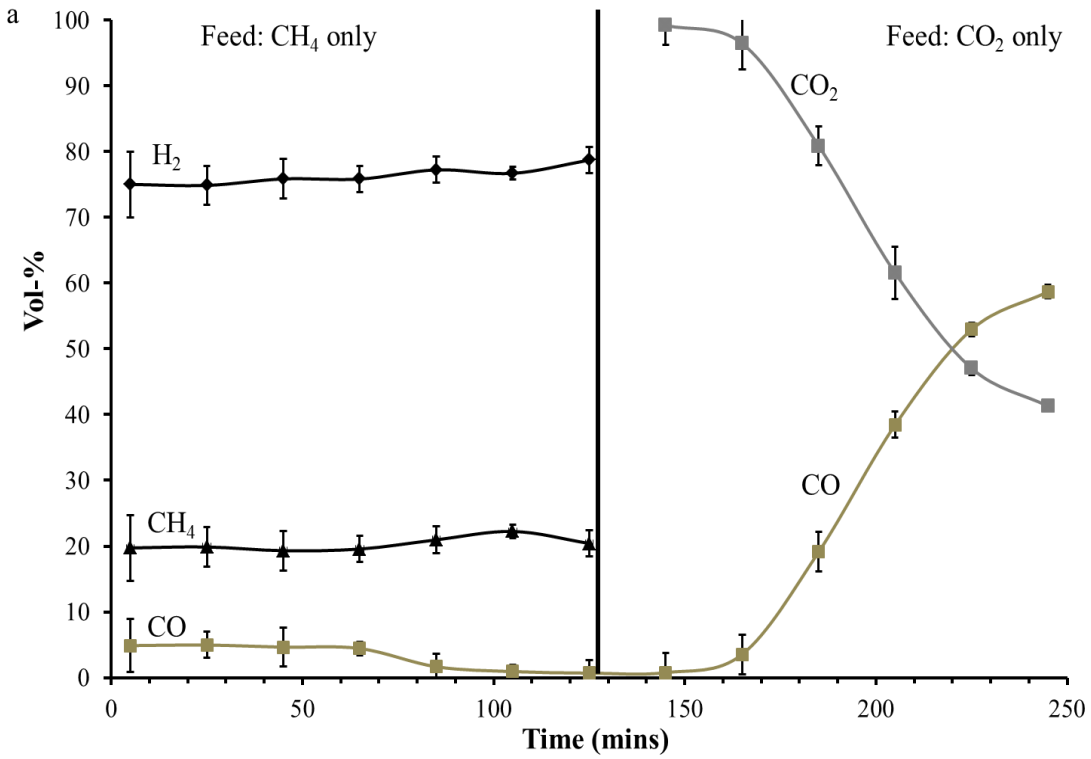

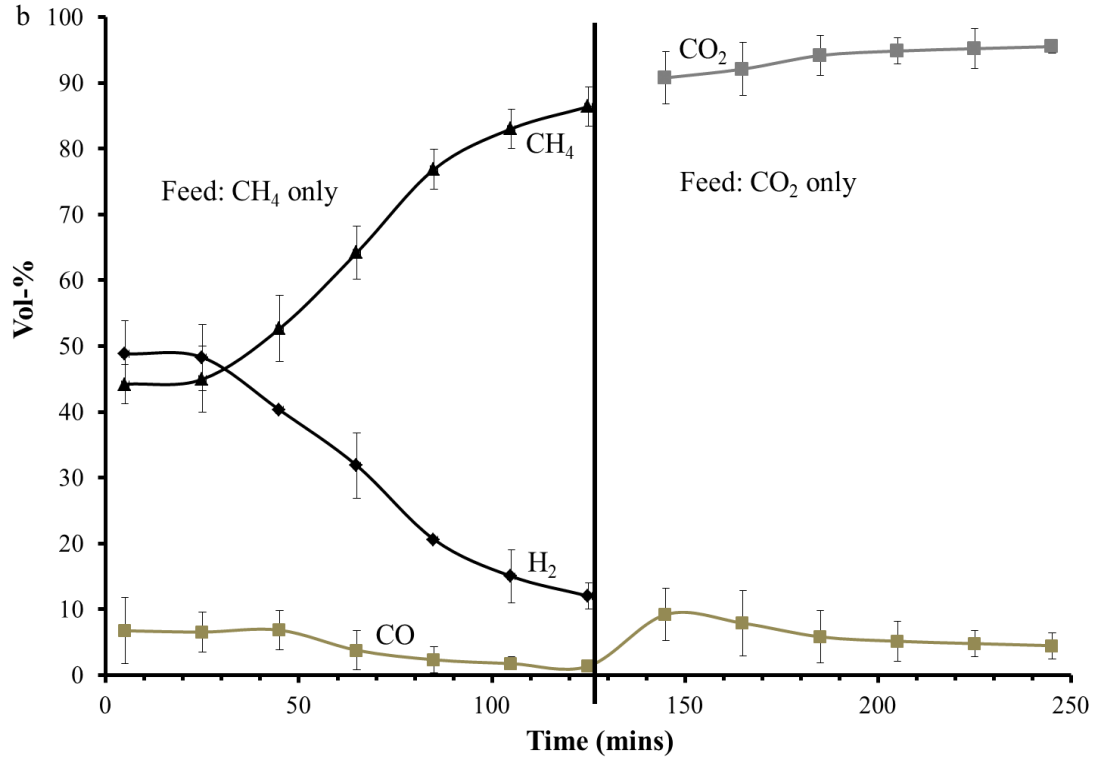
b
Vol-%
Time (mins)
Feed: CH4 only
Feed: CO2 only
CH4
CO2
H2
CO

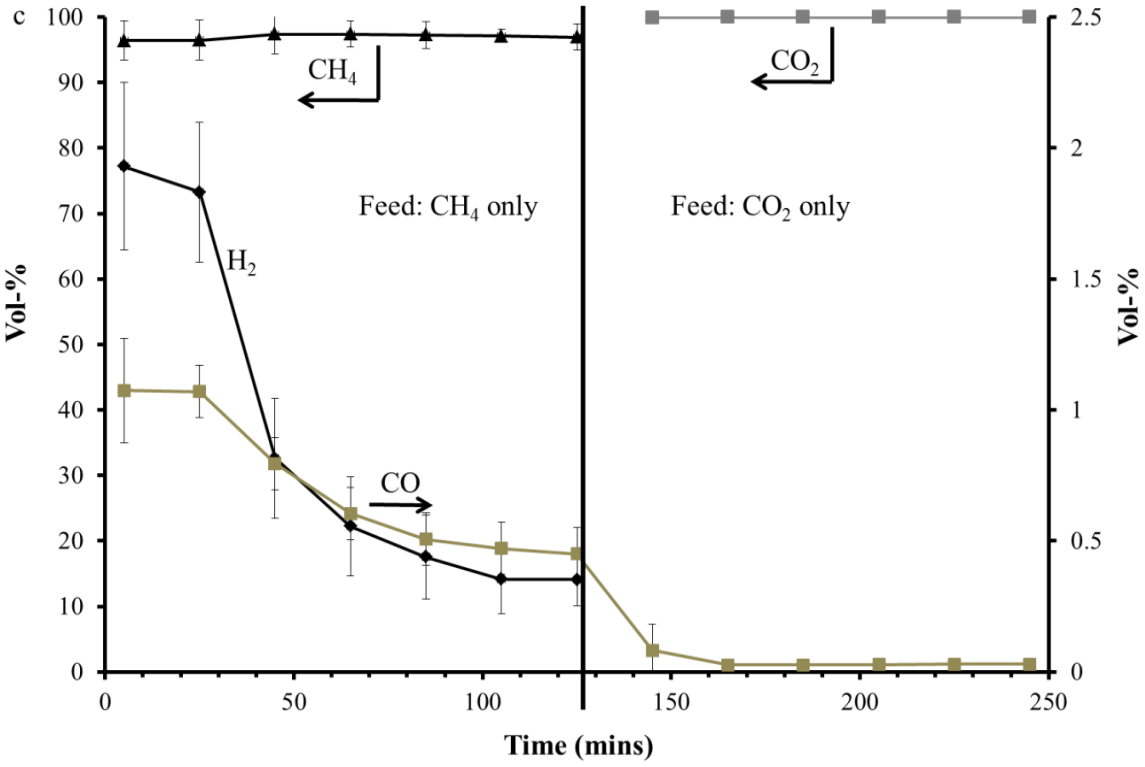
c
Vol-%
Vol-%
Time (mins)
Feed: CH4 only
Feed: CO2 only
CH4
CO2
H2
CO

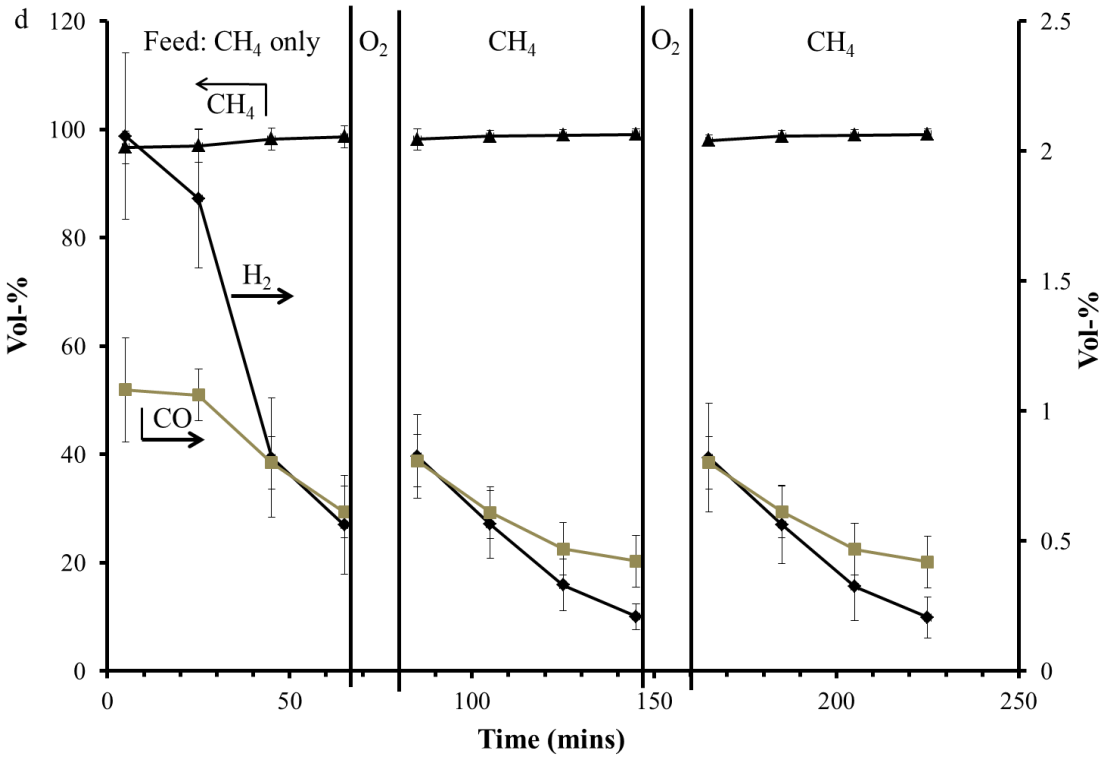

Figure 3-9 Catalytic reactions of CH_4 decomposition followed by CO_2 dissociation on a) Pd−Ni/Y_2O_3 catalyst, b) Pd−Ni/Al_2O_3 catalyst, c) pure Y_2O_3, and d) CH_4 decomposition followed by oxygen on pure Y_2O_3.

Reaction condition: P_{total} 1 atm, T = 700°C, CH_4/He, CO_2/He or O_2/He = 1/1, GHSV = 12000 $cm^3/g/h$

3.3.8 Characterization of spent catalysts

Since metal sintering is one of the factors causing catalyst deactivation, TEM was performed on the spent catalysts to measure the metal particle size after reaction and the results are tabulated in Table 3-3. It can be seen that the metal particle size of all spent catalysts after 8 h reaction time increases significantly compared to those of the fresh catalysts. However, further observation on the spent catalysts after 24 h reaction time

reveals that the metal particle size of Pd−Ni/La_2O_3 catalyst still increases while the metal particle size of Pd−Ni/Al_2O_3 and Pd−Ni/Y_2O_3 catalysts are the same with those of spent catalysts after 8 h reaction time, indicating that the presence of metal−support compound (MSC) on the Pd−Ni/Al_2O_3 and Pd−Ni/Y_2O_3 catalysts can prevent metal sintering.

Figure 3-10 shows the TGA results of spent Pd−Ni catalysts. The carbon formation rate decreases in the following order: Pd−Ni/CeO_2 > Pd−Ni/TiO_2 > Pd−Ni/La_2O_3 > Pd−Ni/Al_2O_3 > Pd−Ni/Y_2O_3. Interestingly, this order is reversed compared with the catalytic performance. Therefore, it is very clear to point out that high carbon formation is the main cause of reactor blockage on the Pd−Ni/CeO_2 and Pd−Ni/TiO_2 catalysts.

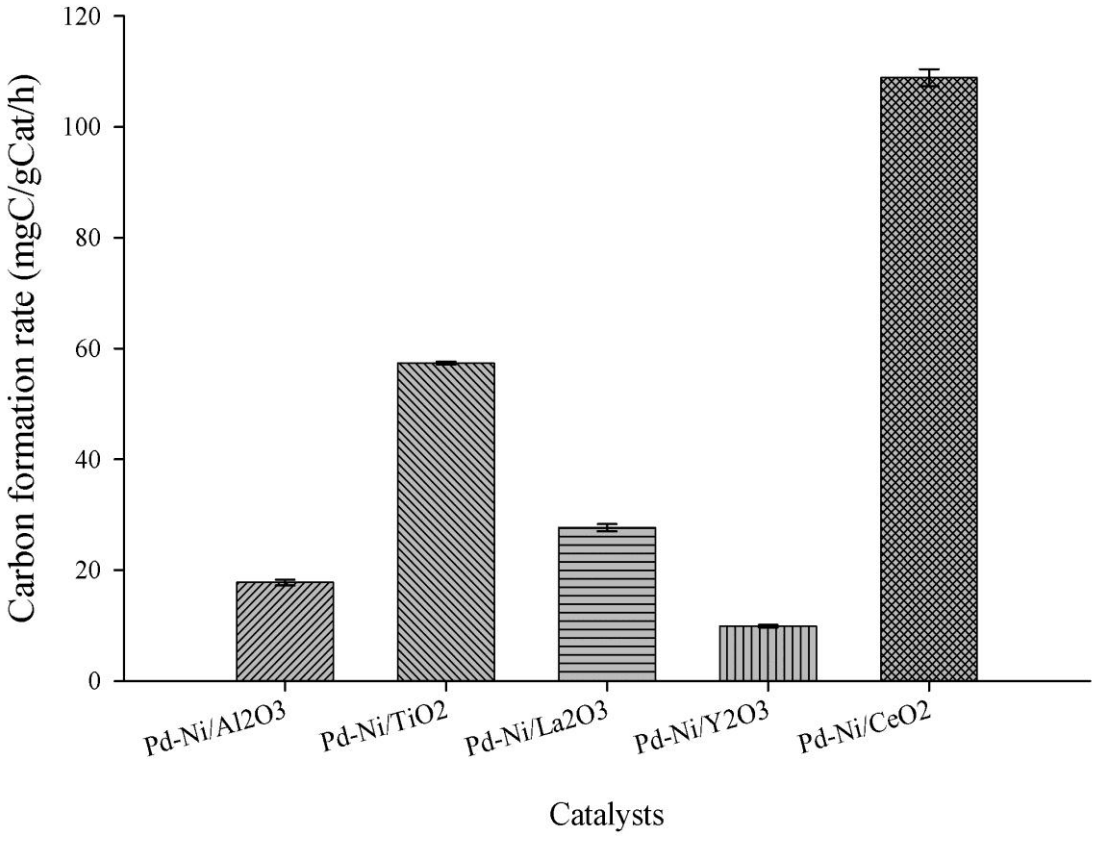

Figure 3-10 Amount of deposited carbon on spent Pd−Ni catalysts

Different types of deposited carbon can be revealed from the DTA profiles of spent Pd−Ni catalyst (Figure 3-11). The spent Pd−Ni/Y_2O_3 catalyst has small peak around 550°C, corresponding to the amorphous carbon (usually at below 600°C) [203], which is much easier to be oxidized compared to the graphitic carbon. However, the spent Pd−Ni/La_2O_3 catalyst shows not only the peak at around 575°C, but also another peak at around 630°C, corresponding to the graphitic carbon, such as filamentous while the other spent catalysts (Pd−Ni/Al_2O_3, Pd−Ni/CeO_2, and Pd−Ni/TiO_2) show only one peak at more than 600°C, indicating all these catalysts produces the graphitic carbon.

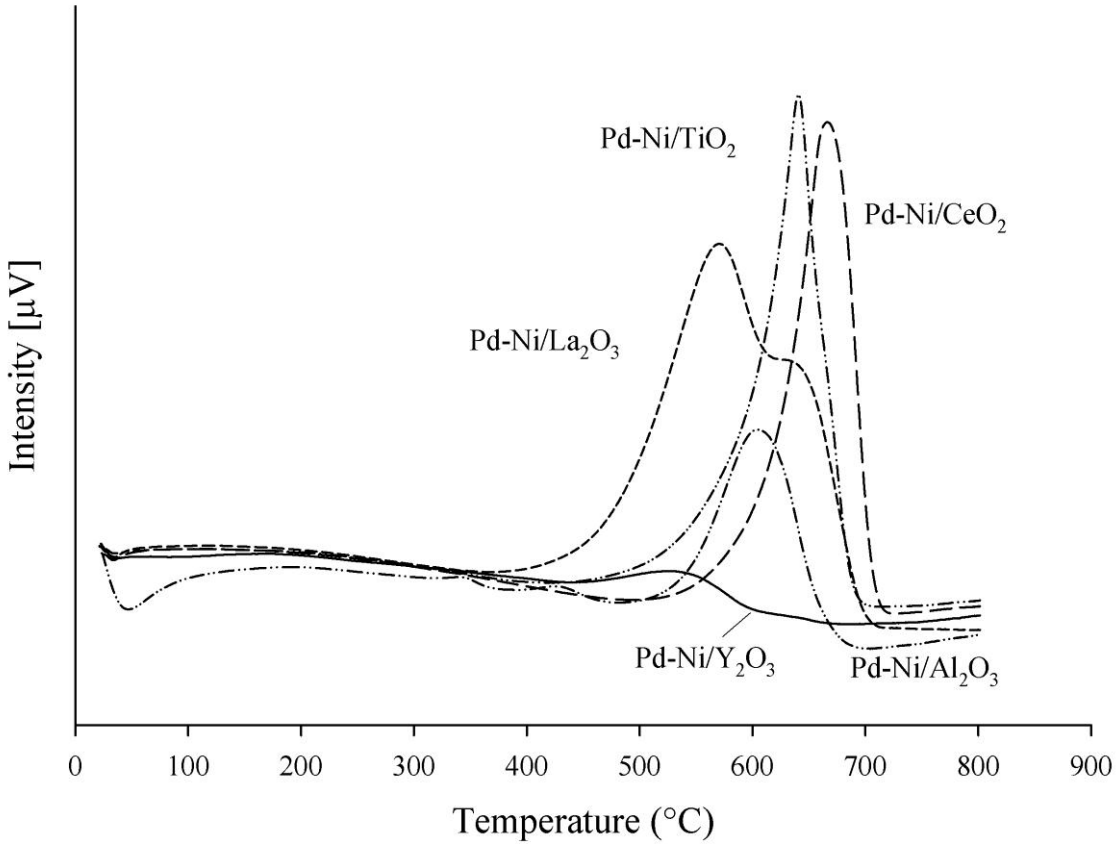

Figure 3-11 DTA profiles of spent Pd−Ni catalysts (Pd−Ni/TiO_2 and Pd−Ni/CeO_2 1 h)

FESEM images of the spent Pd−Ni catalysts (Figure 3-12) shows that filamentous carbons are observed on the Pd−Ni/Al_2O_3, Pd−Ni/La_2O_3, and Pd−Ni/CeO_2 catalysts. However, the filamentous carbons are hardly observed on the Pd−Ni/Y_2O_3 catalyst due to the presence of the amorphous carbon which has irregular shape. Even though the filamentous carbons are also hardly observed on the Pd−Ni/TiO_2 catalyst, the above DTA result shows the presence of the graphitic carbon, indicating that the filamentous carbons on the Pd−Ni/TiO_2 catalyst are not able to grow.

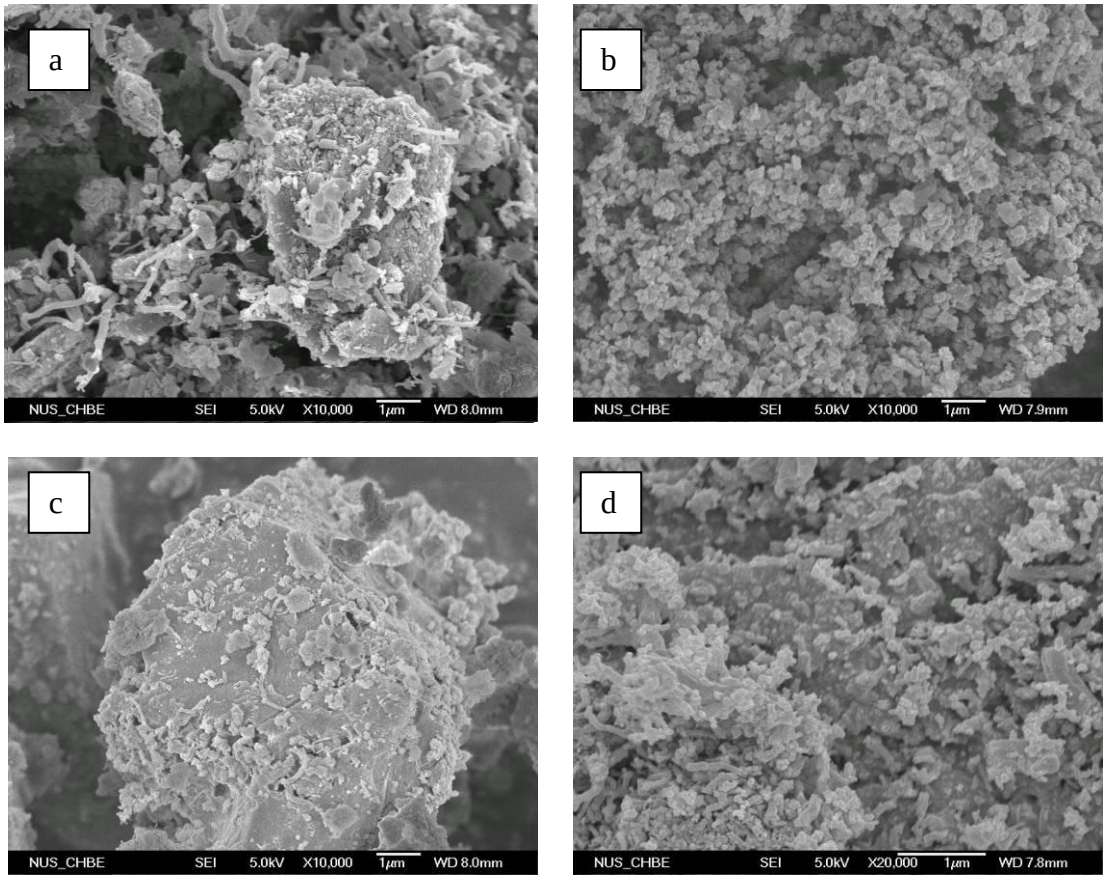

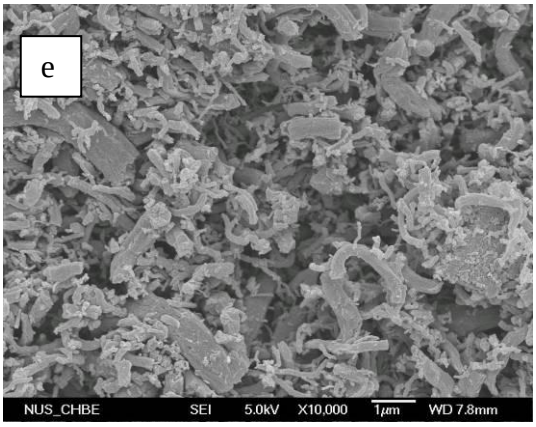

Figure 3-12 FESEM images of spent a) Pd−Ni/Al_2O_3; b) Pd−Ni/TiO_2; c) Pd−Ni/Y_2O_3; d) Pd−Ni/La_2O_3; and e) Pd−Ni/CeO_2

3.3.9 Proposed reaction mechanism for Pd−Ni/Y_2O_3 catalyst

As the Pd−Ni/Y_2O_3 catalyst shows the highest stability and conversions of CH_4 and CO_2 among other catalysts, the reaction mechanism of the OCRM reaction is therefore proposed for the Pd−Ni/Y_2O_3 catalyst as shown in Figure 3-13. The formation of Pd−Ni alloy is proposed since the metal particle size of Pd−Ni/Y_2O_3 catalyst (4-6nm) is much smaller than either Ni/Y_2O_3 catalyst (15-20nm) or Pd/Y_2O_3 catalyst (8-10nm). Otsuka et al. [204-206] and Tomishige et al. [207-213] also reported the formation of Pd−Ni alloy observed from EXAFS. However, there are two possibilities of the location of metallic sites on Pd−Ni alloy, i.e. Ni is located atop Pd or Pd is located atop Ni. Since the TPR result of the Pd−Ni/Y_2O_3 catalyst shows the formation of MSC between Pd and Y_2O_3 support, the Ni atop Pd structure is more likely to happen than the Pd atop Ni structure on the catalyst surface.

During the OCRM reaction, the following reactions are proposed:

$$2\ CH_4 + 2\ \beta{-}O \rightarrow 2\ CO + 4\ H_2 \qquad (5)$$

$$O_2 \rightarrow 2\ \beta{-}O \quad (6)$$

$$CH_4 \rightarrow CH_x \rightarrow C + 2\ H_2 \quad (7)$$

$$CO_2 + Y_2O_3 \rightarrow Y_2O_2CO_3 \quad (8)$$

$$Y_2O_2CO_3 + C \rightarrow Y_2O_3 + 2CO \quad (9)$$

The β−oxygen species on the Y_2O_3 support can promote the cracking of C−H bond in CH_4 to form H_2 and CO (reaction 5). The depleted β−oxygen species will be replenished by the oxygen in the feed (reaction 6). In addition, methane will form CH_x intermediates and decompose to produce hydrogen and surface carbon on metallic sites of the Pd−Ni/Y_2O_3 catalyst (reaction 7), while CO_2 is adsorbed on Y_2O_3 to form $Y_2O_2CO_3$ (reaction 8). The oxycarbonate species would react with surface carbon to form CO (reaction 9). Since the catalytic performance of the Pd−Ni/Y_2O_3 catalyst is very stable, the carbon deposition rate from the methane decomposition reaction is probably the same as the carbon removal rate from oxycarbonate species, leading to the rejuvenation of the catalyst during the OCRM reaction.

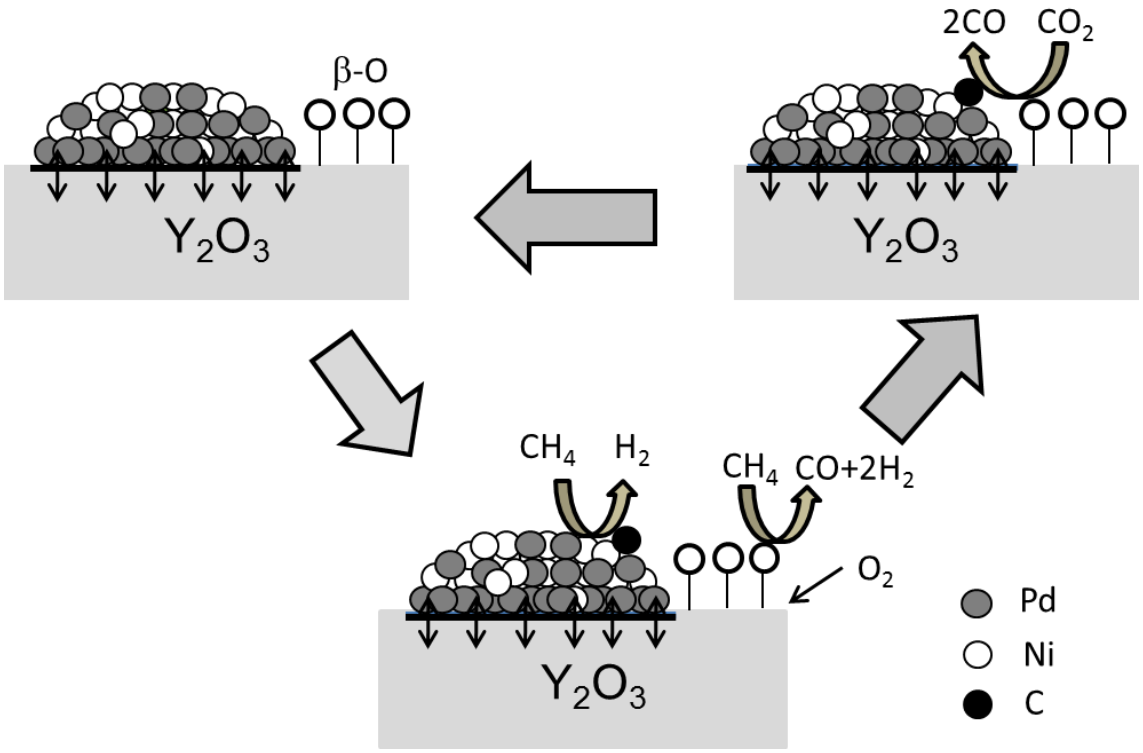

Figure 3-13 Proposed reaction mechanism of OCRM reaction on Pd−Ni/Y_2O_3 catalyst

3.4 Conclusions

Pd−Ni/Y_2O_3 catalyst shows the highest CH_4 and CO_2 conversions and high stability in the OCRM reaction compared to other Pd−Ni catalysts. The high activity and stability of the Pd−Ni/Y_2O_3 catalyst can be attributed to the formation of metal−support compound ($Pd_xO_yY_z$ compound) on the catalyst, the presence of β−oxygen species and the ability of Y_2O_3 to form oxycarbonate species. The β−oxygen species on Y_2O_3 support can promote the cracking of C−H bond in the CH_4 and the oxycarbonate species can oxidize the surface carbon on the metal.

Pd−Ni/Al_2O_3 catalyst also shows comparable initial performance with those of Pd−Ni/Y_2O_3 catalyst due to the formation of $NiAl_2O_4$ compound and the presence of

β−oxygen, but the performance of Pd−Ni/Al_2O_3 catalyst decreases with time on stream due to higher amount of deposited carbon on the spent catalyst

CHAPTER 4

Roles of Pd precursors on catalytic performance of Pd−Ni/Y_2O_3 catalyst

This chapter describes the effect of Pd precursors on catalyst activity and stability of Pd-Ni/Y_2O_3 catalyst for oxy-CO_2 reforming of methane. A series of Pd−Ni/Y_2O_3 catalysts with different Pd precursors ($PdCl_2$ and $Pd(NO_3)_2$) was prepared using wet−impregnation method over Y_2O_3 support. The catalytic activities in terms of CH_4 and CO_2 conversions of the Pd(C)−Ni/Y_2O_3 catalyst (Pd−Ni/Y_2O_3 catalyst prepared from $PdCl_2$) are higher than those produced from Pd(N)−Ni/Y_2O_3 catalyst (Pd−Ni/Y_2O_3 catalyst prepared from $Pd(NO_3)_2$) due to smaller metal particle size resulted from the formation of Pd−Y_2O_3 compound on the Pd(C)−Ni/Y_2O_3 catalyst. The effect of metal particle size on catalytic activities is clearly shown in Pd(C)−Ni/Y_2O_3 catalyst with various Pd/Ni ratios. Besides small metal particle size, the presence of bimetallic particles, as indicated from XPS results, also plays an important role in catalytic activity. The presence of chloride in the Pd(C)-Ni/Y_2O_3 catalyst helps to form Pd-Y_2O_3 compound, which is found to play an important role in high catalyst stability of the Pd(C)-Ni/Y_2O_3 catalyst.

4.1 Introduction

In recent years, the rapid increase of CO_2, which is the largest amount of greenhouse effect gas causing global warming, has been attracting a great interest from academic and industrial researchers. Enormous efforts are currently being undertaken to utilize CO_2. One of the potential ways to utilize CO_2 is via catalytic CO_2 (dry) reforming with methane (DRM). This reaction is attractive for industry as it yields low H_2/CO ratio,

which is preferable for hydroformylation and carbonylation reactions [12]. In addition, methane is also reported as the second largest greenhouse effect gas after CO_2 [11].

A variety of catalysts for DRM reaction, such as Rh, Ru, Pt, Pd, Ir [214-215], Ni [216−221], and Co [222] catalysts, has been extensively investigated. The catalysts made from noble metals, such as Rh, Ru, Pt, Pd, and Ir have comparable activity than the nickel catalysts, but they have lower carbon deposition rate than the nickel catalyst. Generally, the carbon deposition rate decreases in the order as follows: Ni >> Rh > Ir = Ru > Pt = Pd at 773 K and Ni > Pd = Rh > Ir > Pt >> Ru at 923 K [14].

Even though high carbon deposition rate causing deactivation on the Ni catalyst is commonly observed, the Ni catalyst appears to be the most suitable catalyst as the noble metal catalyst is expensive. However, the Ni catalyst has to be modified to improve the performance and coke resistance. Numerous studies on catalyst modification show that choosing the suitable catalyst support [15-17] and/or adding other metal as a promoter [17-18, 223] can improve the performance and coke resistance of the nickel catalyst. For an example, Zhang and Verykios [15] studied the effect of catalyst supports and reported that the Ni/La_2O_3 catalyst showed higher activity and stability than the Ni/Al_2O_3 and Ni/CaO catalysts. In addition, many promoters also showed improvement of Ni catalyst. Horiuchi et al. [17] found that addition of basic metal oxides (Na_2O, K_2O, MgO, and CaO) to the Ni catalyst enhanced CO_2 adsorption, resulting in more adsorbed oxygen atoms (O_{ad}). The higher amount of adsorbed oxygen atoms (O_{ad}) prevented adsorbed hydrogen−deficient hydrocarbon species ($CH_{x,ad}$) to decompose to surface carbon since the adsorbed oxygen species could easily react with the adsorbed hydrogen−deficient hydrocarbon species ($CH_{x,ad}$) to form CO.

Even though the catalyst modification can reduce the carbon deposition rate, the energy requirement for the DRM reaction is very huge due to its high endothermicity. The high energy requirement is the drawback to prevent commercialization of the DRM reaction in industries. One way to overcome this drawback is to introduce exothermic reaction such as partial oxidation of methane (POM), resulting in a reaction called oxy−CO_2 reforming of methane (OCRM). The OCRM reaction can reduce not only the amount of carbon deposition since the oxygen can easily oxidize the deposited carbon on the catalyst, but also the total energy requirement since the OCRM reaction combines both the exothermic (POM) and endothermic (DRM) reactions. The energy required from the DRM and released from the POM reactions are shown as follows:

DRM: $CH_4 + CO_2 \rightarrow 2\ H_2 + 2\ CO \quad \Delta H°_{298} = 247.3$ kJ/mol

POM: $CH_4 + ½O_2 \rightarrow 2\ H_2 + \quad CO \quad \Delta H°_{298} = -35.6$ kJ/mol

The previous chapter showed that Pd−Ni/Y_2O_3 catalyst had the highest activity and stability in the OCRM reaction compared to other Pd−Ni catalysts on different supports due to the formation of metal−support compound resulting in small metal particle size, the presence of surface β−oxygen species promoting the cracking of C−H bond in CH_4 and the ability of Y_2O_3 to form oxycarbonate species to oxidize the surface carbon on the Pd−Ni/Y_2O_3 catalyst. All those Pd−Ni catalysts were synthesized using $PdCl_2$ as the Pd precursor.

It has been reported in the literature that the use of chlorine-containing-metal precursor hindered the reduction of the Rh^{3+} to metallic Rh on the Rh/CeO_2 catalyst, but the effect of metal precursors on catalyst performance was still unclear [224]. The similar results in the literature were observed for Pd−Ni catalyst in various reactions. For example,

Tomishige et al. [225] showed that the Pd−Ni/Al_2O_3 catalyst synthesized from $Pd(Ac)_2$ precursor had higher bed temperature than the one from $PdCl_2$ precursor in oxidative steam reforming of methane reaction, even though the CH_4 conversion was similar. In addition, Dias and Assaf [172] also showed similar catalytic performance between Pd−Ni/Al_2O_3 catalysts synthesized from $PdCl_2$ and $Pd(NO_3)_2$ precursors in autothermal reforming of methane reaction. However, they observed formation of compound between Pd, Cl and the support, with the general formula $Pd_xO_yCl_z$ on the Pd−Ni/Al_2O_3 catalyst synthesized from $PdCl_2$ precursor. The presence of this compound prevented the occurrence of reaction without H_2 reduction prior to the reaction. Moreover, they also observed that the difference in catalytic activity of the Pd−Ni/Al_2O_3 catalyst was mainly due to the difference in the metal surface area.

Since the characterization results of Pd−Ni catalysts synthesized from various Pd precursors showed significant different profiles but the catalytic performance of those catalysts are similar, the conclusion is still unclear. Therefore, in this study, the effect of Pd precursors on catalyst performance of the Pd−Ni/Y_2O_3 catalyst is investigated in the OCRM reaction. The interaction between Pd, Ni, and support is also studied to facilitate better understanding of the catalyst activity and stability in the OCRM reaction.

4.2 Experimental

4.2.1 Catalyst synthesis

A series of Pd−Ni catalysts with different ratios and nominal total loading of 5 wt% was synthesized by wet−impregnation method over Y_2O_3. The Pd precursor was either $PdCl_2$ or $Pd(NO3)_2$, which was purchased from either Strem chemicals or Sigma−Aldrich, respectively, while the Ni precursor was obtained from Strem Chemicals in the form of $Ni(NO_3)_2.6H_2O$. Y_2O_3 purchased from Strem Chemicals was chosen as the catalyst support. The Pd solution was prepared by either dissolving $PdCl_2$ in 2M HCl solution or $Pd(NO_3)_2$ in deionized water. The catalysts were impregnated at room temperature and dried in oven at 100^{o}C for 12 h. They were then calcined under air at 800^{o}C for 4 h. The catalysts synthesized from $PdCl_2$ are named as Pd(C) and those from $Pd(NO_3)_2$ as Pd(N). The synthesized Pd−Ni catalysts are named as *x*Pd*y*Ni, with the Pd/Ni ratio as *x*/*y*. For example, 1Pd(C)−1Ni stands for the Pd−Ni catalyst prepared from $PdCl_2$ with Pd/Ni ratio of 1/1.

4.2.2 Characterization methods

4.2.2.1 Specific surface area measurement

The specific surface area of each catalyst was measured by adsorption and desorption of N_2 at −196°C on the Autosorb-1. Prior to the surface area measurement, the catalyst was outgassed at 250°C for a minimum of 12 h. The specific surface areas of catalyst were determined from the linear portion of BET plot.

4.2.2.2 TPR measurement

Temperature-programmed reduction (TPR) measurement for the fresh catalyst was performed on Quantachrome Chembet-3000. Prior to the TPR measurement, 0.05 g of catalyst was outgassed in He for 1 h at 350^{o}C to remove any impurities and then cooled down to room temperature. 5%H_2/N_2 gas was then introduced to the catalyst while the temperature of the furnace was increased at a heating rate of 10K/min to 900^{o}C. The reduction degree was calculated with the assumption of hydrogen/metal ratio of 1.

4.2.2.3 X-ray diffraction

The X-ray diffraction pattern of each catalyst was measured on a Shimadzu XRD−6000 diffractometer using Cu Kα radiation. The catalyst was placed on an aluminum slide and scanned from 2θ of 10^{o} to 80^{o} with ramp rate of 2^{o}/min. The beam voltage and current used were 40 kV and 30 mA, respectively.

4.2.2.4 FESEM

The morphology of each catalyst before and after catalytic test was visually observed using a field emission scanning electron microscope (FESEM: JEOL JSM-6700F). Prior to the analysis, the sample was coated using Pt-sputtering for 60 seconds at 20 mA.

4.2.2.5 X-ray photoelectron spectroscopy

The X-ray photoelectron spectroscopy was performed on Kratos AXIS Ultra DLD using concentric hemispherical analyzer. The Al Kα gun with photon energy of 1486.6 eV was used as the X-ray source. The wide scans were performed using 80eV pass energy

while the narrow scans were performed with 40 eV pass energy. Prior to the analysis, the sample was reduced under pure H_2 at 600°C for 1 h, which was same as the reduction condition during reaction. The sample was mounted on the standard sample stub using double-sided adhesive tapes. The core level signals were obtained at a photoelectron takeoff angle (R, measured with respect to the sample surface) of 90°. The X−ray source was run at a reduced power of 150 W (15 kV and 10 mA). The pressure in the analysis chamber was maintained at 10^{-8} Torr or lower during each measurement. All binding energies were referenced to C 1s hydrocarbon peak at 284.5eV.

4.2.2.6 In-situ DRIFT

The infrared spectra were recorded on a Perkin-Elmer Spectrum 2000 Fourier Transform Infrared Spectrometer using the Harrick Praying Mantis DRP-4 DRIFT cell equipped with ZnSe windows. All spectra were collected with resolution of 4 cm^{-1} and scanned 32 times. 100 mg of catalyst was used in each analysis without mixing with KBr powder. Prior to the analysis, the sample was reduced in-situ in H_2 gas at 600°C for 1 h. The spectra of the clean surface after reduction were recorded separately and used as a reference. The diluted CO gas in He gas was then introduced to the cell at room temperature. After 10 minutes exposure of CO followed by evacuation, the spectra were recorded. The spectra were used after subtraction from the corresponding reference spectra.

4.2.2.7 UV-DRS

The presence of chloride on fresh and reduced catalysts was examined using ultra violet-visible diffuse reflective spectroscopy (UV-vis DRS) on a Shimadzu UV-3500

spectrometer. The sample spectra were presented after subtraction from the $BaSO_4$ powder spectrum as the reference material.

4.2.2.8 TEM

The metal particle size was measured visually using HRTEM system JEOL JEM-2100F. The average metal size was then calculated over 50 particles. Prior to the observation, the catalyst was initially reduced at 600˚C under H_2 for 1 h. Sample was then ultrasonically dispersed in ethanol and spread over perforated copper grids.

4.2.3 Catalytic reaction

The catalytic reaction was carried out in a fixed bed quartz reactor with an inner diameter of 4 mm and a length of 400 mm. 0.05 g of catalyst was used in each test and held by the quartz wool placed in the middle of the reactor. The temperature of the catalyst bed was controlled and monitored by a thermocouple that was in contact with the top layer of the catalyst bed. Prior to the catalytic reaction, the catalyst was reduced in 20 mL/min H_2 at 600^{o}C for 1 h, followed by purging in 20 mL/min helium while the temperature was increased to the reaction temperature of 700^{o}C. The feed with $CH_4/CO_2/O_2$ ratio of 5/4/1 was then introduced to the reactor at a flowrate of 20 mL/min. All the gases used here were research grade gases (99.95% CH_4, 99.99% CO_2, 99.8% O_2, and 99.9995% He). A cold trap filled with 50% glycerol and 50% water at temperature of −10^{o}C was installed between the reactor exit and the GC sampling valve to condense any moisture formed. The gas product was analyzed using a gas chromatograph (HP 6890) equipped with a Hayesep D column and a TCD detector. The chromatogram showed peak areas for all reacted gases which were then converted to volume-% through a calibration curve. The total flow rate of

the product gases was measured using bubble flow meter. The conversions of CH_4 and CO_2 were calculated using the following formula:

$$X_{CH_4}(\%) = \frac{n_{CH_4,in} - n_{CH_4,out}}{n_{CH_4,in}} x\,100$$

$$X_{CO_2}(\%) = \frac{n_{CO_2,in} - n_{CO_2,out}}{n_{CO_2,in}} x\,100$$

where *n* is molar flow rate of each gas.

The total amount of deposited carbon on the spent catalysts was measured using thermogravimetric analysis (TGA) on a Shimadzu DTG-60 thermogravimetric analyzer. Around 10 mg of spent catalyst was used in each TGA experiment and heated in air to 800ºC with a heating rate of 10K/min.

4.3 Results and discussion

4.3.1 Surface area of Pd−Ni/Y_2O_3 catalysts

Table 4-1 shows the BET results of the prepared catalysts. It can be seen that the surface area of Y_2O_3 support is 10m^2/g. After impregnation of Y_2O_3 with Ni metal, the surface area of the Ni/Y_2O_3 catalyst decreases. However, the surface area of the Pd/Y_2O_3 catalyst shows a reverse trend when the Pd/Y_2O_3 catalyst is synthesized using either $PdCl_2$ or $Pd(NO_3)_2$ as the catalyst precursor. The increase in the surface area of the Pd(C)/Y_2O_3 catalyst is observed even higher than the one of the Pd(N)/Y_2O_3 catalyst, possibly due to the diluted HCl used to dissolve $PdCl_2$ powder in the preparation of the Pd(C)/Y_2O_3 catalyst. It is well known that Y_2O_3 can fully dissolve in concentrated HCl to form YCl_3 [226]. Therefore, although the HCl used in the $PdCl_2$ solution was in low concentration, it

is still possible that part of Y_2O_3 dissolved in the HCl solution during the process of supporting Pd from $PdCl_2$.

Table 4-1 Physical property of Pd−Ni/Y_2O_3 catalysts

Sample	S_{BET} (m^2/g)	Ni content (wt%)		Pd content (wt%)	
		Calculated	Actual	Calculated	Actual
Y_2O_3	10	−	−	−	−
Ni/Y_2O_3	8	5.0	5.2	−	−
1Pd(C)−9Ni/Y_2O_3	33	4.2	2.7	0.8	0.9
3Pd(C)−7Ni/Y_2O_3	26	2.8	1.6	2.2	2.3
1Pd(C)−1Ni/Y_2O_3	31	1.8	1.4	3.2	2.9
7Pd(C)−3Ni/Y_2O_3	19	1.0	0.6	4.0	4.5
9Pd(C)−1Ni/Y_2O_3	24	0.3	0.2	4.7	5.3
Pd(C)/Y_2O_3	28	−	−	5.0	5.1
Pd(N)/Y_2O_3	21	−	−	5.0	4.7
1Pd(N)−1Ni/Y_2O_3	16	1.8	1.6	3.2	2.8

Chemical composition measured using ICP−MS

4.3.2 Morphologies of Pd−Ni/Y_2O_3 catalysts and Y_2O_3 support

The FESEM images of the Pd−Ni/Y_2O_3 catalysts and Y_2O_3 support are shown in Figure 4-1. It can be seen that the Ni/Y_2O_3 and Pd(N)/Y_2O_3 catalysts show similar morphology with Y_2O_3 support. However, different morphology is observed on the Pd(C)/Y_2O_3 catalyst. It seems that during the impregnation of Pd catalyst from $PdCl_2$

precursor which requires the use of HCl, the crystallinity of Y_2O_3 support might be possibly destroyed by HCl, causing the surface area of the Pd(C)/Y_2O_3 catalyst increase even higher than the Pd(N)/Y_2O_3 catalyst (as shown in Table 4-1). Furthermore, the morphology of the 1Pd(C)−1Ni/Y_2O_3 catalyst is also clearly observed to be similar to the one of the Pd(C)/Y_2O_3 catalyst, suggesting that the destruction of Y_2O_3 crystalline also occurred on the 1Pd(C)−1Ni/Y_2O_3 catalyst.

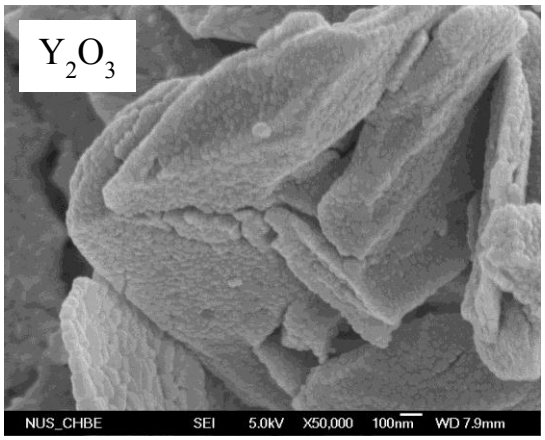

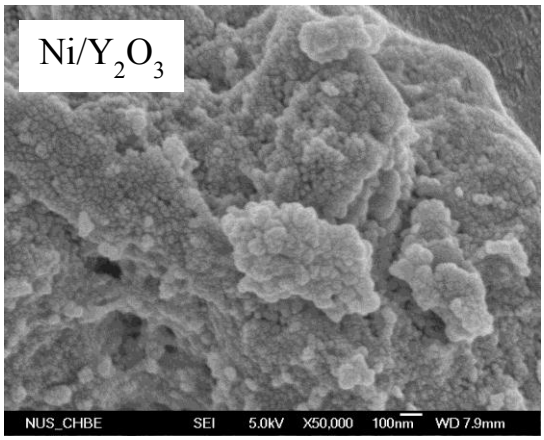

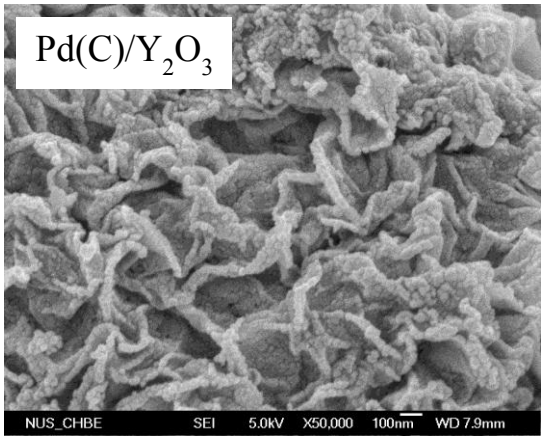

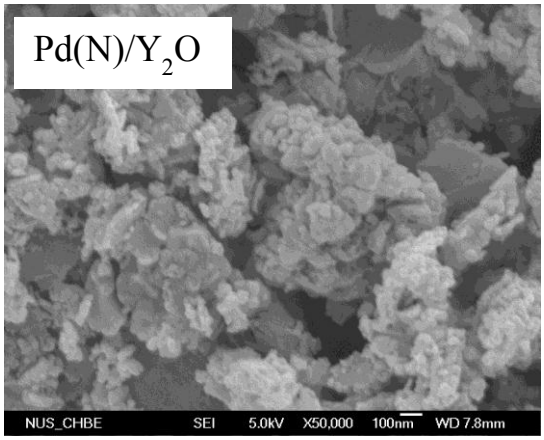

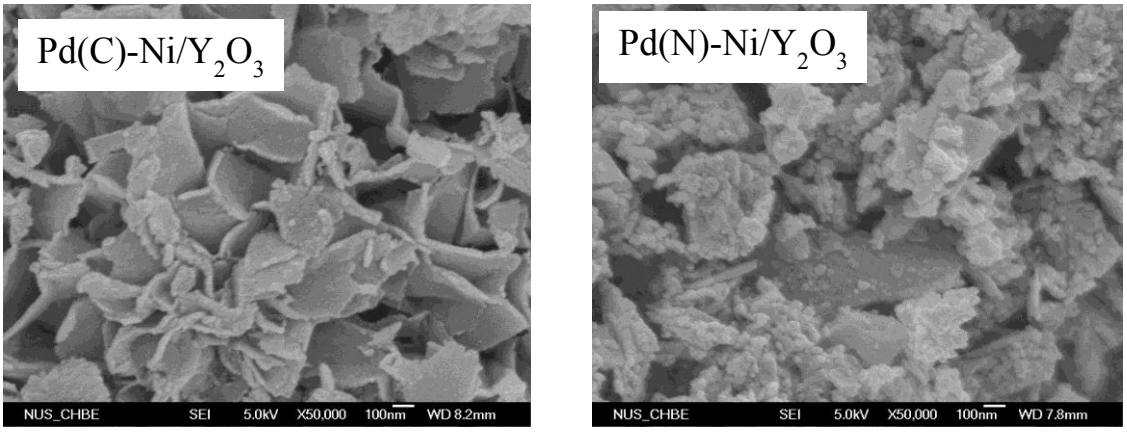

Figure 4−1 FESEM images of Pd−Ni/Y_2O_3 catalysts and Y_2O_3 support

4.3.3 H_2-TPR profiles of Pd−Ni/Y_2O_3 catalysts

Figure 4-2 shows the H_2-TPR profiles of all fresh catalysts and Y_2O_3 support. It can be seen that no peaks are observed on Y_2O_3 support, indicating that Y_2O_3 is hardly reduced. The negative and positive peaks are observed on the Pd(C)/Y_2O_3 catalyst at the temperatures of 100−130°C and 75−230°C, respectively. The negative peak shows the decomposition of β-PdH_x phase, which is formed during the purging of H_2 prior to the TPR experiment. The presence of β-PdH_x is widely associated with the formation of large Pd particles [166]. In addition, the positive peak at 75−230°C can be attributed to the reduction of PdO species [166].

More importantly, there is another peak observed at high temperature around 700°C. This peak has been observed by Costa et al. [163] for the reduction of their Pd/Y_2O_3 catalyst at temperature around 650°C and was attributed to the reduction of Pd_2O_4Y compound. The presence of this compound showed the formation of metal−support compound (MSC) between Pd and Y_2O_3 support, thus causing the shifting of the reduction of palladium to higher temperature. A similar formation of Pd−Al_2O_3 compound with the general formula $Pd_xCl_yO_z$ has also been observed on the Pd/Al_2O_3

catalyst prepared from $PdCl_2$ precursor [172-173]. Therefore, even though many complexes between Pd and Y_2O_3 such as Pd_2O_4Y [169], $Pd_2O_5Y_2$ [170], and $Pd_2O_7Y_2$ [171] have been observed, the high temperature TPR peak for the Pd(C)/Y_2O_3 catalyst observed in our study can be associated to the reduction of $Pd_xCl_yY_z$ compound, which is later shown in UV-DRS result, indicating the formation of Pd-Y_2O_3 compound on the Pd(C)/Y_2O_3 catalyst.

When the Pd nitrate is used as the precursor, there is only one positive peak observed at 75−230°C on the Pd(N)/Y_2O_3 catalyst. This positive TPR peak at low temperature is attributed to the reduction of PdO. However, there is no reduction peak at high temperature around 700°C as observed on the Pd(C)/Y_2O_3 catalyst, indicating that there is no formation of MSC between Pd and Y_2O_3 support on the Pd(N)/Y_2O_3 catalyst.

The peak on the Ni/Y_2O_3 catalyst is observed at temperature from 370^{o}C to 530^{o}C and is attributed to the reduction of NiO species. The total amount of H_2 consumption agrees with the stoichiometry of $NiO + H_2 \rightarrow Ni + H_2O$, suggesting that all Ni species present in the oxidized state are reduced to Ni metal [227].

When Pd and Ni are combined to form the Pd(C)−Ni/Y_2O_3 catalysts, the reduction of NiO peak is observed strongly on the 1Pd(C)−9Ni/Y_2O_3 catalyst. The intensity of the reduction of NiO peak as shown in the H_2 consumption in Table 4-2 decreases with increasing ratio of Pd/Ni due to the decrease of the amount of Ni content. Interestingly, the reduction of NiO peak on those catalysts shifts to lower temperature. The shifting of NiO peak to lower temperature is attributed to the hydrogen spill-over from palladium which is reduced at lower temperature than nickel. Once palladium is reduced, the reduced Pd acts as the dissociation sites for hydrogen and the dissociated hydrogen migrates through the catalyst surface and reduces the nickel more readily than the normal gaseous

molecular hydrogen [172]. Therefore, with a higher content of Pd, a larger amount of dissociated hydrogen could then migrate through the catalyst surface, hence reducing the NiO at lower temperature.

Moreover, there is no negative peak corresponding to the decomposition of β-PdH_x phase on all Pd(C)−Ni/Y_2O_3 catalysts. The absence of β-PdH_x phase on all Pd(C)−Ni/Y_2O_3 catalysts indicates that the particle size of Pd is quite small [167]. It is also interesting to observe that the reduction peak of $Pd_xCl_yY_z$ compound, which is observed to occur generally at a high temperature around 700°C, shifts to even higher temperature and reaches the highest reduction temperature on the 1Pd(C)−1Ni/Y_2O_3 catalyst. The shifting of the $Pd_xCl_yY_z$ reduction peak to higher temperature shows that Pd has a stronger interaction with the catalyst support in the $Pd_xCl_yY_z$ compound with the increasing amount of Pd. This strong interaction of Pd with the catalyst support in the $Pd_xCl_yY_z$ compound is shown later to play an important role in the stability of the Pd(C)−Ni/Y_2O_3 catalyst under high temperature reaction condition.

For the 1Pd(N)−1Ni/Y_2O_3 catalyst, two peaks are observed at 140−190°C and 280−450°C. Those peaks can be attributed to the reduction of PdO and NiO, respectively. The reduction of NiO peak also shifts to lower temperature due to the hydrogen spill−over as observed on the Pd(C)−Ni/Y_2O_3 catalyst. However, the 1Pd(N)−1Ni/Y_2O_3 catalyst has no reduction peak at high temperature around 700°C due to the absence of the $Pd_xCl_yY_z$ compound, in contrast with the one observed on the 1Pd(C)−1Ni/Y_2O_3 catalyst. This result shows that the $PdCl_2$ precursor is a good precursor to form a MSC between Pd and Y_2O_3 support.

In order to elucidate the effect of diluted HCl in the preparation of the Pd(C)/Y_2O_3 and Pd(C)−Ni/Y_2O_3 catalysts, another 1Pd(N)−1Ni/Y_2O_3 catalyst was synthesized with the addition of diluted HCl. It can be seen that two peaks are observed on the 1Pd(N)−1Ni/Y_2O_3 catalyst prepared with HCl. These peaks are exactly same as those observed on the 1Pd(N)−1Ni/Y_2O_3 catalyst prepared without HCl. However, no reduction peak at high temperature around 700°C is observed on the 1Pd(N)−1Ni/Y_2O_3 catalyst prepared with the addition of HCl, showing that the formation of MSC between Pd and Y_2O_3 support in the Pd(C)/Y_2O_3 and Pd(C)−Ni/Y_2O_3 catalysts is due to the use of $PdCl_2$ precursor instead of the use of diluted HCl in the catalyst preparation. This confirms that $PdCl_2$ is a good Pd catalyst precursor to form MSC between Pd and Y_2O_3 support.

Table 4-2 H_2 consumption and reduction degree of Pd−Ni catalysts

Catalyst	H_2 consumption (μmol/g)		Reduction degree (%)	
	Pd	Ni	Pd	Ni
1Pd(C)−9Ni	71	431	84	93
3Pd(C)−7Ni	212	252	98	92
1Pd(C)−1Ni	262	225	96	94
7Pd(C)−3Ni	396	93	93	91
9Pd(C)−1Ni	445	32	89	64
1Pd(N)−1Ni	238	242	90	86

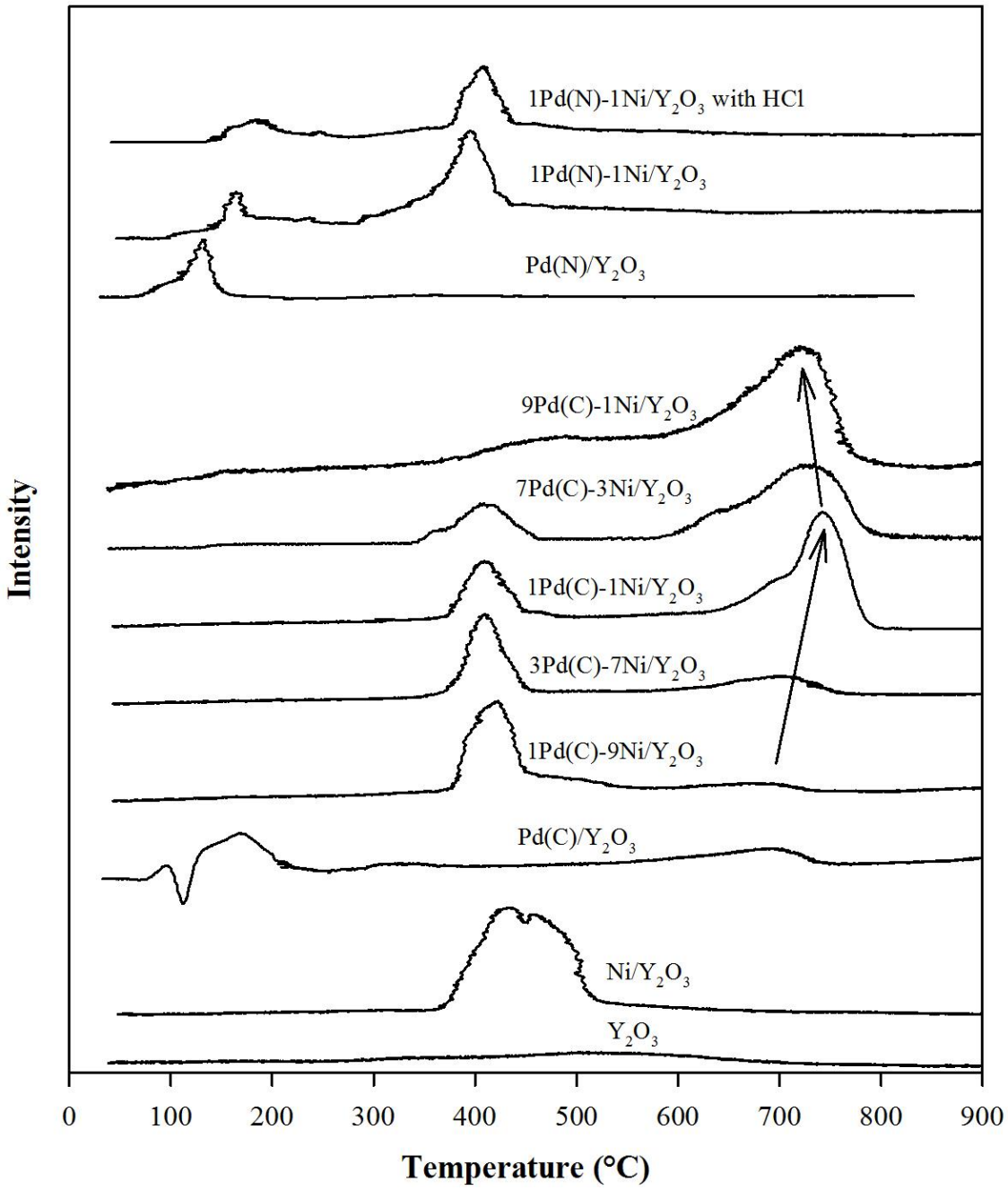

Figure 4-2 TPR profiles of fresh Pd−Ni/Y_2O_3 catalysts

4.3.4 XRD patterns of fresh Pd−Ni/Y_2O_3 catalysts

Figure 4−3 shows the XRD crystal structures of fresh Pd(C)−Ni/Y_2O_3 and Pd(N)−Ni/Y_2O_3 catalysts as well as the Pd(N)/Y_2O_3, Pd(C)/Y_2O_3, and Ni/Y_2O_3 catalysts. The characteristic peaks of the Y_2O_3 catalyst support ($2\theta = 33.77^o$, 48.54^o, and 57.6^o) can be seen in all catalysts. However, no distinguishable peaks indexed to NiO ($2\theta = 37.4^o$ and 43.4^o) and PdO ($2\theta = 33.9°$ and 41.9°) are observed on all these catalysts. This observation indicates that the crystal sizes of NiO and PdO are very small, beyond the detection limit of the XRD equipment, showing that the NiO or PdO particles are highly dispersed on the support. In contrast, there are two small peaks observed at 2θ of 32.5^o and 46.1^o in the Pd−rich Pd(C)−Ni/Y_2O_3 catalyst starting from the Pd:Ni ratio of 7:3 to the Pd(C)/Y_2O_3 catalyst. These peaks can be assigned to the formation of $Pd_xCl_yY_z$ compound, which has been observed from the TPR results. The physical mixing of 5%-wt $PdCl_2$/Y_2O_3 catalyst also does not show these peaks, confirming that these two peaks are the characteristic peaks of $Pd_xO_yY_z$ compound. In contrast, these XRD peaks of $Pd_xCl_yY_z$ compound are not observed on the Pd(N)/Y_2O_3 and 1Pd(N)−1Ni/Y_2O_3 catalysts, showing that $PdCl_2$ is a good precursor to form MSC between Pd and Y_2O_3 support.

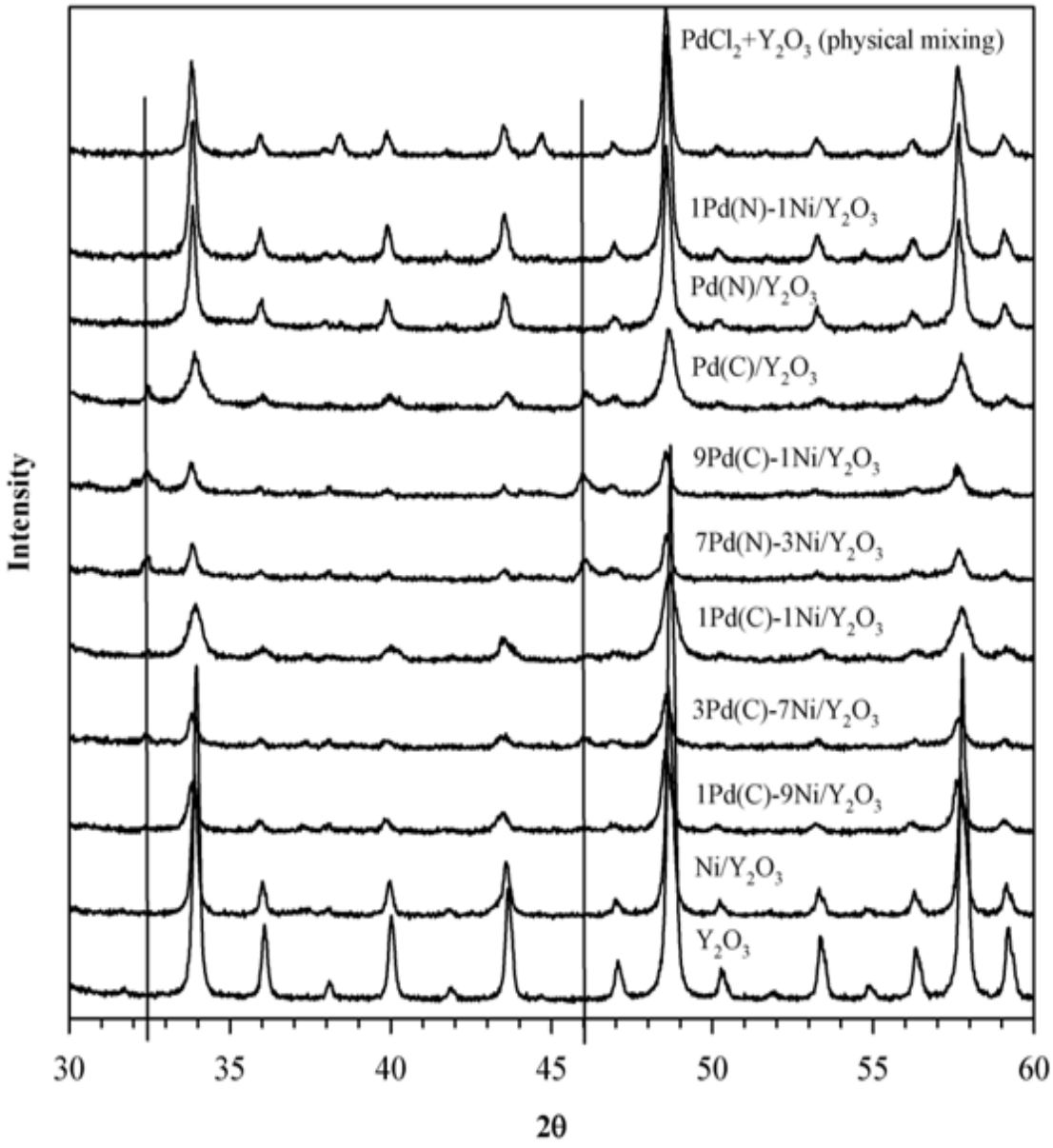

Figure 4-3 XRD profiles of fresh Pd−Ni/Y_2O_3 catalysts

4.3.5 XPS analysis of reduced Pd−Ni/Y_2O_3 catalysts

Figure 4-4 shows the XPS spectra of the Pd(N)/Y_2O_3, Pd(C)/Y_2O_3, Ni/Y_2O_3, Pd−Ni/Y_2O_3 catalysts after reduction at 600°C for 1 hour. The Pd $3d_{5/2}$ peak of Pd(N)/Y_2O_3 catalyst is observed at 334.9 eV which exactly fits to the binding energy of

metallic Pd^0 [228], while the Y 3d peaks of the $Pd(N)/Y_2O_3$ catalyst also exactly fit to the $3d_{5/2}$ and $3d_{3/2}$ peaks of pure Y_2O_3 at 156.4eV and 158.4eV, respectively. The O 1s peak of the $Pd(N)/Y_2O_3$ catalyst is observed at 528.9eV, which exactly fits to the O 1s peak of pure Y_2O_3. This suggests that there is no interaction between Pd and Y_2O_3 support on the $Pd(N)/Y_2O_3$ catalyst since there is hardly any electron transfer between Pd and Y_2O_3 support.

However, the Pd $3d_{5/2}$ peak of $Pd(C)/Y_2O_3$ catalyst is observed at 335.3 eV, which is higher than the Pd^0 binding energy (334.9 eV) [228] but lower than the Pd^{2+} binding energy (336.8 eV) [229]. The shifting of this peak to higher binding energy than Pd^0 suggests the presence of electron deficient Pd^{n+} species, indicating that the electron has been transferred from Pd. The Y $3d_{5/2}$ XPS peaks of the $Pd(C)/Y_2O_3$ catalyst is observed to shift to higher binding energy (0.05eV) while the O 1s XPS peak exactly fit to the peak of pure Y_2O_3, showing that the electron has also been transferred from Y. In addition, the Cl 2p XPS peak was also analyzed since the preparation method of this $Pd(C)/Y_2O_3$ catalyst used HCl to dissolve the $PdCl_2$. The result shows that the Cl 2p XPS peak is observed to shift to lower binding energy (0.35eV). The shifting of the Pd and Y XPS peaks to higher binding energy and the Cl XPS peak to lower binding energy show that the electron has been transferred from Pd particles and Y to Cl, resulting in the formation of MSC. A similar shifting of Pd peak to higher binding energy on the supported palladium catalyst prepared from $PdCl_2$ source has been observed by Shen et al. [230], who also attributed the shifting of metallic elements to higher binding energy to the formation of MSC. This XPS result is in good agreement with the XRD and TPR results which show the formation of $Pd_xCl_yY_z$ compound on the $Pd(C)/Y_2O_3$ catalyst.

The reduced Ni/Y_2O_3 catalyst exhibits the Ni $2p_{3/2}$ main peak at 852.3eV and Ni $2p_{1/2}$ main peak at 869.8eV. These peaks show that the Ni particles on the Ni/Y_2O_3 catalyst are essentially in Ni^0 oxidation state [228], showing that all the surface Ni particles are fully reduced. In addition, the Y 3d peaks and the O 1s peak of the Ni/Y_2O_3 catalyst exactly fit to the Y $3d_{5/2}$, $3d_{3/2}$, and O 1s peaks of pure Y_2O_3 at 156.4eV, 158.4eV, and 528.9eV, respectively. These results of no shifting of XPS peaks show no association between Ni and Y_2O_3 support on the Ni/Y_2O_3 catalyst.

For the $1Pd(N)-1Ni/Y_2O_3$ catalyst, the Pd $3d_{5/2}$ XPS peak is observed at 334.8 eV, which is slightly lower than the Pd^0 binding energy, showing that electron has been transferred to Pd. However, the XPS Ni $2p_{3/2}$ peak of the $1Pd(N)-1Ni/Y_2O_3$ catalyst is observed at 852.4 eV, which is higher than the binding energy of Ni^0 peak, showing that electron has been transferred from Ni. Moreover, the O 1s XPS peak of the 1Pd(N)-$1Ni/Y_2O_3$ catalyst exactly fits to the binding energy of O 1s peak of pure Y_2O_3. The shifting of Pd peak to lower binding energy and Ni peak to higher binding energy show that the electrons have been transferred from Ni to Pd, shows the presence of Pd-Ni bimetallic particles on the 1Pd(N)-$1Ni/Y_2O_3$ catalyst.

The Pd $3d_{5/2}$ XPS peak of the $1Pd(C)-1Ni/Y_2O_3$ catalyst is observed at 335.6 eV, which is even higher than the binding energy of the $Pd(C)/Y_2O_3$ catalyst, suggesting that more electrons have been transferred from Pd. Moreover, the Ni $2p_{3/2}$ and Y 3d XPS peaks of the 1Pd(C)-$1Ni/Y_2O_3$ catalysts are also observed to shift to higher binding energy than the peak of Ni^0 peak and pure Y_2O_3 peak, respectively, showing that electron has been transferred from Ni, while the Cl 2p peak of the 1Pd(C)-$1Ni/Y_2O_3$ catalyst shifts to much lower binding energy (0.65eV) than pure Y_2O_3. The shifting of Pd peak to much higher binding energy, Ni and Y peaks to higher binding energy, and Cl peak to lower binding

energy shows that Ni particles transfer electron to Pd and Pd particles and Y transfer electron to Cl. These results show the presence of Pd-Ni bimetallic particles and the stronger interaction between Pd and Y_2O_3 support in the $Pd_xCl_yY_z$ compound on the 1Pd(C)-1Ni/Y_2O_3 catalyst. These results are in good agreement with the TPR results which show stronger interaction between Pd and Y_2O_3 support in the $Pd_xCl_yY_z$ compound on the 1Pd(C)-1Ni/Y_2O_3 catalyst.

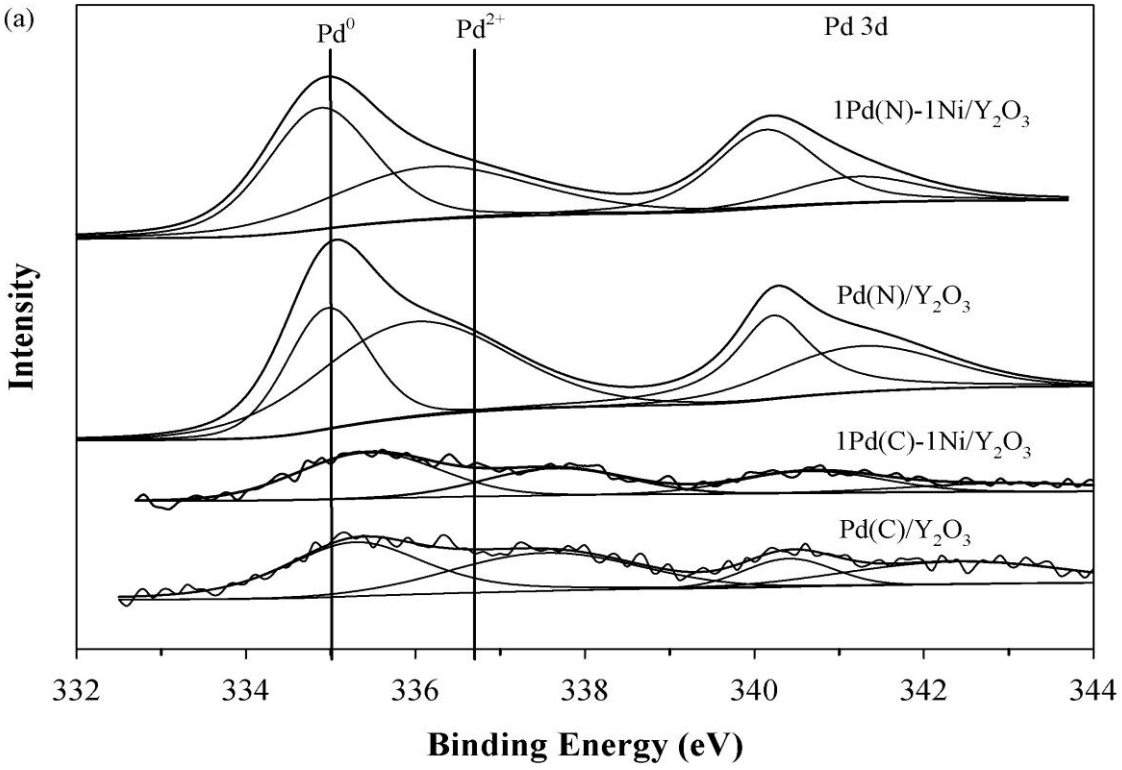

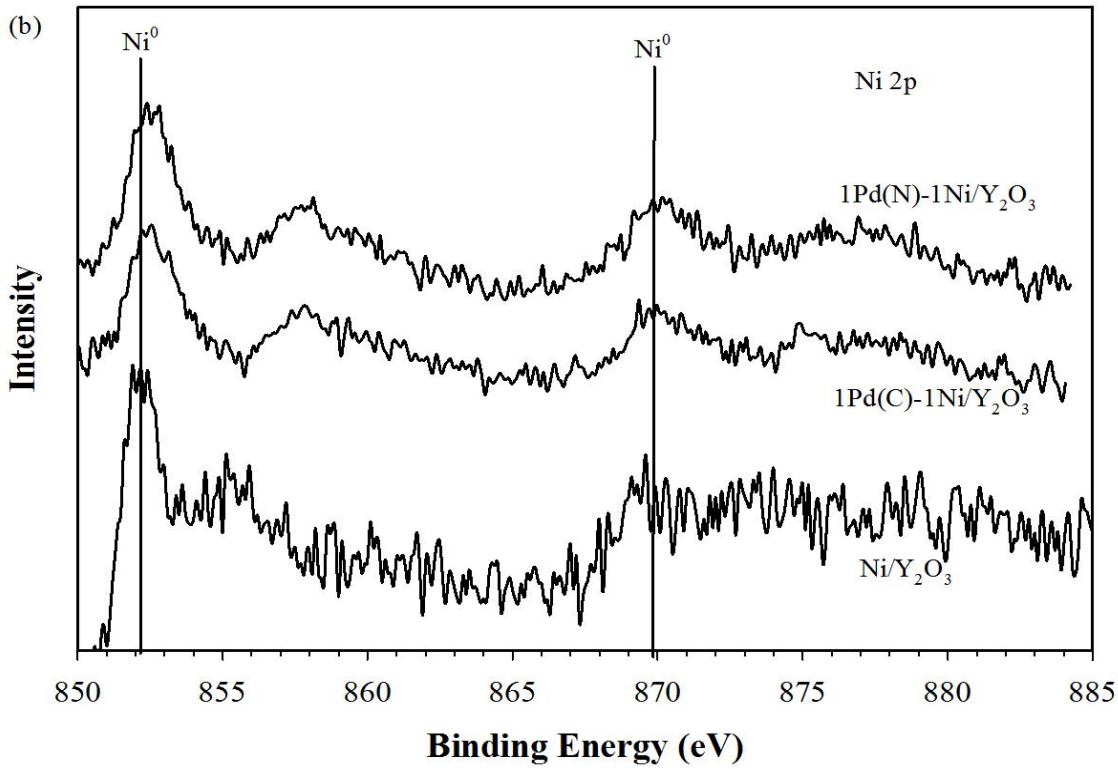
(b)
Ni^0
Ni^0
Ni 2p
1Pd(N)-1Ni/Y$_2$O$_3$
1Pd(C)-1Ni/Y$_2$O$_3$
Ni/Y$_2$O$_3$
Intensity
850
855
860
865
870
875
880
885
Binding Energy (eV)

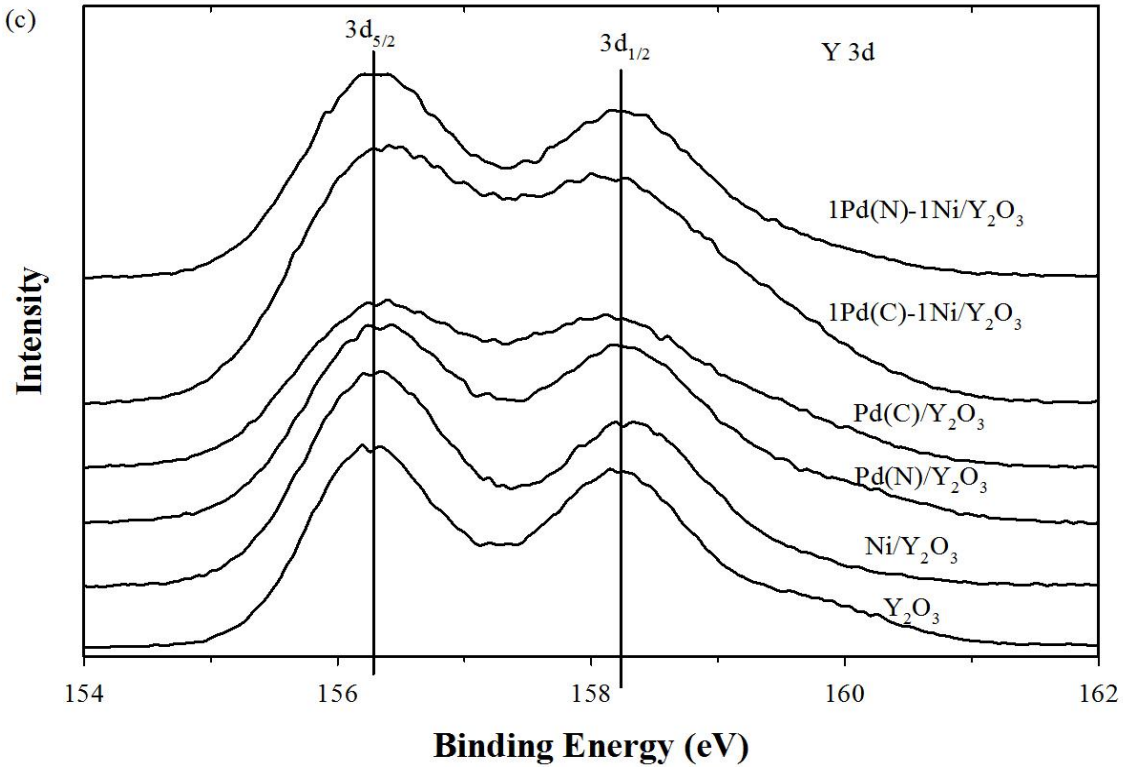
(c)
3d$_{5/2}$
3d$_{1/2}$
Y 3d
1Pd(N)-1Ni/Y$_2$O$_3$
1Pd(C)-1Ni/Y$_2$O$_3$
Pd(C)/Y$_2$O$_3$
Pd(N)/Y$_2$O$_3$
Ni/Y$_2$O$_3$
Y$_2$O$_3$
Intensity
154
156
158
160
162
Binding Energy (eV)

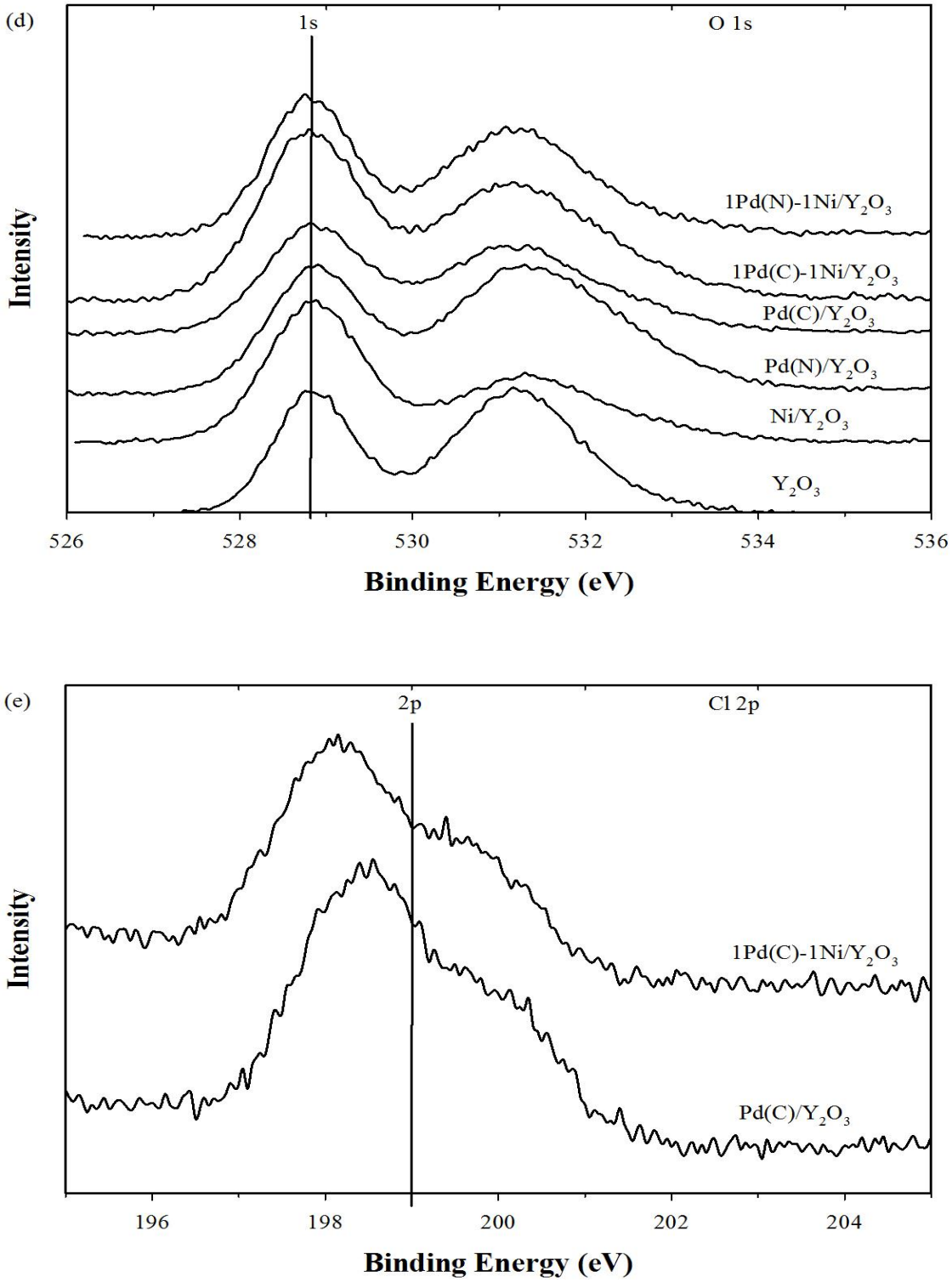

Figure 4-4 XPS of reduced Pd−Ni/Y_2O_3 catalysts

4.3.6 FTIR analysis of Pd−Ni/Y_2O_3 catalysts

Figure 4-5 shows the infrared spectra of the Ni/Y_2O_3, Pd(C)/Y_2O_3, 1Pd(N)−1Ni/Y_2O_3 and 1Pd(C)−1Ni/Y_2O_3 catalysts after pretreatment condition and CO exposure at 400°C. One CO vibration band is observed on the Ni/Y_2O_3 catalyst at 2070 cm^{-1}, corresponding to CO adsorption at linear sites on metallic Ni particles [231]. However, two CO vibration bands are also observed on the Pd(C)/Y_2O_3 catalyst at 1965 and 2090 cm^{-1}, corresponding to bridge and linear CO adsorbed on metallic Pd particles, respectively [232].

For 1Pd(N)-1Ni/Y_2O_3 catalyst, one CO vibration band is observed at 1960 cm^{-1}, This band can be assigned to bridge CO adsorption on metallic Pd particles, suggesting the Pd-rich surface on the 1Pd(N)-1Ni/Y_2O_3 catalyst.

In contrast, two CO vibration bands are observed on 1Pd(C)-1Ni/Y_2O_3 catalyst at 1965 and 2075 cm^{-1}. The band at 1965 cm^{-1} exactly matches with the bridge CO adsorption on metallic Pd particles. It is interesting that the band at 2075 cm^{-1} is located between the linear CO adsorption sites on the Ni/Y_2O_3 catalyst and the linear CO adsorption sites on the Pd(C)/Y_2O_3 catalyst, suggesting that Pd and Ni have interaction to form bimetallic Pd-Ni particles on the 1Pd(C)-1Ni/Y_2O_3 catalyst. In addition, this result also suggests the presence of surface Ni on 1Pd(C)-1Ni/Y_2O_3 catalyst is much higher than the one on 1Pd(N)-1Ni/Y_2O_3 catalyst.

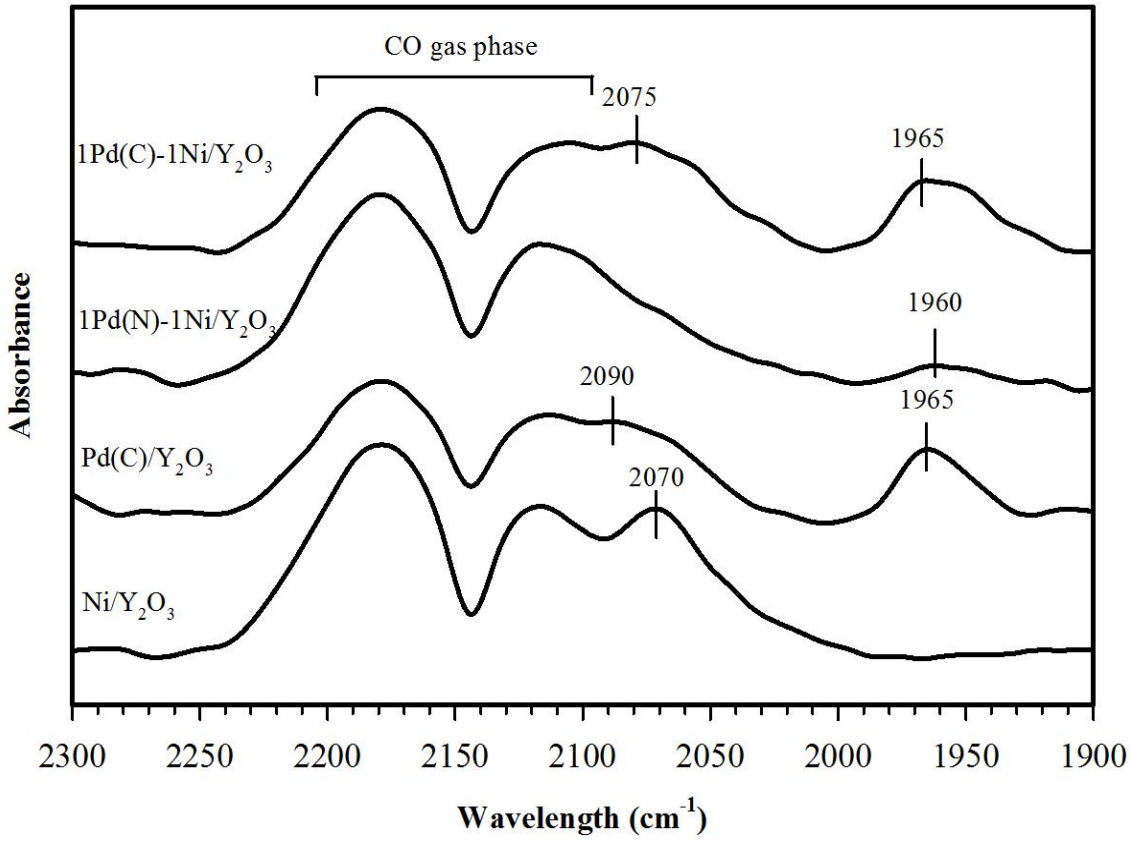

Figure 4-5 FTIR spectra of Pd−Ni/Y_2O_3 catalysts

4.3.7 UV Spectra of Pd-Ni/Y_2O_3 catalysts

Figure 4-6 shows the UV spectra of fresh and reduced Pd(N)/Y_2O_3, Pd(C)/Y_2O_3, 1Pd(N)-1Ni/Y_2O_3, and 1Pd(C)-1Ni/Y_2O_3 catalysts. It can be seen that there is hardly any peaks observed in reduced Pd(N)/Y_2O_3 and 1Pd(N)-1Ni/Y_2O_3 catalysts. However, in the reduced Pd(C)/Y_2O_3 and 1Pd(C)-1Ni/Y_2O_3 catalysts, two obvious peaks are observed, corresponding to the presence of $PdCl_4^{2-}$ [233]. Since TPR and XPS results show the strong interaction between Pd and Y_2O_3, the possible cation attached to the $PdCl_4^{2-}$ is $Y^{\delta+}$. Therefore, the compound formed from interaction between Pd and Y_2O_3 is assigned as $Pd_xCl_yY_z$. Mahata and Vishwanathan [233] reported that the formation of $PdCl_4^{2-}$ using

$PdCl_2$ precursor depended on the catalyst support. The $PdCl_4^{2-}$ compound is only observed for Al_2O_3 support, but not for MgO and zeolite (NaX) supports.

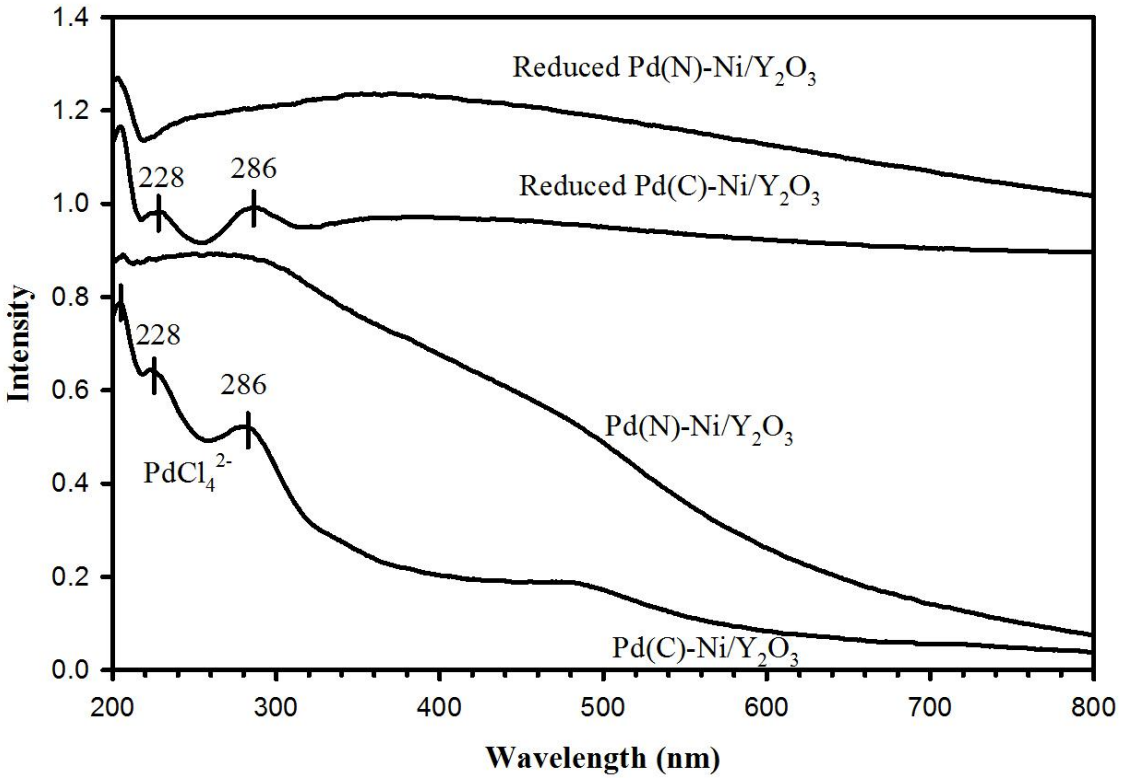

Figure 4-6 UV spectra of fresh and reduced Pd-Ni/Y_2O_3 catalysts

4.3.8 Particle size measurement of Pd−Ni/Y_2O_3 catalysts

Figure 4-7 shows the TEM images of reduced Ni/Y_2O_3, $Pd(N)/Y_2O_3$, $Pd(C)/Y_2O_3$, $1Pd(N)-1Ni/Y_2O_3$, and $1Pd(C)-1Ni/Y_2O_3$ catalysts. It can be seen that the metal particle size of the Ni/Y_2O_3 catalyst is around 15−20nm. It is also observed that aggregation to form big particles occurs on the Ni/Y_2O_3 catalyst, due to lack of interaction between Ni and Y_2O_3 support as shown in our TPR and XPS results. The aggregation of metallic Ni

particles was also observed by Xu et al. [234] on the Ni/SiO_2 catalyst. They explained that metallic nickel particles had high mobility due to lack of interaction between Ni and SiO_2 support, therefore, the particles easily migrated, aggregated, and grow at high temperature.

The measurement of metal particle size of the $Pd(N)/Y_2O_3$ and $Pd(C)/Y_2O_3$ catalysts shows that $Pd(C)/Y_2O_3$ catalyst has comparable metal particle size with $Pd(N)/Y_2O_3$ catalyst, around 8−10nm. However, the small metal particles on the $Pd(C)/Y_2O_3$ catalyst are observed more obvious than the ones on $Pd(N)/Y_2O_3$ catalyst, due to the presence of $Pd_xCl_yY_z$ compound, as observed from the TPR and XPS results. The presence of $Pd_xCl_yY_z$ compound on the $Pd(C)/Y_2O_3$ catalyst prevents aggregation of the metallic Pd particles, resulting in smaller metal particle size. This phenomenon was also observed by Cheng et al. [235], who reported smaller Ni particle size on the Ni/Al_2O_3 catalyst due to the presence of $NiAl_2O_4$ compound.

The metal particle size of the $1Pd(C)\text{-}1Ni/Y_2O_3$ catalyst is observed around 3-5nm and smaller than the one on the $Pd(C)/Y_2O_3$ catalyst due to the MSC formation between $Pd\text{-}Y_2O_3$ support as observed from the TPR and XPS results. It is important to point out that the metal particle size measured for reduced $1Pd(C)\text{-}1Ni/Y_2O_3$ catalyst is for metallic Ni particles, since Pd is not reduced at 600°C, judging from the TPR result of the $1Pd(C)\text{-}1Ni/Y_2O_3$ catalyst. In contrast, the metal particle size of the $1Pd(N)\text{-}1Ni/Y_2O_3$ catalyst is very big, around 30-35nm due to lack of MSC formation between $Pd\text{-}Y_2O_3$ support. These results show that the presence of MSC between Pd and Y_2O_3 support is important to produce small metal particle size.

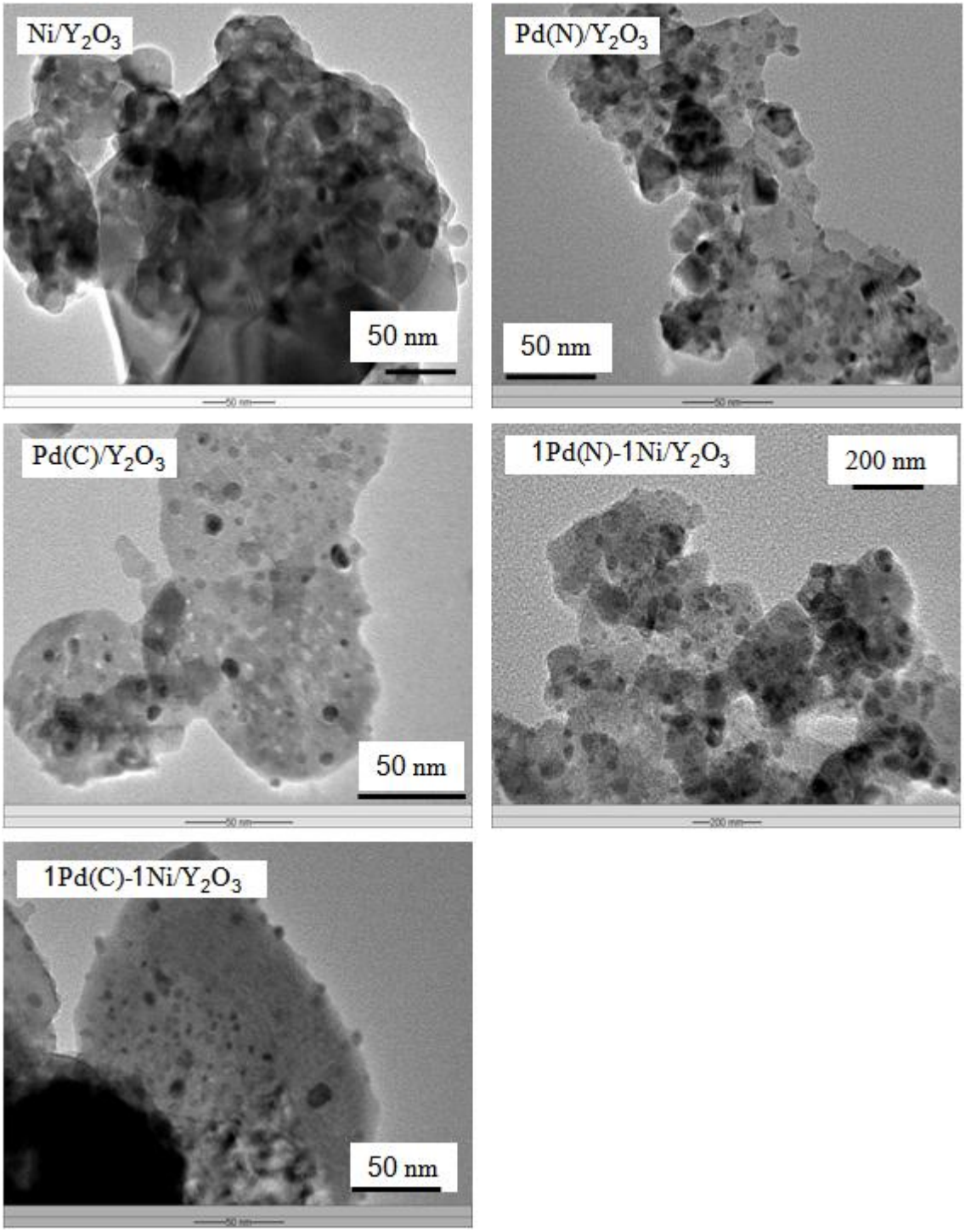

Figure 4-7 TEM images of Pd−Ni/Y_2O_3 catalysts after H_2 reduction

4.3.9 Catalyst activity

Figure 4-8a shows the catalytic performance of the Pd−Ni/Y_2O_3 catalysts after 12 hours of reaction time. Interestingly, the conversions of CH_4 and CO_2 over either the 1Pd(N)−1Ni/Y_2O_3 catalyst or 1Pd(C)−1Ni/Y_2O_3 catalyst are observed to be higher than those produced from either the Ni/Y_2O_3 catalyst or the Pd/Y_2O_3 catalyst. The similar results were observed by Steinhauer et al. [187]. The higher conversion over either the 1Pd(N)−1Ni/Y_2O_3 or 1Pd(C)−1Ni/Y_2O_3 catalyst shows that the addition of Pd to Ni catalyst improves the catalytic activity of the catalyst. According to Dias and Assaf [172] and Damyanova et al. [186], the higher activity of the Pd−Ni catalysts could be attributed to either increase in surface metal area or formation of smaller metal particles. However, our results show that the metal particle size of the 1Pd(N)−1Ni/Y_2O_3 catalyst is bigger than the one of either the Ni/Y_2O_3 catalyst or the Pd/Y_2O_3 catalyst, yet the conversion is still higher than either the Ni/Y_2O_3 catalyst or the Pd/Y_2O_3 catalyst. Therefore, the increase in activity of either the 1Pd(N)−1Ni/Y_2O_3 or 1Pd(C)−1Ni/Y_2O_3 catalyst is attributed to the formation of bimetallic Pd−Ni particles, as shown from our XPS results. The formation of bimetallic Pd−Ni particles was also observed by Otsuka et al. [204-206]. Moreover, Tomishige et al. [207-213] reported that all preparation methods and Pd precursors ($PdCl_2$, $Pd(NO_3)_2$ and $Pd(acetate)_2$) could form Pd−Ni bimetallic particles. Similar formation of bimetallic particles was also observed by Song et al. [236−238] on the Pd−Cu catalyst.

In addition, it is observed that the 1Pd(C)−1Ni/Y_2O_3 catalyst shows higher conversions of CO_2 and CH_4 compared to those over the 1Pd(N)−1Ni/Y_2O_3 catalyst. This higher activity could be attributed to the smaller metal particle size of the 1Pd(C)−1Ni/Y_2O_3 catalyst, in agreement with the results from Dias and Assaf [172] and

Damyanova et al. [186]. Therefore, it can be concluded that both Pd−Ni bimetallic and smaller particles are the main reasons of very high activity on the 1Pd(C)−1Ni/Y_2O_3 catalyst.

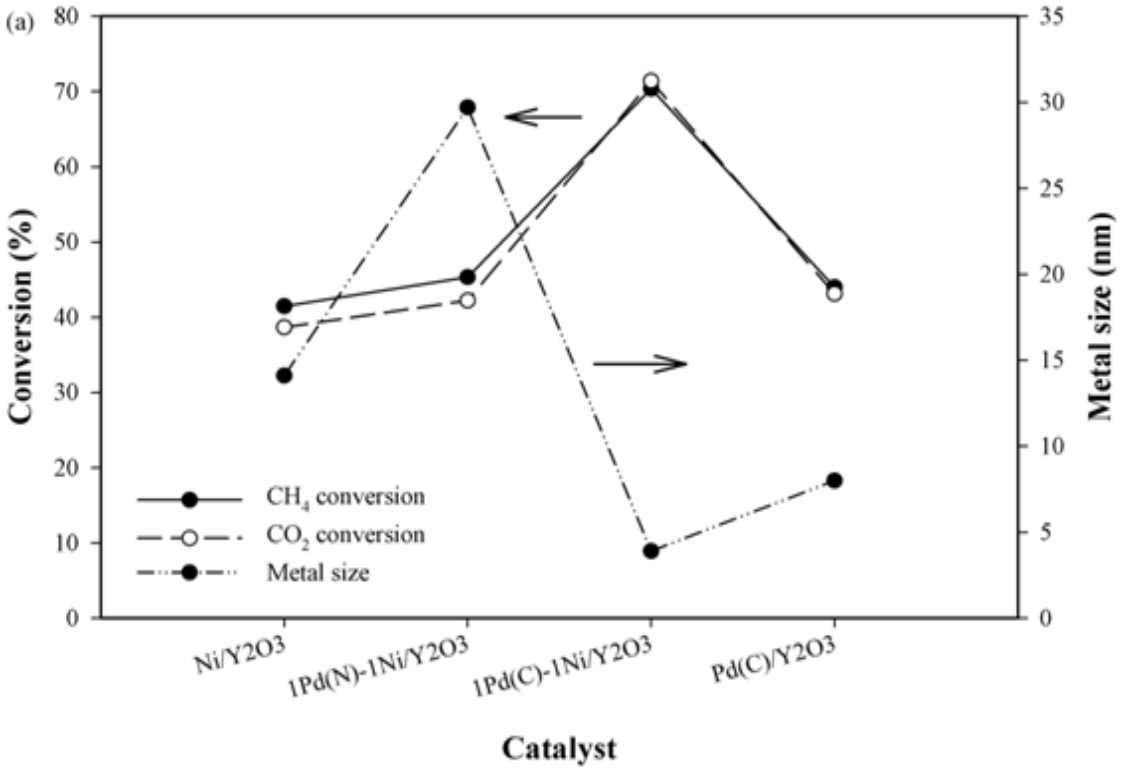

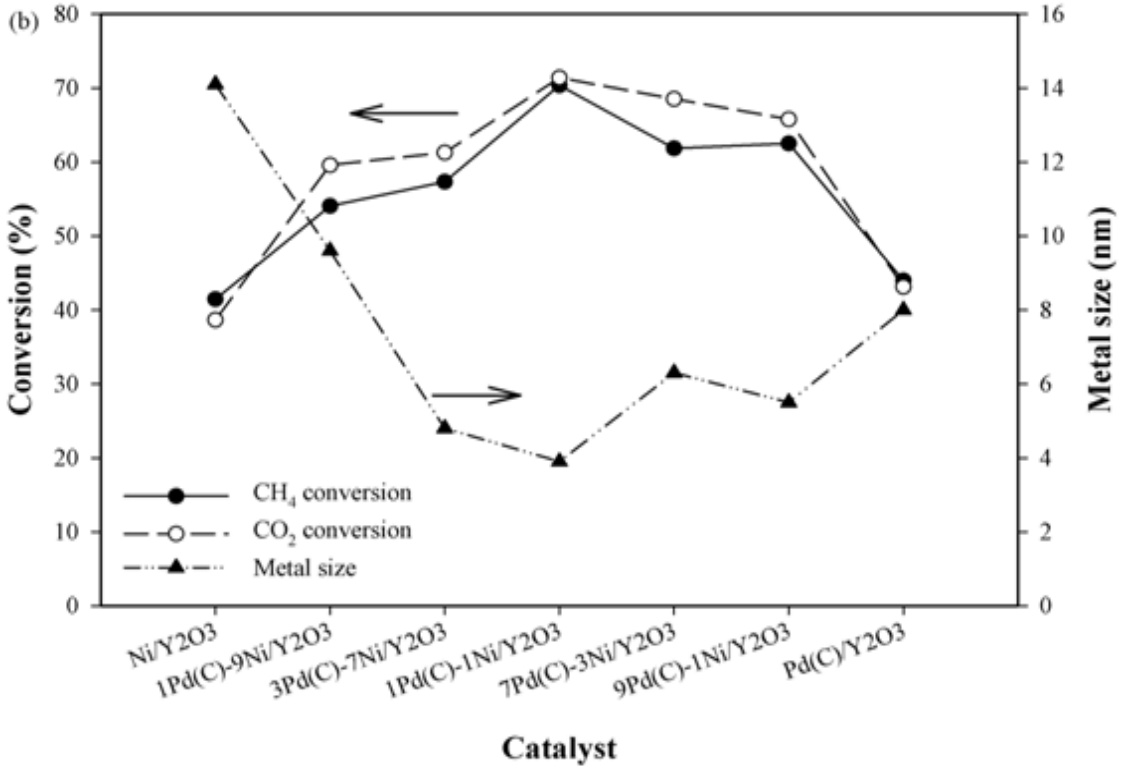

Figure 4-8 Catalytic performance of Pd−Ni/Y_2O_3 catalysts (Reaction condition: P_{total} = 1 atm, T = 700ºC, $CH_4/CO_2/O_2$ = 5/4/1, GHSV = 24000 $cm^3/g/h$)

Since the 1Pd(C)−1Ni/Y_2O_3 catalyst shows the highest activity, it is therefore chosen to study the effect of Pd/Ni ratio. Figure 4-8b shows the catalyst activity of the Pd(C)−Ni/Y_2O_3 catalysts in various ratio of Pd/Ni. It is interesting to observe that the conversions of CH_4 and CO_2 increase while the metal particle size decreases with increasing in Pd content and reach optimum at Pd/Ni ratio of 1/1. The highest catalyst activity is observed on the 1Pd(C)−1Ni/Y_2O_3 catalyst with the smallest metal particle size, showing that metal particles size is crucial for the catalyst activity. These results were also reported by Damyanova et al [186].

4.3.10 Catalyst stability

Figure 4−9 shows the catalytic stability of the Ni/Y_2O_3, Pd/Y_2O_3, and $Pd−Ni/Y_2O_3$ catalysts during the OCRM reaction for 12 h using different Pd precursors. Initially, the Ni/Y_2O_3 catalyst shows high conversions of CH_4 and CO_2, but the conversions decrease with time on stream. The decrease of catalytic activity of the Ni catalyst for DRM reaction is well known due to the high carbon formation rate [92]. On the other hand, the conversions of CH_4 and CO_2 produced from the $Pd(C)/Y_2O_3$ and $Pd(N)/Y_2O_3$ catalysts are initially lower than the Ni/Y_2O_3 catalyst but they are stable during duration of reaction for 12 h. The stable activity of the Pd catalyst has been reported by S. Barama et al. [239] in the DRM reaction, due to low carbon formation rate.

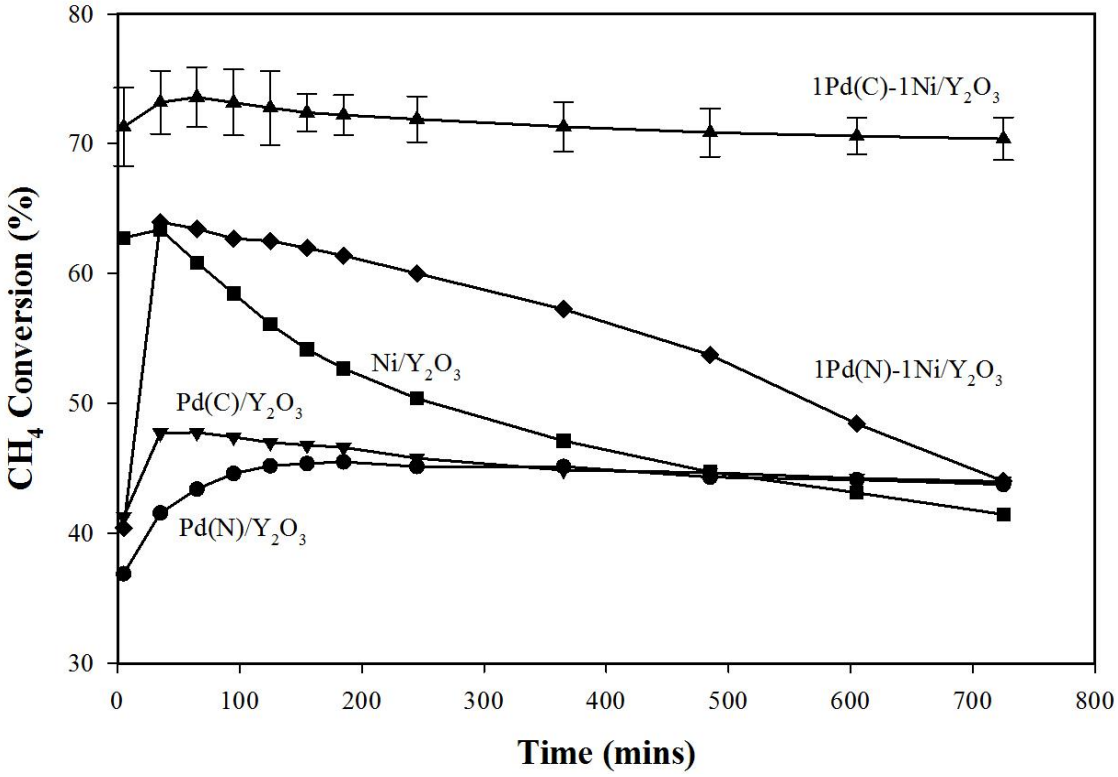

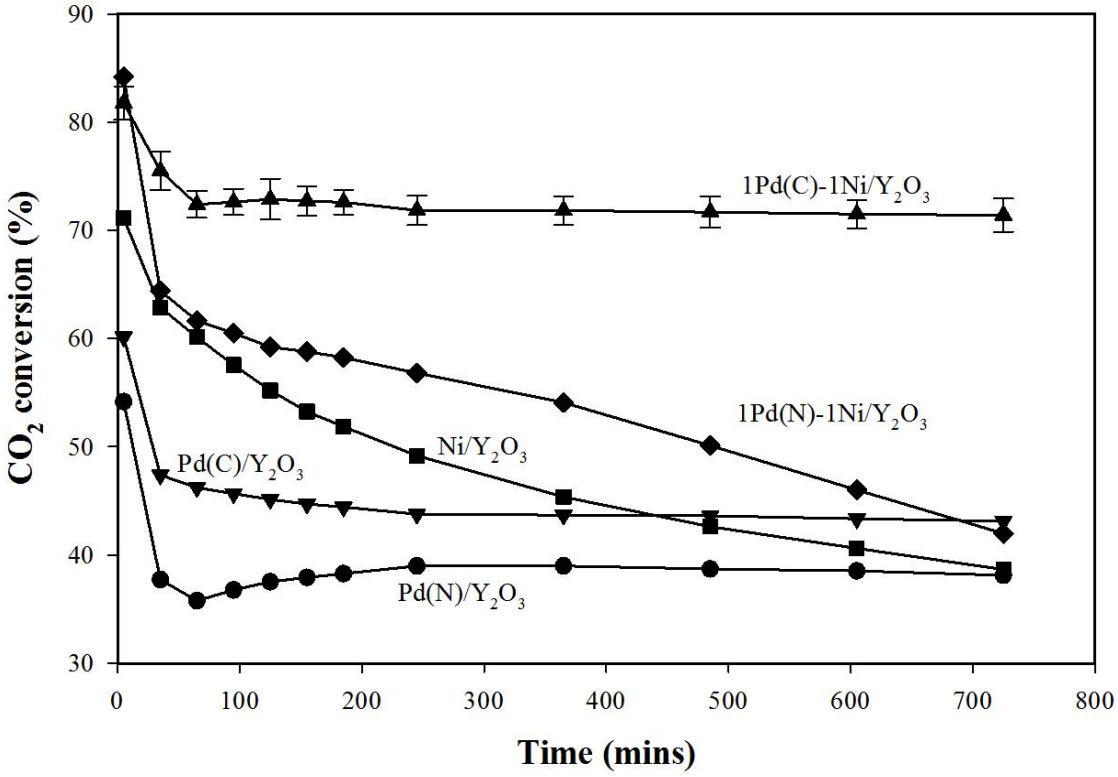

Figure 4-9 Effect of Pd precursors on catalyst stability (Reaction condition: P_{total} = 1 atm, T = 700ºC, $CH_4/CO_2/O_2$ = 5/4/1, GHSV = 24000 $cm^3/g/h$)

The 1Pd(C)−1Ni/Y_2O_3 catalyst also shows stable performance with time on stream while the 1Pd(N)−1Ni/Y_2O_3 catalyst shows decreasing trend in CH_4 and CO_2 conversion, indicates that the carbon formation rate on the 1Pd(C)−1Ni/Y_2O_3 catalyst is much lower than the one on the 1Pd(C)−1Ni/Y_2O_3 catalyst. The low carbon formation rate on the 1Pd(C)−1Ni/Y_2O_3 catalyst can be attributed to the small metal particle size of the 1Pd(C)−1Ni/Y_2O_3 catalyst. Christensen et al. [240] reported that carbon deposition rate strongly depended on metal particle size. The smaller metal particle size resulted in the lower carbon deposition rate. Therefore, the MSC formation between the Pd and Y_2O_3

support resulting in small metal particle size on the 1Pd(C)−1Ni/Y_2O_3 catalyst is crucial for the stability of the Pd(C)−Ni/Y_2O_3 catalyst.

Figure 4-10 shows the catalytic stability of the Pd−Ni/Y_2O_3 catalysts at various Pd/Ni ratios. It can be seen that the stability of the Pd(C)−Ni/Y_2O_3 catalysts is observed to increase with the increase of Pd content and reaches optimum at the Pd/Ni ratio of 1/1. It is also interesting to observe that the metal particle size of the Pd(C)−Ni/Y_2O_3 exactly follows the stability trend of Pd(C)−Ni/Y_2O_3 catalyst which increases with increase of Pd content and reaches optimum at the Pd/Ni ratio of 1/1. Therefore, it is concluded that the stronger interaction between Pd and Y_2O_3 support in the $Pd_xCl_yY_z$ compound resulting in smaller metal particle size on the 1Pd(C)−1Ni/Y_2O_3 catalyst is the main reason for higher stability of the 1Pd(C)−1Ni/Y_2O_3 catalyst during the course of OCRM reaction.

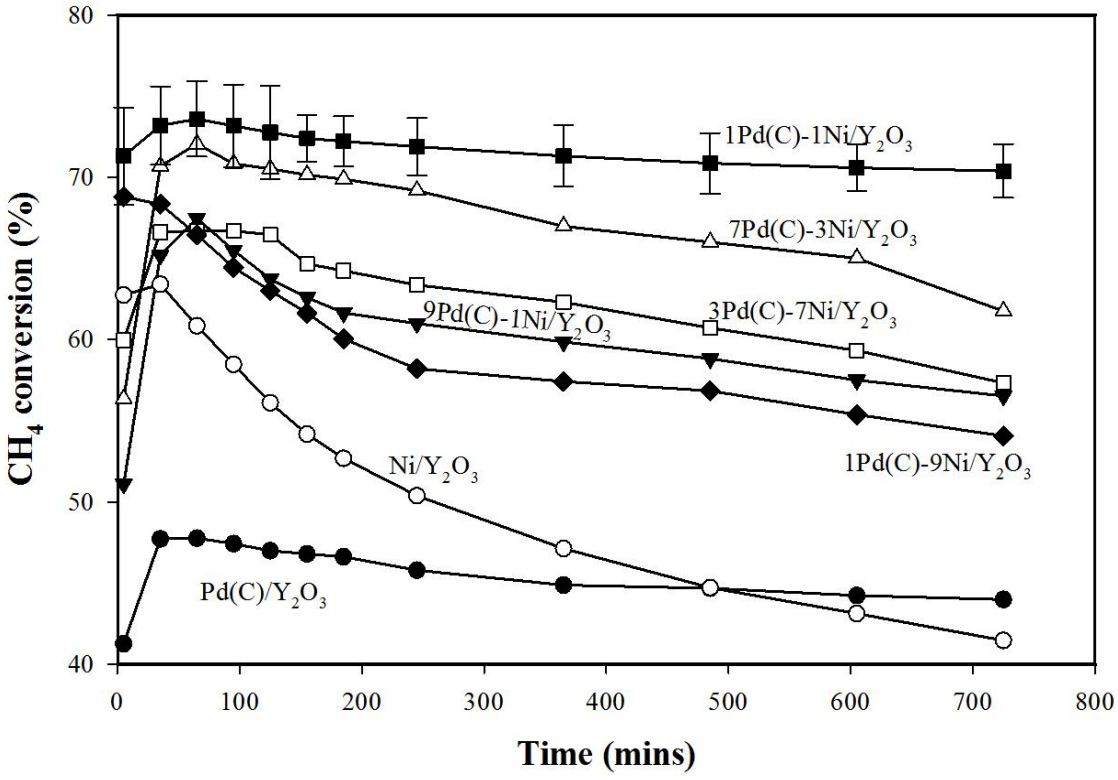

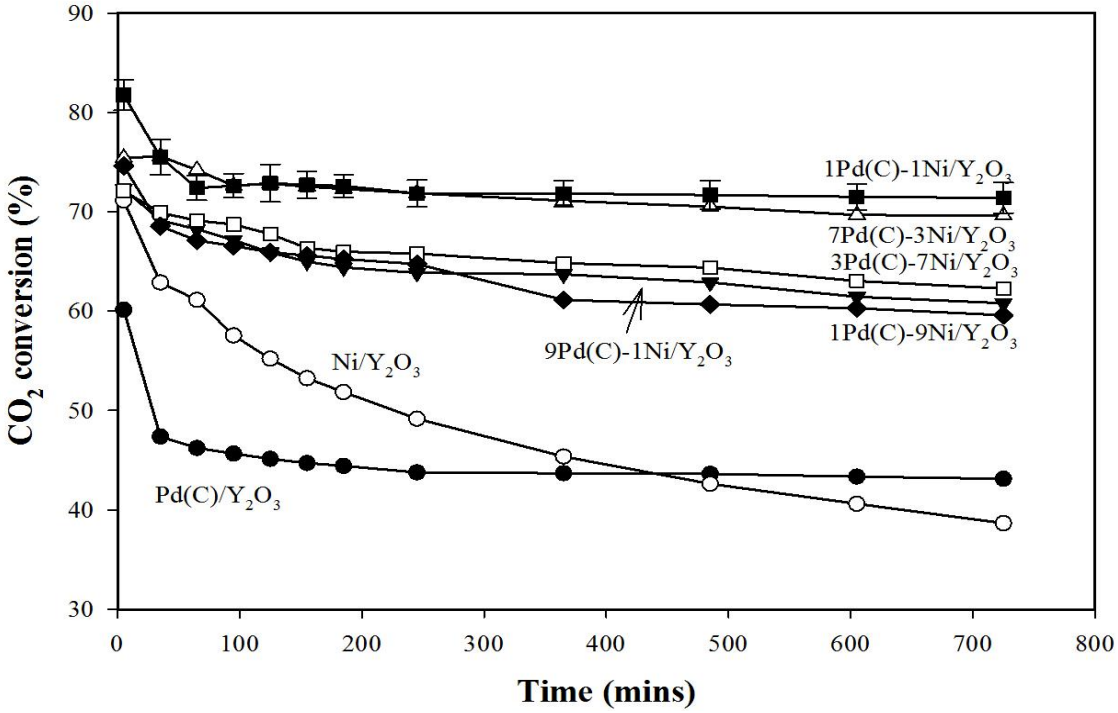

Figure 4-10 Stability study of Pd(C)−Ni/Y_2O_3 catalysts at various Pd/Ni ratio (Reaction condition: P_{total} = 1 atm, T = 700ºC, $CH_4/CO_2/O_2$ = 5/4/1, GHSV = 24000 $cm^3/g/h$)

4.3.11 Carbon formation

FESEM images in Figure 4-11 show that the Ni/Y_2O_3 catalyst produces abundant of carbon nanotubes which are graphitic carbon and difficult to be oxidized at low temperature. Although this type of carbon did not result in deactivation of the nickel surface, it blocked the reactor and caused catalyst destruction [241]. Similar to the spent Ni/Y_2O_3 catalyst, the carbon nanotubes are also observed on the spent $Pd(N)/Y_2O_3$ catalyst. However, carbon nanotubes are hardly observed on the spent $Pd(C)/Y_2O_3$ catalyst. Snoeck et al. [242] proposed the carbon nanotubes mechanism through surface reactions to produce adsorbed carbon atoms, diffusion through active metals, and formation of

filamentous carbon. The formation of carbon nanotubes caused the metal particles separate from the support. Since Ni particles on the Ni/Y_2O_3 catalyst have no interaction with Y_2O_3 support, the carbon nanotubes can easily grow on the Ni/Y_2O_3 catalyst. This phenomenon also occurs on the $Pd(N)/Y_2O_3$ catalyst which has no MSC formation between Pd and Y_2O_3 support. In contrast, it is more difficult to form carbon nanotubes on the $Pd(C)/Y_2O_3$ catalyst since the Pd on the $Pd(C)/Y_2O_3$ catalyst has strong interaction with Y_2O_3 support to form the $Pd_xCl_yY_z$ compound. Therefore, the carbon only covers the surface of the $Pd(C)/Y_2O_3$ catalyst. This carbon is easily oxidized in the presence of CO_2 in the feed as reported in our previous study.

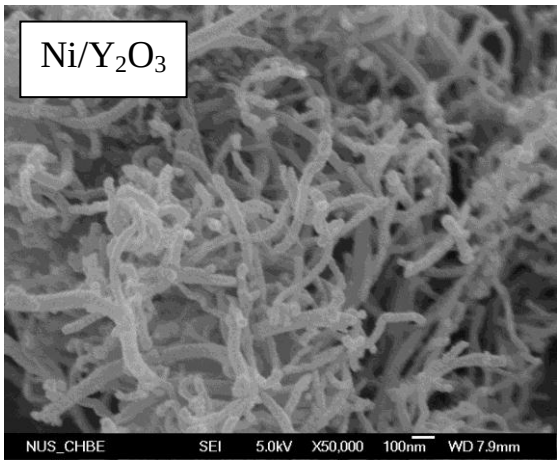

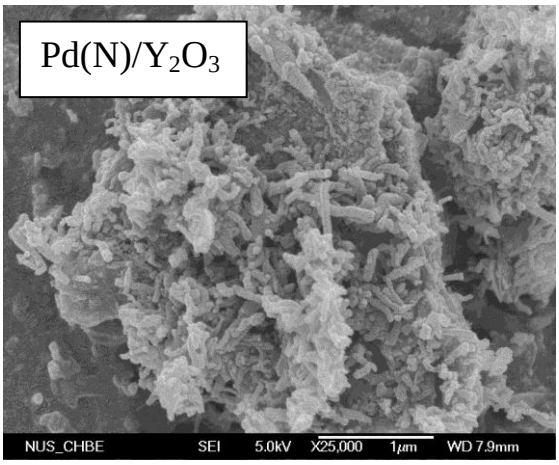

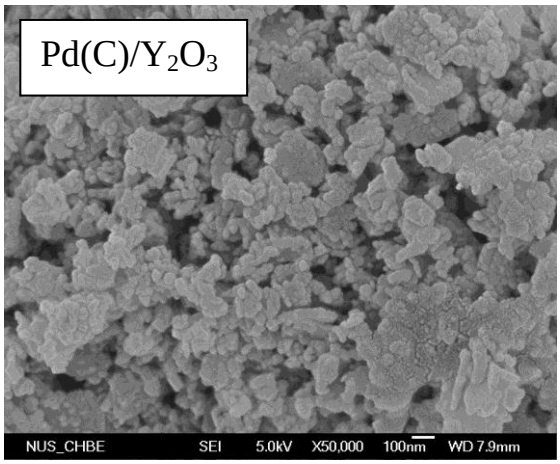

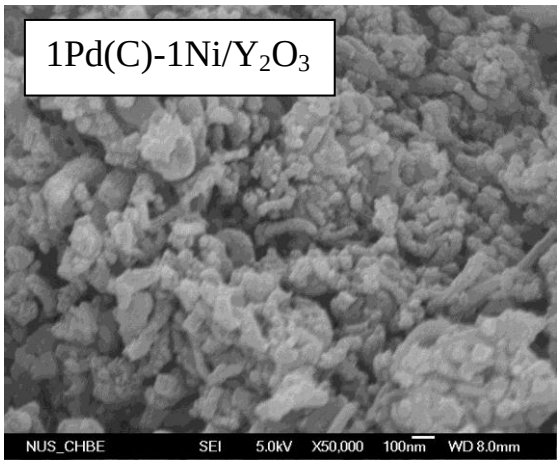

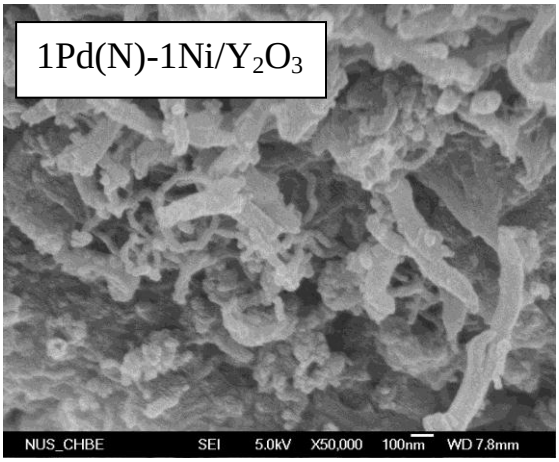

Figure 4-11 FESEM images of spent Pd−Ni/Y_2O_3 catalysts (Reaction condition: P_{total} = 1 atm, T = 700ºC, $CH_4/CO_2/O_2$ = 5/4/1, GHSV = 24000 $cm^3/g/h$)

The FESEM image of the 1Pd(N)−1Ni/Y_2O_3 catalyst shows more carbon nanotubes than the one of the 1Pd(C)−1Ni/Y_2O_3 catalyst. The XPS result of the 1Pd(N)−1Ni/Y_2O_3 catalyst shows interfacial interaction between Ni and Y_2O_3 support. This interaction is not so strong that carbon nanotubes are possible to grow on the 1Pd(N)−1Ni/Y_2O_3 catalyst. On the contrary, the XPS result of the 1Pd(C)−1Ni/Y_2O_3 catalyst show strong interaction between Pd and Y_2O_3 support in the $Pd_xCl_yY_z$ compound. This strong interaction between Pd and Y_2O_3 prevents growing of carbon nanotubes on the 1Pd(C)−1Ni/Y_2O_3 catalyst. Therefore, it is hardly to observe any carbon nanotubes on the spent 1Pd(C)−1Ni/Y_2O_3 catalyst.

The quantitative amount of carbon formation rate analyzed using TGA on the spent Ni/Y_2O_3, 1Pd(N)−1Ni/Y_2O_3, 1Pd(C)−1Ni/Y_2O_3, and Pd(C)/Y_2O_3 catalysts are shown in Figure 4-12a. It can be seen that the carbon formation rate follows order of Ni/Y_2O_3 > 1Pd(N)−1Ni/Y_2O_3 > 1Pd(C)−1Ni/Y_2O_3 > Pd(C)/Y_2O_3 catalysts. This order is the same as the order of catalyst stability (Ni/Y_2O_3 > 1Pd(N)−1Ni/Y_2O_3 > 1Pd(C)−1Ni/Y_2O_3 =

Pd(C)/Y_2O_3), showing high carbon deposition rate is the main reason of low stability on the Ni/Y_2O_3 and 1Pd(N)−1Ni/Y_2O_3 catalysts. It is also observed that the 1Pd(N)−1Ni/Y_2O_3 catalyst, which has big metal particles, produces more carbon than the 1Pd(C)−1Ni/Y_2O_3 catalyst, which has small metal particles, indicating that the metal particle size also affects the carbon formation rate..

Figure 4-12b shows the DTA profile of the spent Ni/Y_2O_3, 1Pd(N)−1Ni/Y_2O_3, 1Pd(C)−1Ni/Y_2O_3, and Pd(C)/Y_2O_3 catalysts. It can be observed that DTA peak of the spent Ni/Y_2O_3 catalyst is observed at around 550−650°C, which is characteristic of carbon nanotubes [243]. This peak is also observed on the spent 1Pd(N)−1Ni/Y_2O_3 catalyst. However, the peak of the spent 1Pd(C)−1Ni/Y_2O_3 catalyst appears at lower temperature around 450−650°C, indicating that the carbon formed on the 1Pd(C)−1Ni/Y_2O_3 catalyst is amorphous which is easier to oxidize.

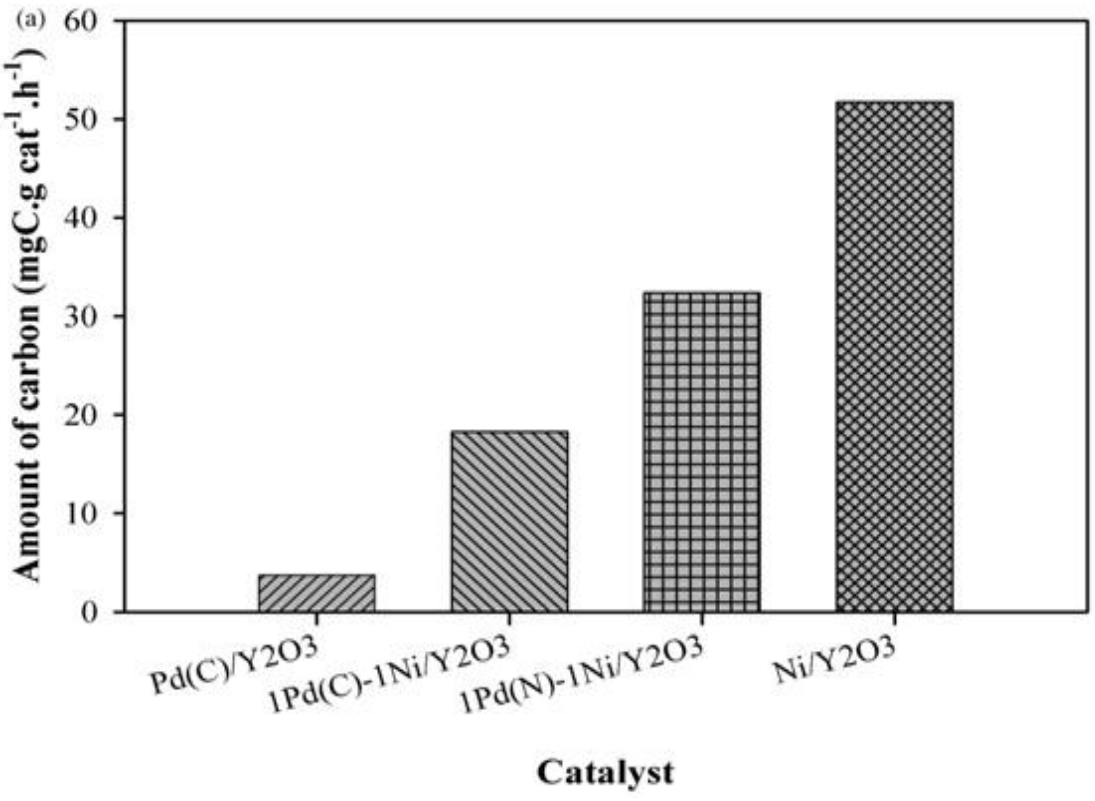

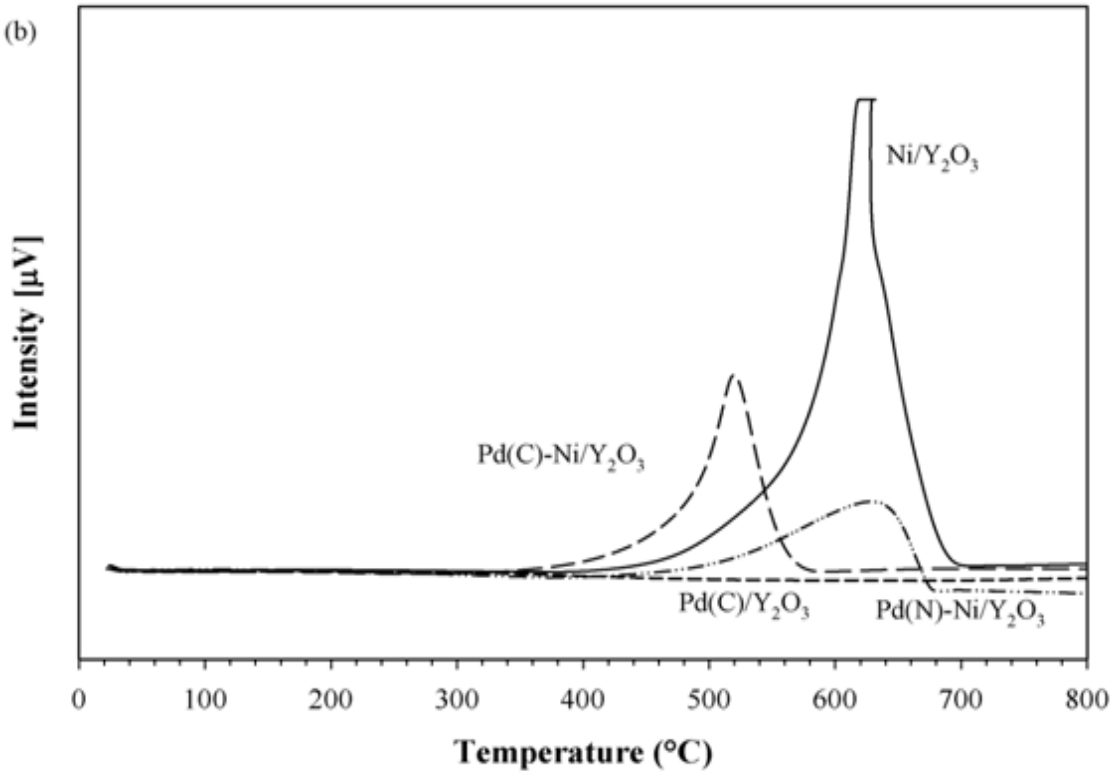

Figure 4-12 (a) Carbon formation rate and (b) DTA profiles of spent Pd−Ni/Y_2O_3 catalysts from different Pd precursors (Reaction condition: P_{total} = 1 atm, T = 700°C, $CH_4/CO_2/O_2$ = 5/4/1, GHSV = 24000 $cm^3/g/h$)

4.3.12 Proposed formation mechanism of bimetallic particles on Pd−Ni/Y_2O_3 catalysts

Based on all characterization results, the formation mechanism of bimetallic Pd-Ni particles on 1Pd(N)−1Ni/Y_2O_3 and 1Pd(C)−1Ni/Y_2O_3 catalysts are proposed in Figure 4-13. The TPR result of 1Pd(N)−1Ni/Y_2O_3 catalyst shows that all PdO particles are fully reduced at 200°C and start to agglomerate. Further increasing temperature to 450°C, NiO particles are fully reduced and move near Pd to form bimetallic Pd-Ni particles since Pd has interaction with Ni. For Pd−Ni system, most of previous reports in the literature

proposed the formation of Pd−Ni alloy [204−213]. Modeling studies of Pd−Ni system [244−245] showed Pd is segregated on the surface of Ni, due to the fact that Pd has a lower surface tension and larger atomic radius than Ni, resulting in expulsion of the Pd metal from bulk and its segregation to the surface. Since there is no MSC formation between Pd and Y_2O_3 support on the 1Pd(N)−1Ni/Y_2O_3 catalyst, it is more likely to find segregation of Pd on the 1Pd(N)−1Ni/Y_2O_3 catalyst surface, similar to the results from modeling studies. The FTIR result of the 1Pd(N)−1Ni/Y_2O_3 catalyst also confirms that the catalyst surface contains more Pd than Ni atoms. In addition, since the XPS results of the 1Pd(N)−1Ni/Y_2O_3 catalyst show that the Ni particles have some interfacial interaction with Y_2O_3 support, the Ni particle is proposed to have contact with Y_2O_3 support.

The formation mechanism of bimetallic Pd-Ni particles on 1Pd(N)−1Ni/Y_2O_3 catalyst is different from the one on the 1Pd(N)−1Ni/Y_2O_3 catalyst. TPR result of 1Pd(N)−1Ni/Y_2O_3 catalyst shows no reduction of PdO is observed at 200°C, but all NiO particles are fully reduced at 450°C and start to move near Pd. Further increasing temperature to 700°C, some of strongly Pd particles interacted with Y_2O_3 are reduced and form bimetallic Pd-Ni particles. Due to the formation of MSC between Pd and Y_2O_3 support on the 1Pd(C)−1Ni/Y_2O_3 catalyst, it is more difficult for Pd atoms to segregate to the surface. The FTIR result of the 1Pd(C)−1Ni/Y_2O_3 catalyst also shows that besides Pd atoms, it is also possible to find Ni atoms on the catalyst surface. Therefore, the catalyst surface of the 1Pd(C)−1Ni/Y_2O_3 catalyst contains more Ni than Pd atoms. The interaction between Pd and the Y_2O_3 support in the $Pd_xCl_yY_z$ compound on the 1Pd(C)−1Ni/Y_2O_3 catalyst is stronger than the one on the Pd(C)/Y_2O_3 catalyst shows that the Pd atoms have even more contact with the Y_2O_3 support on the 1Pd(C)−1Ni/Y_2O_3 catalyst. Therefore, the

Pd surface is proposed to flatten on the 1Pd(C)−1Ni/Y_2O_3 catalyst. The similar structures were reported by Tomishige on Pt−Ni alloy [246] and Pd-Ni alloy [247].

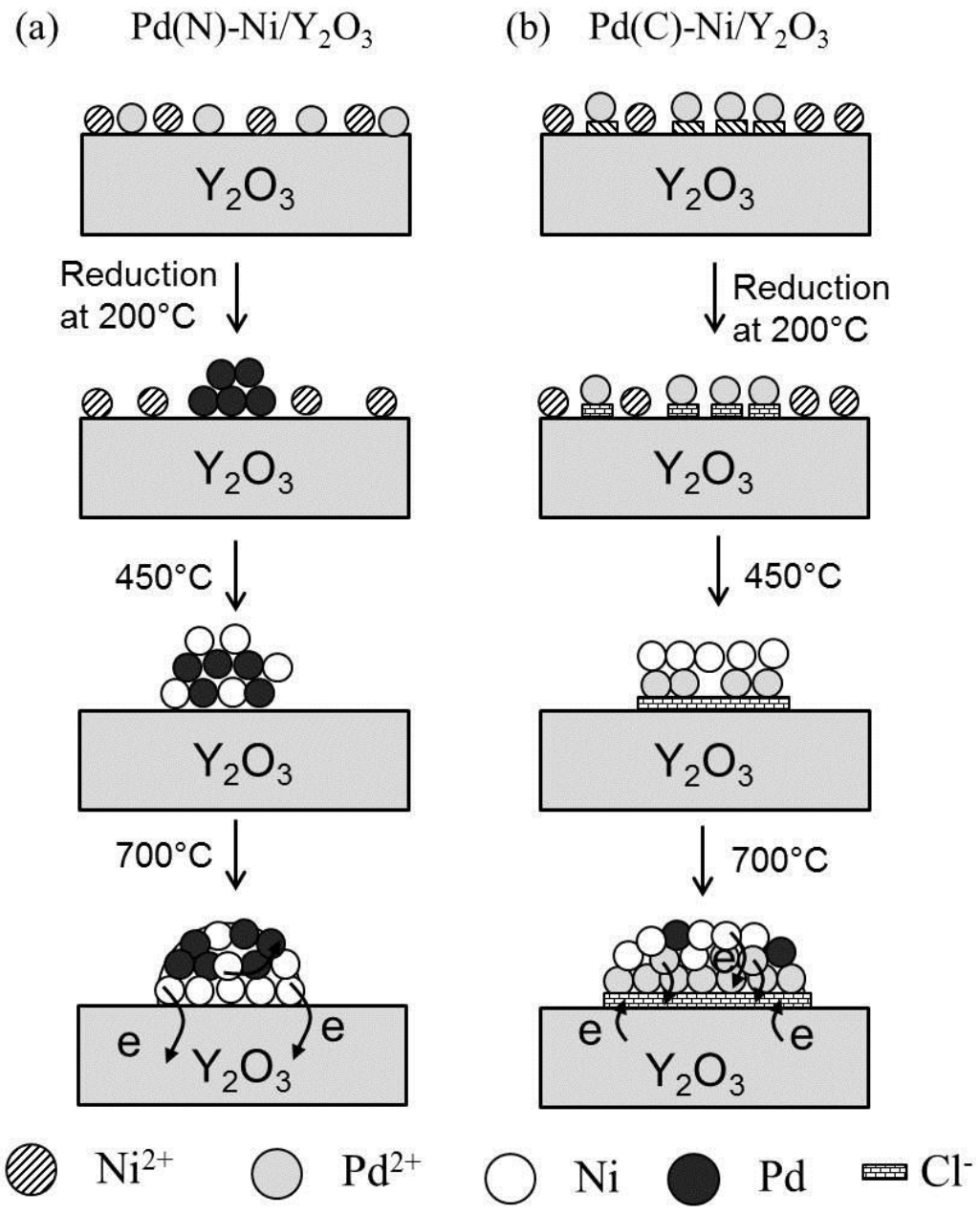

Figure 4-13 Proposed formation of (a) Pd−rich Pd−Ni alloy on Pd(N)−Ni/Y_2O_3 catalyst and (b) Ni−rich Pd−Ni alloy on Pd(C)−Ni/Y_2O_3 catalyst

4.4 Conclusions

The Pd precursors are found to have significant effect on catalytic performance of Pd−Ni/Y_2O_3 catalyst. The 1Pd(C)−1Ni/Y_2O_3 catalyst shows higher activity and stability than the 1Pd(N)−1Ni/Y_2O_3 catalyst due to small metal particle size resulted from the presence of Pd−Y_2O_3 compound on the 1Pd(C)−1Ni/Y_2O_3 catalyst. Further investigation using various Pd/Ni ratios shows that smaller metal particle size has positive effect on catalytic activity of Pd−Ni/Y_2O_3 catalyst. Besides small metal particle size, the presence of bimetallic particles, as indicated from XPS results, also plays an important role in catalytic activity. Moreover, the interaction between Pd and Y_2O_3 support in the $Pd_xCl_yY_z$ compound is also found to be stronger with increasing Pd content and reach an optimum at Pd/Ni ratio of 1/1, showing that the formation of metal−support compound between Pd and Y_2O_3 support plays an important role in catalyst stability.

CHAPTER 5

Role of Surface Oxygen Mobility on Catalytic Activity of Pd−Ni catalyst over Spherical Nanostructured Y_2O_3 support

This chapter describes role of surface oxygen mobility of synthesized Y_2O_3 on catalytic activity of Pd−Ni/Y_2O_3 catalyst. Different sizes of monodisperse spherical Y_2O_3 particles were synthesized using homogeneous precipitation method at various pH of the solution. The synthesized Y_2O_3 particles were then used as the support of Pd−Ni catalysts for oxy-CO_2 reforming of methane reaction. The FESEM results show that particle size of Y_2O_3 particles decreases with decreasing pH of precursor solution from Y5 to Y3. In addition, the crystal size of Y_2O_3 particles calculated from the XRD results also decreases from Y5 to Y3. The TPR results of Y_2O_3 particles show that the intensity of reduction peaks increases from Y5 to Y3 while the position of those peaks shifts to lower temperature from Y5 to Y3, suggesting that the surface oxygen mobility of Y_2O_3 particles increases from Y5 to Y3 due to decrease in crystal size of Y_2O_3 particles. All Pd−Ni/Y_2O_3 catalysts have small metal size (±7nm) due to formation of Pd-Y_2O_3 compound as also observed from TPR and XPS results. Catalytic activity results show that CH_4 and CO_2 conversions as well as H_2 and CO production rates increase from Pd−Ni/Y5 catalyst to Pd−Ni/Y3 catalyst. In contrast, the H_2/CO ratio and carbon deposition rate decreases from Pd−Ni/Y5 catalyst to Pd−Ni/Y3 catalyst. These results show that the highest surface oxygen mobility on Pd−Ni/Y3 catalyst plays important roles in high catalytic activity and suppression of carbon deposition on Pd−Ni/Y3 catalyst in oxy-CO_2 reforming of methane reaction.

5.1 Introduction

The ever-increasing amount of CO_2 has promoted a great interest in CO_2 utilization from academic and industrial researchers. Catalytic CO_2 (dry) reforming of methane (DRM) is an attractive technology to utilize CO_2 and CH_4, the two major greenhouse effect and cheapest carbon-containing gases [240], to produce syngas. . The syngas produced from the reaction is preferable for hydroformylation and carbonylation reactions as it yields lower H_2/CO product ratio while high H_2/CO ratio favors methanation and suppresses chain growth [12].

Catalysts made from noble metals, such as Rh, Ru, Pt, Pd, Ir [238], and non-noble metals such as Ni [236−235] and Co [245] have been extensively investigated for the DRM reaction. Noble metal catalysts generally show higher activity and lower carbon deposition rate than non-noble metal catalysts. The carbon deposition rate decreased in the following order: Ni >> Rh > Ir = Ru > Pt = Pd at 773 K and Ni > Pd = Rh > Ir > Pt >> Ru at 923 K [15]. However, due to the high cost of noble metals, non-noble metals catalyst, especially Ni catalyst, is preferred. Even though Ni catalyst has been modified to improve the activity and coke resistance, the energy requirement of the DRM reaction is very high due to its endothermic nature. The high energy requirement results in high cost and currently seems to hinder the commercialization of the DRM reaction in industries.

To overcome this drawback, it is desirable to introduce exothermic reaction such as partial oxidation of methane (POM). The combination reaction between DRM and POM reaction, named as oxy-CO_2 reforming of methane (OCRM), can reduce the amount of carbon deposition as the oxygen not only can easily oxidize the deposited carbon on the

catalyst, but also can minimize the total energy requirement since it combines both the exothermic (POM) and endothermic (DRM) reactions.

Our previous study on effect of catalyst support over PdNi catalysts showed that catalyst support has profound effect on the catalyst performance. The Pd−Ni/Y_2O_3 catalyst showed the highest activity and the lowest carbon deposition rate compared to the other catalysts due to the formation of metal-support compound resulting in small metal particle size, the presence of surface β-oxygen species promoting the cracking of C−H bond in CH_4 and the ability of Y_2O_3 to form oxycarbonate species to oxidize the surface carbon on the Pd−Ni/Y_2O_3 catalyst. However, the study used commercial metal oxides which had irregular shape.

It is well known that the structure and crystal size of catalyst support plays an important role in the activity and stability of catalyst. For instance, Sun et al [249] found that Y_2O_3 synthesized at different pH had different morphologies and crystal sizes. The smaller crystal size of Y_2O_3 had higher surface oxygen mobility, and hence enhanced the activity of nickel catalyst in oxidative steam reforming of ethanol reaction. However, since the synthesized Y_2O_3 had different morphology, the conclusion was unclear. In order to elucidate the effect of crystal size on the surface oxygen mobility, the synthesized Y_2O_3 should have similar morphology.

In the present study, Y_2O_3 support was synthesized to obtain monodisperse spherical particles. It was then used as the support of Pd−Ni catalysts for the OCRM reaction. The influence of Y_2O_3 crystal size on surface oxygen mobility is investigated. The role of surface oxygen mobility on catalytic performance of Pd−Ni/Y_2O_3 catalyst is then examined for the OCRM reaction.

5.2 Experimental

5.2.1 Support synthesis and catalyst preparation

Y_2O_3 particles were synthesized using homogeneous precipitation method under different pH solution. Typically, 0.02M yttrium nitrate solution and 1M urea solution were used as the precursors. Those solutions were prepared by dissolving either $Y(NO_3)_3.6H_2O$ (Sigma-Aldrich) or $CO(NH_2)_2$ (Sigma-Aldrich) with deionised water in 250 mL volumetric flask. The two prepared solutions were mixed and filtered through a filter paper. The pH of the mixed solution was varied with either 0.1M HNO_3 solution or 0.1M NH_3 solution. The mixed solution was then placed in an isothermal bath, stirred, and heated at 95°C for 1 h. It was then cooled down to room temperature prior to centrifugation to separate the precipitates. The precipitates were thoroughly washed with ethanol, dried at 100°C overnight, and calcined at 800°C for 4 h. The Y_2O_3 samples synthesized at pH3, pH4, and pH5 are designated as Y3, Y4, and Y5, respectively.

Pd−Ni catalysts were synthesized by co-impregnation method over the synthesized Y_2O_3 with nominal total loading of 5 wt-% and Pd/Ni mole ratio of 1/1. Typically, the nickel solution was prepared by dissolving the nickel (II) nitrate hexahydrate (Strem Chemicals) with deionised water while the palladium solution was prepared by dissolving palladium (II) chloride (Strem Chemicals) with 2M hydrochloric acid. The prepared solutions were mixed in a crucible and stirred with the aid of stirrer. The synthesized Y_2O_3 was then added into the crucible. The solution was heated at 80°C until it dried, followed by drying at 100°C for 12 h and calcination at 800°C for 4 h. The resultant catalysts are designated as Pd−Ni/Y3, Pd−Ni/Y4, and Pd−Ni/Y5, respectively.

5.2.2 Support and catalyst characterization methods

5.2.2.1 Specific surface area measurement

The specific surface area of all supports and catalysts was measured by adsorption and desorption of N_2 at −196°C on the Autosorb-1. Prior to the surface area measurement, 0.05g of sample was pelletized and outgassed at 250°C for 24 h. The specific surface area of sample was determined from the linear portion of BET plot.

5.2.2.2 X-ray diffraction

X-ray diffraction pattern of all supports and catalysts was measured on a Shimadzu XRD-6000 diffractometer using Cu Kα radiation. Powder sample was placed on an aluminium slide and scanned from 2θ of 10^o to 80^o with ramp rate of 2^o/min. The beam voltage and current were 40 kV and 30 mA, respectively.

5.2.2.3 FESEM

The morphology of all supports was visually observed using a field emission scanning electron microscope (FESEM: JEOL JSM-6700F). Prior to the test, the sample was coated with Pt using Pt-sputtering at 20 mA for 60 seconds.

5.2.2.4 X-ray photoelectron spectroscopy test

X-ray photoelectron spectroscopy was performed on Kratos AXIS Ultra DLD using concentric hemispherical analyzer. The Al Kα gun with photon energy of 1486.6eV was used as the X-ray source. The wide scans were performed using 80eV pass energy while the narrow scans were performed with 40 eV pass energy. Prior to the analysis, the

sample was reduced under pure H_2 at 600°C for 1 h, which was same as the reduction condition during reaction. The sample was mounted on the standard sample stubs using double-sided adhesive tapes. The core level signals were obtained at a photoelectron takeoff angle (R, measured with respect to the sample surface) of 90°. The X-ray source was run at a reduced power of 150 W (15 kV and 10 mA). The pressure in the analysis chamber was maintained at 10^{-8} Torr or lower during each measurement. All binding energies were referenced to the C 1s hydrocarbon peak at 284.5 eV.

5.2.2.5 TPR and TPD measurements

Temperature-programmed reduction (TPR) measurement for fresh supports and catalysts was performed on Quantachrome Chembet-3000 equipped with a thermal conductivity detector (TCD). Prior to the TPR measurement, 0.05 g sample was outgassed at 250^{o}C under N_2 for 1 h to remove any impurities and then cooled down to room temperature. 5%H_2/He gas was then introduced to the sample while the temperature of furnace was increased from room temperature to 1000^{o}C at a heating rate of 10K/min. The signal of output gas against the furnace temperature was continuously monitored using the TCD and recorded by a computer.

Temperature-programmed desorption of oxygen (TPD−O_2) for fresh catalysts was also performed on Quantachrome Chembet-3000. Prior to the TPD-O_2 measurement, 0.1 g of sample was outgassed under He for 1 h at 300^{o}C to remove any impurities. Purified O_2 gas was then introduced for 1 h, followed by cooling down to room temperature. Purified He gas was then introduced to the system to purge out all the remaining oxygen in the

system. The TPD−O_2 measurement was started from room temperature to maximum furnace temperature of 1000°C under a heating rate of 10K/min.

5.2.2.6 TEM

The metal particle size of Pd−Ni catalysts was measured visually using HRTEM system JEOL JEM−2100F. The average size is then calculated over 50 particles. Prior to the observation, the catalyst was initially reduced at 600˚C by pure H_2 for 60 min. The catalyst was then ultrasonically dispersed in ethanol and spread over perforated copper grids.

5.2.3 Catalytic reaction

Catalytic reaction was performed in a fixed bed quartz reactor with inner diameter 4 mm and length 400 mm. 0.05 g of catalyst was used in each test and held by quartz wool in the middle of the reactor. The temperature of the catalyst bed was controlled and monitored by a thermocouple that was in contact with the top layer of the catalyst bed. Prior to the catalytic test, the catalyst was reduced under H_2 at 600^{o}C for 1 hour, followed by purging under He while the temperature was increased to the reaction temperature. The feed consisting of $CH_4/CO_2/O_2$ with a molar ratio of 5/4/1 was then introduced to the reactor at flowrate of 20 mL/min. All the gases used here were research grade (99.95% CH_4, 99.99% CO_2, 99.8% O_2, and 99.9995% He). A cold trap filled by 50% glycerol and 50% water with a temperature of −10^{o}C was installed between the reactor exit and the GC sampling valve to condense any moisture. The gas product was analyzed using a gas chromatograph (HP 6890) equipped with a Hayesep D column and a TCD detector. The

chromatogram showed peak areas for all reacted gases which were then converted to volume-% through a calibration curve. The total flow rate of the product gases was measured using bubble flow meter The conversions of CH_4 and CO_2 were calculated using the following formula:

$$X_{CH_4}(\%) = \frac{n_{CH_4,in} - n_{CH_4,out}}{n_{CH_4,in}} x\,100$$

$$X_{CO_2}(\%) = \frac{n_{CO_2,in} - n_{CO_2,out}}{n_{CO_2,in}} x\,100$$

where *n* is molar flow rate of each gas.

The total amount of deposited carbon on the spent catalysts was measured using thermogravimetric analysis (TGA) on a Shimadzu DTG−60 thermogravimetric analyzer. Around 10 mg of spent catalyst was used in each TGA experiment and heated in air to 800ºC with a heating rate of 10K/min.

5.3 Results and discussion

5.3.1 Characterizations of Y_2O_3 supports

Figure 5-1 shows the morphology of Y_2O_3 particles synthesized at pH 3, 4, and 5. It can be seen that all Y_2O_3 particles have monodisperse spherical shape. It has been reported in literature that Y_2O_3 particles has various shapes such as spherical particle [250−251], rod or wire [252−254], tube and needle [252], belt [253], prism and nanosheet [249−252] depending on the preparation method. From an engineering point of view, spherical particle with narrow size distribution is preferred for obtaining good fluidization [255] in fluidization reactor for the OCRM reaction [256−257]. The formation of monodispersed spherical Y_2O_3 particles is due to slow decomposition of urea to produce

ammonium and carbonate ions. The slow introduction of carbonate ions or other ligands, such as OH^- or SO_4^{2-}, into the system until the solubility is exceed is the basic principle for homogeneous precipitation of cations throughout the volume. Once the ligand is introduced uniformly throughout the volume, the formation of particles then occurs simultaneously at all points in the system [250]. Sohn et al. [251] suggested the mechanism for formation of monodisperse Y_2O_3 particles through a reaction between yttrium ion (Y^{3+}) and OH^- or CO_3^{2-} from urea dissociation to form $Y(OH)CO_3 \cdot 1.5\ H_2O$ according to the following reactions:

Urea Decomposition:

$$(NH_2)_2CO \leftrightarrow NH_4^+ + OCN^-$$

$$OCN^- + 2H_2O \leftrightarrow CO_3^{2-} + NH_4^+$$

$$CO_3^{2-} + 2H_2O \leftrightarrow 2\ H_2CO_3 + 2OH^-$$

Precipitation:

$$Y^{3+} + OH^- + CO_3^{2-} + 1.5\ H_2O \rightarrow Y(OH)CO_3 \cdot 1.5\ H_2O$$

The $Y(OH)CO_3 \cdot 1.5\ H_2O$ compound undergoes chemical change to Y_2O_3 particle through calcination at 800°C.

In addition, synthesis of monodispersed spherical Y_2O_3 particles was performed only at pH 3, 4, and 5 since below pH 3, severe agglomeration among particles was observed. Since the highest pH of solution during precipitation via decomposition of urea was 5.5, it therefore took very long time to reach pH 6 [251]. Above pH 7.0, the yttrium ions (Y^{3+}) precipitates with OH^- anion in the form of $Y(OH)_3$ with reaction constant $K=[Y^{3+}][OH^-]^3=6.0 \times 10^{-24}$ at 25°C [258]. The $Y(OH)_3$ compound then undergoes chemical change to Y_2O_3 particle through calcinations at high temperature.

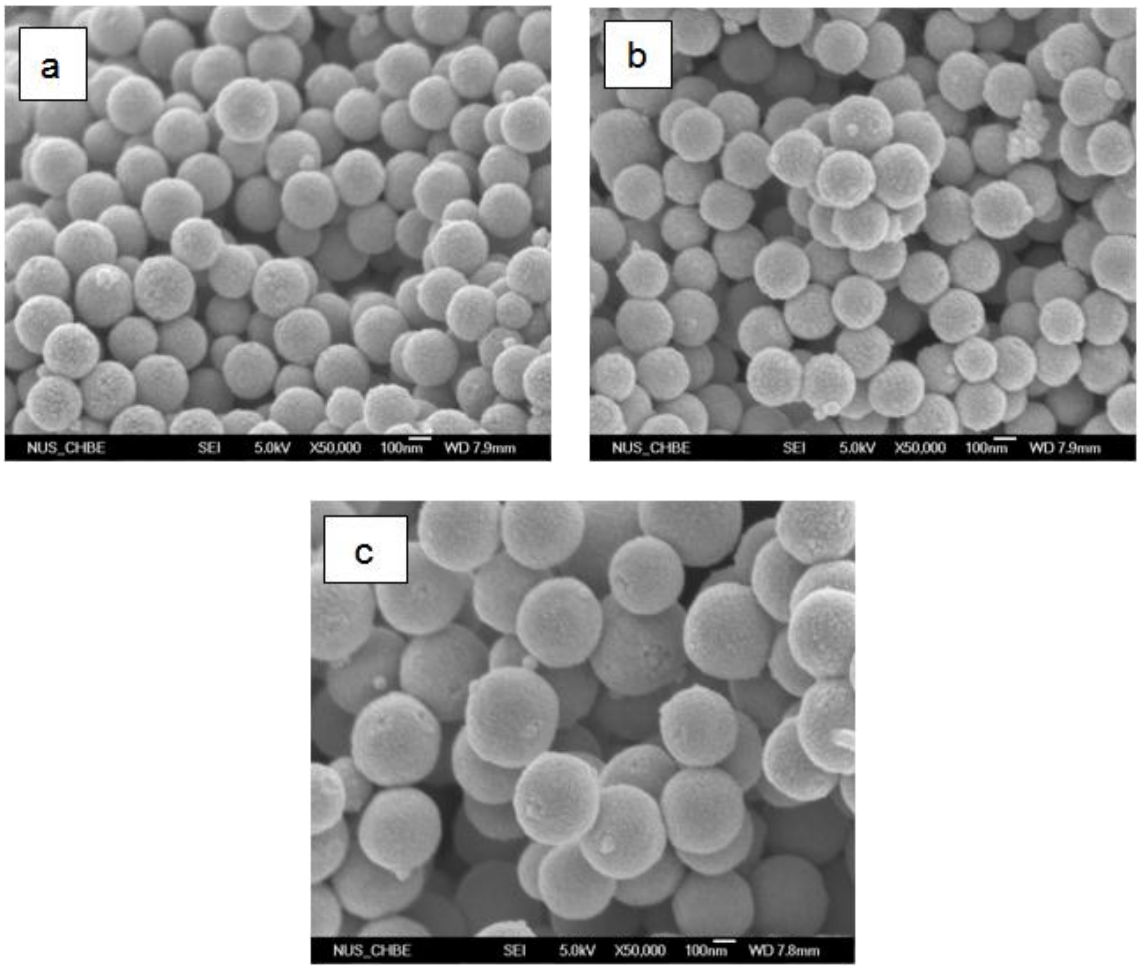

Figure 5-1 FESEM images of Y_2O_3 synthesized at pH of: a) 3; b) 4; and c) 5

Table 5-1 tabulates the average particle size of the synthesized Y_2O_3 measured over 50 particles. It shows that the size of Y_2O_3 particles decrease with decreasing pH of solution from Y5 to Y3, since the OH^- ion from urea decomposition was consumed by the HNO_3 during the pH adjustment in synthesis process, leading to lesser amount of OH^- ion at lower pH solution, hence it forms smaller particles. Table 1 also shows that the surface area of the synthesized Y_2O_3 particles decreases from Y3 to Y5 due to increase in particles size from Y3 to Y5.

Table 5-1 Physical properties of Y_2O_3 synthesized at various pH

Sample	Synthesis pH	S_{BET} (m^2/g)	Particle size[a] (nm)	Crystal size[b] (nm)	H_2 consumption [c] (μmole H_2/g)	H_2 consumption/ S_{BET} (μmole H_2/m^2)
Y3	3	12	231 ± 17	30	124.3	10.3
Y4	4	11	253 ± 20	32	89.8	8.2
Y5	5	10	369 ± 33	34	73.8	7.4

[a] measured over 50 particles using FESEM

[b] calculated using Debye – Scherrer formula

[c] calculated based on integration of H_2-TPR profile up to 1000°C

Figure 5-2 shows the XRD patterns of the synthesized Y_2O_3 crystal structures. It is observed that all the synthesized Y_2O_3 particles exhibit identical patterns with commercial Y_2O_3. Moreover, the diffraction peaks of (211), (222), (400), (440) and (622) are clearly distinguishable and all of them can be indexed to a pure cubic phase of Y_2O_3 crystal structure according to PDF card 00-005-0574. The crystal sizes of the synthesized Y_2O_3 particles calculated using the Debye-Scherrer formula (Table 5-1) slightly increases from Y3 to Y5, indicating that during the growth of spherical Y_2O_3 particles, the crystal of Y_2O_3 also grows bigger. These results show that all Y_2O_3 particles consist of same crystal, but different in the crystal size.

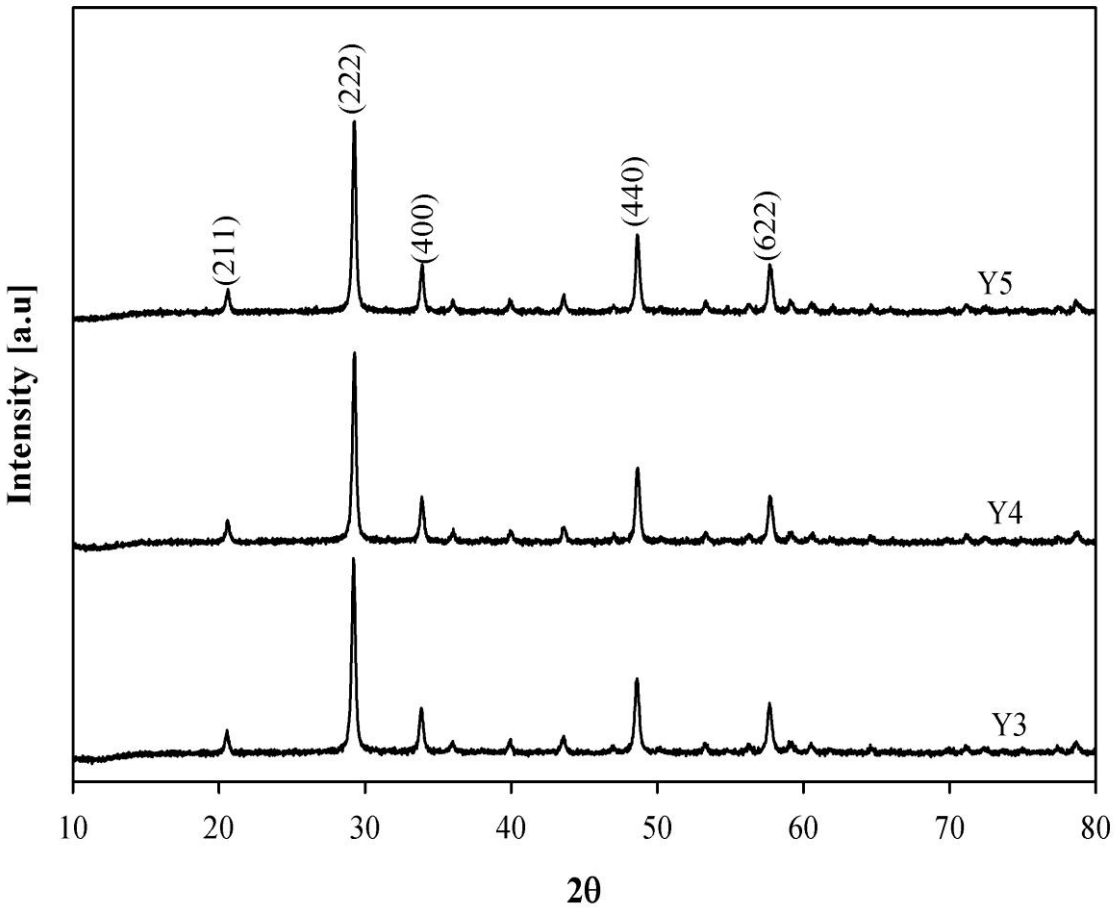

Figure 5-2 XRD pattern of Y_2O_3 supports synthesized at various pH

Figure 5-3 shows the H_2-TPR of synthesized Y_2O_3. It can be seen that all the synthesized Y_2O_3 particles show three peaks from 300°C to 800°C. The intensity of these peaks increases from Y5 to Y3, while the position of the peaks is observed to shift to lower temperature from Y5 to Y3. It was reported that the theoretical H_2 consumption for complete reduction of Y_2O_3 is 13.3mmole/g [249]. However, the calculated hydrogen consumptions tabulated in Table 5-1 are equivalent to only less than 1% of the total reduction of Y_2O_3, showing that only a partial amount of synthesized Y_2O_3 can be reduced during the reduction process. This result indicates that the H_2 molecules might

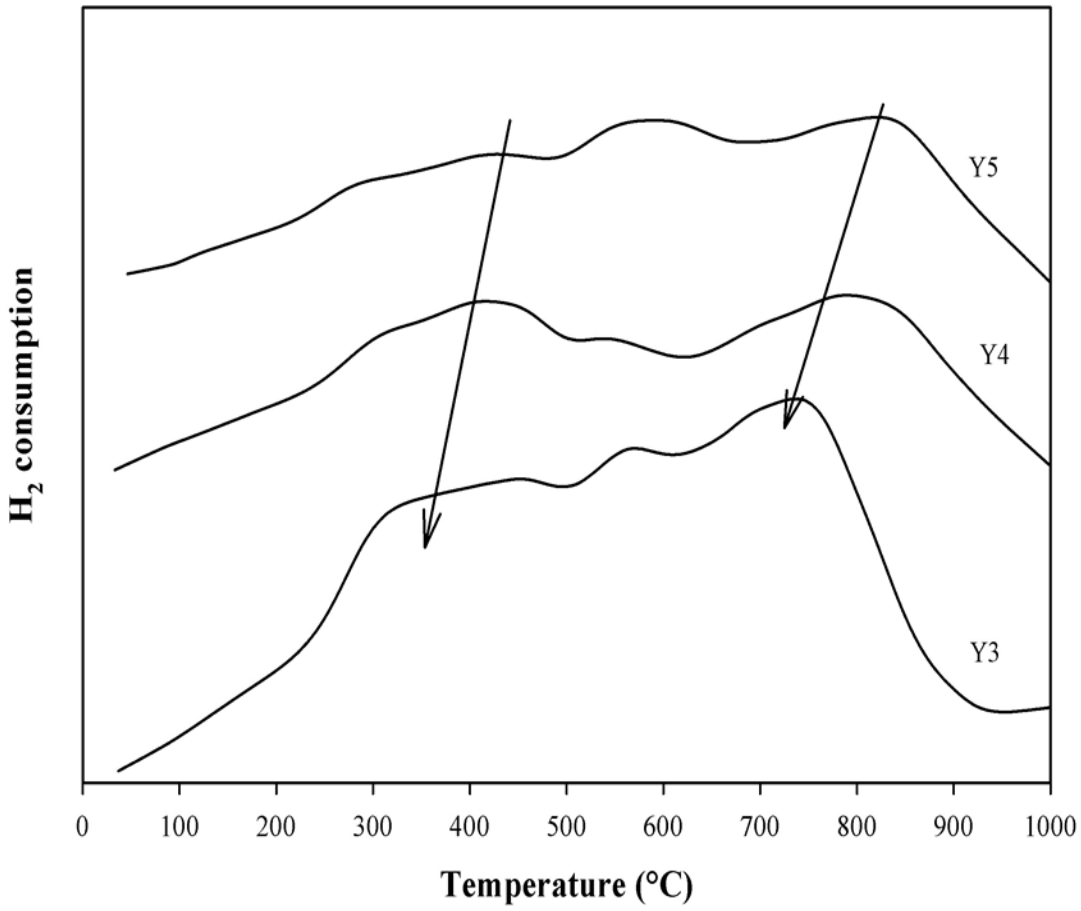

Figure 5-3 TPR profiles of synthesized Y_2O_3 supports

have consumed only the oxygen species located on the surface and/or subsurface of the synthesized Y_2O_3 [227, 259]. Therefore, the position and intensity of the H_2 consumption peaks can be utilized as an indicator of the surface oxygen mobility on Y_2O_3. The relationship between the position of H_2 consumption peak and the surface oxygen mobility species has been reported for CeO_2, ZrO_2, and Y_2O_3 [249, 259−261]. Based on the position and H_2 consumption per BET surface area, the order of the surface oxygen mobility on the synthesized Y_2O_3 supports is Y3 > Y4 > Y5. The highest surface oxygen

mobility in Y3 can be attributed to the smallest crystal size of Y3 since the smallest crystal has the highest surface energy, resulting in reduction in a larger amount of surface oxygen species [249]. Furthermore, Mamontov et al. [262-263] found that the interstitial oxygen was the active ions contributing to oxygen mobility. The concentration of the interstitial oxygen is significantly affected by the amount of crystalline defects. Therefore, since Y3 has the smallest crystal size, it should have the highest amount of crystalline defects, and hence the highest amount of oxygen species. The highest surface oxygen mobility in Y3 also shows that Y3 has the highest oxidizing ability [262-263]. The surface oxygen mobility is later shown to play an important role in increasing catalytic activity and suppression of carbon formation rate.

5.3.2 Characterizations of Pd−Ni/Y_2O_3 catalysts

The BET results (Table 5-2) of Pd−Ni catalysts over synthesized Y_2O_3 supports show that the surface area of Pd−Ni/Y5 is the lowest among the other Pd−Ni catalysts as Y5 has the lowest surface area. In addition, Figure 5-4 and Table 5-2, respectively shows the TEM images of reduced Pd−Ni/Y_2O_3 catalyst and metal particle size measurement of Pd−Ni/Y_2O_3 catalyst. It can be seen that the metal particle size for all reduced Pd−Ni/Y_2O_3 catalysts measured using high resolution TEM is quite constant around 7nm. This result shows that metal particle size is not affected by the surface area and crystal size of the supports.

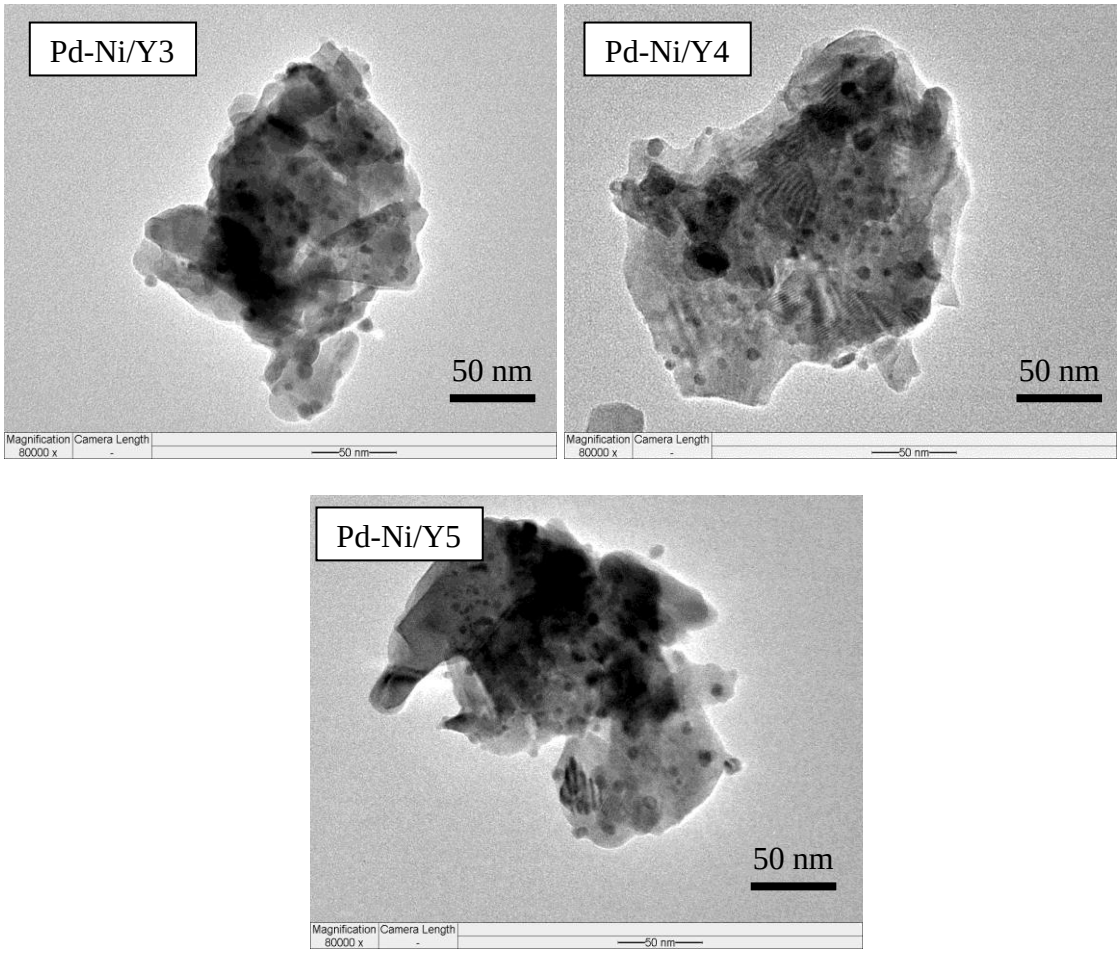

Figure 5-4 TEM images of reduced Pd−Ni/Y_2O_3 catalysts

Table 5-2 Physical properties of Pd−Ni/Y_2O_3 catalysts

Sample	S_{BET} (m^2/g)	Metal particle size[a] (nm)
Pd−Ni/Y3	25	≈ 7.5 ± 2.2
Pd−Ni/Y4	23	≈ 7.0 ± 1.3
Pd−Ni/Y5	20	≈ 7.1 ± 1.5

[a] measured over 50 particles using TEM

The crystal structures of the fresh Pd−Ni catalysts characterized by XRD can be seen in Figure 5-5. The characteristic peaks of Y_2O_3 support can be observed in all catalysts (29.16^o, 33.77^o, 48.54^o, and 57.6^o). However, the peaks of NiO (37.5^o and 43.7^o) and PdO (34° and 42°) are not observed, indicating that the NiO and PdO crystal sizes of the Pd−Ni/Y_2O_3 catalysts are beyond the detection limit of XRD. This suggests that the metallic particles have been highly dispersed on the support using wet impregnation method. On the other hand, two small peaks at 2θ of 32.5^o and 45.9^o are observed in all the Pd−Ni/Y_2O_3 catalysts. This peak is attributed to the formation of metal-support compound (MSC) between Pd and Y_2O_3 support, probably in the form of $Pd_xCl_yY_z$ compound, showing interaction between Pd and Y_2O_3 support as reported in previous chapter.

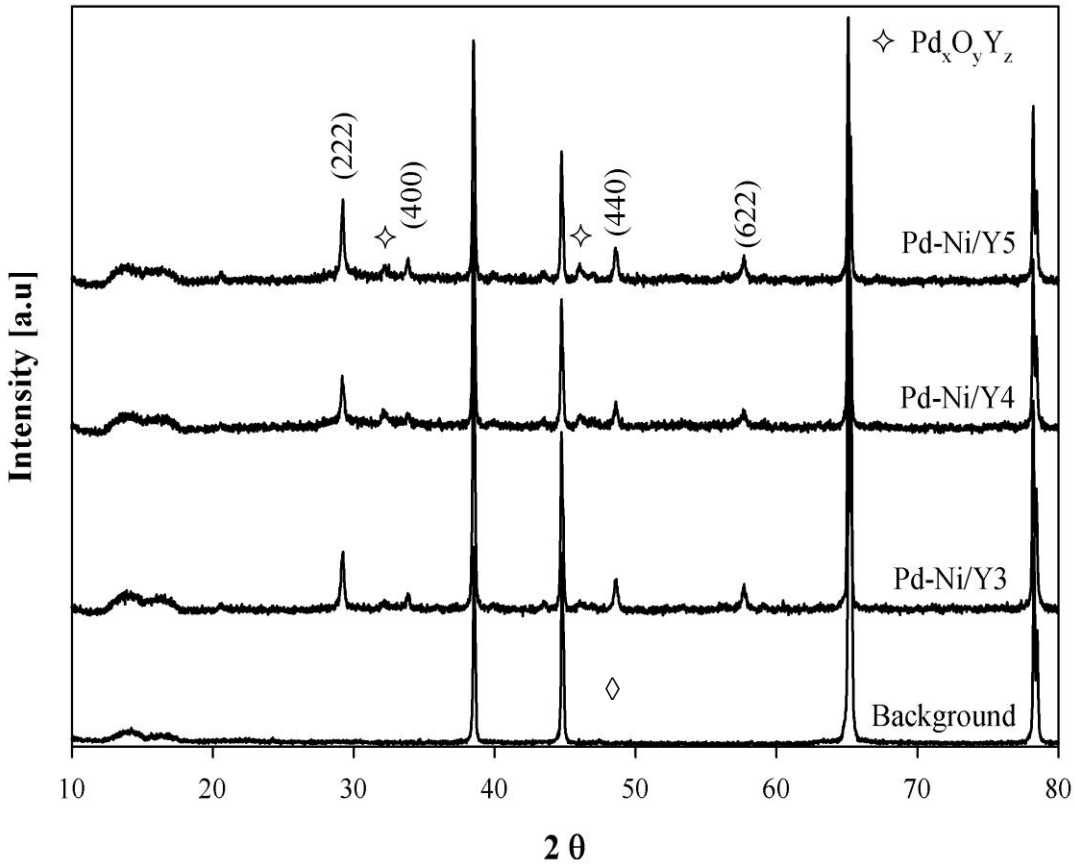

Figure 5-5 XRD patterns of fresh Pd−Ni/Y_2O_3 catalysts

Figure 5-6 shows the TPR profiles of the fresh Pd−Ni/Y_2O_3 catalysts. All the Pd−Ni/Y_2O_3 catalysts have two reduction peaks at temperature of 350°C-450°C and 600°C-750°C separately. The reduction peak at temperature of 350°C-450°C can be assigned to the reduction of NiO species. However, the observed temperature is lower than the one on the Ni catalyst reported by Habimana et al. [264]. The shifting of NiO peak to lower temperature can be attributed to the H_2 spill over from noble metal [175] in this case, Pd. Since Pd is reduced at lower temperature than Ni, once reduced, Pd will act as hydrogen dissociation sites and the dissociated hydrogen migrates through the catalyst surface to reduce Ni easier than the normal gaseous molecular hydrogen [172].

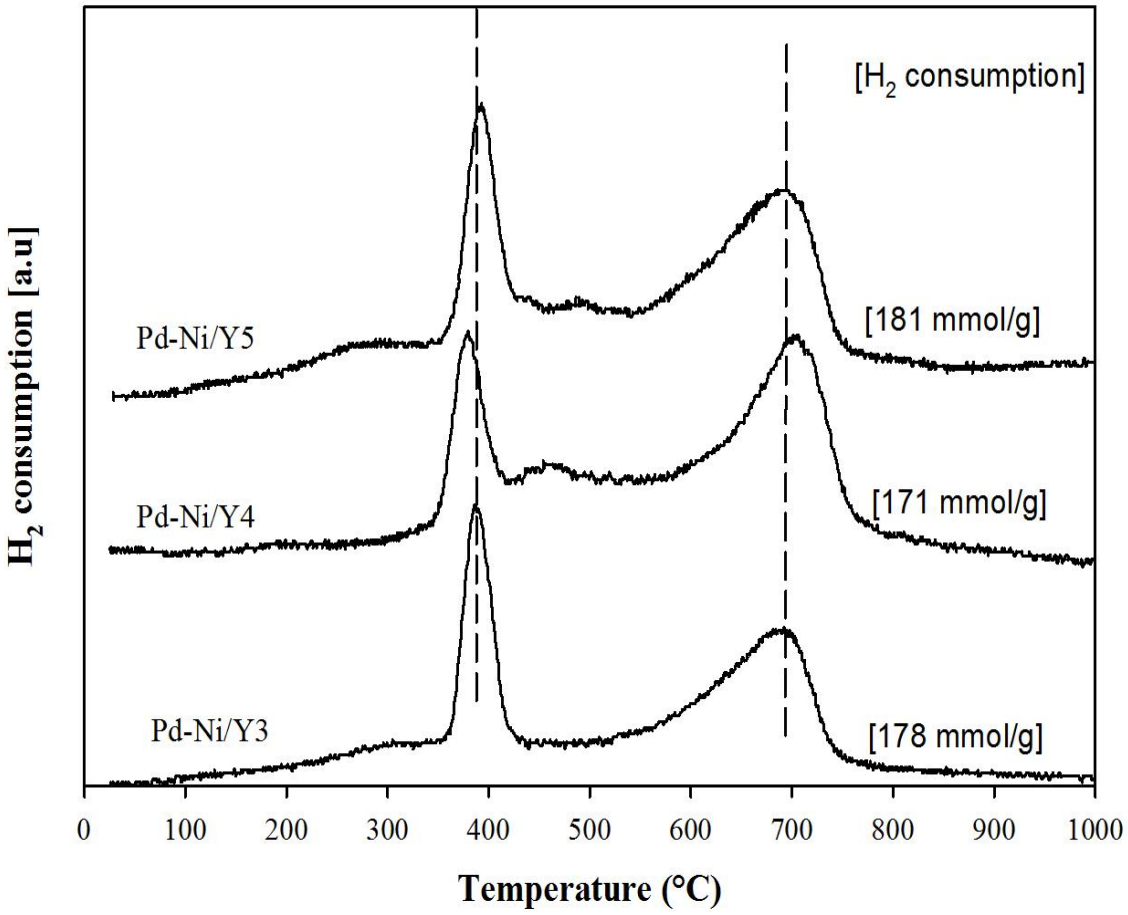

Figure 5-6 TPR profiles of fresh Pd−Ni/Y_2O_3 catalysts

In addition, the TPR peak of the Pd−Ni/Y_2O_3 catalysts at temperature of 600°C-750°C can be assigned to the reduction of a compound containing Pd and Y_2O_3. Based on our previous study, this peak can be assigned to reduction of $Pd_xCl_yY_z$ compound. The presence of $Pd_xCl_yY_z$ compound indicates the interaction between Pd and Y_2O_3 support, which shifts the reduction of palladium to higher temperature. Pospíšil et al. [265] reported that Pd acted as an activator in the reduction process with the Y_2O_3 supports, therefore, exhibiting interaction with Y_2O_3 supports. The amount of H_2 consumption of

Pd-Ni catalysts shows that all catalysts have similar H_2 consumption while the amount of H_2 consumption in synthesized supports increase from Y5 to Y3, showing that the increase in H_2 consumption in synthesized supports from Y5 to Y3 is due to the surface oxygen from synthesized Y_2O_3 support. This TPR results also show that reduction of NiO and $Pd_xCl_yY_z$ compound is not influenced by the oxygen mobility of the support.

Further characterization using TPD-O_2 on the Pd−Ni/Y_2O_3 catalysts (Figure 5-7) reveals that all Pd−Ni/Y_2O_3 catalysts have different oxygen desorption profiles. The Pd−Ni/Y3 catalyst shows one peak around 320-600°C, corresponding to the gaseous chemisorbed oxygen on catalyst support, commonly named as α-oxygen [193]. The peak at similar location is also observed on the Pd−Ni/Y4 and Pd−Ni/Y5 catalysts. However, the peak shifts to higher temperature from Pd−Ni/Y3 to Pd−Ni/Y5 catalysts, suggesting that the surface oxygen mobility decreases from Pd−Ni/Y3 to Pd−Ni/Y5 catalysts. This result is in agreement with TPR result of fresh catalyst supports, which show increasing in surface oxygen mobility from Y5 to Y3 supports.

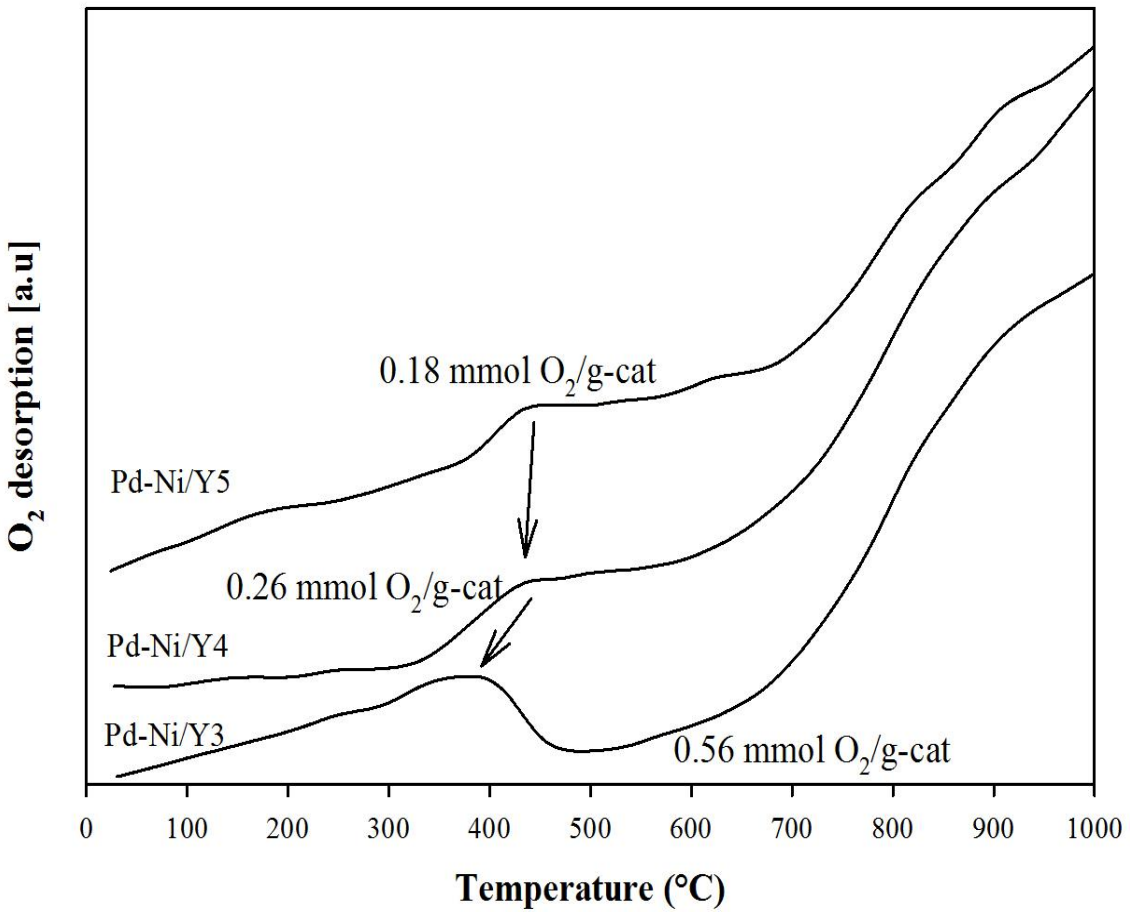

Figure 5-7 TPD- O_2 profiles of Pd−Ni/Y_2O_3 catalyts

Figure 5-8 shows the XPS Pd 3d of the reduced Pd−Ni/Y_2O_3 catalysts. It is observed that Pd has 3 peaks for all catalysts. The former two peaks correspond to the Pd $3d_{5/2}$ and satellite peaks while the latter peak corresponds to the Pd $3d_{3/2}$ peak. The Pd $3d_{5/2}$ peaks of the reduced Pd−Ni/Y3, Pd−Ni/Y4, and Pd−Ni/Y5 catalysts are located at 335.0eV, 335.4eV, and 335.7eV, respectively. The binding energy of this peak on all the Pd−Ni/Y_2O_3 catalysts is higher than the binding enery of Pd^0 (334.9 eV) [229], suggesting the presence of electron deficient Pd^{n+} species whereby the electron has been transferred

from Pd. It is also observed that the shifting of the XPS 3d $Pd_{5/2}$ peak to higher binding energy increases with the following order: Pd−Ni/Y5 > Pd−Ni/Y4 > Pd−Ni/Y3, showing that Pd on the Pd−Ni/Y5 catalyst has been transferred more electrons than Pd on the other Pd−Ni catalysts.

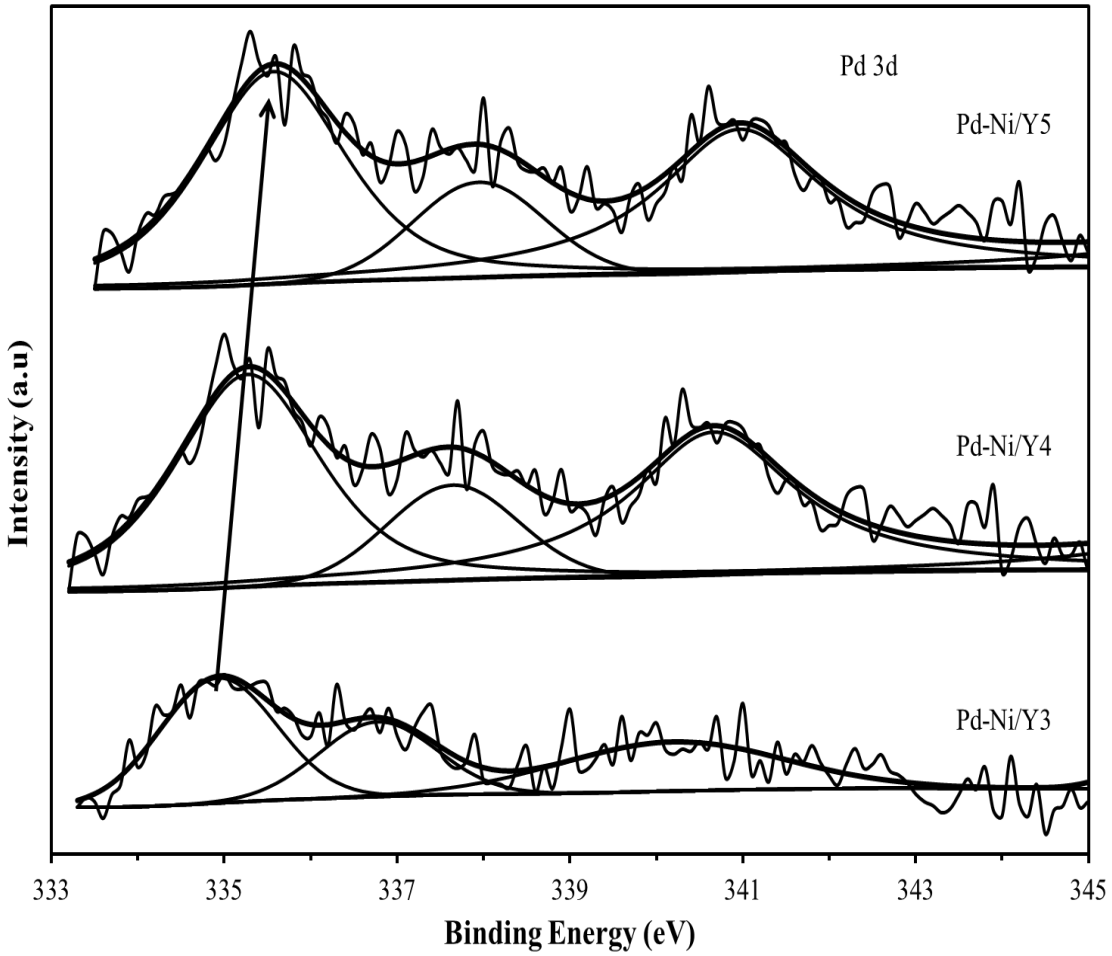

Figure 5-8 XPS Pd 3d patterns of PdNi/Y_2O_3 catalysts

The XPS Ni $2p_{3/2}$ main peak (Figure 5-9) of the reduced Pd−Ni/Y3 catalyst is observed at 855.8eV, which is higher binding energy than the Ni $2p_{3/2}$ peak of NiO at 854.5eV [228], showing that electron has also been transferred from Ni. In addition, it is

also observed that the XPS Ni $2p_{3/2}$ main peak of the reduced Pd−Ni/Y4 and Pd−Ni/Y5 catalysts is also located at the same binding energy with the XPS Ni $2p_{3/2}$ main peak of the reduced Pd−Ni/Y3 catalyst. This result is in agreement with TPR result which shows that all Pd−Ni/Y_2O_3 catalysts have the same reduction temperature of the NiO.

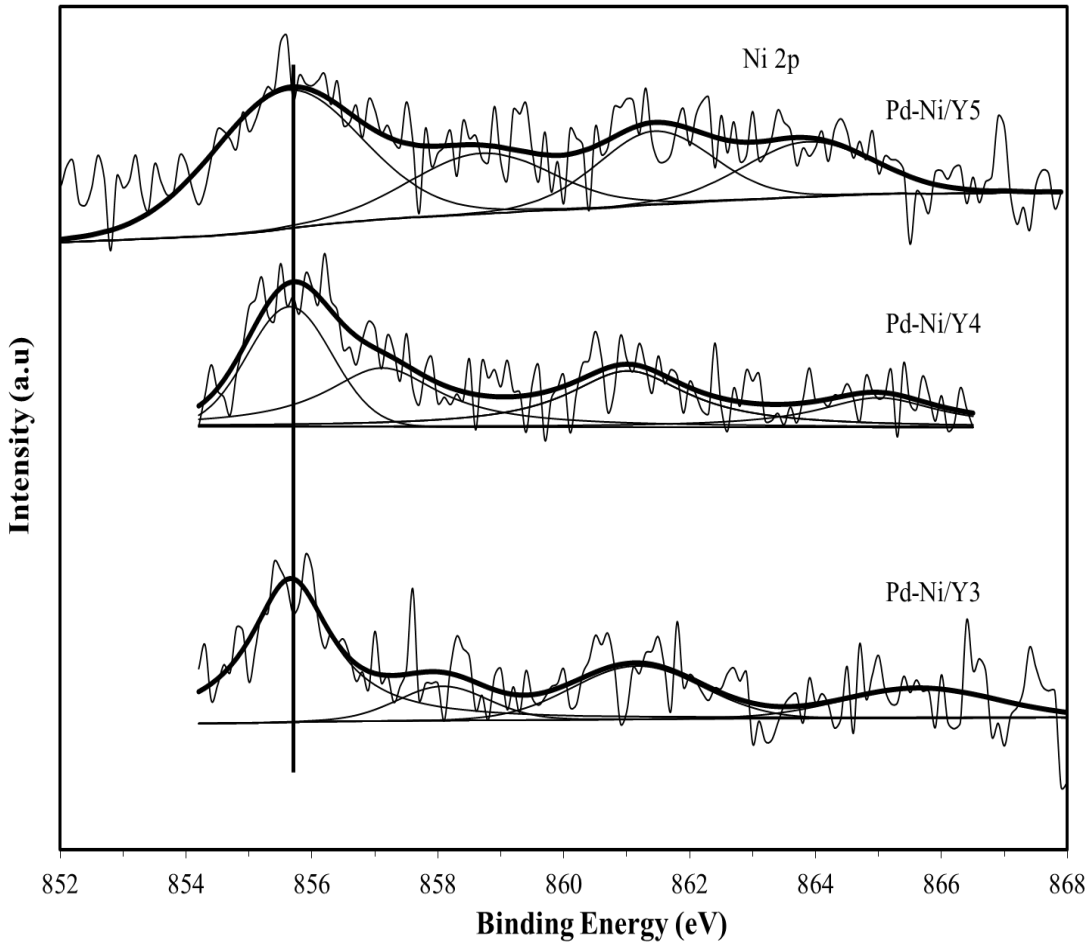

Figure 5-9 XPS Ni 2p patterns of Pd−Ni/Y_2O_3 catalysts

The XPS Y 3d results in Figure 5-10 show that the Y $3d_{5/2}$ peak of the Pd−Ni/Y3, Pd−Ni/Y4, and Pd−Ni/Y5 catalyst is located at 156.6eV, which slightly shifts to higher

binding energy compared to the peak of pure Y_2O_3 [228]. This result shows that electron has been transferred from Y.

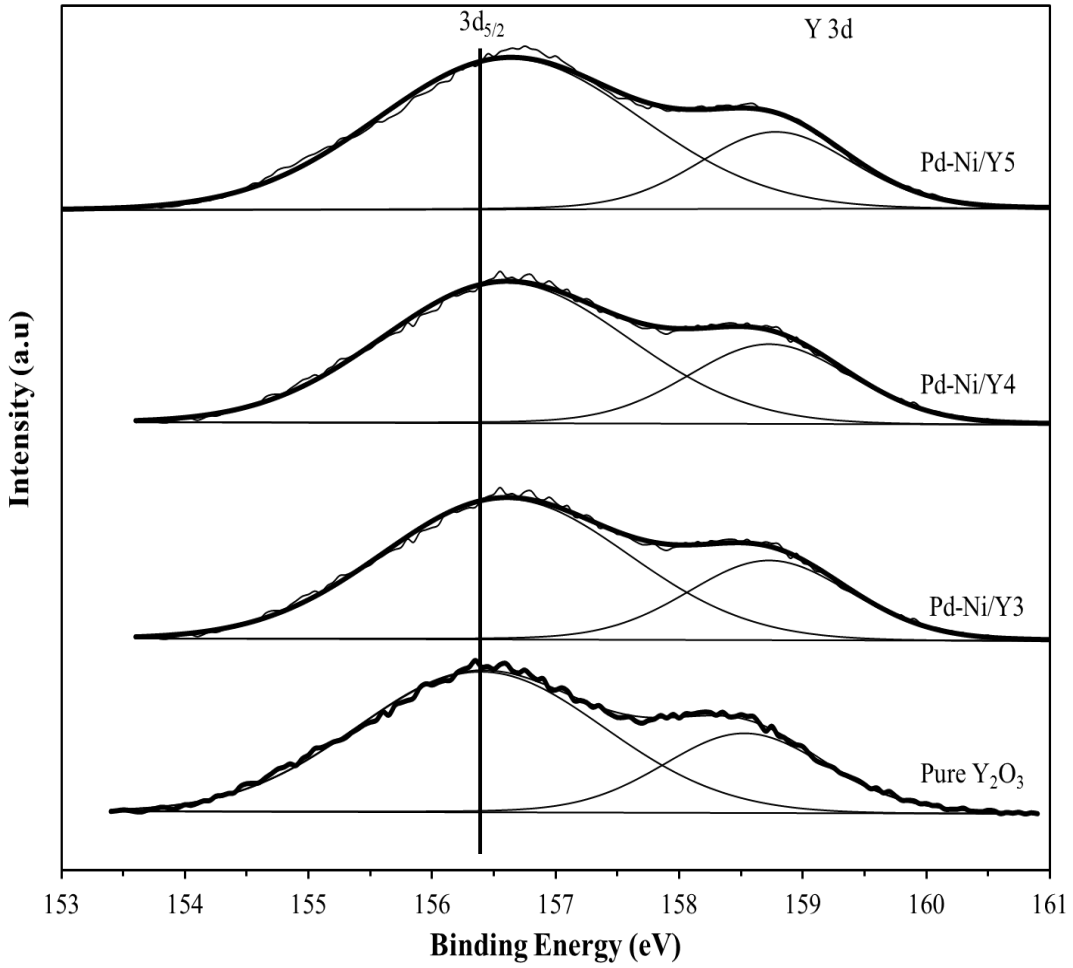

Figure 5-10 XPS Y 3d patterns of Pd−Ni/Y_2O_3 catalysts

In contrast, the XPS O 1s peak of the Pd−Ni/Y_2O_3 catalysts (Figure 5-11) is observed to shift to lower binding energy from Pd−Ni/Y5 to Pd−Ni/Y3 catalysts, showing that electron has been transferred to O. Two main peaks can be observed in all the Pd−Ni/Y_2O_3 catalysts after deconvolution. The characteristic O 1s peaks at around 529eV

and 531.7eV are attributed to O^{2-} and O_2^{2-}/O^-, respectively [260, 266]. It is also observed that the peak shifting to lower binding energy becomes more intense from Pd−Ni/Y5 to Pd−Ni/Y3 catalyst, indicating that the O on the Pd−Ni/Y3 catalyst is more mobile compared to the other catalysts. This result is in agreement with TPR results of the synthesized Y_2O_3, which shows that Y3 has the highest surface oxygen mobility.

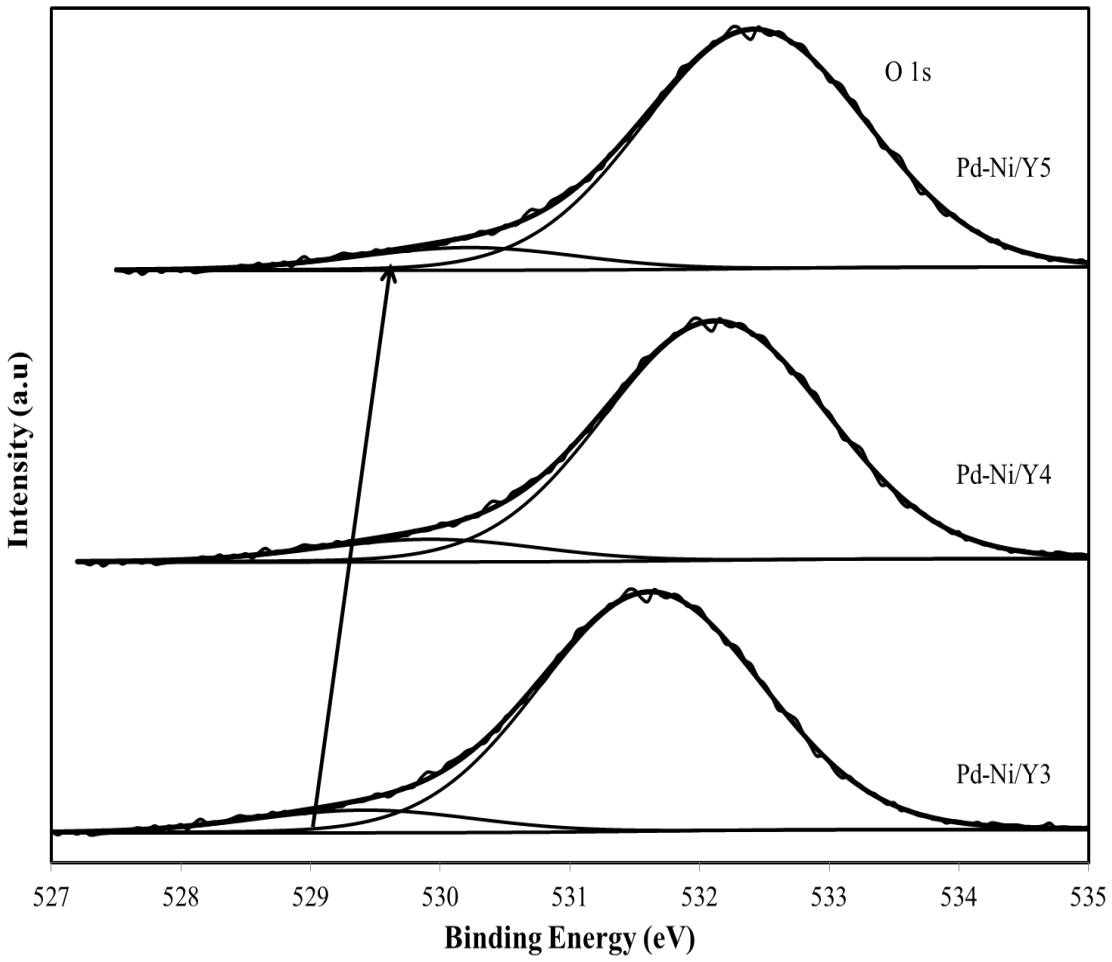

Figure 5-11 XPS O 1s patterns of Pd−Ni/Y_2O_3 catalysts

By combining all the XPS results, it can be seen that Pd, Ni, and Y have transferred electron and O has received electron. Our previous study shows the presence of bimetallic Pd-Ni particles and $Pd_xCl_yY_z$ compound due to transfer electron from Ni to Pd and from Pd and Y to Cl. These results are in agreement with our previous study.

5.3.3 Catalyst activity

Figure 5-12 shows the CH_4 and CO_2 conversions produced from the Pd−Ni/Y_2O_3 catalysts at different temperature. It can be seen that the CH_4 and CO_2 conversion increase with increasing temperature as higher temperature promotes higher reaction rates. The similar increasing in H_2 and CO production rates with increasing temperature is observed in Figure 5-12. The increase in activity of the Pd−Ni/Y_2O_3 catalysts should be attributed to the decrease in crystal size of Y_2O_3 since the specific surface area and metal particle size, and TPR results of all Pd−Ni/Y_2O_3 catalysts are similar. Therefore, specific surface area, metal particle size, and formation of metal-support compound are not the key factors affecting the catalyst activity in this study.

However, it is observed that the increase in activity of the Pd−Ni/Y_2O_3 catalysts has similar trend with the increase in surface oxygen mobility of the Y_2O_3 support. From the TPR results, Y3 has the highest surface oxygen mobility which results in the enhancement of the catalytic performance of the Pd−Ni/Y3 catalyst in the OCRM reaction. Similar observation was found in the study done by Sun et al. [249]. In addition, Bellido & Assaf [227] reported that the incorporation of Y_2O_3 in ZrO_2 enhanced the catalytic performance of Ni catalyst due to the presence of oxygen vacancies in the support. The important role of the surface oxygen mobility on catalytic activity has also been reported

in many catalytic systems, such as ethanol steam reforming [266], CO oxidation [267], and hydrocarbon combustion [268]. For instance, the catalytic activity and stability of Co catalyst on ethanol steam reforming was found to be higher due to higher oxygen mobility of CeO_2 [269]. In addition, the oxygen mobility was found to have positive influence on rate-determining step of CO oxidation [267]. Therefore, surface oxygen mobility is the key factor affecting the catalytic activity of the Pd−Ni/Y_2O_3 catalyst in the OCRM reaction.

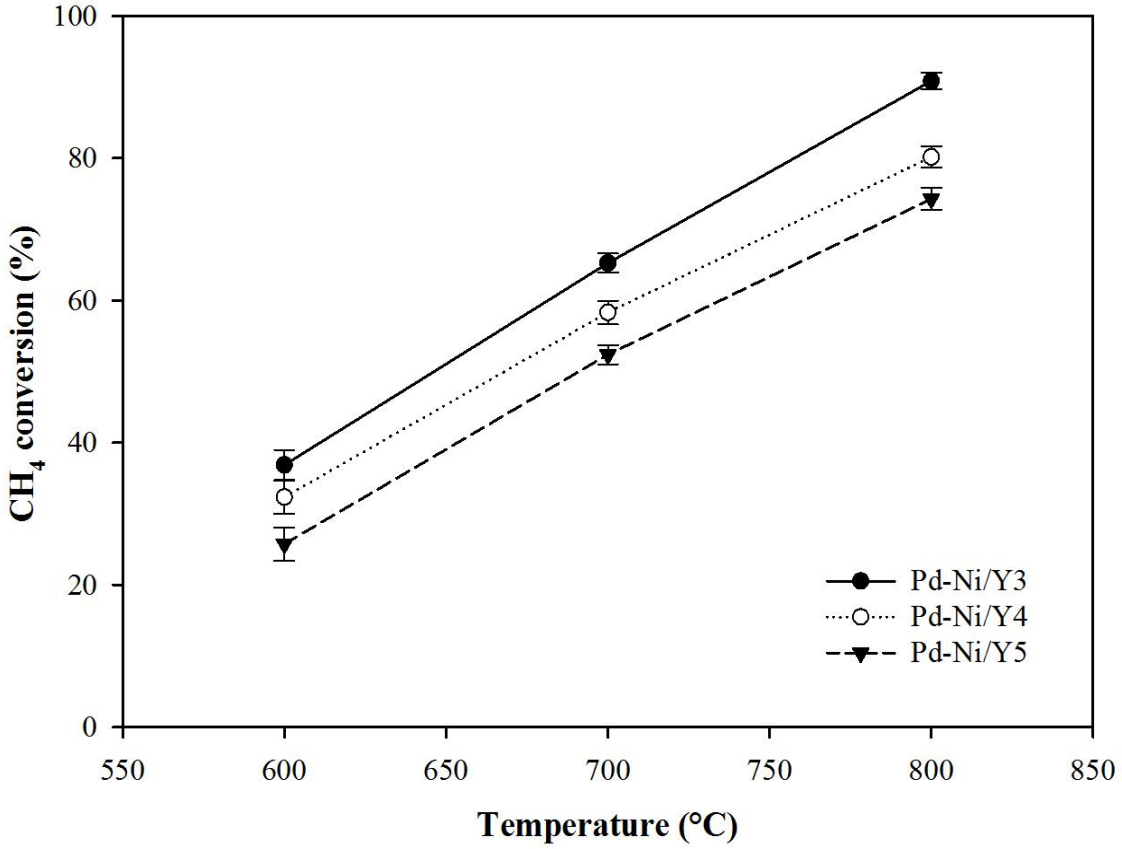

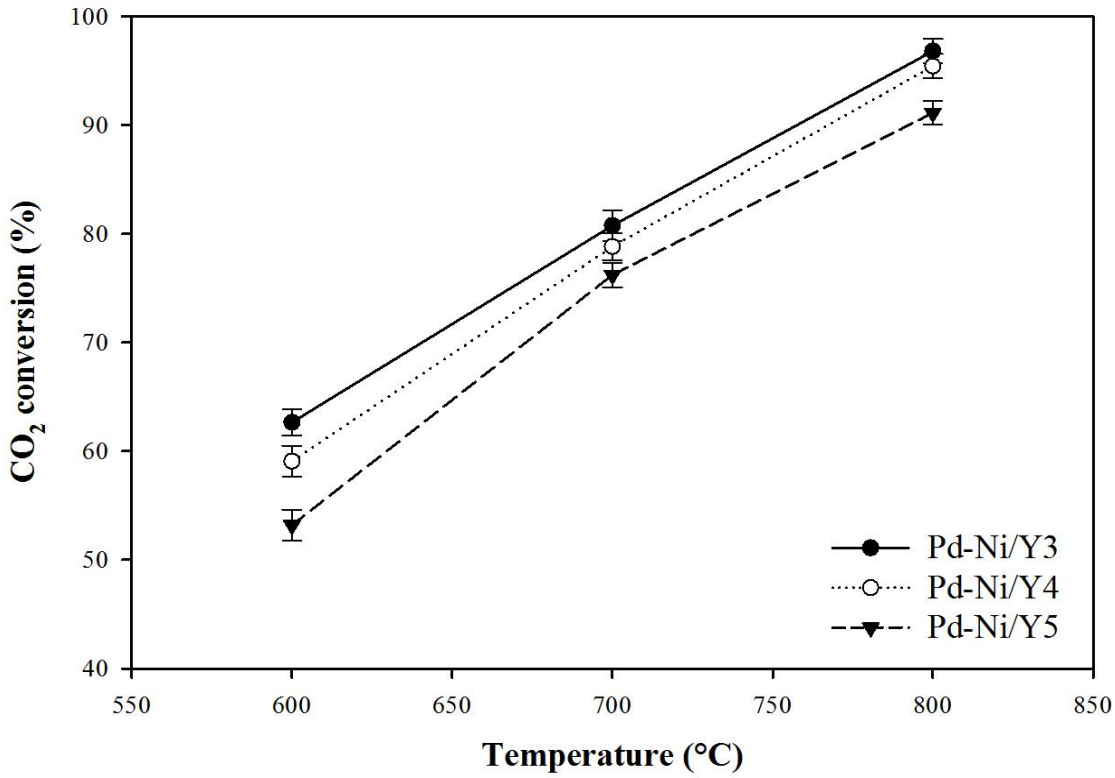
100
90
80
70
60
50
40
550
600
650
700
750
800
850
CO_2 conversion (%)
Temperature (°C)
Pd-Ni/Y3
Pd-Ni/Y4
Pd-Ni/Y5

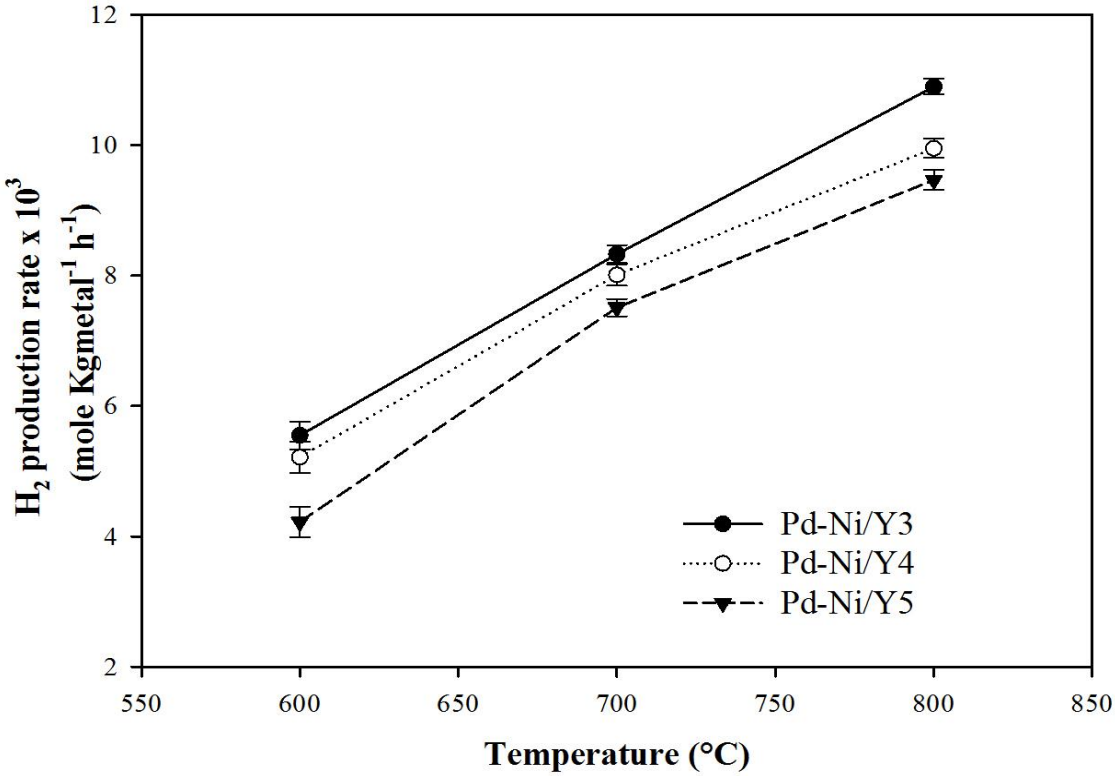
12
10
8
6
4
2
550
600
650
700
750
800
850
H_2 production rate x 10^3 (mole Kgmetal^{-1} h^{-1})
Temperature (°C)
Pd-Ni/Y3
Pd-Ni/Y4
Pd-Ni/Y5

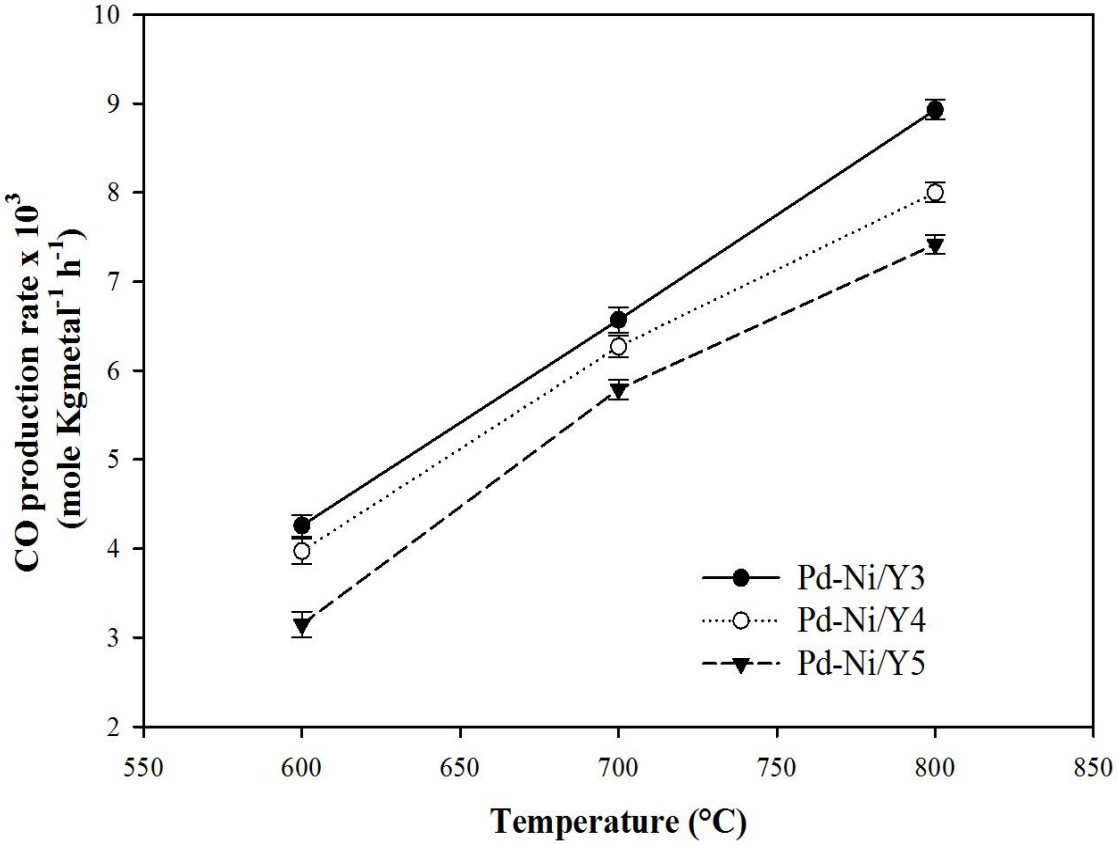

Figure 5-12 CH_4 and CO_2 conversions; and H_2 and CO production rate from Pd−Ni/Y_2O_3 catalysts (P_{total} = 1 atm, T = 700°C, $CH_4/CO_2/O_2$ = 5/4/1, GHSV = 24000 $cm^3/g/h$)

Table 5-3 shows the H_2 and CO production rates and the H_2/CO ratio. It is interesting to observe that the H_2/CO ratio of all Pd−Ni/Y_2O_3 catalysts decreases with increasing temperature, indicating that all Pd−Ni/Y_2O_3 catalysts produce more CO than H_2 at higher temperature. This phenomenon is expected since the DRM reaction favoring at higher temperature produces more CO than the POM reaction. Therefore, the H_2/CO ratio decreases with increasing temperature.

Interestingly, the H_2/CO ratio is also observed to decrease from the Pd−Ni/Y5 to Pd−Ni/Y3 for all reaction temperatures. This result can be attributed to the increase of surface oxygen mobility from Y5 to Y3 since the surface oxygen species on Y_2O_3 can oxidize the deposited carbon species on catalyst surface to produce more CO. Therefore, the Pd−Ni/Y3 catalyst produces more CO than the other Pd−Ni/Y_2O_3 catalysts.

Table 5-3 H_2/CO produced from Pd−Ni/Y_2O_3 catalysts

Catalysts	H_2 production rate (mole Kg_{metal}^{-1} h^{-1})			CO production rate (mole Kg_{metal}^{-1} h^{-1})			H_2/CO		
	600°C	700°C	800°C	600°C	700°C	800°C	600°C	700°C	800°C
Pd−Ni/Y3	5.55	8.33	10.90	4.26	6.57	8.93	1.30	1.27	1.22
Pd−Ni/Y4	5.21	8.01	9.95	3.97	6.27	8.00	1.31	1.28	1.24
Pd−Ni/Y5	4.22	7.51	9.47	3.15	5.79	7.42	1.34	1.30	1.27

In order to show the role of oxygen mobility, methane decomposition reaction was performed on Pd−Ni/Y3, Pd−Ni/Y4, and Pd−Ni/Y5 catalysts. The result in Figure 5-13 shows that besides H_2 and unreacted CH_4, all Pd−Ni catalysts produce a small amount of CO. It is interesting to see that the mole-% of hydrogen decreases from Pd−Ni/Y3 to Pd−Ni/Y5 at the same reaction time, showing that the Pd−Ni/Y3 catalyst has the best performance among other Pd−Ni catalysts. In addition, the mole-% of CO produced from Pd−Ni/Y3 catalyst is also the highest among other Pd−Ni catalysts. This result is the evidence that the highest oxygen mobility on the Pd−Ni/Y3 catalyst plays an important role in catalytic activity.

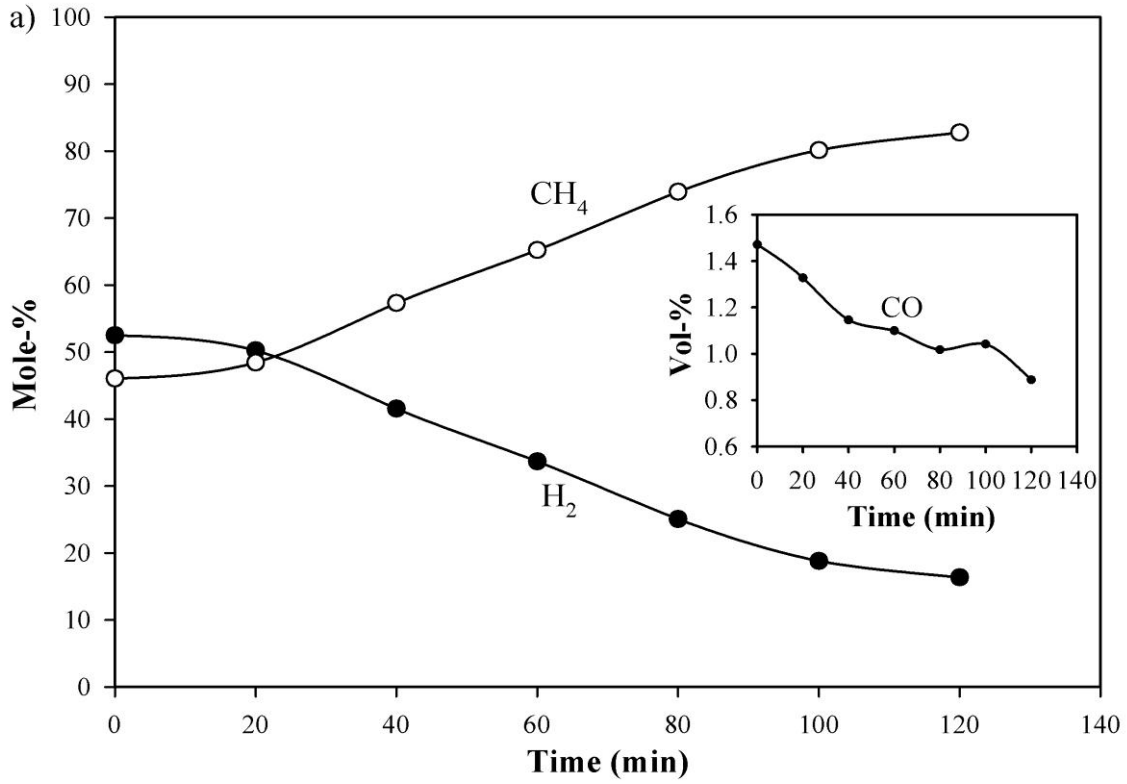
a)
Mole-%
Time (min)
CH4
H2
CO
Vol-%
Time (min)

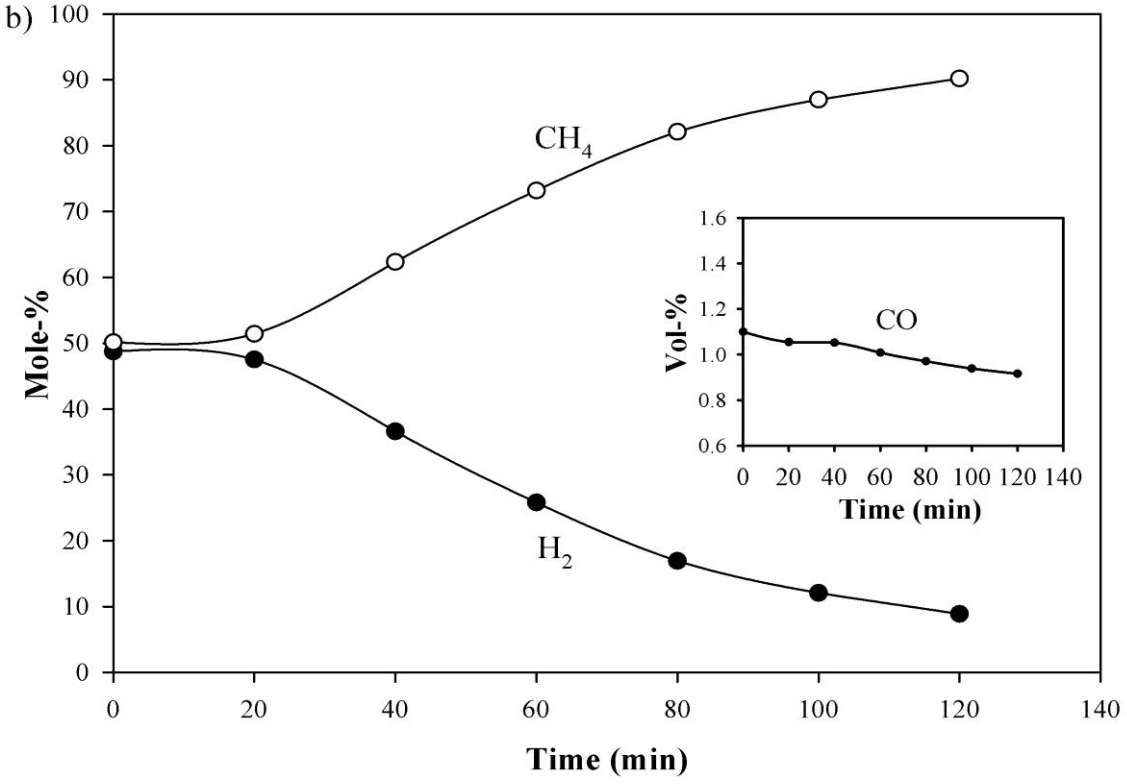
b)
Mole-%
Time (min)
CH4
H2
CO
Vol-%
Time (min)

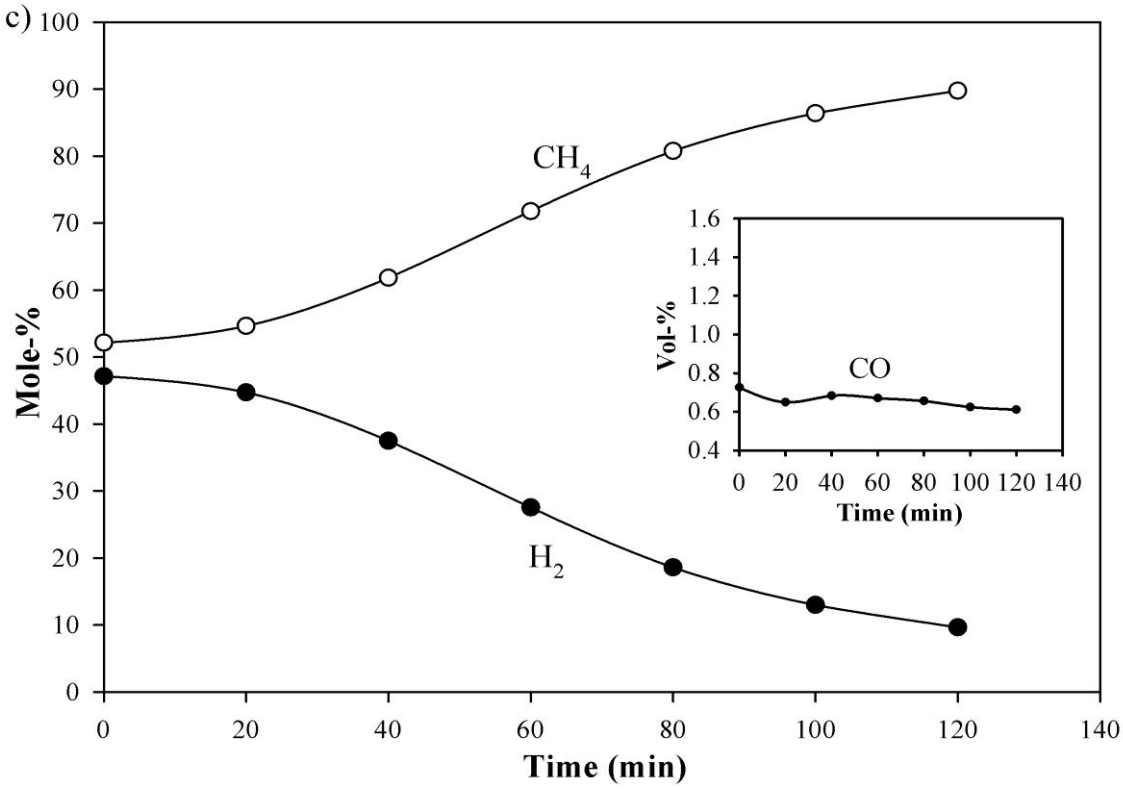

Figure 5-13 Product distribution of methane decomposition over Pd−Ni/Y_2O_3 catalysts (P_{total} = 1 atm, T = 700°C, CH_4/He= 1/1, GHSV = 24000 cm^3/g/h)

5.3.4 Carbon formation

Figure 5-14 shows the carbon deposition rates on the spent Pd−Ni/Y_2O_3 catalysts at various reaction temperatures of 600°C to 800°C. It can be observed that the carbon deposition rates on spent catalysts at reaction temperature of 600°C decreases with the following order: Pd−Ni/Y3> Pd−Ni/Y4>Pd−Ni/Y5. However, the carbon deposition rate on spent Pd−Ni/Y5 catalyst increases significantly with increasing temperature. The increase in carbon deposition rate with increasing temperature is due to higher activity of the catalyst in the OCRM reaction, resulting in higher amount of carbon deposition rate. The increase in carbon deposition rate with increasing temperature is also observed on the

spent Pd−Ni/Y4 catalyst. However, the increase in carbon deposition rate is not as high as the one on the spent Pd−Ni/Y5 catalyst. In contrast, the carbon deposition rate on the spent Pd−Ni/Y3 catalyst decreases significantly with increasing reaction temperature, probably due to the highest surface oxygen mobility on the Pd−Ni/Y3 catalyst. This result can be explained by the fact that the surface oxygen species has higher mobility at higher temperature. Therefore, the surface oxygen species can be more active at higher temperature to oxidize more deposited carbon, thus, the increase in carbon deposition rate at higher temperature can be reduced.

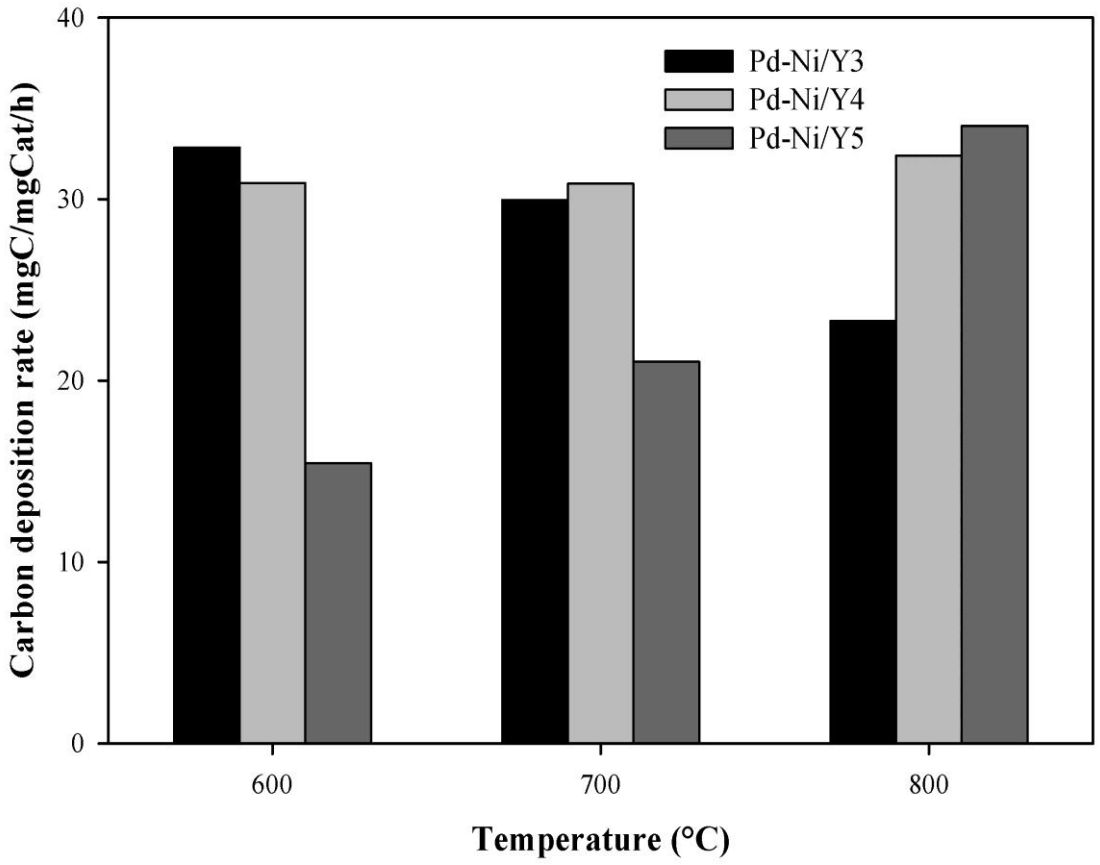

Figure 5-14 Carbon deposition rate on spent Pd−Ni/Y_2O_3 catalysts (P_{total} = 1 atm, T = 700ºC, $CH_4/CO_2/O_2$ = 5/4/1, GHSV = 24000 $cm^3/g/h$).

The DTA profile of the spent Pd−Ni/Y_2O_3 catalysts is shown in Figure 5-15. All the spent Pd−Ni/Y_2O_3 catalysts show peak at below 600°C, indicating that the carbon type is amorphous [203]. However, the peak is observed to shift to lower temperature from the Pd−Ni/Y5 to Pd−Ni/Y3 catalysts, showing that the carbon on the Pd−Ni/Y3 catalyst is easier to be oxidized. This result could be also related with the highest surface oxygen mobility of the Pd−Ni/Y3 catalyst; hence, the Pd−Ni/Y3 catalyst has lower amount and more reactive carbon.

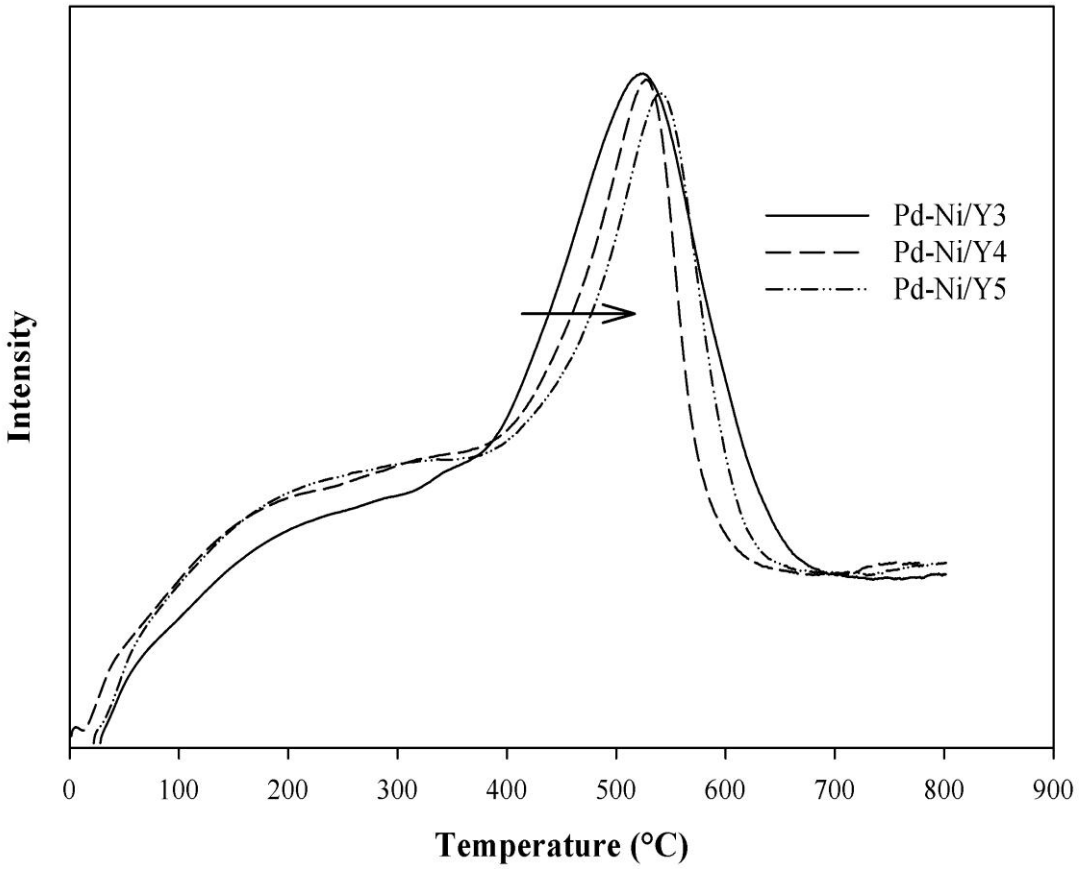

Figure 5-15 DTA profiles of spent Pd−Ni/Y_2O_3 catalysts (P_{total} = 1 atm, T = 700°C, $CH_4/CO_2/O_2$ = 5/4/1, GHSV = 24000 $cm^3/g/h$)

5.4 Conclusions

The spherical monodisperse Y_2O_3 particles with different sizes were successfully synthesized using homogeneous precipitation method. The particle size of synthesized Y_2O_3 particles decreases with decreasing pH solution from Y5 to Y3. In addition, the calculated crystal size of the Y_2O_3 particles also slightly decreases from Y5 to Y3. The TPR results of the synthesized Y_2O_3 particles show that the intensity of reduction peak due to surface oxygen mobility increases from Y5 to Y3, which can be attributed to the smaller crystal size of the synthesized Y_2O_3 particles from Y5 to Y3. Interestingly, the catalytic activity and carbon deposition rate on the Pd−Ni/Y_2O_3 catalysts prepared using the synthesized Y_2O_3 show similar trend with the surface oxygen mobility, showing that the surface oxygen mobility of synthesized Y_2O_3 plays important roles on increasing catalytic activity of the Pd−Ni/Y_2O_3 catalysts and suppression of carbon deposition rate on the Pd−Ni/Y_2O_3 catalyst.

CHAPTER 6

Kinetic Study of Oxy-CO_2 Reforming of Methane on Pd−Ni/Y_2O_3 catalyst

This chapter discusses development of kinetic model for oxidative CO_2 reforming of methane over Pd−Ni/Y_2O_3 catalyst using Langmuir-Hinshelwood (LH) approach. Kinetic study was performed over a wide range of contact times and reaction temperature in fixed bed reactor under the chemical reaction-controlled regime. Two kinetic models were developed based on proposed reaction mechanism. The appropriate kinetic models were obtained after rigorous parameter estimation and model discrimination among all the two kinetic models. The parameters of the kinetic models were estimated by non-linear least square regression. A good agreement was obtained between experimental and model predicted results for the kinetic model based on dissociation of adsorbed methane by adsorbed oxygen for rate determining step of CO_2 reforming of methane and reaction between adsorbed carbon and adsorbed oxygen for rate determining step for partial oxidation of methane.

6.1. Introduction

Carbon dioxide (CO_2) utilization has been getting a new interest from academic and industrial view point due to sharp increase of CO_2 amount. The CO_2 and methane gases are the cheapest carbon-containing materials and the largest amount as well as the most problematic greenhouse gases [269]. Transformation of these both gases into more valuable compounds has been investigated extensively since last decade. The two popular reactions to utilize these both gases are CO_2 reforming of methane and partial oxidation of

methane. The products of both reactions, which are H_2 and CO, have important use in industry and future energy. For example, hydrogen can be used in fuel cells as a power source and syngas (H_2 and CO) can be converted into hydrocarbons via the Fischer-Tropsch synthesis.

CO_2 (dry) reforming of methane (DRM) is a highly endothermic reaction which requires very high energy for the reaction to take place and produces theoretical syngas (H_2/CO) ratio of 1.0. Due to its requirement of external heat exchange, it is a slow process involving long residence time and poor transient response [270]. Moreover, a serious problem in this reaction is high carbon deposition rate on the catalyst by CO disproportionation ($2CO \rightarrow CO_2 + C$) and methane decomposition ($CH_4 \rightarrow C + 2H_2$). These two reactions produce very high amount of carbon deposited on the catalyst, causing deactivation. Although catalyst modification has been carried out extensively to improve the coke resistance of the catalyst, the high energy requirement seems to prevent the commercialization of this reaction in the industry.

In contrast, partial oxidation of methane (POM) is a highly exothermic, compact, rapid start-up, and fast response reaction, which produces theoretical syngas (H_2/CO) ratio of 2.0 [271-272]. However, the actual hydrogen yield is lower and further decreases due to side reactions consuming H_2, such as reverse water gas shift reaction. Moreover, the drawbacks include the presence of hot spots due to exothermicity and the difficulty in operation, particularly in large-scale reactor [273].

Therefore, an alternative process which has been developed in order to compensate for the energy extremes of both reactions is the oxidative CO_2 reforming of methane (OCRM) [271-272, 18]. This process requires lower energy requirement and more efficient than the DRM reaction since it combines the endothermic DRM and the

exothermic POM reactions [271], enabling generation of energy in-situ during reaction. Moreover, high methane conversion can also be achieved with excellent syngas selectivities at extremely high space velocities [143]. Presence of O_2 in the feed also can reduce carbon formation due to oxidation of the carbon precursors species (partially hydrogenated CH_x species) [143]; thereby minimizing effect of catalyst deactivation. Another distinct advantage is that this reaction enables production of gas streams with various composition of H_2/CO via manipulation of the feedstreams [274].

In previous chapter, we have investigated the effect of Pd addition to Ni catalyst over Y_2O_3 support and found that the catalyst synthesized from $PdCl_2$ precursors with Pd/Ni mole ratio of 1/1 is the best catalyst among a series of Pd−Ni catalysts tested for OCRM reaction. The high activity of this catalyst is mainly due to formation of Pd−Ni bimetallic particles while the small metal particle size produced from strong interaction between Pd and Y_2O_3 support resulted in high stability. We also reported that catalyst support has profound effect on the catalyst performance. The catalytic order decreased in the order of Pd−Ni/Y_2O_3> Pd−Ni/Al_2O_3> Pd−Ni/La_2O_3> Pd−Ni/CeO_2> Pd−Ni/TiO_2. The Pd−Ni/Y_2O_3 catalyst showed the highest activity and the lowest carbon deposition rate than other catalysts due to the formation of metal−support compound ($Pd_xCl_yY_z$ compound) on the catalyst, the presence of β−oxygen species and the ability of Y_2O_3 to form oxycarbonate species.

Due to the potential application of this process in the industry, reaction mechanism is compulsory to understand at fundamental level. However, to our knowledge, there is no study reporting on the reaction mechanism for the OCRM process. The reaction mechanisms in the published reports are only available for single reaction such as the

DRM or the POM reaction. Therefore, in the present study, the kinetic study of the OCRM process has been carried out to develop the mechanistic kinetic model. The reaction mechanism will be proposed based on the available reaction mechanisms in the literature for the DRM and POM, since OCRM is a combination of them.

6.2. Experimental

The Pd−Ni catalyst was prepared using co-impregnation of $Ni(NO_3)_2$ and $PdCl_2$ solutions with Pd/Ni ratio of 1/1 and commercial Y_2O_3 as the catalyst support. The details of catalyst preparation and characterization are the same with the ones in chapter 3. The steady state kinetic was studied in a quartz micro-catalytic reactor (ID 4 mm) in a single pass, steady-state plug flow mode. 50 mg of catalyst was used in each test and held by the quartz wool placed in the middle of the reactor. The temperature of the catalyst bed was controlled and monitored by a thermocouple that was in contact with the top layer of the catalyst bed. Prior to the catalytic test, the catalyst was reduced by purified hydrogen at 600°C for 1 hour and followed by purging with purified helium to reaction temperature. All the gases used here were research grade gases (99.95% CH_4, 99.99% CO_2, 99.8% O_2, and 99.9995% He). A cold trap filled with 50% glycerol and 50% water at temperature of -10^oC was installed between reactor exit and the GC sampling valve to condense any moisture formed. The gas product was analyzed using a gas chromatograph (HP 6890) equipped with a Hayesep D column and a TCD detector. The CH_4 conversion was calculated from the difference of CH_4 flowrate between the inlet and outlet stream of the reactor. The same calculation was used for CO_2 conversion. Preliminary runs were performed to achieve the negligible film and pore diffusion effects on kinetic data. The plug flow condition was used to avoid back mixing and channeling; and maintained by

providing catalyst bed height to catalyst particle size ratio, L/Dp ≥ 50 and using an internal diameter of reactor to catalyst particle size ratio, D/Dp ≥ 30 [275].

6.3. Results and discussion

6.3.1. Mass transfer effect

Some preliminary runs were performed at various conditions to obtain the kinetic data in the chemical reaction controlled regime by eliminating pore diffusion and film diffusion [276]. Figure 6-1 shows the effect of catalyst particle size on CH_4 conversion on Pd−Ni catalyst. By varying the average catalyst particle size from 0.1mm to 0.2 mm, the effect of pore diffusion was investigated. It can be seen that the CH_4 conversion increases with decreasing average particle size. However, the CH_4 conversion almost remains constant for catalyst with particle size lower than 0.15 mm, showing that effect of pore diffusion is negligible on the catalyst with particle size lower than 0.15 mm. Therefore, an average particle size of 0.10 mm was chosen for all kinetic experiments.

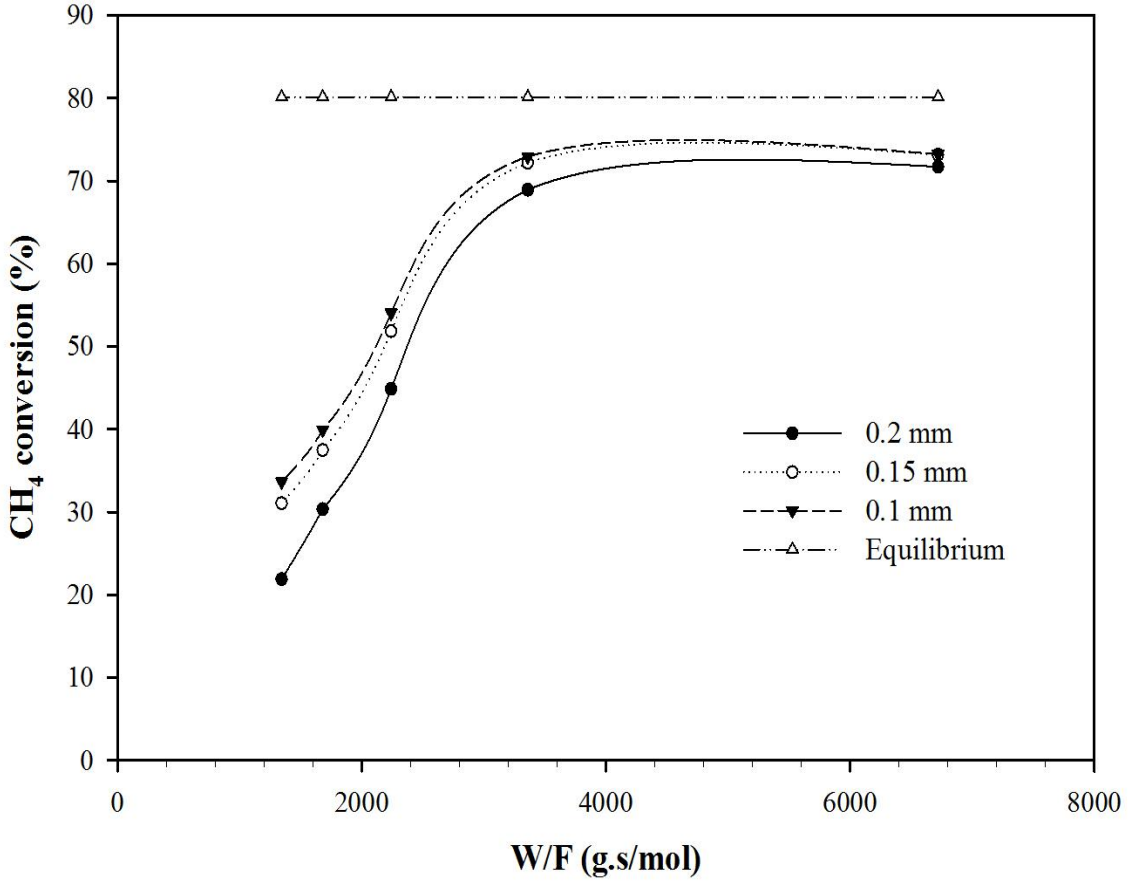

Figure 6-1 Effect of catalyst particle size on catalyst activity (T=700°C, $CH_4/CO_2/O_2$=5/4/1, P=1 atm)

Furthermore, by varying the total feed flow rates, the effect of film diffusion was investigated. The total volumetric feed flow rate was varied by adjusting the inert helium flow rate while the reactants (CH_4, CO_2, O_2) flow rates were kept constant. Figure 6-2 shows the effect of total flow rate on the catalytic activity of Pd−Ni catalyst. It can be seen that the methane conversion increases with increasing total flowrate and reaches maximum at total flowrate of 140mL/min. Above the total flowrate of 140 mL/min, the increase of methane conversion is not significant, showing that external mass transfer

limitation does not prevail. Therefore, all the kinetic data were collected at total flowrate of 140mL/min using particle size of 0.10 mm.

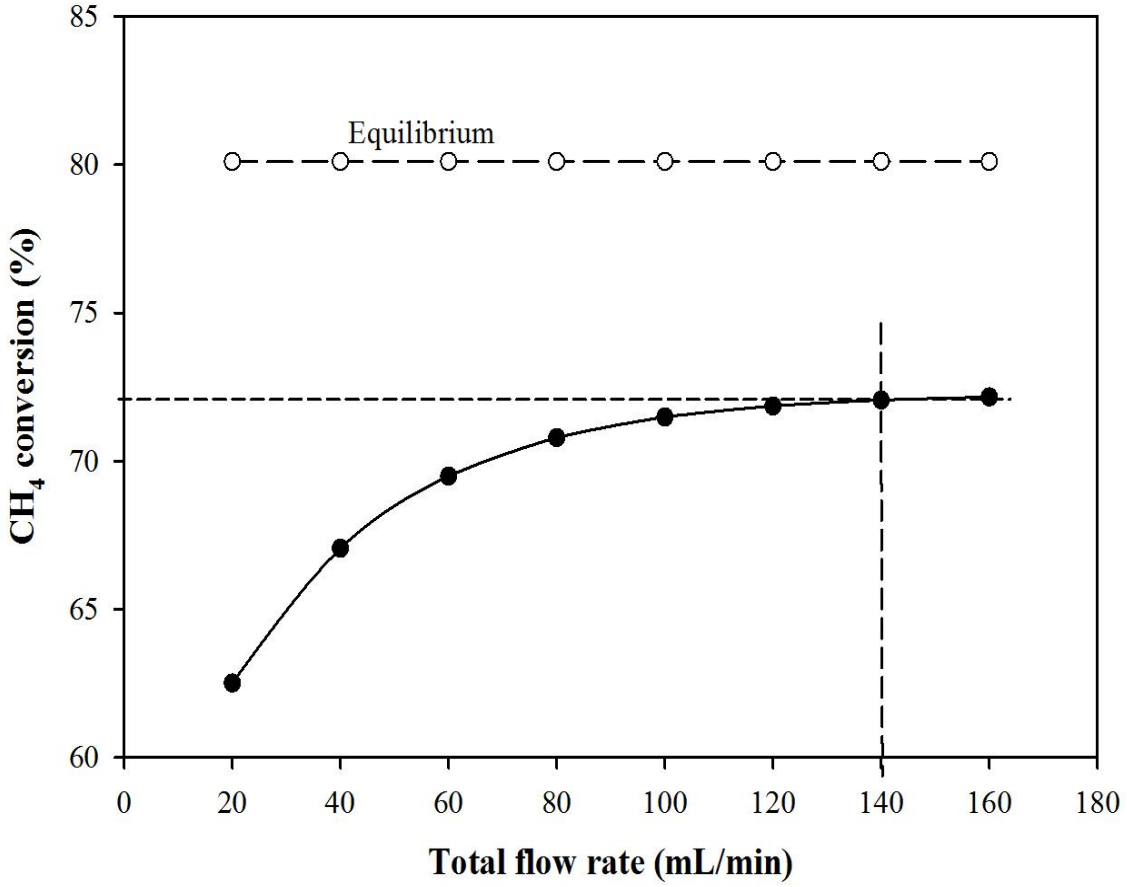

Figure 6-2 Effect of total flow rate on catalyst activity (T=700°C, $CH_4/CO_2/O_2$=5/4/1, P=1 atm)

6.3.2. Catalytic reaction

The catalytic activity for kinetic modeling were performed using Pd−Ni/Y_2O_3 catalyst at atmospheric pressure in the temperature range of 600-750°C with total flow rate of 140 mL/min. Figure 6-3 shows the effect of partial pressure of CH_4 on CH_4 and CO_2 conversion. The partial pressure of CO_2 and O_2 was kept constant for all tests. It can

be seen that the CH_4 conversion decreases with increasing partial pressure of CH_4 at all reaction temperatures. However, the CO_2 conversion is observed to be stable at all reaction temperatures. The decrease trend in CH_4 conversion with increasing temperature is expected since according to thermodynamic point of view, the higher reaction temperature enhances the catalytic activity.

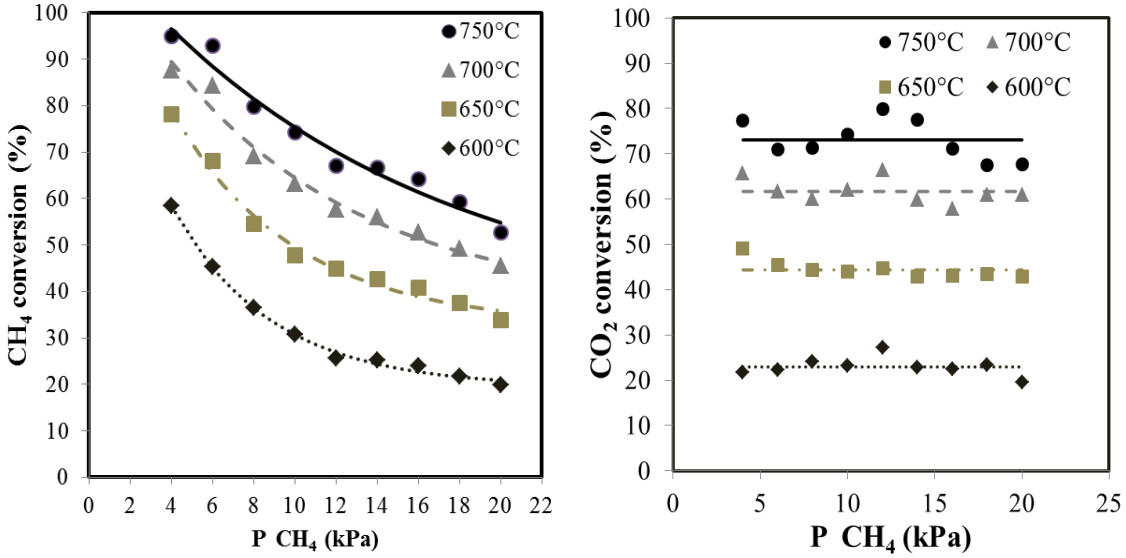

Figure 6-3 Influence of CH_4 partial pressure on the CH_4 and CO_2 conversions over Pd−Ni/Y_2O_3 catalyst ($P(CO_2)$ = 8kPa, $P(O_2)$ = 2kPa, P(He) = 70-88kPa, total flowrate=140mL/min)

Figure 6-4 shows the effect of CO_2 partial pressure on CH_4 and CO_2 conversion for OCRM reaction. The partial pressure of CH_4 and O_2 was kept constant for all tests. It can be seen that at 600°C, the CO_2 conversion is quite low, around 20%, and slightly decreases with increasing partial pressure of CO_2. Meanwhile, at that temperature, CH_4 conversion is also quite low around 28% and stable with increasing partial pressure of

CO_2. With increasing reaction temperature, the CO_2 and CH_4 conversions increase significantly, but the increase in CO_2 conversion is more dramatic than the one in CH_4 conversion. The tremendous increase in CO_2 conversion with reaction temperature is in agreement with the endothermicity of the DRM reaction which favors high temperature. However, the decreasing trend in CO_2 conversion is observed with increasing partial pressure of CO_2, showing that the CO_2 is in excess. It should be noted that methane combustion to produce more CO_2 may also take place and compete with the POM reaction to produce CO. In contrast, even though the CH_4 conversion increases with increasing reaction temperature, it is found that there is no effect of partial pressure of CO_2 on the CH_4 conversion.

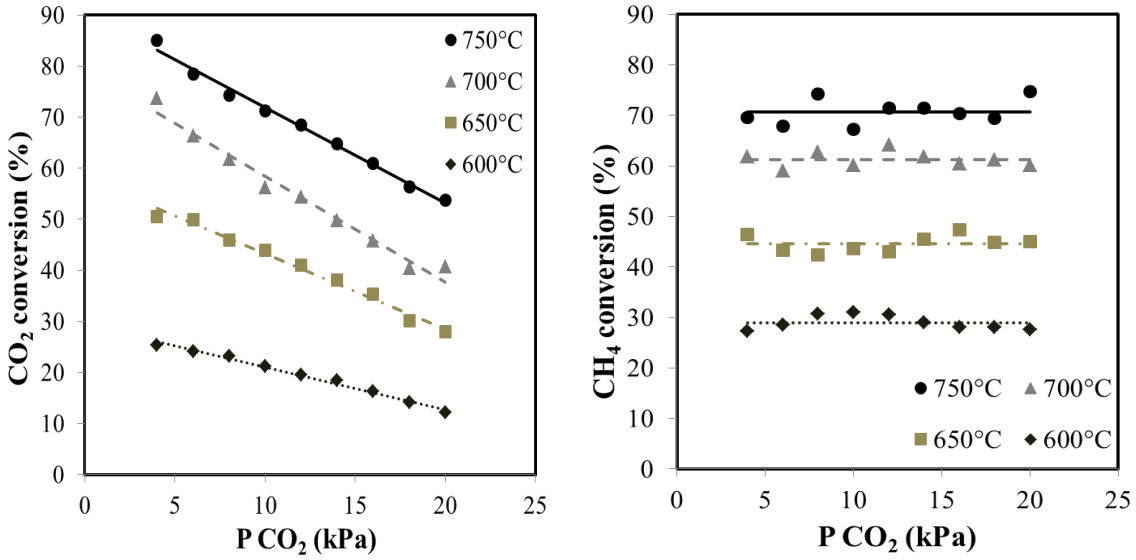

Figure 6-4 Influence of CO_2 partial pressure on CO_2 and CH_4 conversions over Pd−Ni/Y_2O_3 catalyst ($P(CH_4)$ = 10kPa, $P(O_2)$ = 2kPa, P(He) = 68-84kPa, total flowrate=140mL/min)

6.3.3. Development of kinetic models

Figure 6-5 shows the effect of partial pressure of CH_4 on reaction rate of CH_4 over Pd−Ni/Y_2O_3 catalyst for the OCRM reaction. It can be seen that the reaction rate increases with increasing reaction temperature. In addition, the reaction rate also increases linearly with increasing partial pressure of CH_4, indicating that the reaction rate is first order to the partial pressure of methane. However, at low partial pressure, the effect of reaction temperature is not significant. Moreover, at high partial pressure of CH_4, the reaction rate of CH_4 is quite constant, indicating that CH_4 is already in excess.

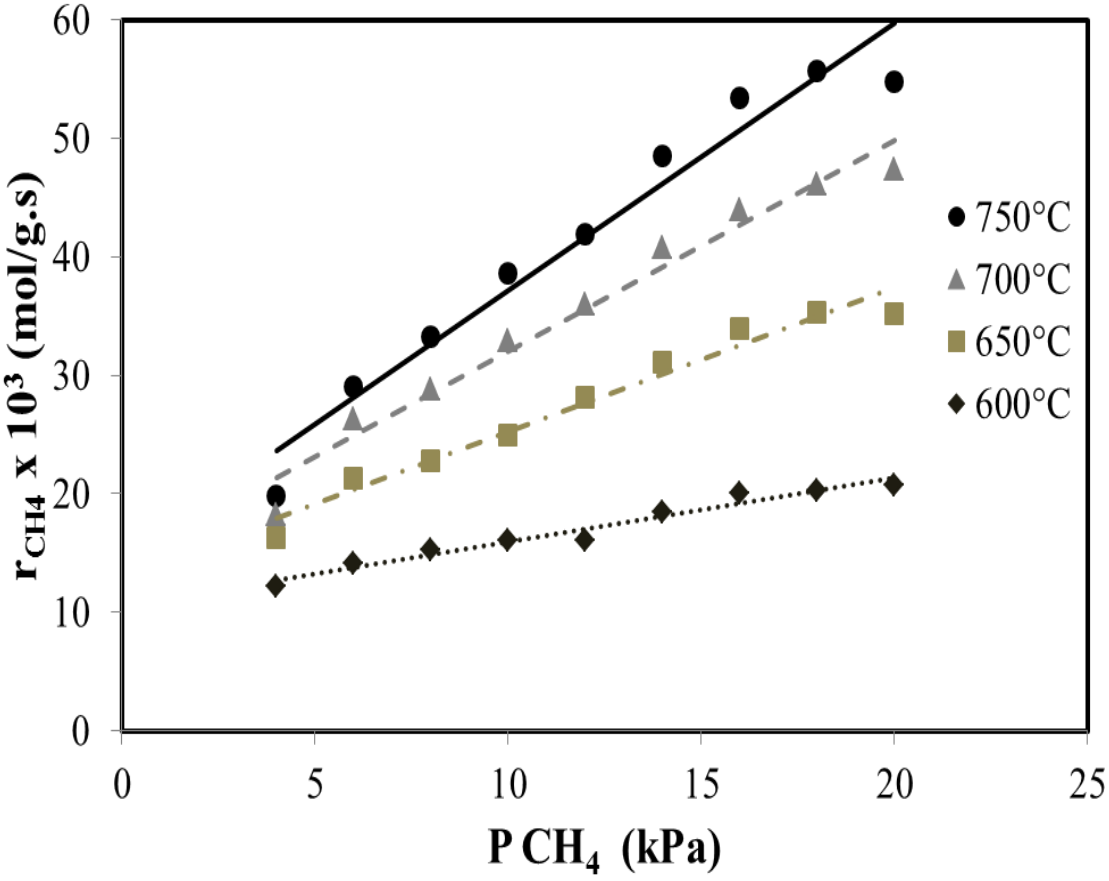

Figure 6-5 Influence of CH_4 partial pressure on the reaction rate over Pd−Ni/Y_2O_3 catalyst ($P(CO_2)$= 8kPa, $P(O_2)$=2kPa, P(He)=70-88kPa, total flowrate=140mL/min)

Figure 6-6 shows the effect of partial pressure of CO_2 on reaction rate of CO_2 over Pd−Ni/Y_2O_3 catalyst. Similar to the reaction rate of CH_4 in Figure 6-5, the reaction rate increases with increasing reaction temperature. In addition, the reaction rate also increases linearly with increasing partial pressure of CO2, indicating that the reaction rate is first order to the partial pressure of CO_2. However, unlike CH_4, the reaction rate of CO_2 is strongly affected by reaction temperature and partial pressure of CO_2 as it always increases significantly. This suggests that OCRM reaction at higher temperature and higher partial pressure of CO_2 is favorable.

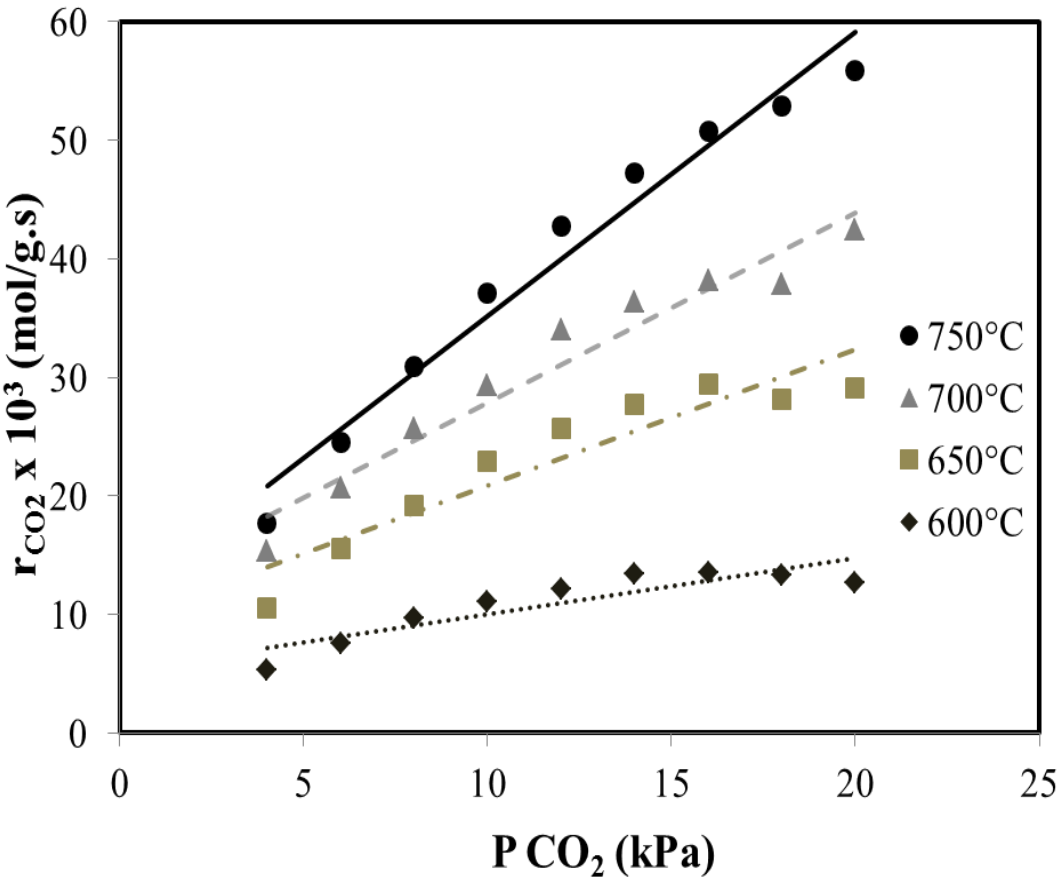

Figure 6-6 Influence of CO_2 partial pressure on the reaction rate over Pd−Ni/Y_2O_3 catalyst (P(CH_4)= 10kPa, P(O_2)=2kPa, P(He)=68-84kPa, total flowrate=140mL/min)

Even though oxidative CO_2 reforming has been studied since 1991 starting from Ashcroft et al. work [18], there is no literature available on the reaction mechanism. Choudhary et al. [143] suggested that a set of reactions occur during the OCRM reaction as follows:

$$CH_4 + CO_2 \rightarrow 2CO + 2H_2 \qquad \Delta H°_{298} = +61 \text{ kcal/mol} \qquad (1)$$

$$CH_4 + \tfrac{1}{2} O_2 \rightarrow CO + 2H_2 \qquad \Delta H°_{298} = -5 \text{ kcal/mol} \qquad (2)$$

$$CH_4 + 2O_2 \rightarrow CO_2 + 2H_2O \qquad \Delta H°_{298} = -192 \text{ kcal/mol} \qquad (3)$$

$$CH_4 + H_2O \rightarrow CO + 3H_2 \qquad \Delta H°_{298} = +54 \text{ kcal/mol} \qquad (4)$$

$$CH_4 + 1\tfrac{1}{2} O_2 \rightarrow CO + 2H_2O \qquad \Delta H°_{298} = -124 \text{ kcal/mol} \qquad (5)$$

$$CO + H_2O \rightarrow CO_2 + 2H_2 \qquad \Delta H°_{298} = -8 \text{ kcal/mol} \qquad (6)$$

$$CO_2 + 2H_2 \rightarrow CO + H_2O \qquad \Delta H°_{298} = +8 \text{ kcal/mol} \qquad (7)$$

Reaction (1) represents CO_2 (dry) reforming of methane (DRM) reaction while reaction (2) represents partial oxidation of methane (POM) reaction. Both are the main reactions in oxy-CO_2 reforming of methane and increase the energy efficiency of the process. However, reactions (3) to (7) are possibly occur concurrently with the main reactions. Reactions (3) and (5) represent methane combustion reactions which are possible with excess of oxygen. Reaction (4) represents steam methane reforming to produce syngas. Reaction (6) and (7) are the water gas shift (WGS) and the reverse water gas shift reactions, respectively.

Since the OCRM reaction involves the DRM and POM reactions with reverse water gas shift (rWGS) reaction as the side reaction, the available reaction mechanisms in literature for DRM, POM, and rWGS are useful for deriving the kinetic model for the OCRM reaction. The reaction mechanism for the DRM reaction has been studied long

time ago. Even though the reaction mechanism also depends on the type of active metal and catalyst supports, it has similarity in the basic concept. Laosiripojana and Assabumrungrat [46] derived the kinetic model for the DRM reaction over high surface area ceria based on the following proposed model:

$$CH_4 + 2S_{Ce} \rightleftharpoons CH_3 - S_{Ce} + H - S_{Ce} \quad \text{RDS} \quad (8)$$

$$CH_3 - S_{Ce} + S_{Ce} \rightleftharpoons CH_2 - S_{Ce} + H - S_{Ce} \quad (9)$$

$$CH_2 - S_{Ce} + S_{Ce} \rightleftharpoons CH - S_{Ce} + H - S_{Ce} \quad (10)$$

$$CH - S_{Ce} + S_{Ce} \rightleftharpoons C - S_{Ce} + H - S_{Ce} \quad (11)$$

$$C - S_{Ce} + O_x \rightleftharpoons CO + O_{x-1} + S_{Ce} \quad (12)$$

$$CO_2 + O_{x-1} \rightleftharpoons O_x + CO \quad (13)$$

$$CO_2 + O_{x-1} \rightleftharpoons O_x + CO \quad (14)$$

$$2H - S_{Ce} \rightleftharpoons H_2 + 2S_{Ce} \quad (15)$$

$$H_2 + O_x \rightleftharpoons O_{x-1} + H_2O \quad (16)$$

According to their proposed reaction mechanism, the rate determining step in the DRM reaction is the surface methane adsorption on two active sites of ceria. Since ceria is well known to have oxygen storage, the surface oxygen molecules from ceria easily oxidize the adsorbed carbon to CO instead of CO_2. However, their reaction mechanism of the rWGS reaction as the side reaction is not clearly described. On the other hand, Tsipouriari and Verykios [86] proposed methane decomposition as the rate determining step on Rh/La_2O_3 catalyst. Their proposed mechanism is as follows:

$$CH_4 + S \rightleftharpoons CH_4 - S \quad \text{equilibrium} \quad (17)$$

$$CH_4 - S \rightarrow C - S + 2H_2 \quad \text{slow} \quad (18)$$

$$CO_2 + La_2O_3 \rightleftharpoons La_2O_2CO_3 \quad \text{equilibrium} \quad (19)$$

$$La_2O_2CO_3 + C-S \rightarrow La_2O_3 + 2CO + S \quad \text{slow} \quad (20)$$

$$H_2 + 2S \rightleftharpoons 2H-S \quad \text{equilibrium} \quad (21)$$

Using transient studies, they observed that the rate dissociation of CO_2 is not significant as compared to the one of CH_4. Furthermore, the active carbon-containing species on the catalyst surface consist of carbon only, and not $CH_{x,x>0}$, species. Therefore, the carbon deposition mainly derives from CH_4 molecules. Moreover, they also observed the strong interaction between CO_2 and La_2O_3 to form $La_2O_2CO_3$ species. This step is very fast and considered to be at equilibrium. In addition, they also proposed the rWGS reaction mechanism as follows:

$$CO_2 + S \rightleftharpoons CO_2 - S \quad (22)$$

$$CO_2 - S + H - S \rightleftharpoons CO - S + OH - S \quad \text{slow} \quad (23)$$

$$OH - S + H - S \rightleftharpoons H_2O + 2S \quad (24)$$

Similar to the DRM reaction, the POM reaction mechanism has also been studied long time ago. There are two types of reaction mechanism proposed for the POM reaction, i.e. Combustion-Reforming Reaction mechanism (CRR) and Direct Partial Oxidation mechanism (DPO).

The CRR mechanism consists of exothermic methane combustion to produce carbon dioxide and water at the beginning of reaction, followed by endothermic reactions (CO_2 reforming of methane and steam reforming of methane) and water-gas shift reaction to produce syngas. Further studies by Vernon et al. [117] showed that at higher space velocities or methane/oxygen ratio, the selectivity to carbon dioxide and water increased. This indicated that syngas was a secondary product and confirmed the CRR mechanism.

This CPO mechanism proposed by Hickman and Schmidt [132-135] showed that syngas is produced as a primary product instead of secondary product. They observed that there was no significant improvement in methane conversion and CO selectivity when the space velocity was reduced to half. Therefore, they proposed the CPO mechanism as follows:

$$CH_4 \rightarrow CH_{x,s} + (4-x)H_s \quad (25)$$

$$2H_s \rightarrow H_{2,g} \quad (26)$$

$$O_{2,g} \rightarrow 2O_s \quad (27)$$

$$C_s + O_s \rightarrow CO_s \rightarrow CO_g \quad (28)$$

The side reactions involving OH to produce H_2O and CO_2 have to be considered and proposed to occur according to following reactions:

$$CH_{x,s} + O_s \rightarrow CH_{x-1,s} + OH_s \quad (29)$$

$$H_s + O_s \rightarrow OH_s \quad (30)$$

$$OH_s + H_s \rightarrow H_2O_g \quad (31)$$

$$CO_s + O_s \rightarrow CO_{2,g} \quad (32)$$

Even though there are two types of reaction mechanism for the POM, most of the kinetic models available in the literature are based on the CRR mechanism. Verykios [277] proposed a kinetic model for the POM reaction over Ni/La_2O_3 catalyst based on following elementary reactions:

$$CH_4 + S_1 \rightarrow \text{Intermediate} \rightarrow C.S_1 + 4H.S_1 \quad \text{RDS} \quad (33)$$

$$O_2 + S_2 \rightleftharpoons O_2.S_2 \quad \text{Equilibrium} \quad (34)$$

$$O_2.S_2 + S_2 \rightleftharpoons 2O.S_2 \quad \text{Fast} \quad (35)$$

$$C.S_1 + O.S_2 \rightleftharpoons CO.S_1 + S_2 \quad \text{RDS} \quad (36)$$

$$CO.S_1 + O.S_2 \rightarrow CO_2 + S_1 + S_2 \quad \text{Fast} \quad (37)$$

$$H.S_1 + O.S_2 \rightarrow OH.S_1 + S_2 \quad \text{Very fast} \quad (38)$$

$$OH.S_1 + H.S_1 \rightarrow H_2O + 2S_1 \quad \text{Very fast} \quad (39)$$

According to them, methane adsorption on particular sites (S1) on the Ni surface is the rate determining step, followed by methane decomposition to adsorbed C and H. Oxygen adsorbs on different sites (S2) via molecular precursor. The adsorbed carbon reacts with the adsorbed oxygen to form CO, which is also a rate determining step. The produced CO reacts rapidly with adsorbed oxygen to produce CO_2. The adsorbed hydrogen also reacts rapidly to form H_2O.

Recently, Gubanova et al [278] evaluated the available kinetic models in the literature and based on the evaluation, they proposed the following reaction mechanism:

$$O_2 + 2S \overset{k_{1,-1}}{\rightleftharpoons} 2O.S \quad (40)$$

$$CH_{4,g} + 5S \xrightarrow{k_2} C.S + 4H.S \quad \text{RDS} \quad (41)$$

$$C.S + O.S \overset{k_{3,-3}}{\rightleftharpoons} CO.S + S \quad (42)$$

$$CO.S + O.S \overset{k_{4,-4}}{\rightleftharpoons} CO_{2,g} + 2S \quad (43)$$

$$CO.S \overset{k_{5,-5}}{\rightleftharpoons} CO_g + S \quad (44)$$

$$2H.S \overset{k_{6,-6}}{\rightleftharpoons} H_{2,g} + 2S \quad (45)$$

$$2H.S + O.S \overset{k_{7,-7}}{\rightleftharpoons} H_2O_g + 3S \quad (46)$$

Using degree of rate control developed by Campbell [279], they concluded that the oxidation of carbonaceous intermediates to adsorbed carbon monoxide was less important than methane activation. Therefore, the reaction (41) was the rate determining step. This RDS is same as the rate determining step proposed by Verykios [277].

The kinetic model for reverse water gas shift reaction (rWGS) has been studied long time ago. Ginés et al. [280] proposed the kinetic model based on surface redox mechanism as follows:

$$CO_{2,g} + 2S \rightleftharpoons CO.S + O.S \qquad \text{RDS} \qquad (47)$$

$$CO.S \rightleftharpoons CO_g + S \qquad \text{very fast} \qquad (48)$$

$$H_{2,g} + 2S \rightleftharpoons 2H.S \qquad \text{Equlibrium} \qquad (49)$$

$$2H.S + O.S \rightleftharpoons H_2O.S + 2S \qquad \text{Equilibrium} \qquad (50)$$

$$H_2O.S \rightleftharpoons H_2O_g + S \qquad \text{very fast} \qquad (51)$$

The CO_2 dissociation was suggested to be the rate determining step based on the work of Nakamura et al. [281] since the rate of the dissociative adsorption of carbon dioxide on Cu (110) was similar to the rate of the rWGS reaction.

Based on the elementary reactions of the DRM, POM, and rWGS reactions available in the literature as discussed above, two reaction mechanisms for the OCRM have been proposed in this study to develop Langmuir-Hinshelwood kinetic models. The first reaction mechanism (RM-I) is proposed as follows:

$$CH_4 + S \xrightleftharpoons{k_{1,-1}} CH_4.S \qquad \text{RDS: DRM \& POM} \qquad (52)$$

$$CH_4.S + 4S \xrightleftharpoons{k_{2,-2}} C.S + 4H.S \qquad \text{equilibrium} \qquad (53)$$

$$O_2 + 2S \xrightleftharpoons{k_{3,-3}} 2O.S \qquad \text{fast} \qquad (54)$$

$$CO_2 + 2S \overset{k_{4,-4}}{\rightleftharpoons} CO.S + O.S \qquad \text{RDS: rWGS} \qquad (55)$$

$$C.S + O.S \overset{k_{5,-5}}{\rightleftharpoons} CO.S + S \qquad \text{very fast} \qquad (56)$$

$$2H.S + O.S \overset{k_{6,-6}}{\rightleftharpoons} H_2O.S + 2S \qquad \text{equilibrium} \qquad (57)$$

$$H_2O.S \overset{k_{7,-7}}{\rightleftharpoons} H_2O + S \qquad \text{very fast} \qquad (58)$$

$$2H.S \overset{k_{8,-8}}{\rightleftharpoons} H_2 + 2S \qquad \text{very fast} \qquad (59)$$

$$CO.S \overset{k_{9,-9}}{\rightleftharpoons} CO + S \qquad \text{very fast} \qquad (60)$$

The first kinetic model (LH-I) has been developed using the rate determining step (RDS) for dry reforming of methane as methane adsorption (reaction 52) and that for reverse water gas shift reaction as CO_2 adsorption (reaction 55). All reactions are assumed to be at equilibrium except the rate determining steps. These equations are written in terms of the known concentrations as follows. The equilibrium constants are lumped to reduce the number of parameters.

$$C_{CH_4.S} = \frac{P_{CO}P_{H_2}^2 K_6 K_7 C_s}{K_2 K_5 K_8^3 K_9 P_{H_2O}} = \frac{K_{CH_4.S} P_{CO} P_{H_2}^2 C_s}{P_{H_2O}} \qquad (61)$$

$$C_{C.S} = \frac{K_6 K_7 P_{CO} C_s}{K_5 K_9 P_{H_2O}} = \frac{K_{CO.S} P_{CO} C_s}{P_{H_2O}} \qquad (62)$$

$$C_{O_2.S} = K_3^{1/2} P_{O_2}^{1/2} C_s \qquad (63)$$

or

$$C_{O.S} = \frac{K_8 P_{H_2O} C_s}{K_6 K_7 P_{H_2}} = \frac{K_{H_2O.S} P_{H_2O}}{P_{H_2}} \qquad (64)$$

$$C_{H_2O.S} = \frac{P_{H_2O} C_s}{K_7} = K_{H_2O} P_{H_2O} C_s \qquad (65)$$

$$C_{H.S} = \frac{P_{H_2}^{1/2} C_s}{K_8^{1/2}} = K_{H_2} P_{H_2}^{1/2} C_s \quad (66)$$

$$C_{CO.S} = \frac{P_{CO} C_s}{K_9} = K_{CO} P_{CO} C_s \quad (67)$$

$$C_T = C_s + C_{CH_4.s} + C_{C.s} + C_{O.s} + C_{H_2O.s} + C_{H.s} + C_{CO.s} \quad (68)$$

$$C_s = \frac{C_T}{1 + K_{CH_4.S} P_{CO} P_{H_2}^2 / P_{H_2O} + K_{CO.S} P_{CO} / P_{H_2O} + K_{H_2O.S} P_{H_2O} / P_{H_2} + K_{H_2O} P_{H_2O} + K_{H_2} P_{H_2}^{1/2} + K_{CO} P_{CO}} \quad (69)$$

Since reactions (56), (58), (59), and (60) are very fast, suggesting that the equilibrium constants (K) of those reactions are very big, the $C_{H_2O.S}$, $C_{H.S}$, and $C_{CO.S}$ are equal to zero. Therefore, equation (69) can be simplified as follows:

$$C_s = \frac{C_T}{1 + K_{CH_4.S} P_{CO} P_{H_2}^2 / P_{H_2O} + K_{CO.S} P_{CO} / P_{H_2O} + K_{H_2O.S} P_{H_2O} / P_{H_2}} \quad (70)$$

The rate of the DRM reaction using methane adsorption (reaction 52) as the RDS can be written as:

$$r_{DRM} = k'_{DRM} P_{CH_4} C_s \quad (71)$$

$$r_{DRM} = \frac{k_{DRM} P_{CH_4}}{1 + K_{CH_4.S} P_{CO} P_{H_2}^2 / P_{H_2O} + K_{CO.S} P_{CO} / P_{H_2O} + K_{H_2O.S} P_{H_2O} / P_{H_2}} \quad (72)$$

Where $k_{DRM} = k'_{DRM} C_T$.

The rate of the rWGS reaction using CO_2 adsorption (reaction 55) as the RDS can be written as:

$$r_{rWGS} = k'_{rWGS} P_{CO_2} C_s^2 \quad (73)$$

$$r_{rWGS} = \frac{k_{rWGS} P_{CO_2}}{\left[1 + K_{CH_4.S} P_{CO} P_{H_2}^2 / P_{H_2O} + K_{CO.S} P_{CO} / P_{H_2O} + K_{H_2O.S} P_{H_2O} / P_{H_2}\right]^2} \quad (74)$$

where $k_{rWGS} = k'_{rWGS} C_T^2$

Erdöhelyi et al. [77] studied individual dissociation reaction of CO_2 and CH_4 as well as CH_4+CO_2 interaction reaction over palladium catalyst and reported that dissociation of CO_2 was enhanced in the presence of CH_4, due to effect of hydrogen formed in the decomposition of CH_4 since no formation of any surface complexes between CO_2 and CH_4 was observed. Therefore, they proposed that the rate determining step was activation of CH_4 by adsorbed oxygen formed in the dissociation of CO_2.

Further investigation by Bitter et al. [282] using IR spectroscopy of CO_2 adsorption showed formation of carbonate species on the catalyst support, such as ZrO_2. The carbonate species was then reduced by adsorbed hydrogen from CH_4 decomposition on the metal to form an OH group and formate species, which subsequently decomposed to CO and an OH group. The OH group was later desorbed as water. The same phenomenon was reported by Ferreira-Aparicio et al. [283].

Patel and Pant [284] studied kinetic modeling of oxidative steam reforming of methanol and proposed decomposition of formate species to form CO and OH group as rate determining step of rWGS reaction.

Based on above literatures, the second reaction mechanism (RM-II) is proposed as follows:

$$O_2 + 2S \underset{k_{1,-1}}{\rightleftharpoons} 2O.S \quad \text{Fast} \quad (75)$$

$CO_2 + S \underset{}{\overset{k_{2,-2}}{\rightleftharpoons}} CO_2.S$	Equilibrium	(76)
$CH_4 + S \underset{}{\overset{k_{3,-3}}{\rightleftharpoons}} CH_4.S$	Equilibrium	(77)
$CH_4.S + O.S \underset{}{\overset{k_{4,-4}}{\rightleftharpoons}} CH_3.S + OH.S$	RDS: DRM	(78)
$CH_4.S + S \underset{}{\overset{k_{5,-5}}{\rightleftharpoons}} CH_3.S + H.S$	Fast	(79)
$CH_3.S + S \underset{}{\overset{k_{6,-6}}{\rightleftharpoons}} CH_2.S + H.S$	Fast	(80)
$CH_2.S + S \underset{}{\overset{k_{7,-7}}{\rightleftharpoons}} CH.S + H.S$	Fast	(81)
$CH.S + S \underset{}{\overset{k_{8,-8}}{\rightleftharpoons}} C.S + H.S$	Fast	(82)
$O.S + CO_2.S \underset{}{\overset{k_{9,-9}}{\rightleftharpoons}} COOO.S + S$	Fast	(83)
$2H.S + COOO.S \underset{}{\overset{k_{10,-10}}{\rightleftharpoons}} HCOO.S + OH.S + S$	Fast	(84)
$HCOO.S + S \underset{}{\overset{k_{11,-11}}{\rightleftharpoons}} CO.S + OH.S$	RDS: rWGS	(85)
$H.S + CO_2.S \underset{}{\overset{k_{12,-12}}{\rightleftharpoons}} CO.S + OH.S$	Equilibrium	(86)
$C.S + O.S \underset{}{\overset{k_{13,-13}}{\rightleftharpoons}} CO.S + S$	RDS: POM	(87)
$2H.S + O.S \underset{}{\overset{k_{14,-14}}{\rightleftharpoons}} H_2O.S + 2S$	Equilibrium	(88)
$H.S + OH.S \underset{}{\overset{k_{15,-15}}{\rightleftharpoons}} H_2O.S + S$	very fast	(89)
$H_2O.S \underset{}{\overset{k_{16,-16}}{\rightleftharpoons}} H_2O + S$	very fast	(90)
$2H.S \underset{}{\overset{k_{17,-17}}{\rightleftharpoons}} H_2 + 2S$	very fast	(91)
$CO.S \underset{}{\overset{k_{18,-18}}{\rightleftharpoons}} CO + S$	very fast	(92)

The second kinetic model (LH-II) has been developed using the rate determining step (RDS) for DRM as dissociation of adsorbed methane by adsorbed oxygen (reaction 78), RDS for POM as reaction between adsorbed carbon and adsorbed oxygen (reaction 87), and RDS for rWGS as formation of adsorbed CO and surface hydroxyl from formate species (reaction 85).

$$C_{O.S} = K_1^{1/2} P_{O_2}^{1/2} C_s = K_{O_2} P_{O_2}^{1/2} C_s \text{ or } C_{O.S} = \frac{K_{17} P_{H_2O} C_s}{K_{14} K_{16} P_{H_2}} = \frac{K_{O_2} P_{H_2O} C_s}{P_{H_2}} \quad (93)$$

$$C_{CO_2.S} = K_2 P_{CO_2} C_S = K_{CO_2} P_{CO_2} C_S \quad (94)$$

$$C_{CH_4.S} = K_3 P_{CH_4} C_S = K_{CH_4} P_{CH_4} C_S \quad (95)$$

$$C_{CH_3.S} = \frac{K_5 K_3 K_{17}^{1/2} P_{CH_4.S} C_S}{P_{H_2}^{1/2}} = \frac{K_{CH_3.S} P_{CH_4} C_S}{P_{H_2}^{1/2}} \quad (96)$$

$$C_{C.S} = \frac{K_8 K_7 K_6 K_5 K_3 K_{17}^2 P_{CH_4.S} C_S}{P_{H_2}^2} = \frac{K_{C.S} P_{CH_4.S} C_S}{P_{H_2}^2} \quad (97)$$

$$C_{HCOO.S} = \frac{K_{10} K_9 K_{17}^{1/2} P_{H_2O} P_{CO} C_s}{K_{12} K_{14} K_{16} P_{H_2}^{1/2}} = \frac{K_{HCOO.S} P_{H_2O} P_{CO} C_s}{P_{H_2}^{1/2}} \quad (98)$$

$$C_{OH.S} = \frac{K_{12} K_2 K_{18} P_{H_2}^{1/2} P_{CO_2} C_s}{K_{17}^{1/2} P_{CO}} = \frac{K_{OH.S} P_{H_2}^{1/2} P_{CO_2} C_s}{P_{CO}} \quad (99)$$

$$C_{H_2O.S} = \frac{P_{H_2O} C_s}{K_{16}} = K_{H_2O} P_{H_2O} C_s \quad (100)$$

$$C_{H.S} = \frac{P_{H_2}^{1/2} C_s}{K_{17}^{1/2}} = K_{H_2} P_{H_2}^{1/2} C_s \quad (101)$$

$$C_{CO.S} = \frac{P_{CO} C_s}{K_{18}} = K_{CO} P_{CO} C_s \quad (102)$$

$$C_T = C_S + C_{O.S} + C_{CO_2.S} + C_{CH_4.S} + C_{CH_3.S} + C_{HCOO.S} \quad (103)$$

$$C_s = \frac{C_T}{1 + K_{O_2} P_{H_2O} C_s / P_{H_2} + K_{CO_2} P_{CO_2} + K_{CH_4} P_{CH_4} + K_{CH_3.S} P_{CH_4} / P_{H_2}^{1/2} + K_{HCOO.S} P_{H_2O} P_{CO} / P_{H_2}^{1/2}} \quad (104)$$

Since reactions (75) and (80) are very fast, suggesting that the equilibrium constants (K) of those reactions are very big, the $C_{O.S}$ and $C_{CH3.S}$ is equal to zero. Therefore, equation (104) can be simplified as follows:

$$C_s = \frac{C_T}{1 + K_{CO_2} P_{CO_2} + K_{CH_4} P_{CH_4} + K_{HCOO.S} P_{H_2O} P_{CO} / P_{H_2}^{1/2} + K_{OH.S} P_{H_2}^{1/2} P_{CO_2} / P_{CO}} \quad (105)$$

The rate of the DRM reaction using dissociation of adsorbed methane by adsorbed oxygen (reaction 55) as the RDS can be written as:

$$r_{DRM} = k'_{DRM} C_{CH_4.S} C_{O.S} \quad (106)$$

$$r_{DRM} = k'_{DRM} \left(K_{CH_4} P_{CH_4} C_S \right) \left(\frac{K_{O_2} P_{H_2O} C_s}{P_{H_2}} \right) \quad (107)$$

$$r_{DRM} = \frac{k_{DRM} K_{CH_4} K_{O_2} P_{CH_4} P_{H_2O} / P_{H_2}}{\left(1 + K_{CO_2} P_{CO_2} + K_{CH_4} P_{CH_4} + K_{HCOO.S} P_{H_2O} P_{CO} / P_{H_2}^{1/2} + K_{OH.S} P_{H_2}^{1/2} P_{CO_2} / P_{CO}\right)^2} \quad (108)$$

Where $k_{DRM} = k'_{DRM} C_T^2$

The rate of the POM reaction using reaction between adsorbed carbon and adsorbed oxygen (reaction 65) as the RDS can be written as:

$$r_{POM} = k'_{POM} C_{C.S} C_{O.S}$$

$$r_{POM} = k'_{POM} \left(\frac{K_{C.S} P_{CH_4} C_S}{P_{H_2}^2} \right) \left(\frac{K_{O_2} P_{H_2O} C_s}{P_{H_2}} \right) \quad (109)$$

$$r_{POM} = \frac{k'_{POM} K_{C.S} K_{O_2} \left(\frac{P_{CH_4} P_{H_2O}}{P_{H_2}^3} \right)}{\left(1 + K_{CO_2} P_{CO_2} + K_{CH_4} P_{CH_4} + K_{HCOO.S} P_{H_2O} P_{CO} / P_{H_2}^{1/2} + K_{OH.S} P_{H_2}^{1/2} P_{CO_2} / P_{CO}\right)^2} \quad (110)$$

Where $k_{POM} = k'_{POM} C_T^2$

The rate of the rWGS reaction using formation of adsorbed CO and surface hydroxyl from formate species (reaction 63) as the RDS can be written as:

$$r_{rWGS} = k'_{rWGS} C_{HCOO.S} C_S - k'_{-rWGS} C_{CO.S} C_{OH.S} \quad (111)$$

$$r_{rWGS} = k'_{rWGS} \left(\frac{K_{HCOO.S} P_{H_2O} P_{CO} C_s}{P_{H_2}^{1/2}} \right) C_s$$

$$r_{rWGS} = \frac{k_{rWGS} P_{H_2O} P_{CO} / P_{H_2}^{1/2}}{\left(1 + K_{CO_2} P_{CO_2} + K_{CH_4} P_{CH_4} + K_{HCOO.S} P_{H_2O} P_{CO} / P_{H_2}^{1/2} + K_{OH.S} P_{H_2}^{1/2} P_{CO_2} / P_{CO}\right)^2} \quad (112)$$

where $k_{rWGS} = k'_{rWGS} K_{HCOO.S} C_T^2$

6.3.4. Parameter estimation and model validation

The rate of individual components in terms of mol g_{cat}^{-1} s^{-1} was determined using the stoichiometry of DRM and rWGS reaction as follows:

$$r_{CH_4} = -(r_{DRM} + r_{POM}).S_A \quad (113)$$

$$r_{CO_2} = -(r_{DRM} + r_{rWGS}).S_A \quad (114)$$

$$r_{CO} = (2r_{DRM} + r_{POM} + r_{rWGS}).S_A \quad (115)$$

$$r_{H_2} = (2r_{DRM} + 2r_{POM} - r_{rWGS}).S_A \quad (116)$$

$$r_{H_2O} = r_{rWGS}.S_A \quad (117)$$

The parameter estimation for all kinetic parameters is based on minimization algorithm using a combination of Gauss-Newton and Levenberg-Marquardt methods. The non-linear regression software used to fit the experiment data to reaction rate equations is NLREG, which compute the sum of squared residuals for one set of parameter values and then slightly alter each parameters value and recalculate the sum of squared residuals to see the effect of parameter value change to the sum value of squared residuals. The equation can be expressed as [276]:

$$\sum_{i=1}^{m} w_i \sum_{j}^{n} (r_{ij,\exp} - r_{ij,calc})^2$$

Where m and n are the number of parameters and observations, respectively; w_i is the weight factor for response i, r_{exp} and r_{calc} are experimental and calculated reaction rates, respectively.

In order to obtain all parameters value as a function of temperature, Arrhenius equation was used to obtain activation energy and pre-exponential factor according to following equation:

$$k_i = A_i \exp\left[\frac{-E_i}{RT}\right] \quad (118)$$

Meanwhile, the equilibrium constants of the adsorbed species as a function of temperature were estimated using a van't Hoff expression as follows:

$$\ln K_i = \frac{-\Delta H_i}{RT} + \frac{\Delta S_i}{R} \quad (119)$$

Table 6-1 shows all parameters for kinetic model LH-I and LH-II as functions of temperature. It is observed that the minimization algorithm using a combination of Gauss-Newton and Levenberg-Marquardt methods is only suitable for up to 2 reactions, such as individual DRM with rWGS as a side reaction. However, it is not suitable for complex reaction such as OCRM, which consists of more than 2 reactions. Therefore, the kinetic parameters for the kinetic model LH-I and LH-II are only available for DRM with rWGS as side reaction and simultaneous DRM-POM reactions, respectively.

In addition, it can be seen from the modeling results that the activation energy for DRM reaction for LH-I (3.71kJ/mol) is much lower than for LH-II (9.88kJ/mol). Bradford and Vannice [27] compiled a large amount of kinetic parameters for DRM reaction and reported that the activation energies values varied from 29 to 359kJ/mol. They also pointed out that the most frequently activation energy was observed at 58±4 kJ/mol which is coincidence with the activation energy for CH_4 dissociation on Ni catalyst.

Tomishige [246] studied the reaction mechanism of oxidative steam reforming of methane (OSRM) and suggested that the OSRM reaction proceeded with combustion and/ or partial oxidation of methane followed by CO_2 and/or steam reforming of methane. Since the OCRM reaction has similarity with OSRM, it therefore suggests that the combustion reaction either combustion or partial oxidation of methane takes place followed by CO_2 reforming of methane. Therefore, it is expected that the activation energies for DRM and POM reaction are lower than the individual reactions.

Table 6-1 Estimated parameters for kinetic model LH-I and LH-II

Reaction mechanism	Rate constant	A_i (mol m^{-2} s^{-1})	E_i (kJ mol^{-1})	ΔH_i (kJ mol^{-1})	ΔS_i (kJ mol^{-1} K^{-1})
LH-I	k_{DRM}	4.02E+26	3.71	-	-
	K_{DRM}	-	-	1.40	0.33
	$K_{CH_4.S}$	-	-	1.54	0.35
	k_{rWGS}	2.25E+26	3.63	-	-
	K_{rWGS}	-	-	-0.15	-0.029
LH-II	k_{DRM}	3.65E+23	9.88	-	-
	$K_{CH_4.S}$	-	-	2.58	0.45
	k_{POM}	3.19E+11	4.92	-	-
	$K_{C.S}$	-	-	4.97	0.68
	K_{O2}	-	-	-4.40	0.49
	K_{CO2}	-	-	3.04	0.49

Furthermore, Imanaka et al. [202] showed that Y_2O_3 can form $Y_2O_2CO_3$ (yttrium oxycarbonate) species during introduction of CO_2, similar to the $La_2O_2CO_3$ (lanthanum oxycarbonate) species. Moreover, Verykios [55] showed that the oxycarbonate species can interact with surface carbon species from CH_4 decomposition to form CO gas. These steps are in agreement with the proposed elementary reactions of the LH-II model.

The large numbers of experimental and predicted data of CH_4 conversion of LH-II model was compared by means of parity plots as shown in Figure 6-7. It can be seen that there is no significant deviation about the line of parity and the correlation coefficient is

around 0.98. A good fit was obtained CH4 conversion indicates that the proposed LH-II model is suitable for representing the OCRM reaction.

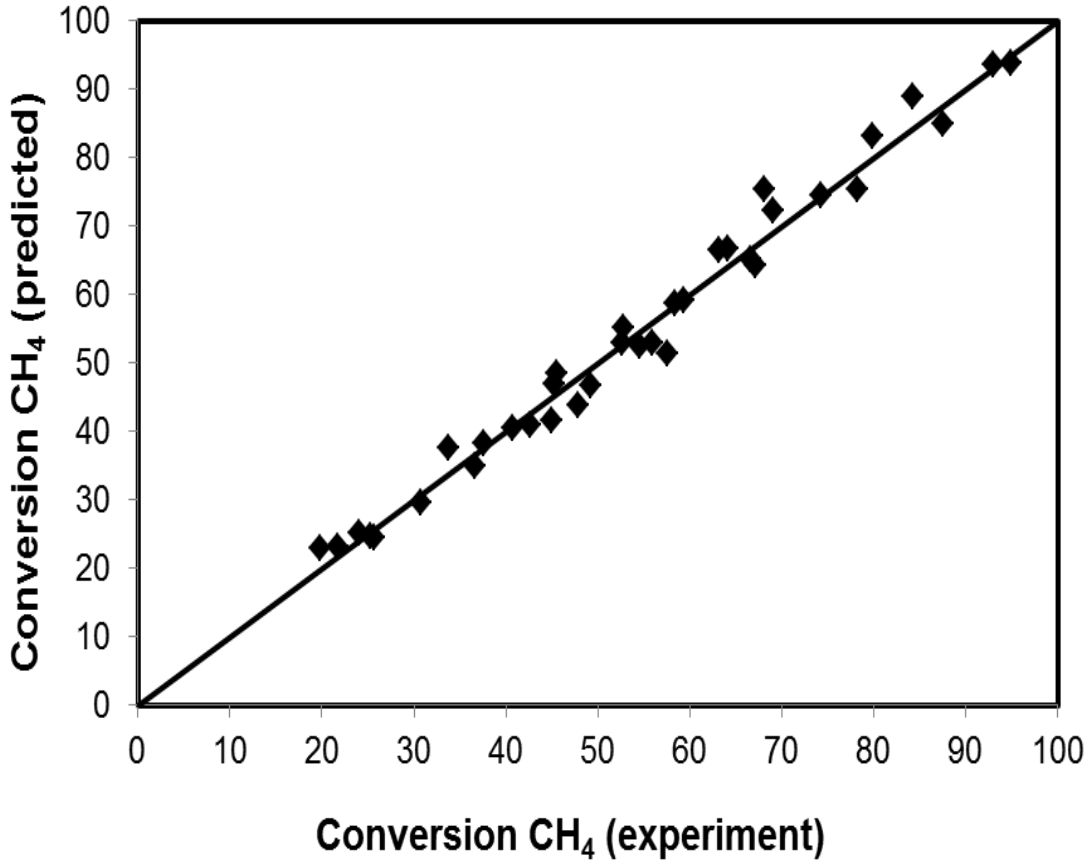

Figure 6-7 Parity plot of experimental and predicted conversion of CH_4. Correlation coefficient $r^2 = 0.98$. (T = 600-750°C, W/F = 0.96-4.8 $kg_{cat}.s.mol^{-1}$, P = 1 atm)

6.4. Conclusion

A kinetic study of oxidative CO_2 reforming of methane was performed over Pd−Ni/Y_2O_3 catalyst with Pd/Ni ratio of 1/1 for the OCRM reaction. The reaction rate was found to be influenced by partial pressure of CH_4 and CO_2. However, the increase in CO_2 partial pressure has more dramatic effect on reaction rate than the one of CH_4. Since there

is no available literatures of kinetic study for the OCRM reaction, the proposed kinetic models are based on combination of kinetic study of individual reactions probably occurred in the OCRM reaction, i.e. DRM, POM, and rWGS. Two kinetic models were proposed considering different reaction mechanisms and rate-determining steps. The curve fitting results show a good agreement between experiment data and kinetic model based on dissociation of adsorbed methane by adsorbed oxygen as the rate determining step of DRM reaction and reaction between adsorbed carbon and adsorbed oxygen as the rate determining step of POM reaction.

CHAPTER 7

Conclusions and Recommendations

7.1. Conclusions

This thesis is one of the first theses to demonstrate the energy-efficient OCRM reaction resulted from combination between endothermic reaction (DRM) and exothermic reaction (POM). The catalyst developed in this thesis provides superior and viable alternative to usual Ni catalyst that easily deactivates. It also provides alternative to the popular Ni perovskites catalyst used for reforming reaction. The principal contributions from this thesis are the synergetic effect of bimetallic particles on catalyst activity, the role of metal-support interaction on the catalyst activity and stability, the unique properties of Y_2O_3 support and its roles in OCRM reaction, the effect of surface oxygen mobility, and the kinetic modeling of OCRM reaction.

The monometallic Ni/Y_2O_3 catalyst has high initial activity but severe deactivation due to high carbon deposition rate, while the monometallic Pd/Y_2O_3 catalyst has low initial activity but stable during OCRM reaction. In order to take the advantage of both Ni/Y_2O_3 and Pd/Y_2O_3 catalysts, the Ni/Y_2O_3 catalyst was modified with a certain amount of Pd. Two types of Pd precursors, i.e. $PdCl_2$ and $Pd(NO_3)_2$ were used to synthesize $Pd{-}Ni/Y_2O_3$ catalysts. The catalytic result shows that both $Pd{-}Ni/Y_2O_3$ catalysts synthesized from either $PdCl_2$ or $Pd(NO_3)_2$ precursor has much higher performance in terms of CH_4 and CO_2 conversions than either Ni/Y_2O_3 catalyst or Pd/Y_2O_3 catalyst, due to the presence of bimetallic particles on $Pd{-}Ni/Y_2O_3$ catalyst. This result shows that the combination of Pd and Ni has synergistic effect on catalyst activity.

However, the catalyst activity of Pd(C)−Ni/Y_2O_3 catalyst (Pd−Ni/Y_2O_3 catalyst synthesized from $PdCl_2$) is higher than the one of Pd(N)-Ni/Y_2O_3 catalyst (Pd−Ni/Y_2O_3 catalyst synthesized from $Pd(NO_3)_2$). The characterization result shows formation of metal-support compound and small metal particle size on Pd(C)−Ni/Y_2O_3 catalyst while no metal-support compound and big metal particle size was observed on Pd(N)−Ni/Y_2O_3 catalyst, showing that the small metal particle size is resulted from the presence of metal-support compound. Further observation using various Pd/Ni ratios of Pd(C)−Ni/Y_2O_3 catalysts shows that the higher the reduction peak of the metal-support compound on Pd(C)−Ni/Y_2O_3, the smaller the metal particle size. Therefore, it can be concluded that the small metal particle size resulted from the presence of metal-support compound is important for high catalyst activity.

The catalyst activity and stability of Pd−Ni catalyst was further studied over various commercial catalyst supports. Among all tested Pd−Ni catalysts, Pd−Ni/Y_2O_3 and Pd−Ni/Al_2O_3 catalysts show very high initial CH_4 and CO_2 conversions, due to formation of metal-support compound (MSC) on these two catalysts. However, the type of metal interacting with the support is different in Pd−Ni/Y_2O_3 and Pd−Ni/Al_2O_3 catalyst. Pd interacts with Y in Pd−Ni/Y_2O_3 catalyst to form $Pd_xCl_yY_z$ compound, while Ni interacts with Al in Pd−Ni/Al_2O_3 catalyst to form $NiAl_2O_4$ compound. The formation of metal-support compound was observed to be able to prevent severe metal sintering on catalyst during reaction. However, the amount of carbon produced from Pd−Ni/Y_2O_3 catalyst is much lower than the one from Pd−Ni/Al_2O_3 catalyst, due to the presence of surface β−oxygen species and ability of Y_2O_3 to form oxycarbonate species, resulting in stable catalytic performance without noticeable deactivation during reaction. The surface

β−oxygen species are found to promote cracking of C−H bond in CH_4 while the oxycarbonate species can oxidize the deposited carbon, respectively, hence leading to the stability of the Pd−Ni/Y_2O_3 catalyst. A reaction mechanism over Pd−Ni/Y_2O_3 catalyst was then proposed.

Surface oxygen mobility has been reported to affect the catalyst performance in many reactions. This thesis shows the formation of monodispersed Y_2O_3 particles synthesized using homogeneous precipitation method at various pH solutions. It was found that Y_2O_3 synthesized at lower pH solution has smaller particle size and higher oxygen mobility due to smaller crystal size. When the synthesized Y_2O_3 was used as support, the Pd−Ni/Y_2O_3 catalyst with higher oxygen mobility shows higher activity and lower carbon deposition rate. Furthermore, CH_4 decomposition reaction was also performed on the Pd−Ni/Y_2O_3 catalysts and the result shows the higher amount of CO produced from Pd−Ni/Y_2O_3 catalyst with smaller crystal size. This study shows that surface oxygen mobility has crucial roles on catalytic activity and suppression of carbon deposition on Pd−Ni/Y_2O_3 catalyst.

Finally, this thesis demonstrates the kinetic study and models for the OCRM reaction over the Pd−Ni/Y_2O_3 catalyst. Up to date, this is the first study to develop the kinetic model using Langmuir-Hinshelwood (LH) approach for OCRM reaction. Based on the proposed reaction mechanism and those of individual reactions probably occurred during OCRM reaction, two kinetic models for OCRM reaction over Pd−Ni/Y_2O_3 catalyst have been developed using Langmuir-Hinshelwood (LH) approach. A good agreement was obtained between experimental and model for the kinetic model based on dissociation of adsorbed methane by adsorbed oxygen for rate determining step (RDS) of

DRM and reaction between adsorbed carbon and adsorbed oxygen for RDS of POM. This kinetic model is useful for understanding the effect of process conditions to catalyst performance and scaling-up to commercial reactor.

7.2. Recommendations

The work in this thesis provides the fundamentals for developing catalyst with high activity and stability in reforming reactions. Since Pd is expensive metal, the developed Pd−Ni catalyst is unsuitable for commercialization. Therefore, using the fundamentals observed in this thesis, there is more room to develop cheaper catalyst with same or even higher catalyst activity and stability. In addition, the chloride residue in catalyst usually has negative impact to catalytic stability in many reactions. However, this thesis shows that the use of $PdCl_2$ as Pd precursor in Pd−Ni/Y_2O_3 catalyst shows high stability without deactivation. The positive effect of precursors from chloride on catalyst stability may open up new area in catalysis for other reactions.

The kinetic study in this thesis used the method which has been reported in literature for complex reaction such as oxidative steam reforming of methanol [284]. The result of the method showed a good kinetic model even though the conversion is high. However, the conversion for kinetic measurement is usually very low, less than 10%. Therefore, it is recommended to collect the kinetic data at very low conversion and perform another kinetic model for good comparison. Moreover, the validity of the model needs to be supported by experiment work such as various characterizations of reduced and spent catalysts. In addition, the experiment work to prove the reaction mechanism of OCRM reaction has not been touched in this thesis. The work represents an interesting

extension for future work. In addition, since the numerical method used to obtain the kinetic parameters for the kinetic model developed in this thesis can be used only for up to 2 reactions while the OCRM reaction may consist of more than 2 reactions, it is therefore important to consider another numerical method which can solve complex reactions such as OCRM reaction.

References

1. Wang, J.S.; Manovic V.; Wu Y.H.; Anthony E.J. *Appl. Energ*. **2010**, 87, 1453–1458.
2. Huang, J.; Zou, J.; Winston Ho, W. S. *Ind. Eng. Chem. Res.* **2008**, 47, 1261.
3. Vázquez,G.; Alvarez, E.; Navaza, J.M.; Rendo, R.; Romero, E. *J. Chem. Eng. Data* **1997**, 42, 57–61.
4. Shiflett, M.B.; Yokozeki, A. *Ind. Eng. Chem. Res.* **2005**, 44, 4453–4464.
5. Schaefer, M.; Behrendt, F.; Hammer, T; *Front. Chem. Eng. China* **2010**, 4(2), 172-183.
6. Kim, J-Hl; Paxton, E. R.; Tomasko, D. L. *Biotechnol. Progr*. **1996**, 12 (5), 650-661.
7. Xiao-Bing, L.; Ying-Ju Z.; Bin L.; Xiao L.; Hui W. *J. Mol. Catal. A.: Chem.* **2004**, 210, 31-34.
8. Tomishige, K.; Yasuda, H.; Yoshida, Y.; Nurunnabi, M.; Li, B.; Kunimori, K. *Green Chem.* **2004**, 6, 206-214.
9. Darensbourg, D.J.; Holtcamp, M.W. *Coord. Chem. Rev.* **1996**, 153, 155-174.
10. Hu, Y.H.; Ruckenstein, E. *Adv. Catal.* **2004**, 48, 297-345.
11. Energy Information Administration, *Annual Energy Review 2006*, **2007**.
12. Mark, M.F.; Maier, W. F. *J. Catal.* **1996**, 164, 122-130.
13. Rezaei, M.; Alavi, S.M.; Sahebdelfar, S.; Yan, Z.-F. *J. Nat. Gas. Chem.* **2006**, 15**,** 327-334.
14. Ruckenstein, E.; Hu, Y.H. *J. Catal.* **1996**, 162, 230-238.
15. Zhang, Z.L.; Verykios, X.E. J. Chem. Soc., *Chem. Comm.* **1995**, 1, 71-72.
16. Wang, S.; Lu, G.Q. (Max). *Appl. Catal. B: Environ.* **1998**, 19**,** 267-277.

17. Horiuchi, T.; Sakuma, K.; Fukui, T.; Kubo, Y.; Osaki, T.; Mori, T. *Appl. Catal. A: Gen.* **1996**, 144, 111-120.

18. Ashcroft, A.T.; Cheetham, A.K.; Green, M.L.H.; Vernon, P.D.F. *Nature* **1991**, 352, 225-226.

19. Dissanayake, D.; Rosynek, M.P.; and Lunsford, J.H. *J. Catal.* **1991**, 132, 117-127.

20. Yoshida, K.; Begum, N.; Ito, S.-I.; Tomishige, K. *Appl. Catal. A: Gen* **2009**, 358, 186-192.

21. Ruckenstein, E.; Hu, Y.H. *Ind. Eng. Chem. Res* **1998**, 37, 1744-1747.

22. He, S.; Hong, W.; Yu, W.; Mo, L.; Lou, H.; Zheng, X. *Int. J. Hydrogen Energ.* **2009**, 34, 839-843.

23. Gadalla, A.M.; Bower, B. *Chem. Eng. Sci.* **1988**, 43, 3049-3062.

24. Wang, S; Lu, G.Q.(Max); Millar, G. *Energ. Fuel* **1996**, 10, 896–904.

25. Zhang, J.; Wang, H.; Ajay, K.D. *J. Catal.* **2007**, 249, 300–310.

26. Sacco, A. Jr.; Geurts, F.W.A.H.; Jablonski, G.A.; Lee, S.; Gatell, R.A. *J. Catal.* **1989**, 119, 322-341.

27. Bradford, M.C.J.; Vannice, M.A. *Catal. Rev. Sci. Eng.* **1999**, 41, 1–42.

28. Rostrup-Nielsen, J.R.; Bak Hansen, J-H. *J. Catal.* **1993**, 144, 38-49.

29. Ruckenstein, E.; Hu, Y. H. *J. Catal.* **1996**, 162, 230-238.

30. Hu, Y. H.; Ruckenstein, E. *J. Phys. Chem. B* **1999**, 101, 7563-7565.

31. Takayasu, O.; Takegahara, Y.; and Matsuura, I. *Energ. Convers. Manage.* **1995**, 36, 597-600.

32. Chen, Y.G.; Ren, J. *Catal. Lett.* **1994**, 29, 39-48.

33. Sridhar, S.; Sichen, D.; Seetharaman, S. Z. *Metallkd.* **1994**, 85, 615-620.

34. Bhattacharyya, A.; Chang, V.W. *Stud. Surf. Sci. Catal.* **1994**, 88, 207-213.

35. Wang, S.; Lu, G.Q. (Max). *Appl. Catal. B: Environ.* **1998**, 19, 267–277.

36. Xu, G.L.; Shi, K.Y.; Gao, Y.; Xu, H.Y.; Wei, Y.D. *J. Mol. Catal. A: Chem.* **1999**, 147, 47-54.

37. Bradford, M.C.J.; Vannice, M.A. *Appl. Catal. A: Gen.* **1996**, 142, 73-96.

38. Ruckenstein, E.; Hu, Y.H. *Chem. Innovat.* **2000**, 30, 39-43.

39. Hu, Y.H.; Ruckenstein, E. *J. Catal.* **1999**, 184, 298-302.

40. Hu, Y.H.; Ruckenstein, E. *J. Catal.* **1996**, 163, 306-311.

41. Hu, Y.H.; Ruckenstein, E. Langmuir **1997**, 13, 2055-2058.

42. Hu, Y.H.; Ruckenstein, E. *Catal. Rev.Sci. Eng.* **2002**, 44, 423-454.

43. Ruckenstein, E.; Hu, Y.H. *Appl. Catal. A: Gen.* **1995**, 133, 149-161.

44. Tomishige, K.; Chen, Y.-G.; Fujimoto, K. *J. Catal.* **1999**, 181, 91-103.

45. Horiuchi, T.; Sakuma, K.; Fukui, T.; Kubo, Y.; Osaki, T.; Mori, T. *Appl. Catal. A: Gen.* **1996**, 144, 111-120.

46. Laosiripojana, N.; Assabumrungrat, S. *Appl. Catal. B: Environ.* **2005**, 60, 107-116.

47. Hally, W.; Bitter, J.H.; Seshan, K.; Lercher, J.A.; Ross, J.R.H. *Stud. Surf. Sci. Catal.* **1994**, 88, 167-173.

48. Li, X.S.; Chang, J.S.; Lee, F.K.; Park, S.E. *React. Kinet. Catal. Lett.* **1999**, 67, 375-381.

49. Li, X.S.; Chang, J.S.; Lee, F.K.; Park, S.E. *React. Kinet. Catal. Lett.* **1999**, 67, 383-389.

50. Lercher, J.A.; Bitter, J.H.; Halley, W.; Niessen, W.; Seshan, K. *Stud. Surf. Sci. Catal.* **1996**, 101, 463-472.

51. Wei, J.-M.; Xu, B.-Q.; Li, J.-L.; Cheng, Z.-X.; Zu, Q.-M. *Appl. Catal. A: Gen.* **2000**, 196, L167–L172.

52. Rezaei, M., Alavi, S.M.; Sahebdelfar, S.; Bai, P.; Liu, X.; Yan, Z.-F. *Appl. Catal. B: Environ.* **2007**, 77, 346-354.

53. Zhang, Z.L.; Verykios, X.E., *J. Chem. Soc, Chem. Comm.* **1995**, 71-72.

54. Verykios, X.E. *Int. J. Hydrogen Energ.* **2003**, 28, 1045 – 1063.

55. Ruckenstein, E.; Hu, Y.H., *J. Catal.* **1996**, 161, 55-61.

56. Halliche, D.; Bouarab, R.; Cherifi, O.; Bettahar, M.M. *Catal. Today* **1996**, 29, 373-377.

57. Choi, J.S.; Moon, K.I.; Kim, Y.G.; Lee, J.S.; Kim, C.H.; Trimm, D.L. *Catal. Lett.* **1998**, 52, 43-47.

58. Seok, S.H.; Han, S.H.; Lee, J.S. *Appl. Catal. A: Gen.* **2001**, 215, 31-38.

59. Quincoces, C.E.; de Vargas, S.P.; Grange, P.; Gonzalez, M.G. *Mater. Lett.* **2002**, 56, 698-704.

60. Cheng, Z.; Wu, Q.; Li, J.; Zhu, Q. *Catal. Today* **1996**, 30, 147-155.

61. Li, X.S.; Chang, J.S.; Tian, M.Y.; Park, S.E. *Appl. Organometal. Chem.* **2001**, 15, 109-112.

62. Slagtern, A.; Olsbye, U.; Blom, R.; Dahl, I.M.; Fjellvag, H.; *Appl. Catal. A: Gen.* **1997**, 165, 379-390.

63. Montoya, J.A.; Romero-Pascual, E.; Gimon, C.; Del Angel, P.; Monzón, A. *Catal. Today* **2000**, 63, 71-85.

64. Osaki, T.; Masuda, H.; Horiuchi, T.; Mori, T. *Catal. Lett.* **1995**, 34, 59-63.

65. Ruckenstein, E.; Wang, H. Y. *J. Catal.* **2002**, 205, 289-293.

66. Ruckenstein, E.; Wang, H.Y., *Appl. Catal. A: Gen.* **2000**, 204, 257-263.

67. Ruckenstein, E.; Wang, H.Y. *Catal. Lett.* **2001**, 73, 99-105.

68. Guerrero-Ruiz, A.; Sepulveda-Escribano, A.; Rodriguez-Ramos, I. *Catal. Today* **1994**, 21, 545-550.

69. Takanabe, K.; Nagaoka, K.; Nariai, K.; Aika, K.-I. *J. Catal.* **2005**, 232, 268-275.

70. Zhang, Z. L.; Tsipouriari, V.A.; Efstathiou, A.M.; Verykios, X.E. *J. Catal.* **1996**, 158, 51-63.

71. Yokota, S.; Okumura, K.; Niwa, M. *Catal. Lett.* **2002**, 84, 131-134.

72. Nagaoka, K.; Seshan, K.; Aika, K.-I.; Lercher, J.A. *J. Catal.* **2001**, 197, 34-42.

73. Souza, M.M.V.M.; Aranda, D.A.G.; Schmal, M. *J. Catal.* **2001**, 204, 498-511.

74. Souza, M.M.V.M.; Aranda, D.A.G.; Schmal, M. *Ind. Eng. Chem. Res.* **2002**, 41, 4681 (2002).

75. Bitter, J.H., Hally, W.; Seshan, K.; van Ommen, J.G.; Lercher, J.A. *Catal. Today* **1996**, 29, 349-353.

76. Bitter, J.H., Seshan, K., and Lercher, J.A., *J. Catal.* **1999**, 183, 336-343.

77. Erdöhelyi, A.; Cserényi, J.; Papp, E.; Solymosi, F. *Appl. Catal. A: Gen.* 1994, 108, 205-219.

78. Itkulova, Sh. S.; Zhunusova, K. Z.; Zakumbaeva, G. D. *Appl. Organometal. Chem.* **2000**, 14, 850–852.

79. Nagaoka, K.; Takanabe, K.; Aika, K. *Appl. Catal. A: Gen.* **2004**, 268, 151–158.

80. Chen, Y-.G.; Yamazaki, O.; Tomishige, K.; Fujimoto, K. *Catal. Lett.* **1996**, 39, 91-95.

81. Tejuca, L.G.; Fierro, J.L.G.; Tascón, J.M.D.; Tejuca, L.G. *Adv. Catal.* **1989**, 36, 237–328.

82. Peña, M.A.; Fierro, J.L.G. *Chem. Rev.* **2001**, 101, 1981–2018.

83. Fan, M.-S.; Abdullah, A.Z.; Bhatia, S. *ChemCatChem*. **2009**, 1, 192 – 208.

84. Batiot-Dupeyrat, C.; Valderrama, G.; Meneses, A.; Martinez, F.; Barrault, J.; Tatibouë, J.M. *Appl. Catal. A: Gen.* **2003**, 248, 143-151.

85. Gallego, G.S.; Mondragón, F.; Barrault, J.; Tatibouët, J.-M.; Batiot-Dupeyrat, C. *Appl. Catal. A: Gen.* **2006**, 311, 164-171.

86. Tsipouriari, V.A.; Verykios, X.E. *Catal. Today* **2001**, 64, 83–90.

87. Topalidis, A.; Petrakis, D.E.; Ladavos, A.; Loukatzikou, L.; Pomonis, P. *J. Catal. Today* **2007**, 127, 238–245.

88. Ferreira-Aparicio, P.; Rodríguez-Ramos, I.; Anderson, J.A.; Guerrero-Ruiz, A. *Appl. Catal. A: Gen.* **2000**, 202, 183–196.

89. Nakamura, J.; Aikawa, K.; Sato, K.; Uchijima, T. *Catal. Lett.* **1994**, 25, 265–270.

90. Edwards, J.H.; Maitra, A.M. *Fuel Process. Technol.* **1995**, 42, 269-289.

91. Erdöhelyi, A.; Cserényi, J.; Solymosi, F. *J. Catal.* **1993**, 141, 287-299.

92. Rostrup-Nielsen, J.R.; Bak Hansen, J-H. *J. Catal.* **1993**, 144, 38-49.

93. Basini, L.; Sanfilippo, D. *J. Catal.* **1995**, 157, 162-178.

94. Verykios, X.E. *Int. J. Hydrogen Energ.* **2003**, 28, 1045-1063.

95. York, A.P.E.; Xiao, T.; Green, M.L.H. *Top. Catal.* **2003**, 22, 345-358.

96. Lødeng, R; Bjørgum, E.; Enger, B.C.; Eilertsen, J.S.; Holmen, A.; Krogh, B.; Rønnekleiv, M.; Rytter, E. *Appl. Catal. A: Gen.* **2007**, 333, 11-23.

97. Prettre, M.; Eichner, Ch.; Perrin, M. *Trans. Faraday Soc.* **1946**, 42, 335b-339.

98. Choudhary, V.R.; Rajput, A.M.; Prabhakar, B. *Catal. Lett.* **1992**, 15, 363-370.

99. Choudhary, V.R.; Rajput, A.M.; Prabhakar, B. *J. Catal.* **1993**, 139, 326-328.

100. Choudhary, V.R.; Rane, V.H.; Rajput, A.M. *Catal. Lett.* **1993**, 22, 289-297.

101. Choudhary, V.R.; Rajput, A.M.; Rane, V.H. *Catal. Lett.* **1992**, 16, 269-272.

102. Drago, R.S.; Jurczyk, K.; Kob, N.; Bhattacharyya, A.; Masin, *J. Catal. Lett.* **1998**, 51, 177-181.

103. Zhu, T.L.; Flytzani-Stephanopoulos, M. *Appl. Catal. A: Gen.* **2001**, 208, 403-417.

104. Takehira, K.; Shishido, T.; Kondo, M.; *J. Catal.* **2002**, 207, 307-316.

105. Tang, S.; Lin, J.; Tan, K.L. *Catal. Lett.* **1998**, 51, 169-175.

106. Tsipouriari, V.A.; Zhang, Z.; Verykios, X.E. *J. Catal.* **1998**, 179, 283-291.

107. Choudhary, V.R.; Uphade, B.S.; Mamman, A.S. *J. Catal.* **1997**, 172, 281-293.

108. Cao, L.; Chen, Y.; Li, W. *Stud. Surf. Sci. Catal.* **1997**, 107, 467-471.

109. Liu, S.L.; Xiong, G.X.; Sheng, S.S.; Miao, Q.; Yang, W.S. *Stud. Surf. Sci. Catal.* **1998**, 119, 747-752.

110. Wang, J.G., Liu, C.J., Zhang, Y.P., Zhu, X.L., Zou, J.J., Yu, K.L., and Eliasson, B., *Chem. Lett*. **2002**, 31, 1068-1069.

111. Vernon, P.D.F.; Green, M.L.H.; Cheetham, A.K.; Ashcroft, A.T. *Catal. Lett.* **1990**, 6, 181-186.

112. Vernon, P.D.F.; Green, M.L.H.; Cheetham, A.K.; Ashcroft, A.T. *Catal. Today* **1992**, 13, 417-426.

113. Claridge, J.B.; Green, M.L.H.; Tsang, S.C.; York, A.P.E.; Ashcroft, A.T.; Battle, P.D. *Catal. Lett.* **1993**, 22, 299-305.

114. Matsui, N.-o.; Nakagawa, K.; Ikenaga, N.-o.; Suzuki, T. *J. Catal.* **2000**, 194, 115-121.

115. Boucouvalas, J.; Efstathiou, A.M.; Zhang, Z.L.; Verykios, X.E. *Stud. Surf. Sci. Catal.* **1997**, 107, 435-440.

116. Elmasides, C.; Kondarides, D. I.; Grünert, W.; Verykios, X. E. J. Phys. Chem B. **1999**, 103, 5227-5239.

117. Ashcroft; A.T. ; Cheetham, A.K.; Foord, J.S.; Green, M.L.H.; Grey, C.P.; Murrell, A.J.; Vernon, P.D.F. Nature **1990**, 344, 319-321.

118. Nakagawa, K.; Anzai, K.; Matsui, N.; Ikenaga, N.; Suzuki, T.; Teng, Y.; Kobayashi, T.; Haruta, M. *Catal. Lett.* **1998**, 51, 163.

119. Nakagawa, K.; Ikenaga, N.; Suzuki, T.; Kobayashi, T.; Haruta, M. *Appl. Catal. A: Gen.* **1998**, 169, 281-290.

120. Jones, R.H.; Ashcroft, A.T.; Waller, D.; Cheetham, A.K.; Thomas, J.M. *Catal. Lett.*, **1991**, 8, 169-.174.

121. Buyevskaya, O.V.; Wolf, D.; Baerns, M. *Catal. Lett.* **1994**, 29, 249-260.

122. Wang, D.; Dewaele, O.; De Groote, A.M.; Froment, G.F. *J. Catal.* **1996**, 159, 418-426.

123. Baranova, E.A.; Fóti, G.; Comninellis, C. *Electrochem. Commun.* **2004**, 6, 170-175.

124. Otsuka, K.; Wang, Y.; Sunada, E.; Yamanaka, I. *J. Catal.* **1998**, 175, 152-160.

125. Fathi, M.; Bjorgum, E.; Viig, T.; Rokstad, O.A. *Catal. Today* **2000**, 63, 489-497.

126. Yan, Q.-G.; Chu, W.; Gao, L.-Z.; Yu, Z.-L.; Yuan, S.-Y. *Stud. Surf. Sci. Catal.* **1998**, 119, 855-860.

127. Mattos, L.V.; de Oliveira, E.R.; Resende, P.D.; Noronha, F.B.; Passos, F.B. *Catal. Today* **2002**, 77, 245-256.

128. Fangli, S.; Meiqing, S.; Yanan, F.; Jun, W.; Duan, W.; *J. Rare Earth* **2007**, 25, 316-320.

129. Feio, L.S.F.; Hori, C.E.; Mattos, L.V.; Zanchet, D.; Noronha, F.B.; Bueno, J.M.C. *Appl. Catal. A: Gen.* **2008**, 348, 183, 192.

130. Ryu, J.-H.; Lee, K.-Y.; Kim, H.-J.; Yang, J.-I.; Jung, H. *Appl. Catal. B: Environ.* **2008**, 80. 306-312.

131. Tsang, S.C.; Claridge, J.B.; Green, M.L.H. *Catal. Today* **1995**, 23, 3-15.

132. Hickmann, D.A.; Schmidt, L.D. *J. Catal.* **1992**, 138, 267-282.

133. Hickmann, D.A.; Schmidt, L.D. *Science* **1993**, 259, 343-346.

134. Hickmann, D.A.; Haupfear, E.A.; Schmidt, L.D. *Catal. Lett.* **1993**, 17, 223-237.

135. Hickmann, D.A.; Schmidt, L.D. *AIChE J.* **1993**, 39, 1164-1177.

136. Liu, T.; Snyder, C.; Veser, G. *Ind. Eng. Chem. Res.* **2007**, 46, 9045-9052.

137. Nogare, D.D.; Degenstein, N.J.; Horn, R.; Canu, P.; Schmidt, L.D. *J. Catal.* **2008**, 258, 131–142.

138. Tanaka, H.; Kaino, R.; Okumura, K.; Kizuka, T.; Tomishige, K. *J. Catal.* **268,** 2009, 1–8.

139. Chin, Y.-H.; Buda, C.; Neurock, M.; Iglesia, E. *JACS* **133**, 2011, 15958-15978.

140. García-Diéguez, M.; Chin, Y.-H.; Iglesia, E. *J. Catal.* **285**, 2012, 260-272.

141. Tavazzi, I.; Beretta, A.; Groppi, G.; Forzatti, P. *Stud. Surf. Sci. Catal.* **2004**, 147, 163-168.

142. Donazzi, A.; Beretta, A.; Groppi, G.; Forzatti, P. *J. Catal.* **2008**, 255, 241-258.

143. Choudhary, V.R.; Mondal, K.C.; Choudhary, T.V. *Fuel* **2006**, 85, 2484-2488.

144. Choudhary, V.R.; Uphade, B.S.; Mamman, A.S. *Appl. Catal. A: Gen.* **1998**, 168, 33-46.

145. Jing, Q.; Lou, H.; Fei, J.; Hou, Z.; Zheng, X. *Int. J. Hydrogen Energ.* **2004**, 29, 1245-1251.

146. Choudhary, V.R; Choudhary, T.V. *Angew. Chem. Int. Ed.* **2008**, 47, 1828-1847.

147. Yu, W.; Xu, Y.; Mo, L.; Lou, H.; Zheng, X. *React. Kinet. Catal. Lett.* **2009**, 98,303-309.

148. He, S.; Jing, Q.; Yu, W.; Mo, L.; Lou, H.; Zheng, X. *Catal. Today* **2009**, 148, 130-133.

149. Ruckenstein, E.; Hu, Y.H. *Ind. Eng. Chem. Res.* **1998**, 37, 1744-1747.

150. Ruckenstein, E.; Wang, H.Y. *Catal. Lett.* **2001**, 73, 99-105.

151. Choudhary, V.R.; Mamman, A.S. *J. Chem. Technol. Biotechnol.* **1998**, 73, 345-350.

152. Choudhary, V.R.; Mondal, K.C.; Choudhary, T.V. *Appl. Catal. A: Gen.* **2006**, 306, 45-50.

153. Goldwasser, M.R.; Rivas, M.E.; Lugo, M.L.; Pietri, E.; Pérez-Zurita, J.; Cubeiro, M.L.; Griboval-Constant, A.; Leclercq, G. *Catal. Today* **2005**, 107–108, 106–113.

154. Wang, W.; Stagg-Williams, S.M.; Noronha, F.B.; Mattos, L.V.; Passos, F.B. *Catal. Today* **2004**, 98, 553, 563.

155. Tomishige, K. Kanazawa, S.; Ito, S.-I.; Kunimori, K. *Appl. Catal. A: Gen.* **2003**, 244, 71-82.

156. Tomishige, K. Kanazawa, S.; Sato, M.; Ikushima, K.; Kunimori, K. *Catal. Lett.* **2002**, 84, 69-74.

157. Mondal, K.C.; Choudhary, V.R.; Joshi, U.A. *Appl. Catal. A: Gen.* **2007**, 316, 47-52.

158. Zhang, G.; Dong, Y.; Feng, M.; Zhang, Y.; Zhao, W.; Cao, H. *Chem. Eng. J.* **2010**, 156, 519-523.

159. Liu, B.S.; Au, C.T. *Appl. Catal. A: Gen.* **2003**, 244, 181-195.

160. Yang, M.; Papp, H. *Catal. Today* **2006**, 115, 199-204.

161. Wang, D. *Chinese Sci. Bull.* **1999**, 44, 1153-1157.

162. Liu, D.; Quek, X.-Y.; Wah, H.H.A.; Zeng, G.; Li, Y.; Yang, Y. *Catal. Today* **2009**, 148, 243-250.

163. Shang, S.; Liu, G.; Chai, X.; Tao, X.; Li, X.; Bai, M.; Chu, W.; Dai, X.; Zhao, Y.; Yin, Y. *Catal. Today* **2009**, 268-274.

164. Daza, C.E.; Gallego, J.; Mondragón, F.; Moreno, S.; Molina, R. *Fuel* **2010**, 89, 592-603.

165. Valderrama, G.; Kiennemann, A.; Goldwasser, M.R. *J. Power Sources* **2010**, 195, 1765-1771.

166. Pereñíguez, R.; González-DelaCruz, V.M., Holgado, J.P.; Caballero, A. *Appl. Catal. B: Environ.* **2010**, 93, 346-353.

167. Babu, N.S.; Lingaiah, N.; Gopinath, R.; Reddy, P.S.S.; Prasad, P.S.S. *J. Phys. Chem. C* **2007**, 111, 6447-6453.

168. Bakker, J.J.W.; van der Neut, A.G.; Kreutzer, M.T.; Moulijn, J.A.; Kapteijn, F.; *J. Catal.* **2010**, 274, 176–191.

169. Costa, L.O.O.; Silva, M.; Borges, E.P.; Mattos, V.; Noronha, F.B. *Catal. Today* **2008**, 138, 147-151.

170. Doetzer, R.; Eysel, W. *JCPDS-ICDD*, PDF No. 049-0357.

171. Sleight, A.W. *Mater. Res. Bull.* **1968**, 3, 699-704.

172. Dias, J.A.C.; Assaf, J.M. *Appl. Catal. A: Gen.* **2008**, 334, 243-250.

173. Gaspar, A.B.; Dieguez, L.C. *Appl. Catal. A: Gen.* **2000**, 201, 241–251.

174. Hao, Z.; Zhu, Q.; Jianga, Z.; Baolin, H.; Hongzhong, L. *Fuel Process Technol.* **2009**, 90, 113-121.

175. Conner, Jr. W.C.; Falconer, J.L. *Chem. Rev.* **1995**, 95, 759-708.

176. Moulder, J. F.; Chastain (Eds.), *Handbook of X-ray Photoelectron Spectroscopy*, Perkin-Elmer, **1992**.

177. Velu, S.; Suzuki, K.; Vijayaraj, M.; Barman, S.; Gopinath, C.S. *Appl. Catal. B: Environ.* **2005**, 55, 287–299.

178. Stojanović, M.; Haverkamp, R.G.; Mims, C.A.; Moudallal, H. Jacobson, A.J. *J. Catal.* **1997**, 165, 315-323.

179. Lei, H.; Song, Z.; Bao, X.; Mu, X.; Zong, B.; Min, E. *Surf. Interface Anal.* **2001**, 32, 210–213.

180. Cheng, X.; Qi, Z.; Zhang, G.; Zhou, H.; Zhang, W.; Yin, M. *Physica B* **2009**, 404, 146-149.

181. Strohmeier, B. R.; Levden, D. E.; Field, R. S.; Hercules D. M. *J. Catal.* **1985**, 94, 514-530.

182. Uwamino, Y.; Ishizuka, Y.; Yamatera H. *J. Electron Spectrosc. Relat. Phenom.* **1984**, 34, 67-78.

183. Slinkard, W. E.; DeGroot, P. B. *J. Catal.* **1981**, 68, 423-432.

184. Dauscher, A.; Hilarie, L.; Le Normand, F.; Müller, W.; Maire, G.; Vasquez, A. *Surf. Interface Anal.* **1990**, 16, 341-346.

185. Kugai, J.; Subramani, V.; Song, C.; Engelhard, M.H.; Chin, Y.-H. *J. Catal*. **2006**, 238, 430-440.

186. Damyanova, S.; Pawelec, B.; Arishtirova, K.; Fierro, J.L.G.; Sener, C.; Dogu, T. *Appl. Catal. B: Environ.* **2009**, 92, 250–261.

187. Steinhauer, B.; Kasireddy, M.R.; Radnik, J.; Martin, A. *Appl. Catal. A: Gen.* **2009**, 366, 333–341.

188. Múnera, J.F.; Irusta, S.; Cornaglia, L.M.; Lombardo, E.A.; Cesar, D.V.; Schmal, M. *J Catal.* **2007**, 245, 25–34.

189. Trovarelli, A. *Catal. Rev. Sci. Eng.* **1996**, 38, 439-520.

190. Cunningham, J.; O'Brien, S.; Sanz, J.; Rojo, J.M.; Soria, J.; Fierro, J.L.G. *J. Mol. Catal.* **1990**, 57, 379-396.

191. Fan L.; Fujimoto, K. *J. Catal.* **1997**, 172, 238-242.

192. Tauster, S.J. *Acc. Chem. Res.* **1987**, 20, 389-394.

193. Li, B.; Maruyama, K.; Nurunnabi, M.; Kunimori, K.; Tomishige, K. *Ind. Eng. Chem Res.* **2005**, 44, 485-494.

194. Li, B.; Watanabe, R.; Maruyama, K.; Nurunnabi, M.; Kunimori, K.; Tomishige, K. *Appl. Catal. A* **2005**, 290, 36-45.

195. Li, B.; Maruyama, K.; Nurunnabi, M.; Kunimori, K.; Tomishige, K. *Appl. Catal. A* **2004**, 275, 157-172.

196. Tomishige, K.; Kanazawa, S.; Sato, M.; Ikushima, K.; Kunimori, K. *Catal. Lett.* **2002**, 84, 69-74.

197. Tomishige, K.; Kanazawa, S.; Ito, S.-I.; Kunimori, K. *Appl. Catal. A* **2003**, 244, 71-82.

198. Tomishige, K.; Nurunnabi, M.; Maruyama, K.; Kunimori, K. *Fuel Proc. Technol.* **2004**, 85, 1103-1120.

199. Zhao, Z.; Yang, X.; Wu, Y. *Appl. Catal. B: Environ.* **1996**, 8, 281–297.

200. Vernoux, P.; Guth, M.; Li, X. *Electrochem. Solid St.* **2009**, 12, E9-E11.

201. Seiyama, T.; Yamazoe, N.; Eguchi, K.; *Ind. Eng. Chem. Prod. Res. Dev.* **1985**, 24, 19-27.

202. N. Imanaka, T. Masui, Y. Mayama, and K. Koyabu, J. Solid State Chem. 178 (2005) 3601–3603.

203. Zhang, W.D.; Liu, B.S.; Zhu, C.; Tian, Y.L. *Appl. Catal. A: Gen.* **2005**, 292, 138-143.

204. Takenaka, S.; Shigeta, Y.; Tanabe, E.; Otsuka, K. *J. Catal.* **2003**, 220, 468-477.

205. Ogihara, H.; Takenaka, S.; Yamanaka, I.; Tanabe, E.; Genseki, A.; Otsuka, K. *J. Catal.* **2006**, 238, 353-360.

206. Takenaka, S.; Shigeta, Y.; Tanabe, E.; Otsuka, K. *J. Phys. Chem. B* **2004**, 108, 7656-7664.

207. Mukainakano, Y.; Li, B.; Kado, S.; Miyazawa, T.; Yoshida, K.; Okumura, K.; Miyao, T.; Naito, S.; Kunimori, K.; Tomishige, K. *Appl. Catal. A* **2007**, 318, 252–264.

208. Mukainakano, Y.; Yoshida, K.; Okumura, K.; Kunimori, K.; Tomishige, K. *Catal. Today* **2008**, 132, 101–108.

209. Yoshida, K.; Okumura, K.; Miyao, T.; Naito, S.; Ito, S.; Kunimori, K.; Tomishige, K. *Appl. Catal. A* **2008**, 351, 217–225.

210. Yoshida, K.; Begum, N.; Ito, S.; Tomishige, K. *Appl. Catal. A* **2009**, 358, 186–192.

211. Nurunnabi, M.; Kado, S.; Suzuki, K.; Fujimoto, K.; Kunimori, K.; Tomishige, K. *Cat. Comm.* **2006**, 7, 488-493.

212. Nurunnabi, M.; Mukainakano, Y.; Kado, S.; Miyao, T.; Naito, S.; Okumura, K.; Kunimori, K.; Tomishige, K. *Appl. Catal. A* **2007**, 325, 154–162.

213. Nurunnabi, M.; Mukainakano, Y.; Kado, S.; Miyazawa, T.; Okumura, K.; Miyao, T. Naito, S.; Suzuki, K.; Fujimoto, K.; Kunimori, K.; Tomishige, K. *Appl. Catal. A* **2006**, 308, 1–12.

214. Solymosi, F.; Kutsán, G.; Erdöhlyi, A. *Catal. Lett.* **1991**, 11, 149-156.

215. Zhao, Y.; Pan, Y.-X.; Xie, Y.; Liu, C.-J. *Catal. Comm.* **2008**, 9, 1558-1562.

216. Fidalgo, B.; Zubizarreta, L.; Bermúdez, J.M.; Arenillas, A.; Menéndez, J.A. *Fuel Process. Technol.* **2010**, 91, 765-769.

217. Quek, X.-Y.; Liu, D.; Cheo, W.N.E.; Wang, H.; Chen, Y.; Yang, Y. *Appl. Catal. B: Environ*. **2010**, 95, 374-382.

218. Kambolis, A.; Matralis, H.; Trovarelli, A.; Papadopoulou, Ch. *Appl. Catal. A: Gen.* **2010**, 377, 16-26.

219. García-Diéguez, M.; Pieta, I.S.; Herrera, M.C.; Larrubia, M.A.; Alemany, L.J. *J. Catal.* **2010**, 270, 136-145.

220. Sun, N.; Wen, X.; Wang, F.; Wei, W.; Sun, Y. *Energ. Environ. Sci.* **2010**, 3, 366-369.

221. Daza, C.E.; Gallego, J.; Mondragón, F.; Moreno, S.; Molina, R. Fuel **2010**, 89, 592-603.

222. Wang, N.; Chu, W.; Huang, L.; Zhang, T. *J. Nat. Gas. Chem.* **2010**, 19, 117-122.

223. Crisafulli, C.; Scirè, S.; Maggiore, R.; Minicò, S.; Galvagno, S. *Catal. Lett.* **1999**, 59, 21-26.

224. Kondarides, D.I. and Verykios, X.E. *J. Catal.* **1998**, 174, 52-64.

225. Yoshida, K.; Okumura, K.; Miyao, T.; Naito, S.; Ito, S.; Kunimori, K.; Tomishige, K. *Appl. Catal. A: Gen.* **2008**, 351, 217–225.

226. Aydin, R. *J. Chem. Eng. Data* **2007**, 52, 2400-2404.

227. Bellido, J.D.A.; Assaf, M.A. *Appl. Catal. A: Gen.* **2009**, 352, 179-187.

228. Wagner, C.D.; Riggs, W.M.; Davis, L.E.; Moulder, J.F.; Muilenberg, G.E. (Editor), *Handbook of X-Ray Photoelectron Spectroscopy*, Perkin-Elmer, **1979**.

229. Gigola, C.E.; Moreno, M.S.; Costilla, I.; Sánchez, M.D. *Appl. Surf. Sci.* **2007**, 254, 325–329.

230. Shen, W.J.; Ichihashi, Y.; Okumura, M.; Matsumura, Y. *Catal. Lett.* **2000**, 64, 23–25.

231. Coulter, K.; Xueping, X.; Goodman, D.W. *J. Phys. Chem* **1994**, 98, 1245-1249.

232. Alexeev, O.S.; Krishnamoorthy, S.; Jensen, C.; Ziebarth, M.S.; Yaluris, G.; Roberie, T.G.; Amiridis, M.D. *Catal. Today* **2007**, 127, 189-198.

233. Mahata, N.; Vishwanathan, V. *J. Catal.* **2000**, 196, 262-270.

234. Xu, Z.; Li, Y.; Zhang, J.; Chang, L.; R. Zhou, R.; Duan, Z. *Appl. Catal. A: Gen.* **2001**, 210, 45–53.

235. Cheng, Z.X.; Wu, Q.; Li, J.L.; Zhu, Q.M. *Catal. Today* **1996**, 30, 147-155.

236. Bickford, E. S.; Velu, S.; Song, C. *Catal. Today* **2005**, 99, 347-357.

237. Fox, E.B.; Velu, S.; Engelhard, M.H.; Chin, Y.-H.; Miller, J.T.; Kropf, J.; Song, C. *J. Catal.* **2008**, 260, 358-370.

238. Kugai, J.; Miller, J.T.; Guo, N.; Song, C. *J. Catal.* **2011**, 277, 46-53.

239. Barama, S.; Dupeyrat-Batiot, C.; Capron, M.; Bordes-Richard, E.; Bakhti-Mohammedi, O. *Catal. Today* **2009**, 141, 385-392.

240. Christensen, K.O.; Chen, D.; Lødeng, R.; Holmen, A. *Appl. Catal. A: Gen.* **2006**, 314, 9-22.

241. York, A. P. E.; Xiao, T.; Green, M. L. H.; Claridge, J.B. *Catal. Rev.* **2007**, 49, 511-560.

242. Snoeck, J.-W.; Froment, G.F.; Fowles, M. *J. Catal.* **1997**, 169, 240-249.

243. Zhang, W.D.; Liu, B.S.; Zhu, C.; Tian, Y.L. *Appl. Catal. A: Gen.* **2005**, 292, 138-143.

244. Bozzolo, G.; Noebe, R.D. *Acta Mater*. **2003**, 51, 4395-4409.

245. Helfensteyn, S.; Luyten, J.; Feyaerts, L.; Creemers, C. *Appl. Surf. Sci.* **2003**, 212-213, 844-849.

246. Tomishige, K. *J. Jpn. Petrol. Inst.* **2007**, 50, 287-298.

247. Dalin, L.; Nakagawaa, Y.; Tomishige, K. *Appl. Catal. A: Gen.* **2011**, 408, 1-24.

248. Song, C. *Catal. Today* **2006**, 115, 2-32.

249. Sun, G.B.; Hidajat, K.; Wu, X.S.; Kawi, S. *Appl. Catal. B: Environ.* **2008**, 81, 303–312.

250. Sordelet, D.; Akinc, M. *J. Colloid Interf. Sci.* **1998**, 122, 47-59.

251. Sohn, S.; Kwon, Y.; Kim, Y.; Kim, D. *Powder Technol.* **2004**, 142, 136-153.

252. Li, N.; Yanagisawa, K. *J. Solid State Chem.* **2008**, 181, 1738-1743.

253. Wu, X.; Tao, Y.; Dong, L.; Hu, Z. *J. Cryst. Growth* **2005,** 277, 643-649.

254. Wan, J.; Wang, Z.; Chen, X.; Mu, L.; Qian, Y. *J Cryst. Growth* **2005**, 284, 538-543.

255. Ertl, G.; Knozinger, H.; Weitkamp, J. *Preparation of solid catalysts* **1999**, Singapore: Wiley VCH.

256. Matsuo, Y.; Yoshinaga, Y.; Sekine, Y.; Tomishege, K.; Fujimoto, K. *Catal. Today* **2000**, 63, 439-445.

257. Mo, L.Y.; Zheng, X.M.; Chen, Y.H.; Fei, J.H. *Catal. Lett.* **2003**, 78, 237-242.

258. D.C. Harris, Quantitative Chemical Analysis, 2nd ed., Freeman, New York, 1987, p. 726.

259. Bellido, J.D.A.; Souza, J.E.D.; Peko, J.-C.M.; Assaf, E.M. *Appl. Catal. A: Gen.* **2009**, 358, 215-223.

260. Wu, X.; Kawi, S. *Cryst. Growth Des.* **2010**, 10, 1833-1841.

261. Lina, S.S.; Chen, C.L.; Chang, D.J.; C. C. Chen *Water Res.* **2002**, 36, 3009-3014.

262. Mamontov, E.; Egami, T.; Brezny, R.; Koranne, M.; Tyagi, S. *J. Phys. Chem. B* **2000**, 104, 11110-11116.

263. Mamontov, E.; Egami, T. *J. Phys. Chem. Solids* **2000**, 61, 1345–1356.

264. Habimana, F.; Li, X.; Ji, S.; Lang, B.; Sun, D.; Li, C. *J. Nat. Gas Chem.* **2009**, 18, 392–398.

265. Pospíšil, M.; Kaňoková, P. J. Therm. Anal. Calorim. 1997, 58, 77-88.

266. Song, H.; Ozkan, U.S. *J. Catal.* **2009**, 261, 66‑74.

267. Liu, Y.; Wen, C.; Guo, Y.; Lu, G.; Wang, Y. *J. Mol. Catal. A: Chem.* **2010**, 316, 59–64.

268. Alifanti, M.; Kirchnerova, J.; Delmon, B.; Klvana, D. *Appl. Catal. A: Gen.* **2004**, 262, 167–176.

269. Xu, Z.; Li, Y.; Zhang, J.; Chang, L.; Zhou, R.; Duan, Z. *Appl. Catal. A: Gen.* **2001**, 210, 45–53.

270. Navarro, R.M.; Álvarez-Galván, M.C.; Rosa, F.; Fierro, J.L.G. *Appl. Catal. A: Gen* .**2006**, 297, 60-72.

271. Choudhary, V.R.; Rajput, A.M.; Rane, V.H. *Catal. Lett.* **1992**, 16, 269–272.

272. Choudhary, V.R.; Mammon, A.S.; Sansare, S.D. *Angew. Chem. Int. Ed.***1992**, 31, 1189-1190.

273. Tanaka, H.; Kaino, R.; Okumura, K.; Kizuka, T.; Tomishige, K. *J. Catal.* **2009**, 268, 1-8.

274. Araujo, J.C.S.; Zanchet, D.; Rinaldi, R.; Schuchardt, U.; Hori, C.E.; Fierro, J.L.G.; Bueno, J.M.C. *Appl. Catal. B: Environ.* **2008**, 84, 552-562.

275. Froment, G.F.; Bischoff, K.B. *Chemical Reactor Analysis and Design*, 2nd ed., Wiley, New York, **1990**.

276. Akpan, E.; Sun, Y.; Kumar, P.; Ibrahim, H.; Aboudheir, A.; Idem, R. *Chem. Eng. Sci.* **2007**, 62, 4012-4024.

277. Verykios, X.E. *Stud. Surf. Sci. Catal.* **1998**, 119, 795-800.

278. Gubanova, E.L.; Schuurman, Y.; Sadykov, V.A.; Mirodatosa, C.; van Veen, A.C. *Chem. Eng. J.* **2009**, 154, 174-184.

279. Campbell, C.T. *Topics Catal.* **1994**, 1, 353-366.

280. Ginés, M.J.L.; Marchi, A.J.; Apesteguía, C.R. *Appl. Catal. A: Gen* .**1997**, 154, 155-171.

281. Nakamura, J.; Rodriguez, J.A.; Campbell, C.T. *J. Phys.: Condens. Matter* 1989, 1, SB149

282. Bitter, J.H.; Seshan, K.; Lercher, J.A. *J. Catal.* **1998**, 176, 93-101.

283. Ferreira-Aparicio, P.; Fernandez-Garcia, M.; Guerrero-Ruiz, A.; Rodríguez-Ramos,I. *J. Catal.* **2000**, 190, 296-308.

284. Patel, S.; Pant, K.K. *Appl. Catal. A: Gen.* **2009**, 356, 189-200.

APPENDIX

Publications list based on the results obtained in this thesis

Journal Papers

[1] U. Oemar, K. Hidajat, and S. Kawi, Role of catalyst support over PdO–NiO catalysts on catalyst activity and stability for oxy-CO_2 reforming of methane, Applied Catalysis A: General 402 (2011) 176– 187.

[2] U. Oemar, K. Hidajat, and S. Kawi, Roles of Pd precursors on catalyst performance of Pd–Ni/Y_2O_3 catalyst for syngas production via oxy-CO_2 reforming of CH_4, submitted.

[3] U. Oemar, K. Hidajat, and S. Kawi, Pd−Ni catalyst over spherical nanostructured Y_2O_3 support for Oxy-CO_2 reforming of methane: Role of surface oxygen mobility, submitted.

Presentation and Conference Papers

[1] U. Oemar, K. Hidajat, and S. Kawi, Role of catalyst support over PdO-NiO catalysts on catalyst activity and stability for oxy-CO_2 reforming of methane, Poster presentation, 4th Singapore Catalysis Forum in Singapore, May 20, 2011.

[2] U. Oemar, K. Hidajat, and S. Kawi, Bimetallic Pd−Ni catalyst supported on Y_2O_3 nanocrystal: Active and stable catalyst for oxy-CO_2 reforming of methane, Poster presentation, Natural Gas Conversion Symposium (NGCS) 9, Lyon, France, May 30-June 3, 2010.

[3] U. Oemar, K. Hidajat, and S. Kawi, Bimetallic Pd−Ni catalyst supported on Y_2O_3 nanocrystal: Active and stable catalyst for oxy-CO_2 reforming of methane, Poster presentation, 2nd Singapore Catalysis Forum in Singapore, August 17, 2009.

[4] U. Oemar, K. Hidajat, and S. Kawi, Syngas production by Oxy-CO_2 reforming of methane over Pd−Ni catalyst: Role of catalyst support, Poster presentation, 21st North American Catalysis Society Meeting, San Francisco, June 7-12, 2009.

[5] U. Oemar, K. Hidajat, and S. Kawi, Oxy-CO_2 reforming of methane on Pd−Ni/Y_2O_3: Role of Pd−Ni interaction, Oral presentation, 239th ACS National Meeting & Exposition, San Francisco, March 21-25, 2010.

[6] U. Oemar, K. Hidajat, and S. Kawi, Pd−Ni catalyst over spherical nanostructured Y_2O_3 support for Oxy-CO_2 reforming of methane: Role of surface oxygen mobility, Oral presentation, 6th Asia Pacific Chemical Reaction Engineering Symposium, Beijing, China, September 18-21, 2011.